UCLA
UCLA Electronic Theses and Dissertations

Title
Studies of turbulence and flows in the DIII-D tokamak

Permalink
https://escholarship.org/uc/item/61p397qb

Author
Hillesheim, Jon Clark

Publication Date
2012

Peer reviewed|Thesis/dissertation

eScholarship.org Powered by the California Digital Library
University of California

University of California

Los Angeles

Studies of turbulence and flows in the DIII-D tokamak

A dissertation submitted in partial satisfaction

of the requirements for the degree

Doctor of Philosophy in Physics

by

Jon Clark Hillesheim

2012

© Copyright by
Jon Clark Hillesheim
2012

Abstract of the Dissertation

Studies of turbulence and flows in the DIII-D tokamak

by

Jon Clark Hillesheim

Doctor of Philosophy in Physics

University of California, Los Angeles, 2012

Professor Troy A. Carter, Chair

Understanding the turbulent transport of particles, momentum, and heat continues to be an important goal for magnetic confinement fusion energy research. The turbulence in tokamaks and other magnetic confinement devices is widely thought to arise due to linearly unstable gyroradius-scale modes. A long predicted characteristic of these linear instabilities is a critical gradient, where the modes are stable below a critical value related to the gradient providing free energy for the instability and unstable above it. In this dissertation, a critical gradient threshold for long wavelength ($k_\theta \rho_s \lesssim 0.4$) electron temperature fluctuations is reported, where the temperature fluctuations do not change, within uncertainties, below a threshold value in $L_{T_e}^{-1} = |\nabla T_e|/T_e$ and steadily increase above it. This principal result, the direct observation of a critical gradient for electron temperature fluctuations, is also the first observation of critical gradient behavior for *any* locally measured turbulent quantity in the core of a high temperature plasma in a systematic experiment. The critical gradient was found to be $L_{T_e}^{-1}|_{crit} = 2.8 \pm 0.4$ m^{-1}. The experimental value for the critical gradient quantitatively disagrees with analytical predictions for its value. In the experiment, the local value of $L_{T_e}^{-1}$ was systematically varied by changing the deposition location of electron cyclotron heating gyrotrons in the DIII-D tokamak. The temperature fluctuation measurements were acquired with a correlation electron cyclotron emission radiometer. The dimensionless pa-

rameter $\eta_e = L_{n_e}/L_{T_e}$ is found to describe both the temperature fluctuation threshold and a threshold observed in linear gyrofluid growth rate calculations over the measured wave numbers, where a rapid increase at $\eta_e \approx 2$ is observed in both. Doppler backscattering (DBS) measurements of intermediate-scale density fluctuations also show a frequency-localized increase on the electron diamagnetic side of the measured spectrum that increases with $L_{T_e}^{-1}$. Measurements of the crossphase angle between long wavelength electron density and temperature fluctuations, as well as measurements of long wavelength density fluctuation levels were also acquired. Multiple aspects of the fluctuation measurements and calculations are individually consistent with the attribution of the critical gradient to the ∇T_e-driven trapped electron mode. The accumulated evidence strongly enforces this conclusion. The threshold value for the temperature fluctuation measurements was also within uncertainties of a critical gradient for the electron thermal diffusivity found through heat pulse analysis, above which the electron heat flux and electron temperature profile stiffness rapidly increased. Toroidal rotation was also systematically varied with neutral beam injection, which had little effect on the temperature fluctuation measurements. The crossphase measurements indicated the presence of different instabilities below the critical gradient depending on the neutral beam configuration, which is supported by linear gyrofluid calculations.

In a second set of results reported in this dissertation, the geodesic acoustic mode is investigated in detail. Geodesic acoustic modes (GAMs) and zonal flows are nonlinearly driven, axisymmetric ($m = 0,\ n = 0$ potential) $E \times B$ flows, which are thought to play an important role in establishing the saturated level of turbulence in tokamaks. Zonal flows are linearly stable, but are driven to finite amplitude through nonlinear interaction with the turbulence. They are then thought to either shear apart the turbulent eddies or act as a catalyst to transfer energy to damped modes. Results are presented showing the GAM's observed spatial scales, temporal scales, and nonlinear interaction characteristics, which may have implications for the assumptions underpinning turbulence models towards the tokamak edge ($r/a \gtrsim 0.75$). Measurements in the DIII-D tokamak have been made with multichannel Doppler backscattering systems at toroidal locations separated by 180°; analysis reveals that

the GAM is highly coherent between the toroidally separated systems ($\gamma > 0.8$) and that measurements are consistent with the expected $m = 0,\ n = 0$ structure. Observations show that the GAM in L-mode plasmas with $\sim 2.5 - 4.5$ MW auxiliary heating occurs as a radially coherent eigenmode, rather than as a continuum of frequencies as occurs in lower temperature discharges; this is consistent with theoretical expectations when finite ion Larmor radius effects are included. The intermittency of the GAM has been quantified, revealing that its autocorrelation time is fairly short, ranging from about 4 to about 15 GAM periods in cases examined, a difference that is accompanied by a modification to the probability distribution function of the $E \times B$ velocity at the GAM frequency. Conditionally-averaged bispectral analysis shows the strength of the nonlinear interaction of the GAM with broadband turbulence can vary with the magnitude of the GAM. Data also indicates a wave number dependence to the GAM's interaction with turbulence. Measurements also showed the existence of additional low frequency zonal flows (LFZF) at a few kilohertz in the core of DIII-D plasmas. These LFZF also correlated toroidally. The amplitude of both the GAM and LFZF were observed to depend on toroidal rotation, with both types of flows barely detectable in counter-injected plasmas.

In a third set of results the development of diagnostic hardware, techniques used to acquire the above data, and related work is described. A novel multichannel Doppler backscattering system was developed. The five channel system operates in V-band (50-75 GHz) and has an array of 5 frequencies, separated by 350 MHz, which is tunable as a group. Laboratory tests of the hardware are presented. Doppler backscattering is a diagnostic technique for the radially localized measurement of intermediate-scale ($k_\theta \rho_s \sim 1$) density fluctuations and the laboratory frame propagation velocity of turbulent structures. Ray tracing, with experimental profiles and equilibria for inputs, is used to determine the scattering wave number and location. Full wave modeling, also with experimental inputs, is used for a synthetic Doppler backscattering diagnostic for nonlinear turbulence simulations. A number of non-ideal processes for DBS are also investigated; their impact on measurements in DIII-D are found, for the most part, to be small.

The dissertation of Jon Clark Hillesheim is approved.

William A. Peebles

Warren B. Mori

George J. Morales

Chandrasekhar Joshi

Troy A. Carter, Committee Chair

University of California, Los Angeles

2012

To my parents.

Table of Contents

List of Figures

List of Tables

Acknowledgments

There are numerous individuals whose support, guidance, encouragement, and advice I would like to acknowledge. First and foremost, I gratefully acknowledge the steadfast support from my advisors throughout the course of work towards this dissertation, Dr. Tony Peebles and Professor Troy Carter. I would also like to thank my advisor during my ORISE practicum at the University of Maryland, Professor Bill Dorland, for his advice and insightful discussions. I also owe acknowledgment to advisors who helped me get into the field as undergraduate: Professor David T. Anderson at the University of Wisconsin and Dr. Jill Foley with Nova Photonics, my mentor at PPPL through the NUF program. I would like to also thank Dr. Lothar Schmitz and Dr. Terry Rhodes for many discussions and indispensable assistance during experiments. I am also grateful for the assistance of Craig Wannberg and Xuan Nguyen, and also for useful discussions with other current and former members of the UCLA PDG including Professor Anne White, Professor Pierre Gourdain, Dr. Guiding Wang, Dr. Lei Zeng, Dr. Edward Doyle, and Dr. Shige Kubota. I acknowledge Dr. Neal Crocker for many lively and useful discussions. I also acknowledge and thank the UCLA undergraduates Aaron Senter and Robert Martin for their work supporting hardware development and programming. There are a number of researchers at General Atomics I would like to thank, in particular Dr. Jim DeBoo, Dr. Chris Holland, and Dr. Gary Staebler for their assistance, guidance, and discussions. I thank Dr. George McKee and Dr. Zheng Yan for the analysis of beam emission spectroscopy data. I am also thankful for the many discussions with other graduate students and young researchers, including Dr. David Pace, Dr. Chris Cooper, Dr. Michael Barnes, and Jie Zhang.

I thank the organizers and program committee of the 51^{st} APS-DPP meeting, 18^{th} HTPD, the Wolfgang Pauli Institute, the Center for Multi-scale Plasma Dynamics, US TTF 2012, the NSTX experimental science science group at PPPL, and the Alcator C-mod turbulence group at MIT for giving me opportunities to present results to the community.

I gratefully acknowledge support from the Fusion Energy Sciences Graduate Fellowship

Program administered by Oak Ridge Institute for Science and Education under a contract between the U.S. Department of Energy and the Oak Ridge Associated Universities, between the years 2007-2010.

Vita

2000-2003	Jefferson Senior High School, Alexandria, Minnesota, USA
2007	B.S. Physics and B.S. Electrical Engineering University of Wisconsin, Madison, USA
2007-2010	ORISE Fusion Energy Sciences Graduate Fellow UCLA, Los Angeles, California, USA Department of Physics and Astronomy
2007-2012	Physics Division Fellowship Recipient UCLA, Los Angeles, California, USA Department of Physics and Astronomy
2009	M.S. Physics UCLA, Los Angeles, California, USA
2010-2012	Graduate Student Researcher UCLA, Los Angeles, California, USA Department of Physics and Astronomy

Publications and Presentations

Observation of a Critical Gradient Threshold for Electron Temperature Fluctuations in the DIII-D Tokamak

J.C. Hillesheim *et al.*, Phys. Rev. Lett (submitted 2012).

Observation of a Critical Gradient Threshold for Electron Temperature Fluctuations in Low Torque DIII-D Plasmas

J.C. Hillesheim *et al.*, Plenary Talk, U.S. Transport Task Force Workshop, Annapolis, Maryland, April 10, 2012.

2D full wave modeling for a synthetic Doppler backscattering diagnostic
J.C. Hillesheim *et al.*, Rev. Sci. Instrum. **83**, 10E331 (2012).

Experimental investigation of geodesic acoustic mode spatial structure, intermittency, and interaction with turbulence in the DIII-D tokamak
J.C. Hillesheim *et al.*, Phys. Plasmas **19**, 022301 (2012).

New Plasma Measurements with a Multichannel Millimeter-wave Fluctuation Diagnostic System in the DIII-D Tokamak
J.C. Hillesheim *et al.*, Invited Talk, 18^{th} Topical Conference on High Temperature Plasma Diagnostics, Wildwood, New Jersey, May 18, 2010.

New plasma measurements with a multichannel millimeter-wave fluctuation diagnostic system in the DIII-D tokamak (invited)
J.C. Hillesheim *et al.*, Rev. Sci. Instrum. **81**, 10D907 (2010).

Measurements of the Spatial Structure of Geodesic Acoustic Modes in DIII-D
J.C. Hillesheim *et al.*, Contributed Oral, 51^{st} American Physical Society Division of Plasma Physics Meeting, Bull. Am. Phys. Soc. **54**, 59 (2009).

A multichannel, frequency-modulated, tunable Doppler backscattering and reflectometry system
J.C. Hillesheim *et al.*, Rev. Sci. Instrum. **80**, 083507 (2009).

CHAPTER 1

Introduction

It is possible to confine a plasma at sufficiently high temperatures and densities that the constituent ions of the plasma fuse together into heavier nuclei, releasing energy in the process. Gravitational confinement causes this to occur in the core of stars. If this can be done efficiently through other methods on the Earth, nuclear fusion could be a commercially viable power source. One way to confine the plasma is with a strong magnetic field. The magnetic confinement approach to fusion energy has been making progress since its inception in the 1950's. Early fusion energy researchers were optimistic, since if collisional estimates of the transport of particles and heat across magnetic field lines accounted for all transport, then fusion would have proved relatively easily achievable. Transport in magnetically confined plasmas is typically orders of magnitude higher than collisional estimates. An overview of the tokamak approach to fusion energy can be found in Ref. [1] and references therein.

Advances in theory, computation, and measurements have led to the widely-held conclusion that this "anomalous" transport arises due to gyroradius-scale "microinstabilities," which transport particles, momentum, and heat across the magnetic field. A critical issue for the progress of fusion energy science is development of a validated, predictive physical model for plasma turbulence and transport. In the past $\sim$ 10 years, diagnostics and simulations have advanced to the point where measured turbulent fluctuation levels, wave number spectra, crossphases between fluctuating fields, and more have been directly compared to nonlinear simulations through use of synthetic diagnostics. The mix of agreement and disagreement of comparisons so far performed implies that while existing models show great promise, there are still issues that need to be resolved before they can relied upon for

accurate predictions.

The work in this dissertation was performed at the DIII-D tokamak in San Diego, CA, and is organized around three areas: study of the geodesic acoustic mode, study of fluctuations in multiple fields in an experiment where the electron temperature gradient and rotation were systematically varied, and development of diagnostics that enabled these studies to take place.

1.1 Summary of the dissertation

The most significant result presented in this dissertation is the observation of a critical gradient threshold for long wavelength ($k_\theta \rho_s \lesssim 0.4$) electron temperature fluctuations measured with a correlation electron cyclotron emission (CECE) radiometer. Below a threshold in the electron temperature scale length, $L_{T_e}^{-1} = |\nabla T_e|/T_e$, measurements of electron temperature fluctuations did not change within uncertainties, while above the critical value they steadily increased. The threshold was found to be well described by the dimensionless parameter $\eta_e = L_{n_e}/L_{T_e}$ for both the temperature fluctuation measurements and in linear gyrofluid calculations. Measurements of intermediate-scale ($k_\theta \rho_s \sim 0.8$) density fluctuations with Doppler backscattering (DBS) also showed frequency-localized increases in the measured spectra, implying a new mode was being driven unstable. A range of measurements, supported by the linear gyrofluid calculations, were consistent with the attribution of the threshold to the ∇T_e-driven trapped electron mode (TEM) instability. The accumulated evidence strongly constrains this conclusion. It is notable that the linear predictions showed agreement with the measured threshold value for temperature fluctuations. This is compatible with predictions from past simulation work that showed no nonlinear upshift of the ∇T_e-TEM critical gradient (*i.e.* no Dimits shift). This is significant as, in the simulations, this was related to zonal flow shear playing little role for ∇T_e-TEM, which leaves open the question of how ∇T_e-TEM turbulence saturates.

This principal result is also the first direct observation of critical gradient behavior for

measurements of *any* locally measured turbulent quantity in the core of a tokamak in a systematic experiment. This is important as it substantiates the widely-held view that the turbulence in magnetic confinement fusion devices arises from linearly unstable modes. The critical gradient was found to be $L_{T_e}^{-1}|_{crit} = 2.8 \pm 0.4$ m^{-1}. The experimental value for the critical gradient quantitatively disagrees with analytical predictions for its value.

The value of the critical gradient for electron temperature fluctuations was within uncertainties of a critical gradient value found for the electron thermal diffusivity from heat pulse analysis. Above this value, electron profile stiffness increased. Stiffness characterizes the incremental increase in flux for a given incremental increase in gradient. A high value of stiffness results in little change to equilibrium profiles with increased source input. As fusion power is proportional to pressure squared, a high value of stiffness enforces diminishing returns on additional heating for any future reactor. The results presented show that ∇T_e-TEM and the resultant temperature fluctuations play a causal (though likely only partial) role for the increased heat flux, diffusivity, and stiffness. This might be of importance for future burning plasmas, where strong electron heating from alpha particles is expected.

The systematic scans of $L_{T_e}^{-1}$ were performed by changing the deposition location of gyrotrons used for electron cyclotron heating. The direction of momentum direction from neutral beams was used to study the dependence of the critical gradient and stiffness on toroidal rotation. Toroidal rotation was observed to have little effect on the transport, unlike what has previously been observed for ion thermal transport and stiffness (although the latter result was from a different experiment, with different plasma conditions). Measurements of the crossphase angle between electron density and temperature fluctuations made by coupling the CECE system with a reflectometer were also acquired. The crossphase measurements indicated different instabilities were active below the critical gradient for the different rotation cases, which was supported by linear gyrofluid calculations and other measurements.

The geodesic acoustic mode (GAM) was also studied. It was found that the GAM exhibits long range toroidal correlations, which were consistent with the expected axisymmetric (toroidally and poloidally symmetric potential) properties of zonal flows. Zonal flows

are thought to play an important role as a saturation mechanism for core turbulence in tokamaks and other magnetized plasmas. They have also been observed to play a role during L-H transitions in tokamaks. In typical conditions, the GAM is observed to have a constant frequency with radius over a significant fraction of the minor radius (as much as $\sim 1/6$). Theoretical description of this observation requires kinetic finite gyroradius effects to explain. The GAM is also often observed to be radially coherent over dozens of gyroradii–longer than the correlation length of the turbulence itself–which violates the local assumption made in many turbulence simulations. It was found that the GAM appears to have a dependence on toroidal rotation, which has not been predicted.

Studies of the interaction between the GAM and turbulence through bispectral analysis also showed that the strength of the interaction depends on the amplitude of the GAM and that it depends on the wavenumber of the fluctuations.

Measurements also showed the existence of additional low frequency zonal flows (LFZF) at a few kilohertz in the core of DIII-D plasmas. These LFZF also correlated toroidally and exhibited the same rotation dependence as the GAM.

Diagnostic development efforts were necessary to enable these measurements. In particular, a novel multichannel millimeter-wave diagnostic that has been used for DBS and reflectometry measurements was developed in the course of work towards this dissertation. In addition to the diagnostic hardware; data analysis, interpretation, and modeling efforts were also advanced, including a synthetic DBS diagnostic for use with nonlinear gyrokinetic simulations that makes use of full wave modeling.

1.1.1 Summary of publications related to the dissertation

Several publications have resulted both from the diagnostic development efforts undergone in the course of this dissertation and from the application of the diagnostics and data analysis procedures for physics studies. These publications and their relation to work described in later Chapters are summarized here.

Chronologically, the first element of the dissertation completed were a set of analysis routines that integrated gathering equilibrium information, running a ray tracing program, and analyzing the results, which are described in Sec. 3.4.1. These routines were used in Schmitz *et al.* [2] for DBS interpretation and in White *et al.* [3] to estimate refractive effects on the CECE spot size. Schmitz *et al.* [4] studied reductions of electron temperature fluctuations with CECE and intermediate-k density fluctuations with DBS in H-mode DIII-D plasmas. The ray tracing routines were used for DBS interpretation. Further studies incorporating DBS measurements were presented in Schmitz *et al.* [5].

Hillesheim *et al.* [6] described the DBS hardware developed for this dissertation (referred to as DBS-5) and presented the first data from the diagnostic. Documentation of hardware development can be found in Chapter 3. Lessons learned during the development of that hardware informed the design and development of subsequent DBS hardware systems, which was described in Peebles *et al.* [7] (referred to as DBS-8). Optimized quasi-optical components were developed and detailed in Rhodes *et al.* [8].

In an experiment designed to investigate electron turbulence, DBS-5 was used to measure the response of intermediate-scale density fluctuations to modulation of the electron temperature gradient. The experimental results and initial gyrokinetic simulation results were presented in DeBoo *et al.* [9]. Further gyrokinetic simulations of that experiment were conducted and presented in Holland *et al.* [10], which included comparisons between DBS measured changes to intermediate-scale density fluctuations due to the gradient modulation and output from a synthetic DBS diagnostic applied to outputs from a nonlinear gyrokinetic code. Full wave modeling for the synthetic DBS diagnostic is described in Sec. 3.4.2 and published in Hillesheim *et al.* [11]. Results from the experiment in Ref. [9] also led to the experiment described in detail in Chapter 5. Manuscripts related to Chapter 5 have been submitted for publication, including DeBoo *et al.* [12], Hillesheim *et al.* [13], and Hillesheim *et al.* [14].

Hillesheim *et al.* [15] included investigation of the DBS phase for detailed physics studies, application of those techniques to the geodesic acoustic mode, toroidal correlation of

the GAM between DBS-5 and DBS-8, radial propagation of the GAM, and investigation of measurements of the crossphase angle between electron density and temperature fluctuations, α_{n_e,T_e}. The first publication from DIII-D presenting α_{n_e,T_e} measurements–which are acquired through correlations between DBS-5 and CECE, and require between shot ray tracing analysis–was presented in White *et al.* [16], where quantitative agreement was found between measurements of α_{n_e,T_e} and gyrokinetic simulation results. The α_{n_e,T_e} results in Ref. [15] were also used in Wang *et al.* [17], along with other fluctuation measurements.

Work with the Transport Model Validation Task Force at DIII-D was also undertaken during the course of the dissertation, which included participation in the execution of experiments, acquisition of data, analysis, and interpretation. Results were presented in Holland *et al.* [18] and Rhodes *et al.* [19].

Extensive studies of the geodesic acoustic mode were presented in Hillesheim *et al.* [20]. The bulk of Ref. [20] comprises Chapter 4, with portions also found in Chapter 2 and Appendix A.

Studies of limit cycle zonal flow oscillations during slow L-H transitions were presented in Schmitz *et al.* [21], which made extensive use of DBS measurements and analysis routines.

1.2 Outline of the dissertation

This dissertation is divided into six chapters and seven appendices.

Chapter 1 is this introductory chapter.

Chapter 2 provides background context and reviews previous work on turbulence in tokamaks, with a perspective focused on measurable characteristics of the fluctuations.

Chapter 3 describes diagnostics, including hardware development, laboratory testing, data analysis, interpretation, and modeling. Background on the turbulence diagnostics used in this work are also reviewed, covering information on Doppler backscattering, correlation electron cyclotron radiometry, and conventional reflectometry.

Chapter 4 presents a number of measurements of the geodesic acoustic mode and other low frequency zonal flows.

Chapter 5 reports on the study of a range of turbulence measurements in an experiment with the local electron temperature scale length and toroidal rotation were systematically varied.

Chapter 6 summarizes conclusions and discusses future directions motivated by the results.

Appendix A contains statistical analysis definitions used in elsewhere in the dissertation.

Appendix B has historical information regarding the storage and retrieval of data from the turbulence diagnostics used in chapters of the dissertation.

Appendix C contains additional details and information about the experiment discussed in Chapter 5.

Appendix D reports on additional analysis of density-temperature crossphase measurements.

Appendix E discusses an alternate calculation of the coherency that has been used in past work for the CECE-reflectometry correlation measurements.

Appendix F contains a survey of novel analysis approaches and correlations of DBS data.

Appendix G presents an observational survey of additional measurements made with DBS diagnostics.

CHAPTER 2

Turbulence in tokamaks: background and review of existing work

In the absence of equilibrium-scale instabilities (*e.g.* sawteeth, kinks, and tearing modes), it is by now widely accepted that the transport of heat, particles, and momentum in magnetic confinement fusions experiments is determined by turbulent gyroradius-scale "microinstabilites" (*e.g.* ion temperature gradient, electron temperature gradient, microtearing, and trapped electron modes). For the most part, these are linearly unstable drift wave type instabilities, driven by density and temperature gradients in the plasma. In this context, "linear" means solutions of the linearized equations, which result in exponentially growing modes. These instabilities result in small ($\sim 1\%$) fluctuations in potential, density, and presure, which transport plasma across field lines.

The existence of exponentially growing modes immediately raises the question of how the modes saturate. The best understood saturation mechanism is thought to be zonal flows, which are axisymmetric (poloidally and toroidally constant potential) self-generated plasma $E \times B$ flows, which are driven through three-wave coupling with the turbulent modes (or, stated within a fluid framework, by the Reynolds stress). In this chapter, background and past work on turbulence and transport in tokamaks is reviewed, including a basic description of transport and the properties of commonly invoked small-scale instabilities and zonal flows, with a perspective focused on the measurable characteristics and testable predictions.

A critical issue for turbulence and transport in tokamaks is reaching a validated, predictive capability for the turbulent modes and the transport they cause. The leading model for turbulent transport in the core of tokamaks is the gyrokinetic model. Also briefly discussed

in this chapter are the gyrokinetic and gyrofluid models, an example instability (the slab ion temperature gradient mode), and past validation studies where measurements of fluctuations were directly compared to predictions from simulations.

2.1 Introduction

In this section, the basics of turbulent transport in tokamaks are discussed.

Early fusion work in the 1950's was optimistic, assuming the turbulence would not contribute greatly to transport. The theory of collisional transport in toroidal geometry is well-developed, called neoclassical transport theory [22]; unfortunately, measured transport levels are typically at least 1 to 2 orders of magnitude larger than neoclassical predictions. Several reviews of turbulence, transport, and the instabilities thought to cause them are available in the literature [23–27].

The fluctuation-induced fluxes can be written, using the electron heat flux, Q_e, for an example, as [24]

$$Q_e = \langle \tilde{p_e} \tilde{v_r} \rangle \,, \tag{2.1}$$

where $\tilde{p_e}$ are the electron pressure fluctuations, $\tilde{v_r}$ are radial velocity fluctuations, and the brackets $\langle ... \rangle$ denote an ensemble average. Dropping triple correlations and assuming electrostatic fluctuations, this can be expanded:

$$Q_e = \frac{3 n_e T_e}{2B} \sum_{k_\theta} k_\theta \left(\frac{\langle \tilde{n}_{e,k_\theta} \tilde{\varphi}_{k_\theta} \rangle}{n_e} + \frac{\left\langle \tilde{T}_{e,k_\theta} \tilde{\varphi}_{k_\theta} \right\rangle}{T_e} \right) , \tag{2.2}$$

where the k_θ are the poloidal wavenumbers of the fluctuations, n_e is the equilibrium electron density, $\tilde{n}_e$ are the density fluctuations, T_e is the equilibrium electron temperature, $\tilde{T}_e$ are the temperature fluctuations, $\tilde{\varphi}$ are the electrostatic potential fluctuations, and B is the equilibrium magnetic field. If the temperatures and density are taken to be moments of a kinetic distribution function, then this expression is generally correct. For two given fluctuating quantities, X and Y, the ensemble average can be written as $\langle X^* Y \rangle = |S_{xy}| e^{i \alpha_{xy}}$, where S_{xy} is the crosspower and α_{xy} is the crossphase between X and Y. Suppressing the

sum indices, the flux can then be written as

$$Q_e = \frac{3n_eT_e}{2B}k_\theta \left(\frac{|\tilde{n_e}|}{n_e}|\tilde{\varphi}|\gamma_{n_e,\varphi}\sin\alpha_{n_e,\varphi} + \frac{|\tilde{T_e}|}{T_e}|\tilde{\varphi}|\gamma_{T_e,\varphi}\sin\alpha_{T_e,\varphi} \right), \tag{2.3}$$

where γ_{xy} is the coherency between X and Y (sines appear instead of cosines due to the phase shift from $\tilde{v}_r$ to $\tilde{\varphi}$). This expression clearly illustrates that both the amplitude of temperature and density fluctuations can contribute, as well as the crossphase between each quantity and the electrostatic potential fluctuations. These quantities can all be measured in the edge of tokamak plasmas with probes, but accessing them in the core is challenging. Although no measurements of the directly transport related crossphases are presented in this dissertation, measurements of a related quantity, the crossphase between electron density and temperature fluctuations, are presented in later chapters.

2.1.1 Experimental evidence for turbulent transport

Once it was realized that transport in magnetic confinement fusion experiments greatly exceeded collisional calculations, experimental efforts attempted to measure turbulent fluctuations that could be causing the observed levels of transport. A brief overview of the experimental evidence for turbulent transport in the core of fusion devices is presented in this section. Among the first published evidence for for turbulent fluctuations in fusion plasmas were scattering measurements of density fluctuations in the PDX and ATC tokamaks [28–31]. Those measurements showed broad, Doppler-shifted spectra, at 10's to 100's of kHz, consistent with low frequency drift waves. It was also shown that the broad spectra were due to turbulent spectra, and not a broadening due to lack of spatial localization combined with varying rotation [32]. Further scattering studies showed spatial asymmetries and dependencies of the fluctuations [33, 34], evidence for modes propagating in opposite directions [34], and parametric dependencies of the fluctuations [35, 36].

Long wavelength measurements with beam emission spectroscopy (BES) argued that that estimates of the turbulent diffusivities from the low-k fluctuations was of the same order as the diffusivities inferred from power balance [37]. Low-k measurements with BES and re-

flectometry also both showed core density fluctuation levels of $\sim 1\%$ and radial correlation length lengths of a few centerimeters [37–39]. Heavy ion beam probe measurements of density and potential fluctuations also showed low frequency, turbulent spectra [40, 41]. Correlation electron cyclotron emission techniques also showed low frequency, turbulent spectra for electron temperature fluctuation measurements [42]; ion temperature fluctuation measurment were also made with BES [43].

The transition from low confinement (L-mode) to high confinement (H-mode) mode [44–46] was also connected to a reduction in fluctuation levels [47] in the edge.

More recent work aimed toward identification of particular instabilities and direct comparisons between measurements and nonlinear simulations are covered in later sections.

2.2 Gyrokinetic and gyrofluid models

In this section, the models to which experimental fluctuation measurements are to be compared to−gyrokinetics and gyrofluids−are discussed to give context for later chapters, where assumptions and predictions of the models will be compared to experimental measurements.

The dynamics of a non-relativistic, fully-ionized plasma can be fully described by the evolution of the distribution functions, $f_s(\mathbf{x}, \mathbf{v}, t)$, of its constituent species coupled to a closure. The Fokker-Planck equation for each species, where $\mathbf{x}$ is position and $\mathbf{x}$ is velocity, is

$$\frac{\partial f_s}{\partial t} + \frac{\partial f_s}{\partial \mathbf{x}}\frac{\partial \mathbf{x}}{\partial t} + \frac{\partial f_s}{\partial \mathbf{v}}\frac{\partial \mathbf{v}}{\partial t} = C[f_s, f_{s'}], \tag{2.4}$$

where $C[f_s, f_{s'}]$ is a collision operator summed over all other species. This accounts for all spatial and temporal scales, and for practical purposes, is currently too computationally intensive for use in turbulence simulations. The approach taken in gyrokinetics is to use scale separation to reduce the system to an equation which describes the dynamics of the turbulent part of the distribution function only; the system is then closed with the low frequency limit of Maxwell's equations. The gyrokinetic ordering can be traced to Ref. [48] and Ref [49]. More modern perspectives on gyrokinetics are available in Refs [50–52].

The small parameter in the standard gyrokinetic ordering is $\epsilon = \rho/L$, where ρ is a reference small spatial scale, the ion gyroradius, and L is a reference equilibrium scale, typically the minor radius of the tokamak, a. For the plasmas where comparisons between simulation and experiment are conducted in this thesis, core DIII-D L-mode plasmas, typical values of ρ_i/a are in the range $\sim 1/200$ to $\sim 1/600$, so ϵ is a good expansion parameter. The distribution function and fluctuating fields are expanded in ϵ, $f = f_0 + \epsilon f_1 + \epsilon^2 f_2 + ...$, where $\mathcal{O}(f_n/f) \sim \epsilon^n$, then averageed over the gyro-motion of the particles. The equation governing the evolution of the non-Boltzmann portion of the ϵ^1 gyro-averaged turbulent distribution function is the well known gyrokinetic equation:

$$\frac{\partial h}{\partial t} + (v_{||}\hat{\mathbf{b}} + \mathbf{v}_\chi + \mathbf{v_B}) \cdot \nabla h = \langle C[h] \rangle_{\mathbf{R}} + \frac{qF_0}{T} \frac{\partial \langle \chi \rangle_{\mathbf{R}}}{\partial t} - \mathbf{v}_\chi \cdot \nabla F_0. \tag{2.5}$$

Here

$$h = f_1 + \frac{q\Phi}{T} F_M \tag{2.6}$$

is the non-Boltzmann part of the perturbed distribution function. The sum of the curvature and ∇B drift velocities is

$$\mathbf{v_B} = \frac{\hat{\mathbf{b}}}{\Omega} \times \left[v_{||}^2 (\hat{\mathbf{b}} \cdot \nabla)\hat{\mathbf{b}} + \frac{v_{\perp^2}}{2} \frac{\nabla \mathbf{B}}{B} \right]. \tag{2.7}$$

The generalized potential is

$$\chi = \Phi - \frac{\mathbf{v}}{c} \cdot \mathbf{A}, \tag{2.8}$$

making the generalized $E \times B$ velocity

$$\mathbf{v}_\chi = \frac{\mathbf{B} \times \nabla \langle \chi \rangle_{\mathbf{R}}}{B^2}. \tag{2.9}$$

The brackets $\langle \ldots \rangle_{\mathbf{R}}$ indicate a gyroaverage at fixed guiding center $\mathbf{R}$.

$$F_0 = F_M \left(1 - \frac{q\Phi}{T} \right) \tag{2.10}$$

is the lowest order expansion of a Maxwell-Boltzmann distribution. A collision operator is denoted by $\langle C[h] \rangle_{\mathbf{R}}$. Ω is the gryofrequency, Φ is the electrostatic potential, $\mathbf{A}$ is the magnetic vector potential, $\hat{\mathbf{b}} = \mathbf{B}_0/B_0$ is the direction of the magnetic field, q is the species charge, and T is the species temperature. The system is closed with the low frequency limit of Maxwell's equations.

2.2.1 Implementations

The gyrokinetic model has been numerical implemented in several widely used codes. Brief calculations from the codes GYRO [53] and GS2 [54, 55] are presented later in this dissertation. GYRO began with the goal of generalizing GS2 by retaining radial profile variation[1], so they are very similar; although, both codes have received significant independent development over the last decade. Both codes are Eulerian (as opposed to particle-in-cell) solvers for the rigorous ϵ^1 gyrokinetic-Maxwell set of equations. Both codes can operate in the local limit ($\epsilon = \rho_s/a \to 0$), which corresponds to a single input value for each equilibrium parameter (*e.g.* density and temperature gradient scale lengths for each species); GYRO can also perform global runs where those values are allowed to vary radially. Both codes can include electrostatic and electromagnetic (both $A_\parallel$ and $B_\parallel$) fluctuations, multiple fully nonlinear gyrokinetic species, experimental magnetic field geometry, equilibrium $E \times B$ shear, equilibrium toroidal rotation, and collisions (electron-ion pitch angle scattering only for GYRO; GS2 can include energy diffusion terms and ion-ion collisions).

A number of results from the linear Trapped-Gyro-Landau-Fluid (TGLF) code are presented in Chapter 5. The development of the gyrofluid model can be traced to Ref. [56]. The TGLF equations are described in Ref. [57, 58]. The set of equations solved by TGLF are moments of the gyrokinetic equation, with a closure that retains phase mixing and Landau damping effects. The version of the code used in Chapter 5 is v1.93 [59], which includes a more complete collision model than earlier versions. The collision model approximates electron-ion collisions and contains a number of parameters determined through comparisons to GYRO, which has only pitch-angle scattering collisions. If energy diffusion terms play an important role, it would be outside the validity of the model.

[1] (https://fusion.gat.com/theory/Gyrooverview)

2.3 Transport inducing fluctuations and zonal flows

The paradigm most often invoked for the plasma turbulence in magnetically confined plasmas is that the turbulent fluctuations arise due to exponentially growing, linear, gyroradius-scale instabilities. These instabilities saturate through non-linear processes. One commonly invoked mechanism is zonal flows: non-linearly generated flows with axisymmetric (m=0, n=0) potential, but finite radial wavenumber, that are thought to either grow to sufficient amplitude that they shear apart the turbulence [60] or that they can act as a catalyst to transfer energy to linearly damped modes [61, 62]. The fastest growing linear modes are radially elongated, with radial wave number $k_r = 0$ (in simulations) at the outboard midplane (for an up-down symmetric plasma). In non-linear simulations these elongated modes are seen to be significantly affected by zonal flows [63], breaking up into smaller eddies. In some of the initial attempts to compare experimental measurements to simulations, it was found that zonal flows in the simulations were necessary to yield radial correlation lengths on the same order as those measured in experiment [64]. The mean zero frequency zonal flows, often associated with the Rosenbluth-Hinton residual flow [65], have been identified in fusion experiments [66].

Plasma turbulence dynamics are further enriched by mechanisms that can quench the linear instability. $E \times B$ shear suppression [67] is often invoked to explain the suppression of long wavelength turbulent fluctuations. The $E \times B$ drift sets the effective plasma rest frame; $E \times B$ shear is then effectively shear of the plasma rest frame, which limits the size of the turbulent structures. It has also been argued that, rather than reducing the amplitude of turbulence, strong $E \times B$ shear can instead modify the crossphase between the fluctuating fields [68].

Most of the discussion concerning turbulence in the chapter has been from the point of view of linear instabilities. Investigations of the parallel velocity gradient (PVG) instability [69] have also shown that sub-critical turbulence, where modes are linearly stable but grow transiently, is possible in tokamaks. [70–74].

2.3.1 Characteristics of commonly invoked gyroradius-scale instabilities in tokamaks

In this section, an example instability is presented to give context for later discussions. Then characteristics of commonly invoked gyroradius-scale instabilities–including ion temperature gradient, trapped electron, and electron temperature gradient modes–are briefly described, with a particular focus on experimentally measurable characteristics of the modes.

2.3.1.1 Simple example: slab ion temperature gradient instability

For context, derivation is given here of a simple example instability: the slab ion temperature gradient mode.

The linear, electrostatic, collisionless limit of the gyrokinetic equation is

$$\frac{\partial h}{\partial t} + (v_{||}\hat{\mathbf{b}} + \mathbf{v_B}) \cdot \nabla h + \mathbf{v}_{E\times B} \cdot \nabla F_0 = \frac{qF_0}{T}\frac{\partial \langle \Phi \rangle_{\mathbf{R}}}{\partial t}, \tag{2.11}$$

The $E \times B$ velocity is now

$$\mathbf{v}_{E\times B} = \frac{\mathbf{E}\times\mathbf{B}}{B^2} = \frac{\mathbf{B}\times\nabla\langle\Phi\rangle_{\mathbf{R}}}{B^2}. \tag{2.12}$$

This can be used with the quasi-neutrality condition (*i.e.* the gyrokinetic Poisson's equation),

$$\sum_s q_s \int \left(\langle h_s \rangle_{\mathbf{r}} - \frac{q_s \Phi}{T_s} F_{Ms} \right) d^3\mathbf{v} = 0, \tag{2.13}$$

where $\langle \ldots \rangle_{\mathbf{r}}$ indicates a gyroaverage at particle position $\mathbf{r}$, to solve for a linear dispersion relation. In slab geometry $(x,\ y,\ z)$:

$$\mathbf{B} = B_0 \hat{z}, \tag{2.14}$$

$$\frac{\partial n_{0,s}}{\partial x} = \frac{n_{0,s}}{L_{n,s}}, \tag{2.15}$$

$$\frac{\partial T_{0,s}}{\partial x} = \frac{T_{0,s}}{L_{T,s}}, \mathbf{v}_B = 0. \tag{2.16}$$

Take perturbed quantities to be of the form $h = \tilde{h} e^{(i(k_y y + k_z z - \omega t))}$. Then

$$-i\omega\tilde{h} + v_{||}(ik_z)\tilde{h} + \frac{\hat{\mathbf{z}}\times(ik_y\hat{\mathbf{y}})\langle\Phi\rangle_{\mathbf{R}}}{B}\cdot\nabla F_0 = \frac{qF_0}{T}(-i\omega)\langle\Phi\rangle_{\mathbf{R}} \Rightarrow \tag{2.17}$$

$$\omega\tilde{h} - v_{||}k_z\tilde{h} + \frac{k_y\langle\Phi\rangle_{\mathbf{R}}}{B}\hat{\mathbf{x}}\cdot\nabla F_0 = \frac{qF_0}{T}\omega\langle\Phi\rangle_{\mathbf{R}} \tag{2.18}$$

Working out the terms results in

$$\tilde{h} = F_0 \frac{q\langle\Phi\rangle_{\mathbf{R}}}{T} \frac{\omega + \omega_* \left(1 + \eta \left(\frac{v^2}{2v_{th}^2} - \frac{3}{2}\right)\right)}{\omega - v_{||} k_z} \tag{2.19}$$

with

$$\omega_* = \frac{k_y T}{qBL_n},\ \eta = \frac{L_n}{L_T} \tag{2.20}$$

We then have

$$\langle h_s \rangle_{\mathbf{r}} = J_0(\alpha)^2 F_0 \frac{q\Phi}{T} \frac{\omega + \omega_* \left(1 + \eta \left(\frac{v^2}{2v_{th}^2} - \frac{3}{2}\right)\right)}{\omega - v_{||} k_z} \tag{2.21}$$

with $\alpha = \frac{k_\perp v_\perp}{\Omega}$. The Bessel functions arise from the gyroaverage, So, quasineutrality reads

$$\sum_s q_s \int \left(\langle h_s \rangle_{\mathbf{r}} - \frac{q_s \Phi}{T_s} F_{Ms} \right) d^3\mathbf{v} = 0 \Rightarrow \tag{2.22}$$

$$\sum_s \frac{q_s^2 \Phi}{T_s} \int F_M \left(J_0(\alpha_s)^2 \frac{\omega + \omega_{*s} \left(1 + \eta_s \left(\frac{v^2}{2v_{th,s}^2} - \frac{3}{2}\right)\right)}{\omega - v_{||} k_z} - 1 \right) d^3\mathbf{v} = 0 \tag{2.23}$$

Using the definitions

$$\Gamma_0(b_s) = I_0(b_s) e^{-b_s},\ \Gamma_1(b_s) = (I_0(b_s) - I_1(b_s)) e^{-b_s},\ b_s = \frac{\kappa_s^2}{2}, \tag{2.24}$$

and following further manipulations, the resulting dispersion relation is

$$\sum_s \frac{q_s^2 n_{0,s}}{T_s} \Bigg\{ 1 + \zeta_s Z(\zeta_s) \Gamma_0(b_s) + \zeta_s Z(\zeta_s) \frac{\omega_{*s}}{\omega} \left(1 - \eta_s \frac{1}{2}\right) \Gamma_0(b_s) - \\ \zeta_s Z(\zeta_s) \eta_s \frac{\omega_{*s}}{\omega} b_s \Gamma_1(b_s) + \eta_s \frac{\omega_{*s}}{\omega} \Gamma_0(b_s) \zeta^2 \left(1 + \zeta_s Z(\zeta_s)\right) \Bigg\} = 0, \tag{2.25}$$

where $Z(\zeta_s)$ is the plasma dispersion function [75], I_n are modified Bessel functions, and

$$\zeta_s = \frac{\omega}{\sqrt{2} v_{th,s} k_z},\ \eta_s = L_{n,s}/L_{T,s},\ \omega_{*s} = \frac{k_y T_s}{q_s B L_{n,s}},\ \kappa_s = \frac{\sqrt{2} k_\perp v_{th,s}}{\Omega_s}.$$

The $L_n^{-1} \to 0$ limit of Eqn. 2.25, with the notation $\omega_{*T} = \omega_{*s}\eta_s$, yields

$$\sum_s \frac{q_s^2 n_{0,s}}{T_s} \Bigg\{ 1 + \zeta_s Z(\zeta_s) \Gamma_0(b_s) - \\ \frac{\omega_{*T}}{\omega} \left[\zeta_s Z(\zeta_s) \left(\frac{1}{2} \Gamma_0(b_s) + b_s \Gamma_1(b_s) \right) - \Gamma_0(b_s) \zeta^2 \left(1 + \zeta_s Z(\zeta_s)\right) \right] \Bigg\} = 0, \tag{2.26}$$

which is equivalent to the result found in Eqn. 67 of Ref. [76].

In the long wavelength ($\kappa \to 0,\ \zeta \to \infty$), $L_T^{-1} \to 0$ limit of Eqn. 2.25 with Boltzmann electrons ($h_e = 0$), one recovers the drift wave (also assuming a hydrogen isotope and equal temperatures):

$$\sum_s \frac{q_s^2 n_{0,s}}{T_s}\left\{1 - \left(1 + \frac{\omega_{*s}}{\omega}\right)\right\} = 0 \Rightarrow \tag{2.27}$$

$$\frac{q_e^2 n_{0,e}}{T_e} + \frac{q_s^2 n_{0,1}}{T_1} = \frac{q_1^2 n_{0,1}}{T_1}\left(1 + \frac{\omega_{*1}}{\omega}\right) \to \tag{2.28}$$

$$\omega_{*1} = \omega \tag{2.29}$$

In the collisionless limit, ω is real and there is no unstable mode.

The long wavelength limit of Eqn. 2.25 for a hydrogen plasma with $T_e = T_i$ and a Boltzmann electron response results in

$$\frac{e^2 n_e}{T_e} + \frac{Z_i^2 e^2 n_i}{T_i} = \frac{Z_i^2 e^2 n_i}{T_i}\left\{1 + \frac{1}{2\zeta_i^2} + \frac{\omega_{*i}}{\omega}\left[1 + \frac{1}{2\zeta_i^2} - \eta_i \frac{1}{4\zeta_i^2} - \eta_i\right]\right\} \Rightarrow \tag{2.30}$$

$$\omega^3 - \omega^2 \omega_{*i}(1 - \eta_i) - \omega v_{th,i}^2 k_z^2 - v_{th,i}^2 k_z^2 \omega_{*i}(1 - \frac{1}{2}\eta_i) = 0 \Rightarrow \tag{2.31}$$

$$\omega^3 + a_2\omega^2 + a_1\omega + a_0 = 0 \tag{2.32}$$

with

$$a_2 = -\omega_{*i}(1 - \eta_i),\ a_1 = -v_{th,i}^2 k_z^2,\ a_0 = -v_{th,i}^2 k_z^2 \omega_{*i}(1 - \frac{1}{2}\eta_i) \tag{2.33}$$

The determinant of the above cubic equation is given by

$$\Delta = 18 a_2 a_2 a_0 - 4 a_2^3 a_0 + a_2^2 a_1^2 - 4 a_1^3 - 27 a_0^2 \tag{2.34}$$

For $\Delta > 0$ there are three distinct real roots, for $\Delta = 0$ there is one real multiple root, and

for $\Delta < 0$ there is one real root and one pair of complex conjugate roots. We then have

$$\begin{aligned}\Delta = &-18\omega_{*i}^2 v_{th,i}^4 k_z^4 (1-\eta_i)(1-\eta_i/2) \\ &-4\omega_{*i}^4 v_{th,i}^2 k_z^2 (1-\eta_i)^3 (1-\eta_i/2) \\ &+\omega_{*i}^2 v_{th,i}^4 k_z^4 (1-\eta_i)^2 \\ &+4v_{th,i}^6 k_z^6 \\ &-27\omega_{*i}^2 v_{th,i}^4 k_z^4 (1-\eta_i/2)^2 \end{aligned} \tag{2.35}$$

Again, take the long wavelength limit ($k_z \to 0$), keeping only the leading term:

$$\Delta = -4\omega_{*i}^4 v_{th,i}^2 k_z^2 (1-\eta_i)^3 (1-\eta_i/2). \tag{2.36}$$

We arrive at one limit of the classical η_i-mode, which is always unstable for $\eta_i > 2$.

Tokamak geometry induces additional complexities into calculations through the curvature drift, ∇B drift, sheared magnetic field, and separate passing and trapped particle populations. However, we see in this simple example what is called critical gradient behavior, where the plasma is always unstable above a critical threshold. This has important implications for the cross field turbulent transport of particles, momentum, and energy in a plasma; namely, linear instabilities lead to what is known as stiff transport [77] (see also Ref. [78] and references therein). A stiffness parameter (for which various definitions exist) characterizes the incremental change in flux for an incremental change in gradient. A high value of stiffness is referred to as stiff transport; in that situation there will be little response of the equilibrium profiles to additional source input. For situations where a high temperature and density need to be attained–as is the case for a fusion reactor–stiff transport is a significant problem.

2.3.1.2 Ion temperature gradient instability

The ion temperature gradient (ITG) mode is thought to be a major cause of transport in tokamaks. The slab-η_i mode derived in Sec. 2.3.1.1 differs from the ion temperature gradient (ITG) mode often invoked as a cause of long wavelength ($k_\theta \rho_s \sim 0.3$) turbulent

fluctuations due to the addition of curvature drift, magnetic field shear, and other effects in toroidal geometry. Although these effects introduce additional factors, the drive term for ITG is usually cast as η_i or $L_{T_i}^{-1}$. It is also necessary to include the non-Boltzmann electron response to accurately reproduce features of experimental measurements; although, a Boltzmann electron response has often been used in analytical and simulation work. The ITG mode has been studied in detail, see for instance Refs. [79–83]. The standard description for the ITG modes is that is propagates in the ion diamagnetic direction in the plasma frame; however, as will be noted later chapters, when kinetic electrons are included the mode can propagate at close to zero frequency and cross over to the electron direction in some cases.

Although the ITG mode is expected to exhibit critical gradient behavior, nonlinear simulations have shown an upshift in the value of the critical gradient [84]. This nonlinear upshift, known as the "Dimits shift" is thought to arise due to a zonal flow dominated state in between the linear and nonlinear critical gradients.

A long standing observation in tokamaks is that the global energy confinement time in Ohmic plasmas scales linearly with the line-averaged density, then saturates [85]. It is thought that the cause of this is due to a transition from trapped electron modes during the linear regime to ITG in the saturated regime, which has some support from turbulence measurements [34, 86]. This might also be related to reversals of intrinsic rotation that have been observed [87].

It has also been observed that core electron temperature fluctuations decrease significantly across the L-H transition in neutral beam heated plasmas [88]. The strong beam heating would have been expected to destabilize ITG during the L-mode phase; the turbulence was then suppressed during H-mode due to the strong $E \times B$ shear from the neutral beams. If that description were to be true, it would mean that it would be necessary for ITG modes to have a non-Boltzmann electron response in order to explain the temperature fluctuations in L-mode. Later experiments compared measurements of electron temperature fluctuations in L-mode plasmas to nonlinear gyrokinetic simulations, finding agreement at some radii and disagreement at others [89]. In plasmas where linear calculations showed

ITG has the most unstable mode, electron temperature fluctuations were still measured, indicating the necessity of the non-Boltzmann electron distribution.

2.3.1.3 Trapped electron modes

Toroidal geometry also opens the possibility for a class of instabilities related to the trapped particle population. Trapped electron modes (TEM) [90] are often invoked at long wavelengths and at intermediate-scales ($k_\theta \rho_s \sim 1$). Several versions of the TEM exist, with differing gradient drives and instability mechanisms. Both dissipative and collisionless TEM exist; TEM can also be driven by either the electron density or temperature gradient, with opposite dependencies expected for η_e. The collisionless TEM is expected to be destabilized by collisions at low values of the normalized electron collision frequency, $\nu_{ei}/(c_s/a)$, but to eventually be stabilized at high $\nu_{ei}/(c_s/a)$, where trapped electrons no longer complete a bounce orbit before being scattered into passing orbits. See Refs. [91, 92] and references therein for descriptions of the different types of TEM. In most cases, TEMs would be predicted to propagate in the electron diamagnetic direction.

Zonal flows have been shown in simulations to be of different importance for ∇n_e-TEM and ∇T_e-TEM. It was argued in Ref. [91] that zonal flows play a similar role for ∇n_e-TEM as they do for ITG: they are the saturation mechanism and produce a nonlinear upshift of the critical gradient. In Ref. [93], it was shown that zonal flows played little role for ∇T_e-TEM and that there was no Dimits shift. The role of zonal flows was clarified in Ref. [92], where it was shown in simulations that for $\eta_e < 1$ zonal flows are important, but for $\eta_e > 1$ they are not.

It was mentioned in the previous section that it is thought that TEM is the dominant instability during the linear Ohmic confinement regime. It has also been argued through comparison between transport analysis and linear gyrokinetic calculations that ∇T_e-TEM has been indirectly identified by the observed dependence on $L_{T_e}^{-1}$ and stabilization by collisions [94]. The same instability–the dissipative ∇T_e-TEM–is thought to also be responsible

for the observations reported in Chapter 5, where temperature fluctuations are directly observed to increase with $L_{T_e}^{-1}$. The instability mechanism is attributed to collisional detrapping of electrons, which is highly sensitive to the details of the collision operator near the trapped-passing boundary.

2.3.1.4 Electron temperature gradient instability

The electron temperature gradient (ETG) instability is often invoked to explain fluctuations at smaller scales ($k_\theta \rho_s \sim 10$). The ETG mode can be considered isomorphic to the ITG mode, where electrons are treated as Boltzmann for the latter, ions are for the former [55]. It should be noted that there is not necessarily a clear distinction between these various instabilities–in simulations, the TEM is seen to smoothly become the ETG mode as a function of wavenumber. ETG also is expected to have a critical gradient and has been argued to play an important role in electron heat transport, including being a cause of high stiffness [95]. The mode is usually predicted at relatively high frequencies–megahertz range for typical experiments–and to propagate in the electron diamagnetic direction.

It has been argued that ETG turbulence has been identified in a series of experiments in NSTX. Ref. [96] reported transient changes, due to heating, to small scale ($k_r \rho_i \sim 10$) density fluctuations, which were attributed to ETG mode turbulence through support by linear gyrokinetic calculations. In subsequent works, it was argued that the fluctuations identified as ETG could be suppressed by large $E \times B$ flow shear [97], negative magnetic shear [98], and the electron density gradient [99, 100]. Further discussion of this set of results can be found in Chapter 5.

2.3.1.5 Other instabilities

ITG, TEM, and ETG are the most commonly invoked instabilities. Several other modes have been studied in the literature, but have not received as much attention as those three. It was noted above that sub-critical turbulence, due to the parallel velocity gradient insta-

bility, has been studied in simulations. There is also an electromagnetic instability that can occur called the microtearing mode [101, 102], which has received renewed attention in recent years [103, 104]. It has also been argued that nonlinear energy transfer to linearly damped microtearing modes causes magnetic stochasticity and electron heat transport in electromagnetic gyrokinetic simulations [105]. Kinetic ballooning modes are thought to be important in the H-mode pedestal [106] and possibly in high β plasmas. There are also impurity modes that can exist in plasmas with more than one ion species [107].

2.3.1.6 Experimental signatures of commonly invoked instabilities

In addition to stability criteria and parametric dependencies there are several predictions that may be able to experimentally distinguish the various instabilities. For the important case of ITG versus TEM, one clear indication would be the direction of mode propagation in the plasma frame. As noted above, modes propagating in opposite directions have been observed in scattering experiments [34, 86]; however, many of these older works did not have the profile measurements necessary to compare the measurements directly to quantitative theoretical predictions. A possible way to identify mode direction using Doppler backscattering measurements is discussed in Appendix F.

The ratio of fluctuation levels has also been used to argue for mode identification: a high ratio of ion temperature fluctuations to density fluctuations for ITG [43] and a high ratio of electron temperature fluctuations to density fluctuations for TEM [89]. A result similar to the latter is reproduced in Chapter 5.

It has been observed in multi-scale nonlinear gyrokinetic simulations that the slope of the dependence of density fluctuations on wavenumber is different for ITG and TEM [108]. It is in principle possible to test this prediction with DBS measurements [5, 109].

The crossphase between fluctuating fields is another characteristic of an instability. The crossphase between electron temperature fluctuations and density fluctuations, α_{n_e,T_e}, has been measured and directly compared to the output from nonlinear gyrokinetic simula-

tions [16]. This is illustrated in the example calculation shown in Fig. 2.1. The base case parameters from $\rho = 0.5$ of shot 128913 at 1500 ms in Ref. [110] were used as input for linear calculations with GS2, similar to Ref. [16] (which these runs were done to verify against). For subsequent runs the input value of T_e was scanned (along with parameters dependent on it, *e.g.* T_e/T_i and collision frequencies), while keeping $L_{T_e}^{-1}$ constant–this is similar to the effect of adding core ECH in DIII-D L-mode plasmas. There is a jump in real frequency in Fig. 2.1(a), which is coincident with a local minimum in growth rate in Fig. 2.1(b), and a jump in α_{n_e,T_e} in Fig. 2.1(c). Sensitivity studies were consistent with ITG at low $T_e/T_{e,base}$ and TEM at high $T_e/T_{e,base}$ as the fast growing mode. The large predicted change to α_{n_e,T_e} would be measurable in experiment. The GS2 runs did not exactly reproduce the GYRO results in Ref. [16]; in particular, the crossphase appears to have the opposite sign. This might be due to differences in code coordinate systems, as noted in Ref. [111]. There are a few other differences: Ref. [16] used the total electron temperature fluctuation, here only the perpendicular fluctuations were used; a real space synthetic diagnostic was used in Ref. [16], while the calculation was performed spectrally here; and, there are differences between the GYRO and GS2 collision operators.

2.3.2 Zonal flows and the geodesic acoustic mode

Zonal flows are predicted to play an important role in turbulence, both for fusion plasmas and for many contexts in nature [63]. There two are zonal flow type modes widely discussed in the literature. The first is the Rosenbluth-Hinton residual flow [65], which is a linearly undamped poloidal flow thought to be related to the zero mean frequency zonal flows observed in simulations. Measurements have identified zero mean frequency zonal flows in experiments [66]. The second is the geodesic acoustic mode [112], which is discussed in subsequent sections and experimentally investigated in Chapter 4. There are also observations of oscillations with zonal flow characteristics that do not fit neatly into these two categories, such as in Ref. [21] and discussed in Sec. 4.6.

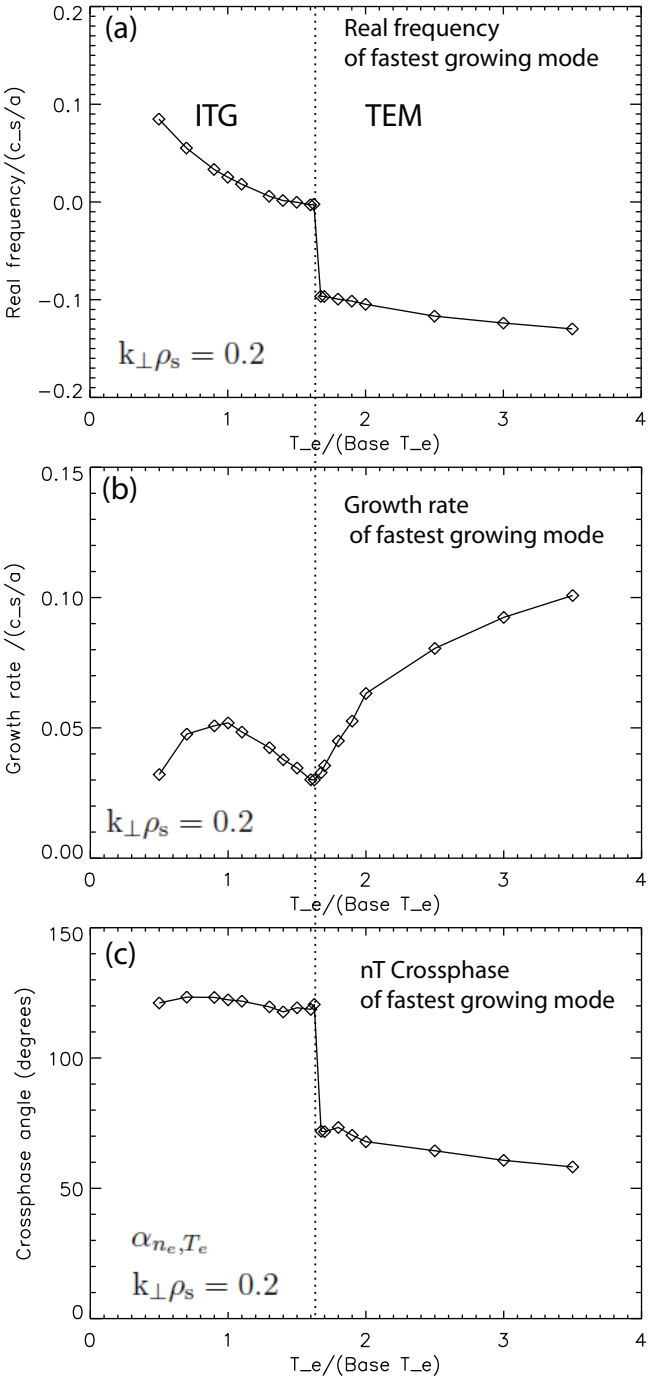

Figure 2.1: (a) Real frequency, (b) growth rate, and (c) crossphase between electron density and temperature fluctuations as a function of $T_e/T_{e,base}$ for $k_\perp \rho_s = 0.2$. Vertical dashed line added for reference.

2.3.2.1 Geodesic acoustic mode background

The geodesic acoustic mode is a plasma oscillation that can occur in tokamaks [112], which has several characteristics in common with the lower frequency zonal flows. The mode is characterized by an axisymmetric (poloidal mode number $m = 0$, toroidal mode number $n = 0$) potential and m=1 density components that oscillate with a frequency of $\omega_{GAM} \approx \sqrt{2(T_e + \frac{7}{4}T_i)/m_i}/R_0$ (neglecting additional geometric, electromagnetic, and kinetic contributions), where R_0 is the major radius, T_e is the electron temperature, T_i is the ion temperature, and m_i is the ion mass. Physically, the GAM can be thought of as the ion acoustic wave coupled to the magnetic field geometry in a tokamak−for systems where the divergence of the $E \times B$ flow is zero, such as a cylinder, the GAM degenerates to the ion acoustic wave. Since the magnetic field magnitude is not constant on a flux surface in a tokamak, the $E \times B$ flow associated with the GAM potential results in an $m = 1$ pressure accumulation, which is then partially balanced by a parallel flow. While toroidally and poloidally symmetric, the GAM has finite radial structure: the mode can propagate radially [113, 114], with measured radial wavenumbers $\mathcal{O}(k_r) \sim 1\ \mathrm{cm}^{-1} \sim 0.1 - 0.2\ k_r\rho_s$ [15, 115–118], where ρ_s is the ion sound radius, the sound speed (in this context, $c_s = \sqrt{T_e/m_i}$) divided by the ion cyclotron frequency, $\rho_s = c_s/\omega_{ci}$.

The two factors that determine the magnitude of observed GAMs are its drive and linear damping (assuming the GAM is of sufficiently small magnitude that it does not itself drive any secondary instabilities and is not impacted by nonlinear Landau damping). The drive is thought to be due to nonlinear interactions with turbulence through three wave coupling; or, stated in a fluid framework, by the Reynolds stress. The mode is weakly damped by ion-ion collisions, and undergoes ion Landau damping, the rate of which has a e^{-q^2} dependence [119], where q is the safety factor. This q-dependence means the GAM is strongly damped in the core, where the lower frequency zonal flows are thought to be more prevalent, and may only exist towards the edge, where it is weakly damped at high q. The damping also has a dependence on the ratio between the electron and ion temperatures and other factors [119, 120].

GAMs are not typically observed in H-mode plasmas, but are nearly always present in Ohmic and L-mode plasmas. Observations show the interaction between GAMs, turbulence, and the equilibrium flow can play an important role in the L-H transition [121]. Therefore, comprehensive understanding of the GAM may yield important implications for transport during L-mode periods (such as the current ramp) and for the dynamics of the L-H transition in future devices.

Numerous publications exist in the literature regarding the GAM. On the experimental side, some of the defining mode characteristics have been observed, including the temperature dependence of the mode frequency and the asymmetry of the density component of the mode [115, 122]. Empirical scalings of mode frequency and amplitude with shaping parameters and magnetic geometry have been conducted [123–126]. Quantitative agreement has been observed between experiment and simulation in a comparison of the GAM's frequency [115], a linear characteristic of the mode. Consistent with the expected q-dependence, the GAM amplitude at the edge has been observed to scale with q (Ref. [124]); furthermore, qualitative comparison between experiment and simulation shows consistency with the q dependence of the damping [127]. Multiple GAMs or splitting of the GAM's spectral peak are at times observed at the same radial location [125, 128]. In addition to flow and density measurements, magnetic [128] and temperature [115] oscillations at the GAM frequency have been reported. Probe studies near the edge of Ohmic discharges in several tokamaks have extensively investigated interactions between the GAM and turbulence [117, 118, 129–135]; salient results include experimental characterization of the interaction between the GAM and turbulence, between the GAM and low frequency zonal flows, and of the three dimensional structure of the GAM for that parameter regime. Radial propagation of the GAM's phase fronts has been observed [15, 115, 136], and radial group propagation has also been observed [117]. The GAM's amplitude has been observed to be intermittent [123, 128, 132]. Low wavenumber density fluctuations and the particle flux has been observed to be modulated at the frequency of the GAM [115, 137].

On the theoretical side, the GAM has been investigated within a number of frame-

works. Findings from recent work include a prediction of an Airy function like radial eigenmode when finite $k_r\rho_i$ terms are included [119, 138–140], a group velocity that scales with temperature ratio and may even reverse direction [113], possible impact of electromagnetic terms [141], and the relation of the GAM to Alfvén eigenmodes [140, 142]. Effects that impact the GAM's radial propagation have been studied [113, 114], although understanding of the physical mechanism for the propagation is not settled [143]. It has been observed that the GAM can play a significant role as a saturation mechanism for turbulence in gyrokinetic simulations [144]. Qualitative comparisons between GAM measurements and gyrokinetic simulations have shown similarity between experiment and simulation in nonlinear energy transfer by convection of density fluctuations by the GAM [145], likeness in the wavenumber-frequency power spectrum [146], and qualitative agreement for the q dependence of GAM damping [127]. Direct, quantitative comparisons of nonlinear mode characteristics have yet to occur.

2.3.2.2 MHD GAM derivation

A starting point for understanding the geodesic acoustic mode is the original derivation in Ref. [112] for the electrostatic GAM, within the framework of magnetohydrodynamics, which is reviewed here. Take the equilibrium and perturbed quantities to be

$$\rho = \rho_0 + \rho_1,\ P = P_0 + P_1,\ \mathbf{v} = \mathbf{v}_1,\ \mathbf{E} = -\nabla\phi_1, \tag{2.37}$$

$$\mathbf{J} = \mathbf{J}_0 + \mathbf{J}_1,\ \mathbf{B} = \mathbf{B}_0, \tag{2.38}$$

where ρ is the mass density, P is the pressure, v is velocity, E is electric field, ϕ is electrostatic potential, $\mathbf{J}$ is the plasma current, and $\mathbf{B}$ is magnetic field, and for each quantity $x = x_0 + x_1$,

assume $x_1/x_0 = \epsilon << 1$. The linearized ideal MHD equations are then

$$\frac{\partial \rho_1}{\partial t} + \nabla \cdot (\rho_0 \mathbf{v}_1) = 0, \tag{2.39}$$

$$\rho_0 \frac{\partial \mathbf{v}_1}{\partial t} = -\nabla \mathrm{P}_1 + \mathbf{J}_1 \times \mathbf{B}_0, \tag{2.40}$$

$$\nabla \cdot \mathbf{J}_1 = 0, \tag{2.41}$$

$$\rho_0^{-\gamma} \frac{\partial \mathrm{P}_1}{\partial t} - \gamma \mathrm{P}_0 \rho_0^{-\gamma-1} \frac{\partial \rho_1}{\partial t} + \mathbf{v}_1 \cdot \nabla \left(\frac{\mathrm{P}_0}{\rho_0^{\gamma}} \right) = 0., \tag{2.42}$$

where γ is the adiabatic index. From the radial force balance equation, assuming no pressure gradient and working in the plasma frame with no equilibrium radial electric field, we also have

$$-E_r = \nabla \phi_1 = \mathbf{v}_1 \times \mathbf{B}. \tag{2.43}$$

Assuming perturbed quantities are proportional to $e^{-i\omega t}$, after some manipulation, one finds the general MHD GAM dispersion relation

$$\omega^2 \int |\rho_1|^2 J ds = \frac{\gamma \mathrm{P}_0}{\rho_0} \left(\frac{\left| \int \rho_1 \frac{\mathbf{B} \times \nabla \psi \cdot \nabla B^2}{B^4} J ds \right|^2}{\int \frac{|\nabla \psi|^2}{B^2} J ds} + \int \frac{|\mathbf{B} \cdot \nabla \rho_1|^2}{B^2} J ds \right), \tag{2.44}$$

where J is the Jacobian and ψ is a radial coordinate labeling the flux surfaces. To arrive at Eqn. 2.44, the assumption of closed magnetic surfaces is used to make integrals of divergences exactly vanish, implying the GAM cannot be supported outside the last closed flux surface in a tokamak. This is also observed experimentally, where the GAM is actually observed to disappear *before* the last closed flux surface (see Sec.4.3.5 for more information). We also see that if $\mathbf{B} \times \nabla \psi \cdot \nabla B^2 = 0$, it reduces to the equation for sound waves propagating along the field lines: $\omega^2 = \gamma \mathrm{P}_0 k_{||}^2 / \rho_0 = c_s^2 k_{||}^2$. Therefore, to support a GAM, the magnetic geometry must have the property that the magnetic field strength changes along the binormal direction within the flux surfaces. We see now that the perpendicular flow accumulates density due to the magnetically curved geometry (the integral in the numerator of the first term in parentheses on the right-hand-side of Eqn. 2.44), which is coupled to the sound wave along the field lines.

Now, use a simplified model for the equilibrium toroidal magnetic field

$$\mathbf{B} = \frac{B_0}{1+\epsilon\cos\theta}(\hat{z} + f(r)\hat{\theta}), \tag{2.45}$$

$$\epsilon = \frac{r}{R_0}, \tag{2.46}$$

$$f(r) = \frac{r}{q(r)}\frac{1}{\sqrt{R_0^2 - r^2}}, \tag{2.47}$$

$$\nabla\psi = r, \tag{2.48}$$

$$Jds = r(1+\epsilon\cos\theta)d\theta dz. \tag{2.49}$$

For a Fourier series in the poloidal direction for ρ_1, the result is

$$\frac{\omega^2}{c_s^2}(1+f(r)^2)\int|\rho_1|^2 d\theta = \tag{2.50}$$
$$\frac{2}{\pi r^2\left(1+\frac{3}{2}\epsilon^2\right)}\left|\int\rho_1\left(\epsilon\sin\theta + \frac{\epsilon^2}{2}\sin(2\theta)\right)d\theta\right|^2 +$$
$$\frac{f(r)^2}{r^2}\int\left|\frac{\partial\rho_1}{\partial\theta}\right|^2 d\theta.$$

Neglecting the ϵ^2 terms, after further manipulation:

$$\frac{\omega^2}{c_s^2}\left(1 + \frac{r^2}{q(r)^2}\frac{1}{R_0^2 - r^2}\right) = \frac{2}{R_0^2} + \frac{1}{q(r)^2}\frac{1}{R_0^2 - r^2} \tag{2.51}$$

Again, neglecting the ϵ^2 terms, we find the standard GAM dispersion relation:

$$\omega^2 = \frac{2c_s^2}{R_0^2}\left(1 + \frac{1}{2q^2}.\right) \tag{2.52}$$

Furthermore, the perpendicular component of the flow–which can be measured with DBS–works out to

$$|v_{E\times B,GAM}| \sim \frac{\tilde{n}}{n}\frac{c_s^2}{R_0\omega}, \tag{2.53}$$

where the mass density has been replaced by the particle density. For $v_{E\times B,GAM} \sim 1$ km/s, $c_s \sim 100$km/s, $R_0 \sim 1.5$m, and $\omega_{GAM} \sim 2\pi * 20$ kHz, one finds $\tilde{n}/n \sim 0.02$. This would be equivalent to a relatively strong GAM in DIII-D.

Although the MHD derivation gives some insight into GAM, there are several important *caveats*. One is that it describes a neutrally stable mode; kinetic calculations show the

electrostatic GAM is linearly stable [119]. A second is that it is a local description for each flux surface, which implies that the frequency of the GAM should vary radially with the temperature.

2.3.2.3 Eigenmode GAM derivation

One of the limitations of the MHD description, the lack of a prediction for radial structure, can be addressed heuristically, as follows from Ref. [138] and which was shown more formally in Ref. [119]. In the MHD derivation, the GAM has no coherent radial variation and each surface is essentially independent, $\omega = \omega_{GAM}(r)$, where the right-hand-side is determined locally as in the preceding section and the left-hand-side is the actual frequency. The GAM can be thought of as balancing a cross-field current due to magnetic field variation and the ion polarization to satisfy $\nabla \cdot \mathbf{J_1} = 0$ to leading order. In the collisionless limit with $T_e >> T_i$, the current due to the magnetic field variation is dominated by electrons and is not affected by finite gyroradius effects; however the ion polarization current is modified by a factor of $1 - k_r^2 \rho_i^2$, this results in

$$(1 - k_r^2 \rho_i^2)\omega^2 = \omega_{GAM}^2(r) \tag{2.54}$$

Introducing radial variation of the temperature gradient:

$$\omega_{GAM}^2(r) = \omega_{GAM}^2(r_0)\left(1 - \frac{r - r_0}{L_T}\right) \tag{2.55}$$

$$(1 - k_r^2 \rho_i^2)\omega^2 = \omega_{GAM}^2(r_0)\left(1 - \frac{r - r_0}{L_T}\right) \tag{2.56}$$

Turn this into an eigenmode equation with $k_r \to \partial/\partial r$ and $\phi e^{(ik_r r - i\omega t)} \to \phi(r) e^{-i\omega t}$; then:

$$\left(1 - \rho_i^2 \frac{\partial^2}{\partial r^2}\right)\phi(r) = \left(1 - \frac{r - r_0}{L_T}\right)\phi(r) \Rightarrow \tag{2.57}$$

$$\rho_i^2 \frac{\partial^2 \phi(r)}{\partial r^2} + \frac{r - r_0}{L_T}\phi(r) = 0 \tag{2.58}$$

Make the substitutions:

$$\lambda = \rho_i^{2/3} L_T^{1/3} \tag{2.59}$$

$$x = \frac{r - r_0}{\lambda} \tag{2.60}$$

So

$$\frac{\partial^2 \phi(x)}{\partial x^2} + x\phi(x) = 0 \tag{2.61}$$

the solution to which is the Airy function [147], $\phi(x) = Ai(-x)$. Note that this solution is for a standing wave, which is created by the interference of an incoming wave that is reflected. The same solution arises for the 1-D Schroedinger equation for a potential with a constant slope and for the 1-D description of reflectometry for a linear density profile. Measurements of the GAM show that it propagates, which is discussed in Chapter 4.

2.3.2.4 Disambiguation: the GAM and the BAE

There has been some ambiguous use of terminology in the literature concerning the geodesic acoustic mode and the beta-induced Alfvén eigenmode (BAE). There is clear reason for ambiguity, as it has been shown that in the limit of low β, the two modes are degenerate, sharing the same dispersion function [140]. There are, however, experimental differences between the two modes. What is referred to as the GAM in this dissertation and investigated thoroughly in Chapter 4 is primarily an electrostatic oscillation that occurs towards the edge of L-mode plasmas, $\rho \gtrsim 0.7$, is driven by the ambient drift wave turbulence, has an axisymmetric potential, and an m=1 density component. The BAE is core-localized to rational q surfaces, driven by energetic particles, has electromagnetic components, and is often observed with $m > 1$ poloidal mode numbers. Although the theoretical description of the modes is similar, they play very different roles in experiments.

2.4 Recent validation experiments and past work

One of the overarching goals for turbulence and transport studies is to arrive at a validated, predictive capability for transport in tokamaks. Discussions of validation, and the related activity of verification, for fusion energy science and plasma physics are available [148, 149].

It is within the last decade that both computational power and fluctuation measurements have matured to the point where rigorous and well-posed comparisons between experiment and simulations have been possible. In this section, past work in this area is reviewed. Many additional works have performed qualitative studies, such as comparisons between changes to linear growth rates and inferred changes to transport or profiles—the scope here is to review quantitative studies where attempts were made to directly compare fluctuation measurements to simulations incorporating experimental conditions.

In one of the early attempts to compare turbulence measurements to nonlinear simulations it was shown that to produce radial correlation lengths of the same order as those measured in a tokamak required zonal flows in the simulations with the particle-in-cell code UCAN [64]. It should, however, be noted that these results came before the accumulation of noise in particle-in-cell codes for gyrokinetic turbulence was understood [150].

A number of turbulence measurements from Tore Supra [151] were compared to nonlinear predictions from GYRO. A reasonable level of agreement was found there across a range of measurements; however, compared to later work relying on synthetic diagnostics, the comparisons can be described as somewhat crude. More recent work from Tore Supra also includes limited comparisons [152].

Phase contrast imaging was compared to predictions from GYRO in a variety of Alcator C-mod plasmas [153, 154], where a range of disagreement and agreement was found. Two dimensional characteristics of density fluctuations in DIII-D measured with Beam Emission Spectroscopy have been compared to GYRO [155], showing reasonably good agreement overall, with several specific points of disagreement discussed in the referenced paper.

Simultaneous measurements of fluctuating quantities in two fields–electron temperature

and density fluctuations–were compared to nonlinear simulations from GYRO [110]. Quantitative agreement was found at $\rho = 0.5$, but disagreement was found at $\rho = 0.7$. The synthetic diagnostics used for the work were thoroughly described, with additional comparisons made in Ref. [156]. Later work compared the crossphase between electron temperature and density fluctuations, finding quantitative agreement [16, 19]. The trend of significant disagreements for $\rho \gtrsim 0.7$ in L-mode plasmas has more recently been identified as a ubiquitous issue and is an area of active research [18].

A series of transport model validation experiments have been conducted at DIII-D, including comparisons of turbulence measurements and nonlinear gyrokinetic simulations with variation of T_e/T_i [19], elongation [18], and investigations of electron dominated regimes [9, 10].

CHAPTER 3

Experimental apparatus, data analysis, and interpretation

3.1 Introduction

This chapter discusses the primary diagnostics used to acquire data discussed in Chapters 4 and 5. A significant effort was put into diagnostic development for this dissertation–including hardware development, data analysis procedures, and data interpretation. Section 3.2 gives an overview of the DIII-D tokamak, where all experimental data was acquired. Section 3.3 describes the principles of the ideal function of the Doppler Backscattering (DBS) diagnostic, data analysis, and description of the hardware development performed for this thesis. Ray tracing and full-wave simulations have been used in interpret and investigate Doppler backscattering data, discussion of which can be found in Sec. 3.4; description of a synthetic DBS diagnostic for gyrokinetic simulations can also be found there. A number of non-ideal effects can impact experimental measurements, discussion of several such effects is included in Sec. 3.5. Temperature fluctuation measurements from a correlation electron cyclotron emission (CECE) radiometer diagnostic are presented in Chapter 5; description of the CECE diagnostic and data analysis can be found in Sec. 3.6. Conventional reflectometry is discussed in Sec 3.7. Finally, Sec. 3.8 details how the crossphase between electron density and temperature fluctuations can be measured by coupling CECE and convential reflectometry diagnostics.

3.2 The DIII-D tokamak

The DIII-D tokamak is a fusion experiment located at General Atomics in San Diego, CA. Detailed information on the experiment can be found in Ref. [157]. The interested reader is directed to Fusion Science and Technology Vol. 48, No.2 (2005)–a special issue on DIII-D–for a broad overview of the experiment, diagnostics, and results.

The majority of results presented in this dissertation are from low confinement, or L-mode discharges. A few examples of data from the high confinement regime, or H-mode [44–46], are also included. Typical L-mode plasma and machine parameters are listed in Table 3.1. Normal operation is for the toroidal magnetic field and plasma current to be oppositely directed. The adopted convention in normal operation is for the sign of the current to be positive and for that of the toroidal field to be negative.

L-mode plasmas, in comparison to H-mode, are characterized by several properties that make them better suited for diagnostic access and experimental turbulence studies: higher fluctuation levels, less flat core density profiles (important for reflectometry and DBS), reduced impact of equilibrium scale instabilities (*e.g.* neoclassical tearing modes), and lack of the edge localized modes (ELMs) that are present in most H-mode regimes, which can deteriorate measurements quality. Although fluctuation levels are higher, the gyrokinetic ordering of $\delta f/f_0 \sim \rho_s/a$ is still thought to be satisfied in both regimes. Furthermore, although core fluctuation levels have been observed to decrease in H-mode plasmas [4, 88], this has been attributed to equilibrium radial electric field shear [5]. These results were obtained in strongly rotating neutral beam-heated discharges. Neutral beams will not be able to penetrate as deeply into the core of future experiments, like ITER, so it is not unambiguously clear that core turbulence in H-modes in those experiments would be expected to exhibit the same reduced core fluctuation levels as H-modes in today's smaller, NBI-dominated tokamaks. L-mode conditions will also be relevant for future experiments and reactors during current ramp-up and ramp-down phases. For all of these reasons, turbulence studies in L-mode plasmas are relevant and important for the broader goals of fusion energy, in addition

Parameter	Symbol	Value
Toroidal magnetic field	B_0	-2 T
Plasma current	I_p	1-2 MA
Major radius	R_0	1.7 m
Minor radius	a	0.6-0.7 m
Plasma duration	τ_{pulse}	5-6 s
Neutral beam heating	P_{NBI}	0-5 MW
Electron cyclotron heating	P_{ECH}	0-3 MW
Main ion species	D	Deuterium
Primary impurity	C	Carbon
Line averaged density	$\langle n_e \rangle$	$2-3\times10^{13}$ cm^{-3}
On-axis electron temperature	$T_e(0)$	2-4 keV
On-axis ion temperature	$T_e(0)$	1-3 keV
Beta	β	$<0.5\%$
Toroidal Mach number	M_ϕ	$\lesssim 0.3$

Table 3.1: Typical L-mode DIII-D parameters

to being well-suited for detailed physics investigations.

3.3 Overview of Doppler backscattering

Doppler backscattering (DBS) is a diagnostic technique that has matured for the past ~ 10 years. The technique originated from investigation of the "phase runaway" problem in conventional reflectometry [158] and was further developed to provide an interpretation of the predominant physical effects that impact the technique using a simple diffraction screen model [159]. It can be thought of as a hybrid of reflectometry and scattering techniques. The diagnostic provides information about the fluctuation level of intermediate wave number ($k_\perp \rho_i \sim 1$) density fluctuations and the lab frame velocity of the scattering structures, the

latter allows much to be inferred about flows in the plasma. This section describes the principles of the basic operation (*i.e.* the leading order effects) of the DBS diagnostic, data analysis, and description of the hardware used to acquire the data in this thesis.

3.3.1 Principles of Doppler backscattering

Doppler backscattering [158, 159] (also called Doppler reflectometry) is a diagnostic technique where a microwave probe beam is launched into a plasma at a frequency that approaches a cutoff and at an angle that is oblique to the cutoff surface. This creates a localized scattering region near the cutoff.

The scattering in question is due to scattering off collective density fluctuations (which result in collective index of refraction fluctuations), not single particle scattering. The criteria for this is $k\lambda_{De} < 1$, where k is the wave number of the scattering entity and λ_{De} is the Debye length. For typical tokamak parameters, $\mathcal{O}(\lambda_{De}) \sim 0.01$ cm or less and for the fluctuations of interest $\mathcal{O}(k) \sim 1 - 10\text{cm}^{-1}$, so the criteria to be in the collective scattering regime is satisfied.

Scattering of electromagnetic radiation requires momentum and energy conservation for the combination of the incident wave, scattering fluctuation, and the scattered wave (subscripts i, n, and s, respectively). This introduces selection terms for frequency, $\omega_i + \omega_n = \omega_s$, and wave number $\mathrm{k}_i + \mathrm{k}_n = \mathrm{k}_s$. The chosen launch frequency is much higher than the fluctuation frequency. The selection terms along with $|\mathrm{k}_i| = |\mathrm{k}_s|$ result in the well-known Bragg condition

$$k_n = 2k_i \sin\left(\frac{\theta_s}{2}\right), \tag{3.1}$$

where θ_s is the angle between the incident and scattered radiation.

For DBS 180° backscattering occurs from turbulent fluctuations that match the Bragg condition, $k_\perp = -2k_i$, where $k_\perp$ is the binormal (perpendicular to both the equilibrium magnetic field and to the normal to the flux surface) wave number of the turbulence and k_i is the local probe wave number in the scattering region; note that as part of the diagnostic

technique there is about a factor of ten difference between k_0 and k_i. The amplitude of the detected backscattered radiation gives information about the fluctuation level, and the Doppler shift of the radiation is determined by the lab frame propagation velocity of the turbulence.

Figure 3.1 shows a schemtic illustrating the basic principles of Doppler backscattering with a monostatic antenna. The beam is launched at frequency ω and vacuum wave number k_0. It approaches a cutoff, where backscattering occurs. The backscattered radiation Doppler shifted to a frequency of $\omega + \omega_D$, where ω_D is the Doppler shift, is detected with the same antenna. The unscattered portion of the launch beam is reflected and continues out of the plasma.

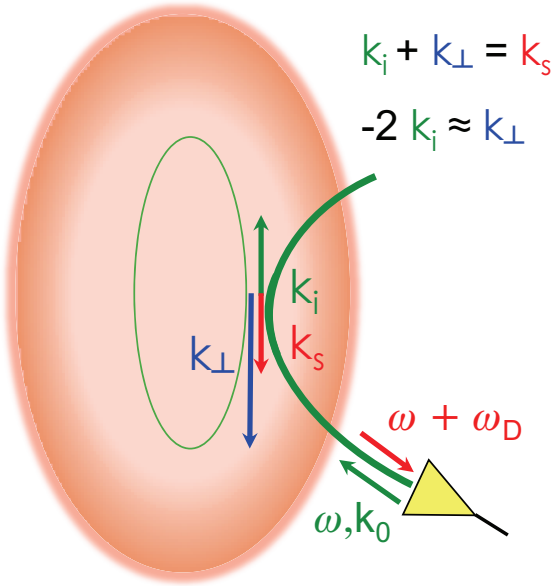

Figure 3.1: DBS schematic.

The lab frame propagation velocity of the turbulence has two components: the $E \times B$ velocity that sets the plasma rest frame and the phase velocity of the turbulence, $v_{\tilde{n}} = v_{E\times B} + v_{phase}$. In most experimental cases, $v_{E\times B}$ dominates, which allows the radial electric field to be inferred from DBS measurements. Direct contributions from toroidal and radial

components of the velocity can generally be neglected.

The quasi-optical antenna system used for DBS systems are usually designed for the launch angle to be modified, which allows $k_\perp$ to be selected. The launch frequency can also be chosen to select the radial location of the measurements.

The wave number of the beam decreases and the amplitude of the beam electric field increases as cutoff is approached. These effects combine to radially localize the measurement, with *sub-centimeter* resolution. The wave number of the beam increases by about a factor ten. The turbulence itself has a wave number dependence, quickly decaying at small scales, with a slope of the power in density fluctuations going as k^{-3} or faster [109]. The scattering efficiency also goes as k^{-2} [160]. These factors highly localize the measurement to the smallest matched wave number along the path of the beam, which provides the spatial resolution of the diagnostic. Temporal resolution is limited by the rate at which the data is digitized, which is sub-microsecond. DBS measurements at DIII-D are typically digitized at 5 or 10 MHz.

Doppler backscattering measurements require the existence of a cutoff in the plasma. Electromagnetic waves that propagate perpendicular to the magnetic field are used for the diagnostic. Either O-mode polarization with the wave electric field parallel to the background magnetic field or X-mode polarization with wave electric field perpendicular the background magnetic field can be used. The cold plasma, normal incidence cutoffs for O-mode and X-mode are given by

$$\omega_O = \omega_{pe} \tag{3.2}$$

$$\omega_X = \frac{1}{2}\left[\pm\omega_{ce} + \sqrt{\omega_{ce}^2 + 4\omega_{pe}^2}\right], \tag{3.3}$$

where ω_{pe} is the plasma frequency and ω_{ce} is the electron cyclotron frequency. The positive sign in ω_X is called the right-hand cutoff and the negative sign is called the left-hand cutoff. The magnetic field configuration, density profile, and launch frequencies possible with diagnostic hardware determine where the measurement is localized. It is preferable to use X-mode when possible, since when arranged to make measurements at the same location,

the scattering efficiency is higher for X-mode than for O-mode [161].

Figure 3.2 shows typical cutoffs and resonances for DIII-D L-mode plasmas. Figure 3.2(a) shows the X-mode and O-mode cutoffs (f_{lh}, f_{rh}, and f_{pe}), and harmonics of the electron cyclotron frequency, f_{pe}, in GHz versus major radius. The profiles are determined from magnetic equilibrium reconstruction and raw (no profile fitting) Thomson scattering data. The locations of the magnetic axis and last closed flux surface (LCFS) are annotated. Figure 3.2(b) shows an example of X-mode cutoff locations for two of the multichannel DBS systems (described in more detail later) using a density profile fit from a typical DIII-D L-mode plasma. Both systems are V-band (50-75 GHz).

Together, these attributes make DBS a very powerful diagnostic; however, there are limitations that must be taken into account. Interpretation of measurements requires knowledge of the scattering wave number, which in turn requires accurate knowledge of the density profile and magnetic geometry to be determined. Accurate determination of $v_{\tilde{n}}$ is most often limited by uncertainties in the density profile, since in a shaped plasma uncertainty in the density profile can lead to a different curvature of the cutoff surface and different angle between the approaching beam and the cutoff surface normal. These uncertainties propagate through the ray tracing analysis into determination of the scattering wave number. Significant errors in magnetic field reconstruction could have a similar effect. Due to needing either an O-mode or X-mode cutoff to function, diagnostic access can be limited in several ways. The first is that hardware able to launch and receive a particular frequency range is limited to a particular density range for O-mode and combination of magnetic field and density for X-mode. Furthermore, O-mode measurements are inaccessible when density profiles are flat or hollow. The electron cyclotron resonances, which absorb the beam, must also be avoided. These factors must be taken into account when planning an experiment.

Figure 3.3 shows example DBS data. The DBS electric field frequency spectrum evolves over a time period in a DIII-D plasma where the direction of the momentum injection from neutral beams is switched. This has a clear effect on the DBS spectrum, where the sign of the Doppler shift changes in response to the direction of momentum injection.

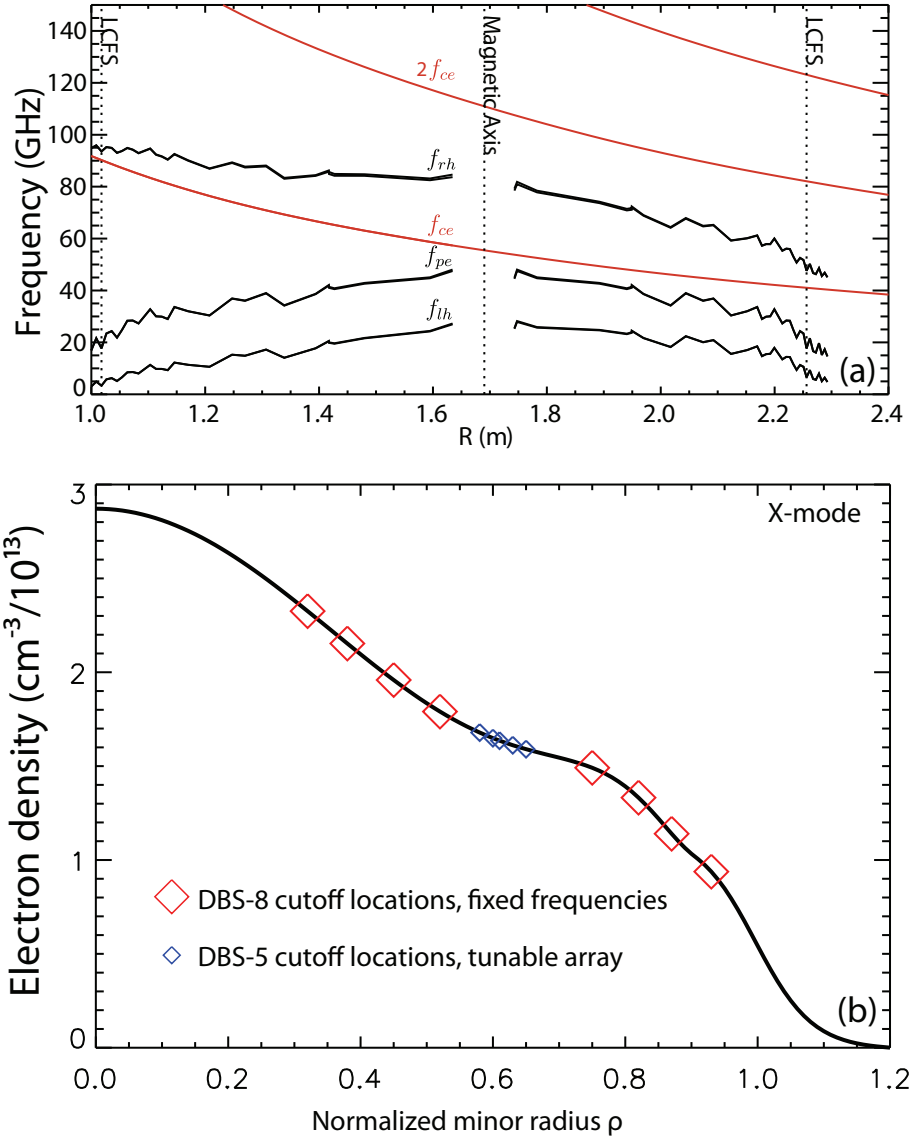

Figure 3.2: (a) All typically relevant cutoff and resonance profiles for DBS in L-mode DIII-D plasmas. (b) Typical X-mode cutoff locations for two DIII-D DBS systems in L-mode.

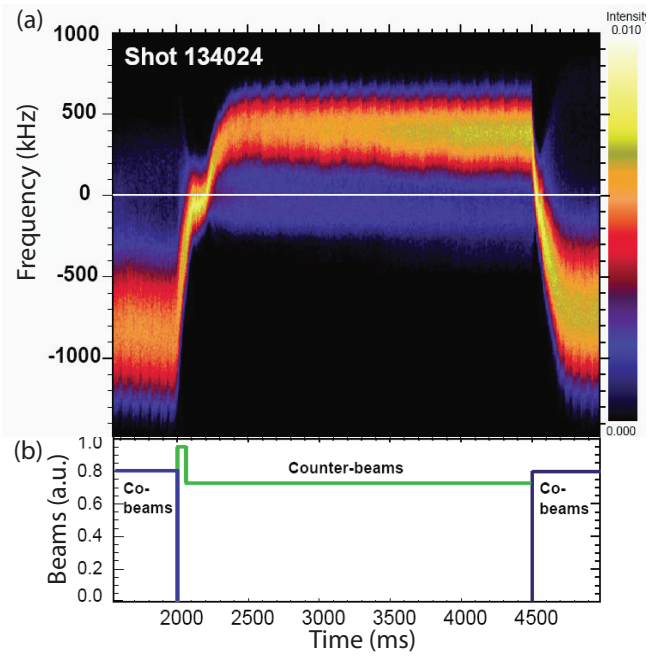

Figure 3.3: (a) DBS quadrature spectrum. (b) Neutral beam timing, with switches between co-beams and counter-beams shown.

3.3.1.1 Spectral width

The Doppler shifted peak in the DBS electric field spectrum has a definite width, $\Delta\omega_{DBS}$ (neglecting the wave number spectrum of the turbulence itself). For cases where the lab frame velocity is dominated by the $E \times B$ velocity associated with the equilibrium rotation, $\Delta\omega_{DBS}$ can be understood in a straight-forward manner. A Gaussian beam with a given beam radius, $2w_0$, will give rise to a finite scattering volume that results in a wave number dependent weighting of the backscattered radiation,

$$F(k) \propto e^{-\left(\frac{k-k_\perp}{\Delta k}\right)^2}. \tag{3.4}$$

For $v_{E\times B} >> v_{phase}$, one then has

$$\Delta\omega_{DBS} = v_{E\times B}\Delta k. \tag{3.5}$$

For a Gaussian beam, one therefore expects a Gaussian DBS electric field spectrum, to leading order. Variation of the wave number spectrum of the density fluctuations over the

finite Δk of the diagnostic can in principle also distort the DBS spectrum, which could be manifested as, for instance, finite skewness. In experiment, skewness of the primary Doppler peak can be difficult to distinguish from secondary contributions to the signal (*e.g.* non-localized backscattering along the path or antenna side lobes) or the influence of the underlying turbulent spectrum when $v_{E\times B}$ and v_{phase} are not well separated. For cases where $v_{E\times B} >> v_{phase}$, one can infer Δk from the spectrum: if $\omega_{DBS} = k_\perp v_{E\times B}$ then

$$\frac{\Delta\omega_{DBS}}{\omega_{DBS}} = \frac{\Delta k}{k_\perp}, \tag{3.6}$$

where ω_{DBS} is the Doppler peak. In addition to finite beam size, the beam and plasma curvature also impact Δk, which is addressed in more detail in Sec. 3.4.3. Doppler backscattering does not measure fluctuations at one specific wave number, but is sensitive to a range centered about the wave number that can be determined by ray tracing. The wave number localization for scattering within a Gaussian beam's Rayleigh zone, including curvature effects, can be approximated as [162]

$$\Delta k_\perp = \frac{2\sqrt{2}}{w_0}\left[1 + \left(\frac{w_0^2 k_i}{R_{plasma}}\right)^2\right]^{1/2}, \tag{3.7}$$

where $\Delta k_\perp$ is the $1/e$ amplitude half-width, the beam diameter is $2w_0$, and R_{plasma} is the curvature of the cutoff layer. The beam diameter within the frequency range of the DIII-D DBS systems is $\sim 4-5$ cm, with the beams focusing in the plasma. For typical geometries in DIII-D, the peak scattering wave number is for intermediate-k, $k_\perp \sim 2-10$ cm^{-1} ($k_\perp\rho_i \sim 1-4$), with wave number localization of $\Delta k/k \lesssim 0.3-0.4$.

Figure 3.4 shows the ensemble averaged spectrum from 4000 to 4400 ms from Fig. 3.3. The spectrum is fit to a Gaussian, which shows a high degree of agreement for the large amplitude, Doppler-shifted peak. This is consistent with the interpretation that the spectral shape is dominated by the Δk determined by the Gaussian beam, rather than the distribution of velocities of the fluctuations that induce the scattering. An exactly zero frequency component in the spectrum, created by direct reflections from lenses and windows, has been removed from the spectrum. Also note a small amplitude secondary peak at ~ -100 kHz in the figure– a much different frequency than would be created by a mirrored signal (see Sec. 3.5.1). Such

a peak could arise if, for instance, the measurements are near a velocity shear layer [163], there is a second mode at the same k with a very different phase velocity, secondary antenna lobes, additional scattering orders, or other effects.

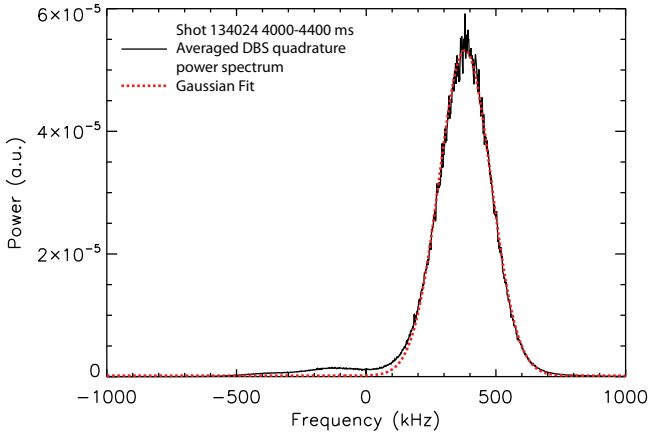

Figure 3.4: DBS quadrature power spectrum from shot 134024, averaged over the time period 4000-4400 ms (solid) and the result of a Gaussian fit to the spectrum (dashed).

Pursuing the line of reasoning that the spectral width is dominated by the Δk from the beam, one would expect that for significant Doppler shifts, $\Delta\omega = \Delta k v_{\tilde{n}}$. One should therefore be able to determine Δk from

$$\Delta k = k_{\perp} \frac{\Delta\omega}{\omega_{DBS}}. \tag{3.8}$$

This is tested in Fig. 3.5, where we define the experiment determined estimate as,

$$\sigma_k = k_{\perp} \frac{\sigma_f}{|f_0|}, \tag{3.9}$$

where $k_{\perp}$ is the DBS scattering wave number determined by ray tracing, and f_0 and σ_f are determined by Gaussian fits to experimental spectra. The vertical axis of figure is truncated so that large values of σ_k where f_0 approaches zero are not pictured. Near zero, for small Doppler shifts, one would expect both Δk and the velocity distribution to contribute, so the approach would be invalid for the omitted points. Indeed, in that regime the velocity distribution of the turbulence can impact the spectral shape—this is used for measurements in Sec. 5.3.3.4. For the plotted points, it does not appear the limit where the expression holds

is entirely satisfied, but it does appear that for $|f_0| \gtrsim 500$ kHz, σ_k is starting to approach an asymptote. A bound can then be set: $\sigma_k < 1.7 \pm 0.2$ cm^{-1} or $\sigma_k/k_\perp \lesssim 0.3 - 0.4$.

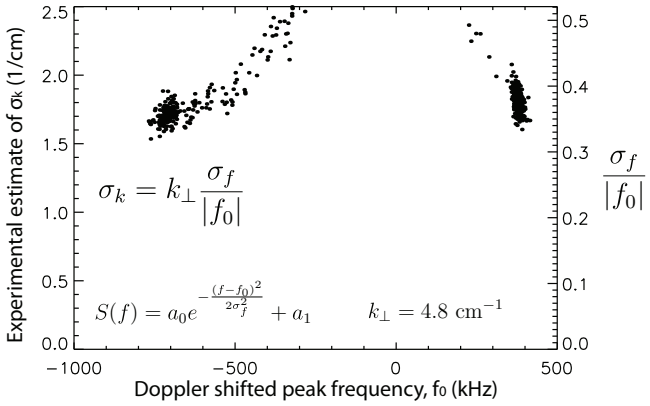

Figure 3.5: Calculation of σ_k for 487 time periods between 4000 and 4800 ms in shot 134024. The DBS scattering wave number determined by ray tracing is $k_\perp = 4.8$ cm^{-1}. The experimental spectra a fit to a Gaussian centered at f_0 and with variance σ_f^2. The right axis gives the ratio σ_f/f_0.

3.3.2 Signal analysis

For Doppler backscattering, detection of the backscattered electric field, $E(t) = A(t)\cos\varphi(t) + iA(t)\sin\varphi(t)$, is accomplished with a quadrature mixer for each launched frequency, where $A(t)$ the electric field amplitude and $\varphi(t)$ is its phase, relative to a reference local oscillator. The outputs of the quadrature mixers–termed the 'in-phase,' $I(t) = A(t)\cos\varphi(t)$, and 'quadrature,' $Q(t) = A(t)\sin\varphi(t)$, signals–are digitized. This allows calculation and analysis of the complex electric field, $E(t) = I(t) + iQ(t)$; the electric field amplitude, $A_{DBS}(t) = \sqrt{I(t)^2 + Q(t)^2}$; and the phase of the electric field, $\varphi_{DBS}(t) = \arctan\left(Q(t)/I(t)\right)$. To minimize the impact of spurious phase jumps, $\varphi_{DBS}(t)$ is determined by calculating the differential phase between time points, which is then integrated. The amplitude contains information about the fluctuation level of intermediate-k density fluctuations. The DBS phase contains the Doppler shift from the lab frame propagation velocity of the backscatter-inducing turbulent structures. The lab frame velocity is due to the sum of the $E \times B$ velocity

and the phase velocity of the turbulence, $v_{Lab} = v_{E\times B} + v_{phase}$, where the radial electric field contributing to the $E \times B$ velocity contains both the equilibrium rotation, oscillatory modes like zonal flows and GAMs, as well as convection or advection by any larger scale potential structures.

The turbulence flow velocity, $v_{\tilde{n}}$, can be extracted from the data in two ways. Either short time windows can be used, during which the Fast Fourier Transform (FFT) of the complex quadrature signal, $I(t) + iQ(t)$, is calculated. From those spectra, the Doppler shifted peak can be determined either by fitting the spectrum or, for cases with sufficiently high data quality, by calculating the first moment of the spectrum. Alternatively, the Doppler shift is also ideally equal to the time derivative of the DBS phase, $\omega_D = \partial\varphi_{DBS}/\partial t$. This can be calculated simply by approximating the time derivative of the DBS phase using finite difference methods, although this introduces additional errors into the analysis. The former approach has been most widely used in DBS analysis, although the latter has seen some application[15, 121, 123]. To fix notation, the former will be referred to as the "Quadrature-FFT" method and the latter as the "DBS phase derivative" method. For fast time scale studies the former is realized, typically, with 128 point FFTs and the Doppler shift is determined by the power-weighted average. Longer records are used when slower time scales are of interest. For the latter method, a 5-point stencil finite difference approximation to the derivative is used to minimize the error introduced. These alternate data analysis approaches are contrasted and compared in Chapter 4 to maximize the transparency of the results and associated uncertainties.

3.3.2.1 Model equation for DBS phase

In previous work, the complex quadrature DBS signal has most commonly been analyzed to yield information about the equilibrium $v_{\mathrm{E\times B}}$ flow and its shear [164–167]. The amplitude and the phase of the backscattered electric field can also be analyzed individually. Similar to the method described below, a finite difference approach has been applied to the DBS phase in previous work [123]. The amplitude contains information about the relative level

of density fluctuations, over a weighted wave number range, and factors in the scattering efficiency with its multiple dependencies [161]. The phase contains information about the equilibrium flow, coherent flow oscillations, turbulent flow fluctuations, and the effect of any optical path length variations. Analysis of the amplitude and phase signals directly allows the additional time-windowing and Fast Fourier Transform (FFT) procedures necessary to analyze the quadrature signal to be side-stepped; the full time resolution of the diagnostic is then available. By not taking finite differences of the phase the possible introduction of numerical artifacts is avoided. In this section a heuristic model equation for the DBS phase will be described, which can be used to guide data analysis and interpret results.

The "DBS phase," $\varphi_{\mathrm{DBS}}(t)$, to be discussed is the difference in phase between the electric field of the backscattered beam, and the phase of a reference local oscillator. This difference depends on the optical path length and the Doppler shift acquired by the backscattered beam in the scattering process, both of which, in general, can be functions of time:

$$\varphi_{\mathrm{DBS}}(t) = \int_{t_0}^{t} \omega_{\mathrm{Dop}}(t)dt + 2\int_{0}^{x_c(t)} k(x,\ t)dx. \tag{3.10}$$

The Doppler shift, $\omega_{\mathrm{Dop}}(t)$, is integrated from a reference time, t_0, to time t. Gaussian beam and geometry effects are neglected to highlight the dominant physical contributions from the plasma. Considering the beam as an optical ray, the second integral is taken along the propagation path from the antenna at $x = 0$, to the cutoff at $x = x_c(t)$. Ideally for DBS, the second term is small and can be neglected. Ideally for reflectometry, the beam is aligned normal to the cutoff surface and the first term can be neglected. In reality, both are present to some extent.

These expressions can be further expanded by taking an *ansatz* for the local velocity of the turbulence. For the propagation velocity of the turbulent structure responsible for the scattering process, assume that there are contributions from the equilibrium $E \times B$ flow, $v_{E\times B}$; from an oscillating coherent mode, v_m, with frequency ω_m; and from the turbulent flows, $\tilde{v}$. In principle, the scattering turbulent structure can be advected or convected by any larger scale structures in the plasma, so that there is actually a sum over all scales larger

than the scattering structure. For a scattering fluctuation with wave number $k_\perp$, the plasma frame velocity of each structure, v_k, then contributes:

$$\tilde{v} = \sum_{k \leq k_\perp} v_k. \tag{3.11}$$

This description is consistent with Ref. [168], where it was argued that the radial correlation length measured with DBS is independent of $k_\perp$. This situation is pointed out to make clear the difficulty of attempting to measure the plasma frame velocity of the turbulence. Including the above terms, the laboratory frame velocity, $v_{\tilde{n}}$, is

$$v_{\tilde{n}} = v_{E\times B} + v_m \cos(\omega_m t) + \tilde{v}. \tag{3.12}$$

The Doppler shift is then $\omega_{\mathrm{Dop}}(t) = k_\perp v_{\tilde{n}}$. (Note that, due to the vertical scattering plane and sheared magnetic field, one expects a wave number mismatch between the turbulence and the beam that results in a projection of the measured flow from the binormal $E \times B$ direction to the poloidal direction. In the core of standard large aspect ratio tokamaks this is a small effect.) An expression for the phase can then be written down that separates the different physical contributions to $\varphi_{DBS}(t)$ into multiple terms:

$$\varphi_{DBS}(t) = k_\perp v_{\mathrm{E\times B}} t + \frac{k_\perp v_m}{\omega_m} \sin(\omega_m t) + \tilde{\varphi}(t) + 2\int_0^{x_c(t)} k(x,\ t) dx \tag{3.13}$$

Depending on the phenomena under investigation, one can then apply appropriate analysis techniques to isolate the desired term. The first term is due to the equilibrium radial electric field and can be extracted most easily by analysis of the complex quadrature signal; although, through smoothing and by taking a derivative, it can be extracted from $\varphi_{\mathrm{DBS}}(t)$. The second term is due to any oscillatory flows in the plasma (in principle, there may of course be multiple coherent modes) and can be examined through spectral analysis of $\varphi_{\mathrm{DBS}}(t)$. The third term is the turbulent flow contribution. In addition to optical path length variations such as islands in the beam path, also accounted for in the fourth term is any backscattering that occurs before the cutoff is reached. This can occur in regions with steep density gradients, or if the beam path is not far above cutoff. These types of effects can occur for any microwave or millimeter-wave diagnostics. With DBS, when there is a significant Doppler shift of the

cutoff-localized contribution, this fourth term, if significant, can be filtered out in post-processing of the complex quadrature signal, since it is centered near zero frequency when it is visible in the data. For reflectometry cases, the fourth term dominates and is essentially due to low-k movements of the cutoff surface; analytical expressions exist [169] for cases where the other terms can be neglected. For DBS configurations, this term is much smaller than the Doppler shift terms.

It is illuminating to take the Fourier transform of Eqn. 3.13. Assuming the linear term is zero for times less than zero, and absorbing the path length term into $\tilde{\varphi}(t)$, one finds

$$\varphi_{\mathrm{DBS}}(\omega) = k_{\perp} v_{\mathrm{E\times B}} \left(\frac{i\delta'(\omega)}{4\pi} - \frac{1}{4\pi^2\omega^2} \right) + \frac{ik_{\perp}v_m}{2\omega_m} \left[\delta(\omega+\omega_m) - \delta(\omega-\omega_m) \right] + \tilde{\varphi}(\omega). \quad (3.14)$$

Here $\delta(\omega)$ is the Dirac delta function and $\delta'(\omega)$ is its derivative. From Eqn. 3.14 one can extract two expectations for the experimental φ_{DBS} spectrum. From the second term in the first set of parentheses, there should be a f^{-2} component in the spectrum due to the equilibrium component of the $E \times B$ flow. From a coherent mode, one expects a peak at the mode frequency, due to the delta functions. These effects can be seen in Figure 3.6, where the f^{-2} character is predominant for much of the DBS phase spectrum, except for the peak at the frequency of a coherent mode, falling off at high frequencies. This f^{-2} spectrum is expected and has a physically meaningful origin, in contrast to the f^{-2} spectrum that can occur in conventional reflectometry due to random phase jumps [169, 170]. This f^{-2} spectrum in Fig. 3.6 is also qualitatively different from the reflectometer spectra, which exist over the entire dynamic range of the diagnostic, whereas the f^{-2} of φ_{DBS} falls off for time scales much faster than equilibrium time scales. This occurs since the equilibrium $v_{E\times B}$ flow is assumed to be constant in the *ansatz*, when in reality it is only constant in a statistical sense. There also a significant amount of power at low frequencies, which could be due to zonal flow activity.

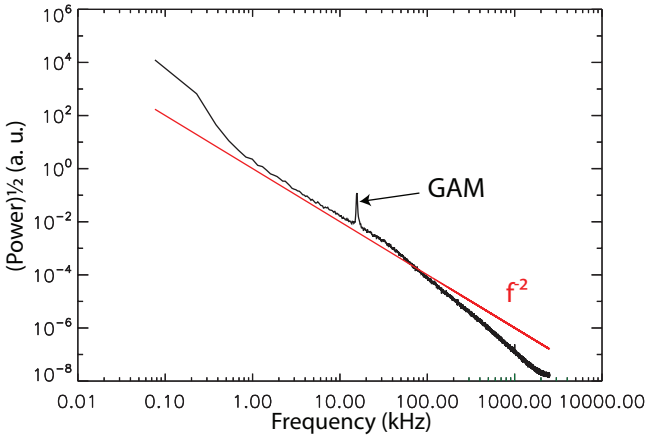

Figure 3.6: Plotted in black is the DBS phase spectrum, ensemble-averaged over 500 ms, of a steady-state L-mode plasma. The spectrum primarily goes as f^{-2}, except for a coherent mode that is present(a GAM in this case), then rolls over at high frequencies where various effects compete.

3.3.3 DBS-5 Hardware

This section describes details of the diagnostic hardware developed in the course of work for this dissertation. This diagnostic system is referred to as "DBS-5" elsewhere in this dissertation and in publications.

3.3.3.1 Frequency Array Generation

Amplitude modulation has previously been used to create a pair of sidebands on a carrier signal for three channel reflectometry systems [171–173]. A two-frequency system has also been used for a differential phase reflectometer [174]. In this section a frequency modulation technique is described which produces multiple sidebands on a carrier signal. If an oscillating high frequency voltage is combined with a DC voltage and used to tune a wideband voltage-controlled oscillator (VCO) the resulting instantaneous frequency of the VCO output, ω_i, is given by

$$\omega_i = \omega_c + \Omega_m \cos(\omega_m t), \tag{3.15}$$

where ω_c is the center frequency set by the DC voltage and ω_m is the modulation frequency. The parameter Ω_m determines the frequency envelope centered at ω_c into which the sidebands fall. The phase, $\varphi(t)$, of the real electric field, $E(t) = E_0 \cos\varphi(t)$, with amplitude E_0, of the microwave output of the VCO is then found by integrating the instantaneous frequency, yielding

$$E(t) = E_0 \cos\left(\omega_c t + \frac{\Omega_m}{\omega_m}\sin(\omega_m t)\right). \tag{3.16}$$

Letting $m = \Omega_m/\omega_m$ be the frequency modulation range parameter divided by the modulation frequency and expanding in terms of Bessel functions of the first kind [147], J_n, one arrives at an expression for the relative electric field amplitude which exposes the sidebands created by the modulation:

$$\begin{aligned}\tfrac{E(t)}{E_0} &= J_0(m)\cos(\omega_c t) + \\ &\textstyle\sum_{n=1}^{\infty} J_n(m)\left[(-1)^n \cos((\omega_c - n\omega_m)t) + \cos((\omega_c + n\omega_m)t)\right].\end{aligned} \tag{3.17}$$

With a sufficiently high modulation frequency it is possible to produce an array of frequencies which is quasi-static on the timescale of plasma turbulence, for which the modulation parameters can be chosen as desired within equipment limitations, and which is tunable by changing the DC voltage. A high frequency slew rate VCO is necessary for the technique to function properly. The modulation approach is also very sensitive to the VCO input voltage, requiring that any noise from the DC tuning source and from the modulation source be minimized.

Figure 3.7 compares the calculated spectrum from Eqn. 3.17 to a screen capture from a spectrum analyzer. The spectrum in Fig. 3.7(b) is from the output of a wide-band voltage controlled oscillator, where the input voltage was modulated at 50 MHz by using a bias-T to combine a DC control voltage with the output of a lower frequency oscillator. The DC voltage was set to produce the center frequency at 20.5 GHz. The amplitude of the 50 MHz oscillator was adjusted so that the pair of sidebands at $20.50 \pm .05$ GHz were minimized, which is equivalent to the first Bessel function zero for Eqn. 3.17. This was tested with

Fig. 3.7(a), where, with the same center and modulation frequencies, the parameter m was chosen to be 3.8317, the first zero of the Bessel function $J_1(m)$. Annotated in Fig. 3.7(a) is a horizontal line approximating the spectrum analyzer noise level. The agreement between the relative amplitudes of the frequency peaks in Fig. 3.7(a-b) demonstrates that the microwave hardware produces an output as expected from the analytical result.

3.3.3.2 Hardware Arrangement

Figure 3.8 shows a schematic of the hardware. The technique described in Section 3.3.3.1 is implemented with a 350 MHz crystal oscillator modulating a 13.5-20.0 GHz VCO. The specified minimum frequency slew rate for the VCO is 20 MHz/μs. A variable attenuator on the crystal oscillator allows the modulation amplitude to be adjusted. The VCO output is doubled, filtered, amplified, and doubled again. The hardware arrangement can operated in the frequency range of $53-78$ GHz, covering most of V-Band ($50-75$ GHz) and into W-Band ($75-110$ GHz). Due to internal mixing, the effect of the doublers is not only to double each input frequency in the array, but also to insert an additional frequency between each other pair of frequencies. The net effect is that the number of sidebands approximately doubles, while the separation frequency remains constant. Part of the millimeter-wave output is diverted with a directional coupler to the radio frequency (RF) input of a V-band mixer to provide reference signals. The remainder is launched into the plasma using a monostatic antenna arrangement. A microwave variable attenuator in the return path allows signal levels to be optimized for operation at different launch frequencies and in different plasma regimes. A second VCO, identical to the modulated VCO, generates a single frequency which is offset to be outside of the modulation envelope. This single frequency is doubled twice, then a directional coupler distributes local oscillator (LO) power to the reference and signal microwave mixers. The down-converted intermediate frequency (IF) outputs from the signal and reference mixers are passed to the receiver hardware where they are amplified, power-divided, and passed through a matched pair of bandpass filter banks. Each pair of bandpass filters selects the reference and return signals at a particular down-converted

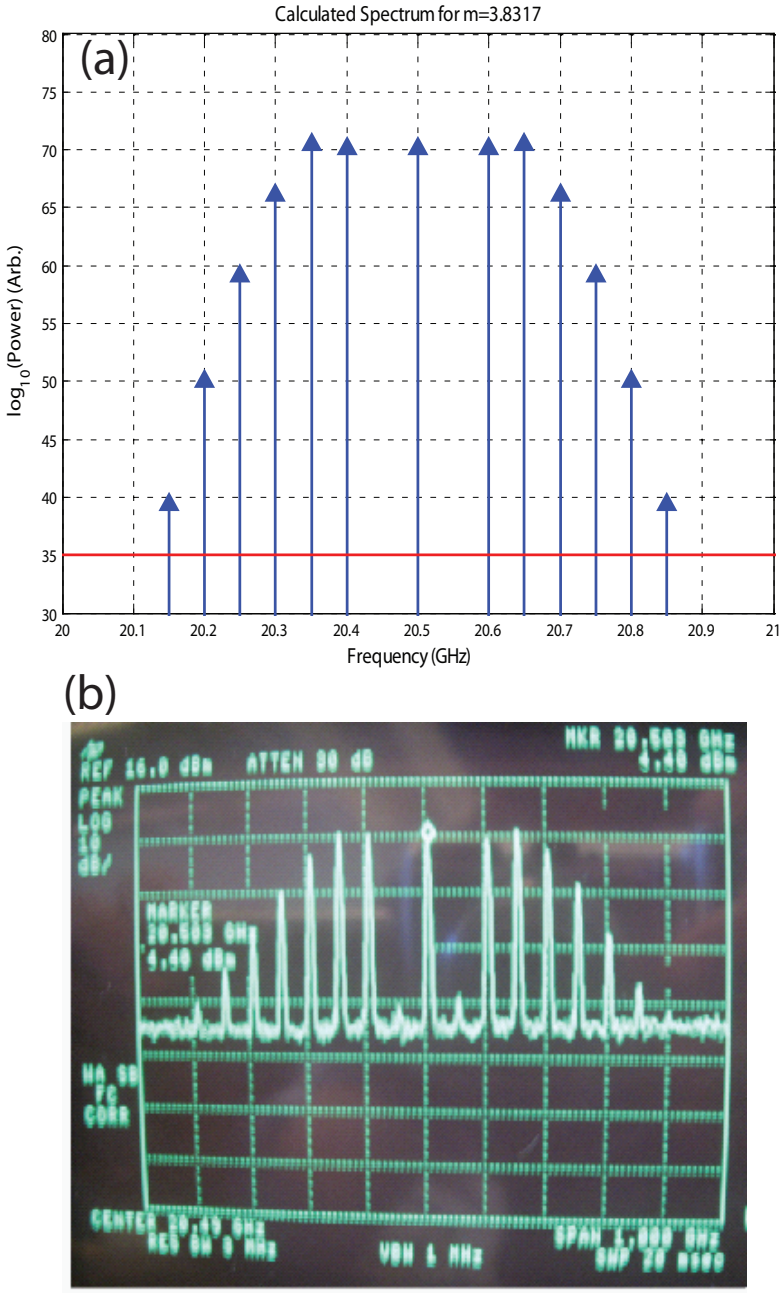

Figure 3.7: (a) Calculated frequency spectrum and (b) spectrum analyzer screen capture showing generation of the frequency array, both on logarithmic scales. The spectrum in (b) is centered at 20.5 GHz and displays 100 MHz/division.

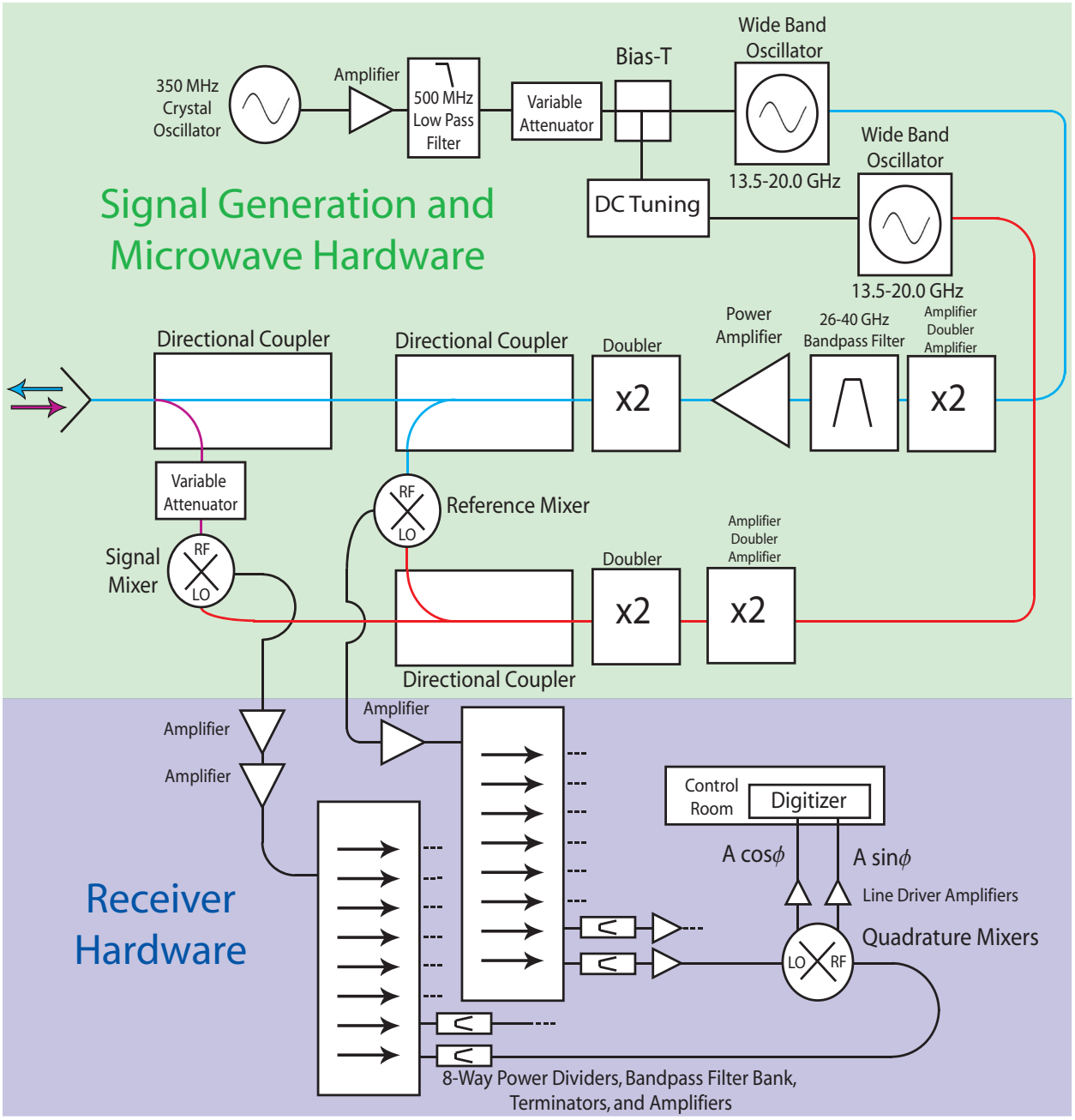

Figure 3.8: Hardware schematic. The portions highlighted in green indicate the signal generation and microwave hardware, and the blue portions indicate the receiver hardware. The blue signal pathway highlights the launched signal. In purple is the received signal. The red pathway shows the offset frequency used to down-convert the reference and received signals. A single quadrature channel is represented in the receiver portion.

frequency from each array. A set of quadrature mixers then provide the "in-phase" and "quadrature" signals which are digitized. Additional amplifiers, pictured in Figure 3.8, and attenuators, not pictured for clarity, are present to adjust power levels as needed. The amplitude, phase, and complex amplitude for each launched frequency are recovered with software analysis.

The launch and LO VCOs are controlled independently rather than through a feedback loop (*i.e* a phase-locked loop), such as if often done for single channel systems. Independent control increases the flexibility of the system. For instance, for low launched frequencies the LO is at a higher frequency than the launched array, whereas for high launched frequencies the LO is at a lower frequency that the array. The entire bandwidth of the launch VCO can therefore be used. Furthermore, a feedback loop would require significant hardware additions to filter only one of the launch frequencies–otherwise the difference frequency enforced by the feedback could be satisfied by one of the sideband frequencies, rather than the center frequency. Independent control does introduce the complication of requiring the voltage-frequency characteristics of the sources to be known sufficiently well for the sources to be tuned such that down-converted signals are within the passbands of the bandpass filter array, which are 150 MHz wide.

A DC power supply or equivalent tuning method with sufficiently low noise may be used to separately control each VCO, allowing the microwave mixer IFs to be kept within the passbands of the filters when the center frequency of the array is adjusted. 8-way power dividers are used, while for the data presented in this section only 4 of the channels were monitored and digitized. The filters have 150 MHz passbands, centered at 3.75 GHz, 4.45 GHz, 4.80 GHz, and 5.15 GHz. In later work a fifth channel was added, centered at 4.10 GHz. The 5 channel version of the system was used for most physics studies, where the system is referred to as DBS-5. Laboratory tests show it is possible to produce array bandwidths up to $\sim$ 4 GHz with the employed hardware. The current arrangement has been adjusted to have an array bandwidth of 1.4 GHz.

3.3.3.3 Laboratory Tests

Figure 3.9 shows an early (August 2007) proof-of-principle of the frequency-modulated DBS system, which was set up in the laboratory for testing. The quasi-optical antenna system actually used in the experiment went through several iterations, described in Sec. 3.3.4 in detail. The setup in Fig. 3.9 uses bistatic antenna (all experimental data used monostatic) and the microwave beams diverge (in experiments, the beam was collimated, then focused); otherwise, similar test setups have been used to test system operation and beam characteristics between run periods. To the right in Fig. 3.9 is the microwave hardware used to launch and receive the beam. To the left is a metallic mirror on tracks, which can be moved to change the optical path length of the detected beam, causing the phase of the detected electric field to change.

Figure 3.9: Laboratory setup for testing a proof-of-principle DBS hardware arrangement.

Data was collected during laboratory tests in February 2008, prior to the run period at DIII-D that year. The system was tested with a replica of the quasi-optical antenna system used during that run period, with a monostatic conical horn (experiments used a scalar horn), a collimating lens, and a focusing parabolic mirror, which directed the beam to a movable flat mirror, as in Fig. 3.9. Figure 3.10 shows a screen capture from a digital Tektronix oscilloscope

set to display the output of the quadrature mixer for the 4.45 GHz bandpass filters, with DBS-5 at a center frequency of 54 GHz. The figure trace in the figure was created by moving the flat mirror approximately one wavelength of the beam. The result was a nearly circular phasor. Similar tests were conducted for all channels. Settings producing either distorted (skewed or unbalanced) phasors or DC offsets near amplifier limits were excluded from use in experiments; although, distortion beyond that in Fig 3.9 was present for many cases and was observed to depend on system temperature. Further tests, both in laboratory and *in situ* at the experiment were conducted intermittently over the years to assure expected operation and to recalibrate frequency settings.

The diagnostic was assembled and extensively tested in the laboratory. A mirror was used to supply a reflected signal and confirm operation of all system components shown in Figure 3.8. Tests revealed that using the frequency modulation technique described in Section 3.3.3.1 is extremely sensitive to any noise on the VCO inputs. It was found that the VCO input noise contribution dominated any noise imparted by amplifiers or other system components. The solution employed at the time the initial data was acquired involved using batteries as the DC source, with potentiometers used in voltage dividers for inter-shot tuning. Later, a method involving optical control of a local microprocessor unit to set the DC voltages via a digital to analog converter was developed. Using optical transmission allows remote tuning while minimizing electrical interference. Employing a local microprocessor unit allows a sequence of voltages to be programmed for use during a discharge, enabling a frequency hopping mode of operation. Additionally, internal reflections in the millimeter-wave hardware components can create standing waves which result in large DC offsets in the quadrature mixer outputs. These offsets vary widely depending on the operating frequencies. Predetermined operating points with small DC offsets were identified across the operational frequency range.

One of the wideband VCOs used in the initial system was found to have a long term drift of its frequency versus voltage characteristics. Drifts of 100-200 MHz were found over some voltage ranges–enough for the down-converted frequencies to drift out of the passbands

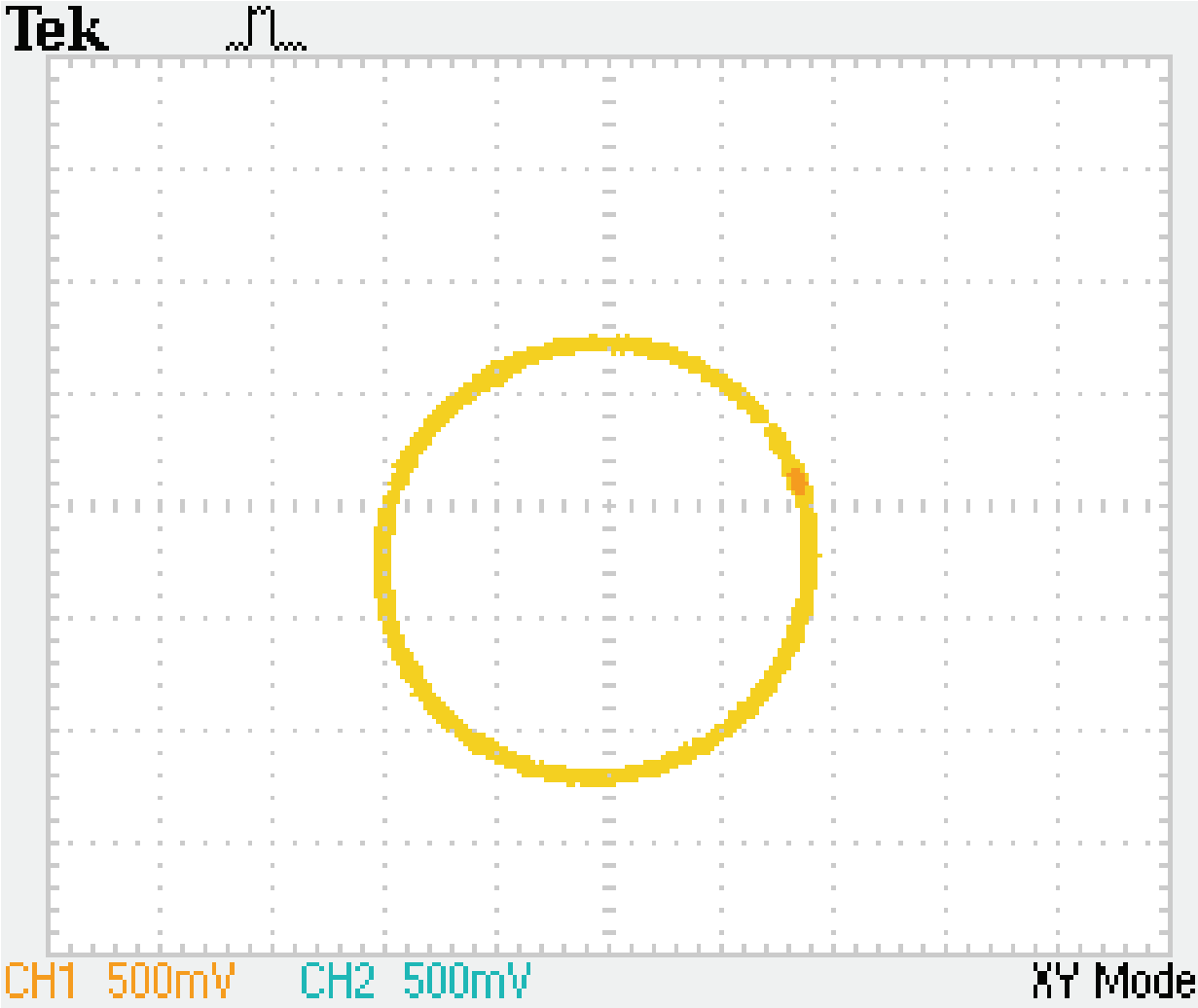

Figure 3.10: Oscilloscope screen capture showing detected electric field phasor.

(this was addressed for experiments with *in situ* recalibrations towards the end of the 2009 and 2010 run periods). Tests were done on a number of factors that could influence the sources. The ambient temperature was found to affect the sources by $\sim 10 - 20$ MHz when a cold aerosol spray was used to quickly change the temperature by a significant amount. The temperature differences between calibration conditions and changes during a day *in situ* at DIII-D were insufficient to account for the drift. The source showing large year-to-year drifts was replaced before the 2011 run period. No further issues have been observed since the replacement.

3.3.4 Quasi-optical antenna systems at DIII-D

Ports at two toroidal locations have been used for DBS measurements at DIII-D, which are separated by 180° toroidally. The two ports are referred to as the 60° Port and the 240° Port, which are indicated in Fig. 3.11. Also shown in the figure are the four beam lines used for neutral beam injection. The three DBS systems−usually referred to as DBS-2 [2], DBS-5 [6], and DBS-8 [7] in this thesis and in publications−have been relocated between the two ports at various times. The specifics of the setup for acquired data are included in later sections, where appropriate.

Figure 3.12 shows components of the quasi-optical antenna system at the 60° Port. A DBS system is coupled through V-band waveguide to a corrugated horn antenna, which launches a beam into an aspherical lens that collimates the beam. The collimated beam is reflected by a flat mirror through a quartz window into a parabolic mirror that focuses the beam into the plasma. The parabolic mirror at the 60° Port can be remotely adjusted to launch the beam between 7° and 15° above the horizontal. There is a remotely controlled shutter that can be activated to protect the system in cases where stray radiation from electron cyclotron heating gyrotron might enter the DBS port (*e.g.* if the plasma goes over-dense, reflecting the ECH power).

A similar quasi-optical system is present at the 240° Port. The salient difference is

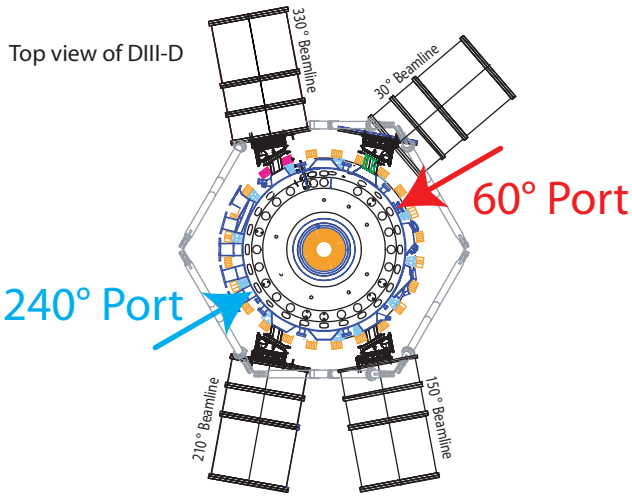

Figure 3.11: Top view of DIII-D showing DBS port locations. Neutral beam locations also shown.

that the parabolic mirror at that location can be adjusted between $-10°$ and $4°$ above the horizontal, so either DBS or conventional reflectometry can be used. The mirror positions as a function of angle are known from measurements; interpolation of the known positions are performed to determine the launch point for ray tracing and full wave modeling.

Figure 3.13 shows an example of a beam spot size measurement for the 240° Port. These measurements are made in laboratory with a duplicate of the quasi-optical antenna system that is present at the experiment. The measurements were made with a detector coupled to a translation stage, where in the oscilloscope capture the horizontal axis is the translation stage position and the vertical is the detected microwave power. The pictured data is the horizontal profile of a beam launched at 58 GHz with a corrugated horn antenna. The focal length of the parabolic mirror is 130 cm and the measurement is 132 cm from the mirror position, which is within the beam's Rayleigh range. The $1/e^2$ beam power diameter for the pictured data in Fig. 3.13 is 4.9 cm. Small side lobes can be observed in the beam profile. Similar data has been tabulated at multiple frequencies for both ports [8, 175]. These tabulations were used for the synthetic DBS diagnostic described in Sec. 3.4.3.

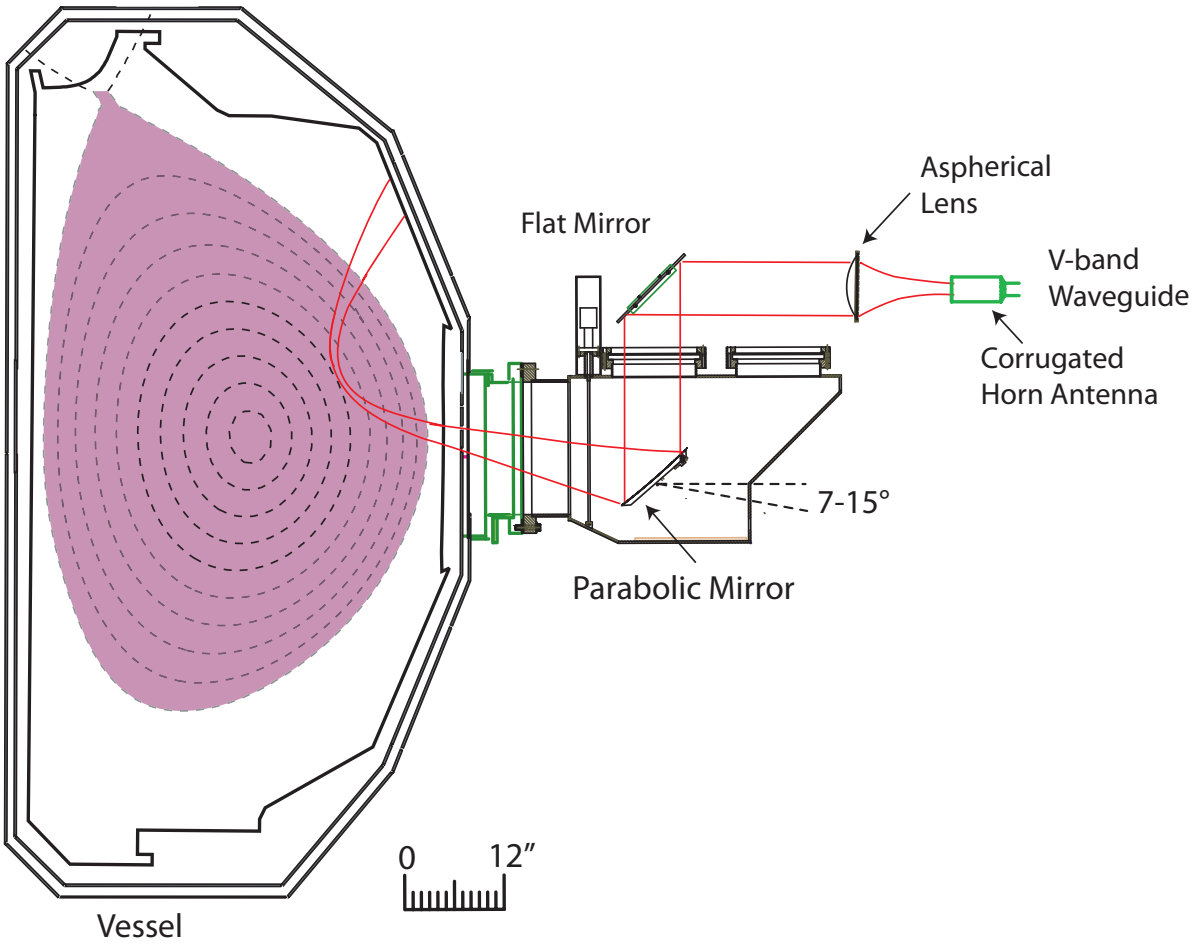

Figure 3.12: Quasi-optical antenna system at 60° port

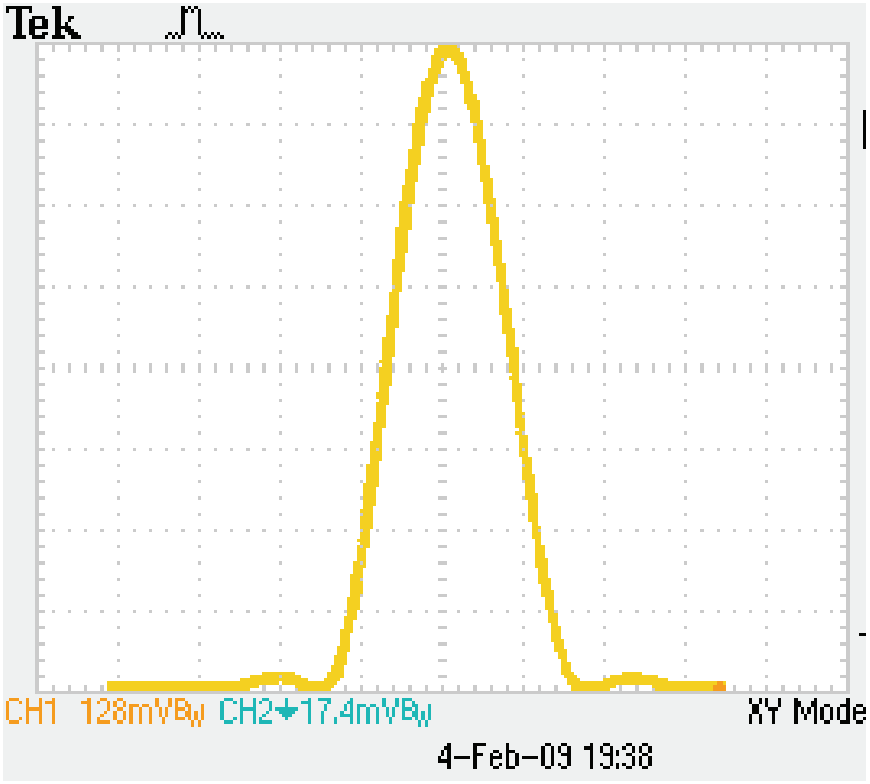

Figure 3.13: Spot size measurement using duplicate of quasi-optical antenna system.

3.3.4.1 Initial DBS-5 data

Figure 3.14 shows a spectrogram of the complex amplitude from one of the launched frequencies. From 3330 to 3350 ms a co-injected (parallel to the plasma current) neutral beam blip is applied. From 3600 ms onward two balanced neutral beam sources are used, one co-injected and one counter-injected. During and following the 20 ms beam blip the change in rotation from the neutral beam introduced momentum results in an increased Doppler shift in the measured DBS spectrum. The two neutral beams cause the plasma to transition to H-mode at $\sim$ 3670 ms. After the transition the density begins to rise sharply, causing the probed location to sweep outward. The scattered power increases as the probed location sweeps outward, followed by a sharp drop in the H-mode pedestal region.

Ray tracing is used to determine the scattering location and probed $k_\perp$ as described in Section 3.4.1. Here, spline fits to Thomson scattering data for density profiles that have been normalized to line-averaged densities from interferometer chords together with equilibria from EFIT [176] are used as inputs for the ray tracing code Genray [177]. For more detailed quantitative analysis, both of these inputs can be improved through use of density profile reflectometer data and with more accurate EFITs for the equilibria to minimize known systematic uncertainties. The data presented here serve to illustrate the analysis methods and capabilities of the diagnostic. Figure 3.15(a) shows the propagation velocity of the turbulence obtained using the ray tracing results shown in Figure 3.15(b) and the Doppler shift determined by calculating the mean frequency of each channel from spectra as pictured in Figure 3.14(a). As is shown later, scattering location calculations such as those shown in Figure 3.15(c) can be used to determine the local velocity shear. When the cutoff location occurs in the steep density gradient region of the pedestal the ray tracing wave number calculation becomes unreliable.

Two time scales associated with momentum input from the neutral beam blips are clearly present in the data. First there is a sharp rise in rotation from direct-loss orbits inducing a radial electric field. Second there is a slow increase in rotation as the fast ion population

deposited by the neutral beams slows down and increases the rotation of the thermal plasma from which the scattering occurs. The wave number for each time slice is found by interpolating between ray tracing results at the EFIT times, which are 25 ms apart. A Savitzky-Golay filter is applied to all figures showing turbulence velocity calculations in order to smooth the data. The assumption behind the mean frequency calculation for extraction of the Doppler shift is that the spectrum is dominated by the main Doppler shifted feature. This approach is valid for the Ohmic and L-mode plasmas treated here, but more care must be taken in less ideal circumstances and in cases where the signal to noise ratio is poor.

A set of neutral beam blips is more closely examined in Figures 3.16 and 3.17. In Figure 3.16(a) a 10 ms neutral beam blip is co-injected with the current from 1330 ms to 1340 ms. This is followed by a 10 ms counter-injected beam blip from 1340 ms to 1350 ms. The change in measured turbulence propagation velocity can therefore be directly attributed to $E \times B$ flow driven by neutral beam momentum input, assuming there is no large modification to the phase velocity of the turbulence. The variation in the magnetic field for all points in Figure 3.16 is small, $\leq 1\%$. For reference, one may convert the values in Figure 3.16 to radial electric field in kV/m by multiplying by 1.6 T, although due to the low rotation in the unperturbed time periods contributions from both $v_{E\times B}$ and v_{phase} are likely significant. The neutral beam induced $v_{\tilde{n}}$ changes, on the other hand, are likely entirely due to $v_{E\times B}$. The local $v_{\tilde{n}}$ increases with the first beam, then reverses as the direction of momentum input changes with the second beam, with a net change of approximately zero at the scattering location. In Figure 3.16(b) the difference from the discharge displayed in Figure 3.16(a) is that from 1340 ms to 1350 ms a second co-injected beam blip is applied, resulting in a large difference in rotation in the period following the beam blips in the respective discharges. Note the difference in scales. Large rotation perturbations from neutral beam blips have previously been observed with DBS [178]. A second observation between the scenarios shown in Figure 3.16(a) and 3.16(b) is a significant difference is the flow response during the sawtooth crash events that exist in both discharges. Figure 3.16(c) shows a core electron cyclotron emission channel to reference the timing of the sawtooth cycle in each discharge. Even though there

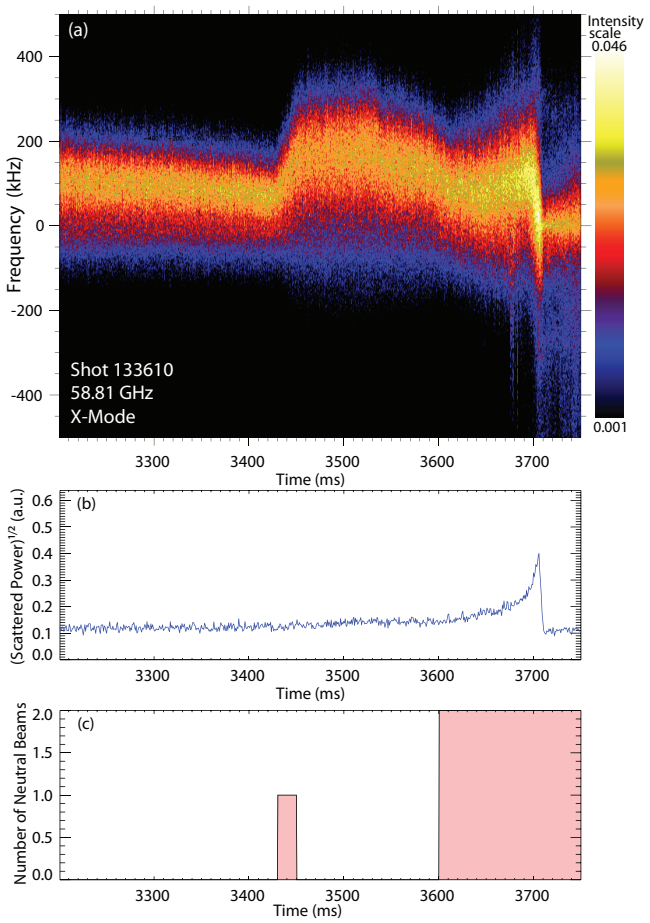

Figure 3.14: (a) Spectrogram of DBS complex amplitude on a logarithmic scale. Positive frequencies indicate positive electric field. (b) During the sweep the scattered power increases as the probed location sweeps outward, then sharply drops in the H-mode pedestal region. (c) Number of beams injected. The beam blip from 3430-3450 ms is co-injected with the plasma current. The two beams starting from 3600 ms are balanced−one co-injected and one counter-injected.

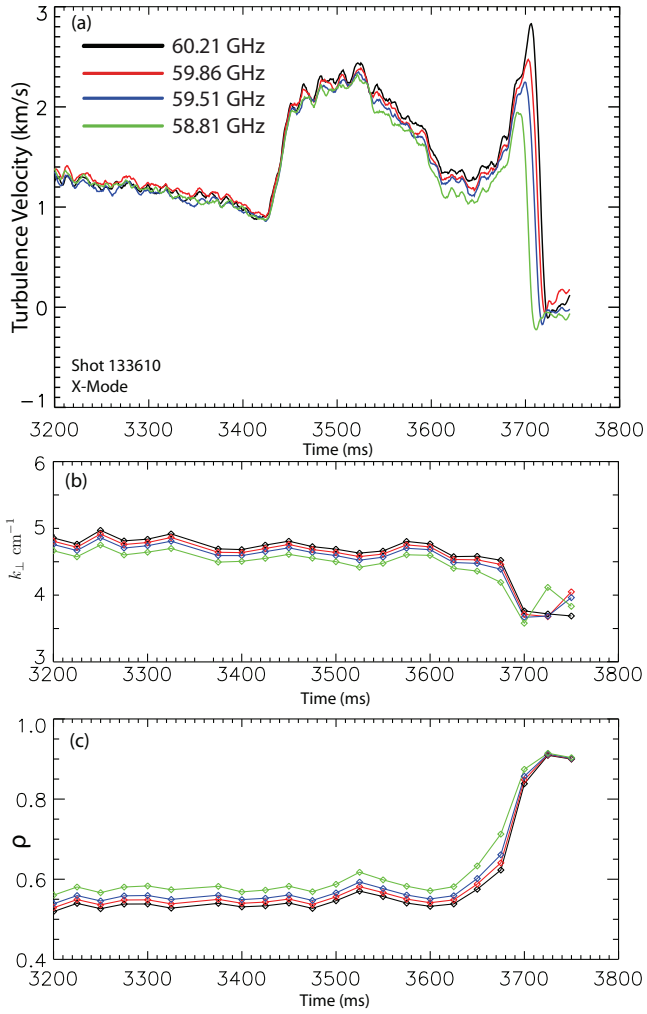

Figure 3.15: (a) Propagation velocity of turbulent structures for 4 DBS channels during the same time period described in Figure 3.14. With the 4 frequency array, the development of the rotation profile following the H-mode transition can be seen as each frequency sequentially sweeps outward. (b) The peak turbulence wave number sensitivity for backscattering for each channel over time. The ray tracing results can be seen to be unreliable for cutoff locations in the edge pedestal. (c) The scattering location of each channel over time from ray tracing, reported terms of ρ, the square root of the normalized toroidal flux.

is not a large difference in the magnitude of the electron temperature perturbation from the sawteeth, there is a significant difference in the flow perturbation in the second case.

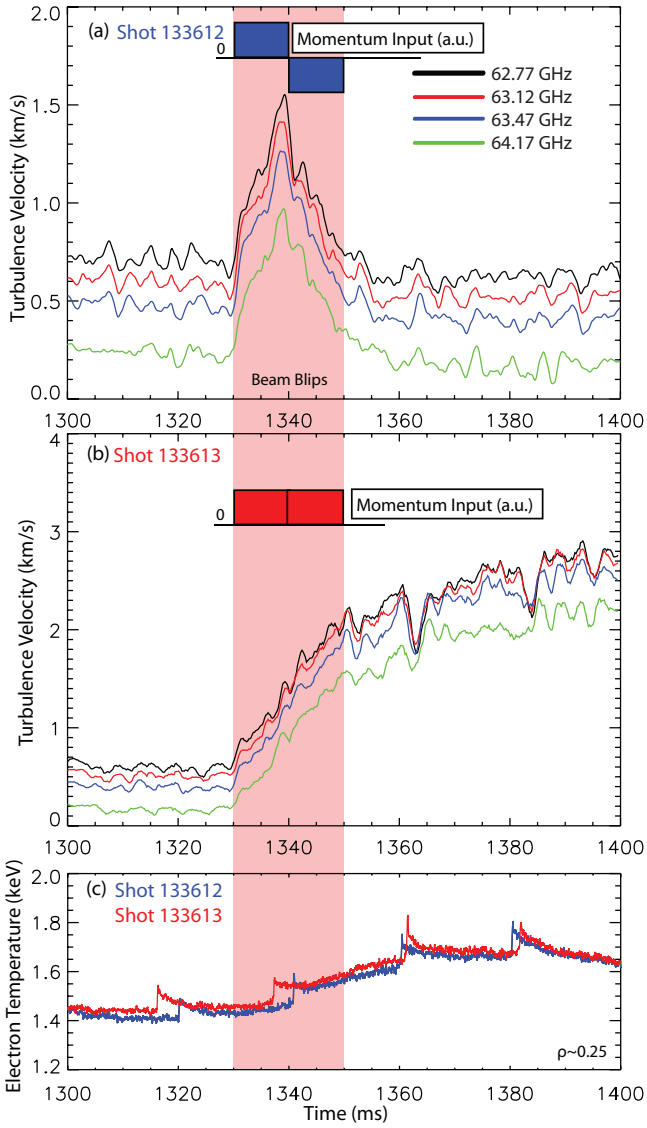

Figure 3.16: (a) Propagation velocity of turbulence for shot 133612. Positive velocity indicates turbulence flowing in the $E \times B$ direction, meaning positive E_r. (b) Turbulence velocity for shot 133613. Inset for reference are indicators of the sign of momentum input from the beam blips. The DBS location is $\rho \sim 0.5$. (c) Electron cyclotron emission measurements of electron temperature in the core, $\rho \sim 0.25$, showing the perturbations from small sawtooth crashes.

Figure 3.17 shows the difference in *local velocity shear* for the same two cases described in Figure 3.16. The local shear is calculated from the difference in turbulence velocity shown in Figure 3.16 and from the scattering locations determined by ray tracing. For 133612 the effect on velocity shear is small and comparable in magnitude to typical fluctuations in the absence of the beams. In 133613 however, there is a small increase in shear during the beams blips followed by a large modulation in the magnitude of the shear that occurs during the sawtooth cycle after the beam blips.

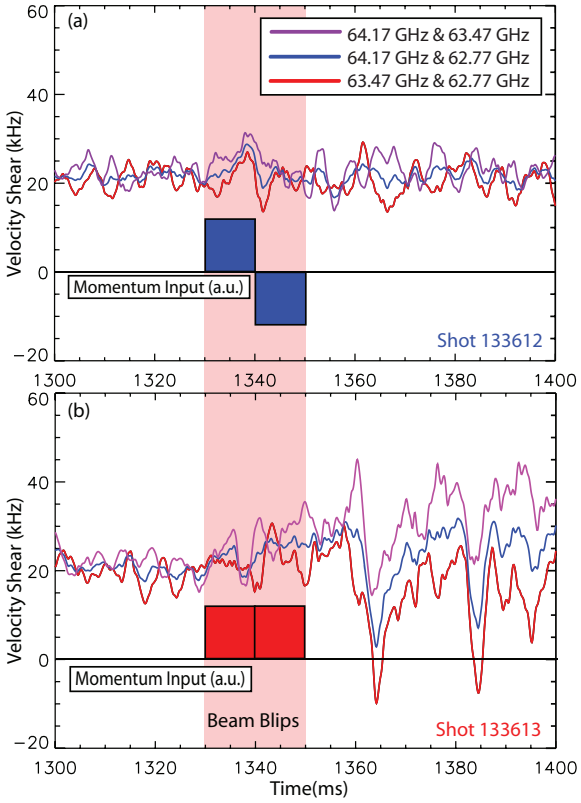

Figure 3.17: Turbulence propagation velocity shear comparing discharges 133612 (a) and 133613 (b). The former has a 10 ms co-injected beam blip followed by a 10 ms counter-injected beam blip. The latter has two consecutive 10 ms co-injected beam blips. The red plot is calculated using the 63.47 GHz and 62.77 GHz channels. Blue using 64.17 GHz and 62.77 GHz. Purple using 64.17 GHz and 63.47 GHz. Inset for reference are indicators of the sign of momentum input from the beam blips. The probed location is $\rho \sim 0.5$ for both discharges.

The capability to study turbulence fluctuation amplitudes and flows with sub-centimeter spatial resolution and fast time resolution at multiple spatial locations enabled detailed studies of the L-H transition in Ref. [21].

3.3.5 Other implementations of DBS

In addition to the DBS-5 [6] system (only fours channels were operational when Ref. [6] was published), two other DBS systems have been used at DIII-D. The initial system, DBS-2, had two tunable channels; it is described in Ref. [2]. The two DBS-2 channels are independently tunable, but each launched frequencies is used as the LO for the other channel, restricting the possible range of difference between the channels. An eight channel, fixed frequency system has also been deployed, DBS-8 [7]. Instead of the frequency modulation approach used for DBS-5, DBS-8 uses a comb generator to produce a set of static frequencies. Frequency difference between channels for DBS-5 is 350 MHz, while for DBS-8 it is 2.5 GHz (with one 5 GHz gap). With one tunable, dense array and one static sparse array, DBS-5 and DBS-8 are very complementary. Example cutoff locations for both systems in an L-mode plasma were shown in Fig. 3.2.

DBS systems have been installed and used at numerous experiments, including ASDEX-U [164], Tore Supra [179], TJ-II [180], and Tuman-3M [181]. DBS is also planned for EAST, KSTAR, and ITER. Several different approaches to analyzing DBS data have also been investigated recently [182, 183].

3.4 Numerical modeling in support of DBS analysis

Although the wave number of the scattering turbulent structures can be calculcated analytically when simplified models are used, a more general approach is to rely on numerical modeling to incorporate experimental equilibrium flux surface shaping and density profiles. The most reduced, and therefore fastest, approach is to treat the propagation of the beam as that of a point-like particle; this is ray tracing and is used because it makes between shot

analysis at DIII-D possible (time between shots $\sim 10-15$ minutes) and allows determination of the most important to quantities of interest: the scattering location and wave number. Two dimensional fullwave simulations have also been used to investigate DBS in DIII-D, and to account for refractive effects on the beam size for a synthetic DBS diagnostic used in gyrokinetic simulations. These topics are described in detail below. Between ray tracing and fullwave simulations, there are additional levels of approximation, such as beam tracing, which have been incorporated into DBS analysis in other work [184].

3.4.1 Ray tracing

Following Ref. [185], a brief description of the ray tracing model is supplied here. The ray tracing equations reduce the partial differential equations governing the propagation of light to a Hamiltonian system of ordinary differential equations, which greatly simplifies the problem−this simplification makes the calculation very fast and suitable for the experimental requirement for between shot analysis. It is used for DBS analysis to determine the scattering location of the wave number of the beam at that location. Conceptually, the ray tracing equations essentially follow the group velocity of the beam−approximated as a single ray−through an inhomogeneous dielectric medium, such as a plasma.

The ray tracing equations are mathematically isomorphic to the Hamiltonian equations of motion. The least action principle of classical mechanics corresponds to Fermat's principle of least time. In the former, the action, $S = \int L dt$, is minimized (where L is the Langragian); in the latter, the optical path length (also called the eikonal), $\psi = \int k dx$, is minimized. Expanding for small changes in ψ, we have

$$\delta\psi(x,t) = \frac{\partial\psi}{\partial x}dx + \frac{\partial\psi}{\partial t}dt \tag{3.18}$$

Comparing this to a plane wave, $\psi = kx - \omega t$, we identify $k = \frac{\partial\psi}{\partial x}$ and $\omega = -\frac{\partial\psi}{\partial t}$. Continuing the analogy, it is known from Hamiltonian dynamics that the action is related to the momentum and Hamiltonian by

$$\mathbf{p} = \frac{\partial S}{\partial \mathbf{x}}, \ \mathrm{H} = -\frac{\partial S}{\partial t}. \tag{3.19}$$

Then, the ray tracing wave number is identified with the momentum,$\mathbf{p} \rightarrow \mathbf{k}$, and the frequency with the Hamiltonian, $\mathrm{H} \rightarrow \omega$. Since the Hamiltonian equations of motion are

$$\dot{\mathbf{p}} = -\frac{\partial \mathrm{H}}{\partial \mathbf{x}}, \ \dot{\mathbf{x}} = \frac{\partial \mathrm{H}}{\partial \mathbf{p}}, \tag{3.20}$$

the corresponding equations for rays are

$$\dot{\mathbf{k}} = -\frac{\partial \omega}{\partial \mathbf{x}}, \ \dot{\mathbf{x}} = \frac{\partial \omega}{\partial \mathbf{k}}. \tag{3.21}$$

For a given plasma dispersion relation $D(\mathbf{x}, \omega, \mathbf{k}) = 0$, it can be written

$$\frac{dD}{dx} = \frac{\partial D}{\partial \omega}\frac{\partial \omega}{\partial x} + \frac{\partial D}{\partial k}\frac{\partial k}{\partial x} + \frac{\partial D}{\partial x}, \tag{3.22}$$

$$\frac{dD}{dk} = \frac{\partial D}{\partial \omega}\frac{\partial \omega}{\partial k} + \frac{\partial D}{\partial x}\frac{\partial x}{\partial k} + \frac{\partial D}{\partial k}. \tag{3.23}$$

Then, holding k and x constant, respectively,

$$\left.\frac{dD}{dx}\right|_k \Rightarrow \frac{\partial D}{\partial \omega}\frac{\partial \omega}{\partial x} = -\frac{\partial D}{\partial x}, \tag{3.24}$$

$$\left.\frac{dD}{dk}\right|_x \Rightarrow \frac{\partial D}{\partial \omega}\frac{\partial \omega}{\partial k} = -\frac{\partial D}{\partial k}. \tag{3.25}$$

We then have the equations that are actually solved in ray tracing simulations:

$$\dot{\mathbf{k}} = \frac{\partial D/\partial \mathbf{x}}{\partial D/\partial \omega}, \tag{3.26}$$

$$\dot{\mathbf{x}} = -\frac{\partial D/\partial \mathbf{k}}{\partial D/\partial \omega}, \tag{3.27}$$

where the dispersion relation, $D(\mathbf{x}, \omega, \mathbf{k}) = 0$, can be chosen to included desired effects. The assumption the model relies on in making the identification between the components of $\delta\psi$ and a plane wave is the WKB approximation: $\nabla k/k^2 << 1$. Using that limit, the same set of equations can be derived from the full set of equations described the wave propagation, rather than by analogy.

To obtain quantitative measurements of turbulence velocity and velocity shear with the DBS technique it is critically important to accurately determine the scattering location and wave number. Since the launched microwave radiation is directed obliquely towards

the cutoff layer, refraction shifts the measurement location slightly radially outward from the normal-incidence cutoff location and modifies the probed wave number. Knowledge of the equilibrium flux surface geometry and of the density profile is essential to accurately determine these quantities. To account for a large range of plasma equilibria and density profiles, numerical simulation is the most expedient method to determine the spatial location and probe wave number. The GENRAY ray tracing code [177] is used for this purpose. Figure 3.18 shows an example of ray tracing calculations. This approach allows determination of the desired quantities between plasma discharges and has been employed to appropriately adjust hardware settings to achieve measurement objectives during experiments. It was also used to guide the design of DBS-5 (*e.g.* choice of channels spacing) and has been applied to explore new experimental configurations.

The Appleton-Hartree dispersion relation (cold plasma) is used for all cases presented in this dissertation, neglecting relativistic effects. GENRAY does allow inclusion of relativistic and warm plasma kinetic effects when desired (*e.g.* high temperature plasmas where relativistic effects on the cutoffs cannot be neglected and for plasma heating or current drive calculations where kinetic effects needed to be included), but they are not relevant for the experimental conditions presented. Free space propagation is assumed until the last closed flux surface, so any effect from plasma in the scrape-off layer is neglected. The validity of the method can break down for cutoff locations in the edge region where the probe wavelength can be on the same order as the density gradient length scale, violating the assumptions of the WKB approximation. Two similar approaches have previously been used for DBS analysis. Gaussian beam tracing has been employed at ASDEX Upgrade [168] and a quasi-optical code has been used at Tore Supra [184]. Both techniques extend ray tracing to also account for interference and diffractive effects upon the beam wavefront evolution, which can be used to estimate the spatial and wave number resolutions for experimental conditions. For accurate determination of the critical quantities, the scattering location and peak wave number sensitivity, ray tracing is sufficient. For a comparison and detailed description of ray tracing, Gaussian beam tracing, and quasi-optical methods see Ref. [186] and references

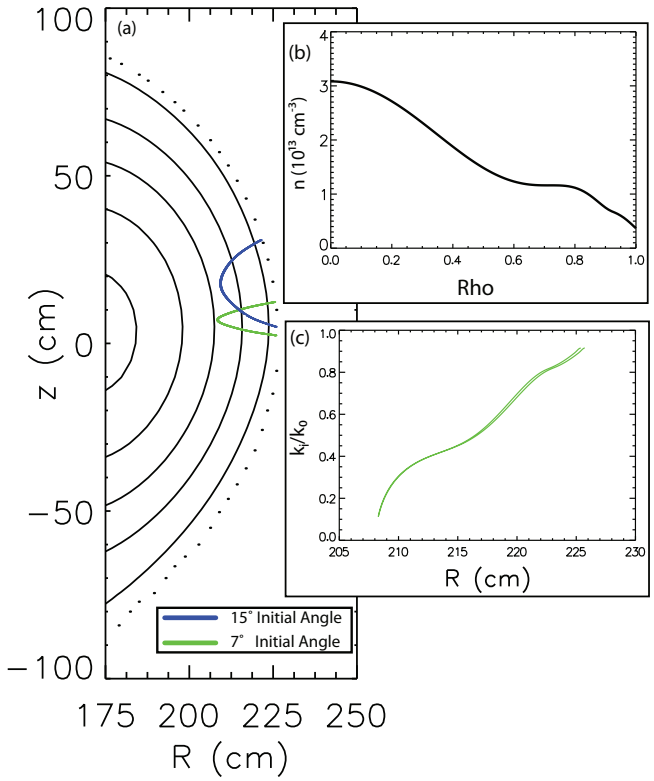

Figure 3.18: (a) Ray tracing examples overlaid on a poloidal cross-section of the low field side of DIII-D. Solid black lines are contours of toroidal magnetic flux. The dotted line indicates the last closed flux surface. The rays are started from R=3.014 m, z=-0.0688 m, the location of the actual antenna. Examples at 7° and 15° initial launch angles from horizontal, the range available from hardware at that port location, are shown. For each initial angle a launched frequency of 60 GHz was used in the calculations. The peak $k_\perp$ sensitivity and scattering location are assumed to occur at the minimum perpendicular index of refraction along the ray. For the 7° case this results in $\rho = 0.68$ and $k_\perp = 2.8$ cm^{-1}. Similarly for 15°, $\rho = 0.72$ and $k_\perp = 7.1$ cm^{-1}. X-mode propagation is assumed for both cases. (b) Density profile used for simulation. (c) Relative perpendicular index of fraction along the 60 GHz, 7° ray, normalized to the vacuum wave number, k_0.

therein.

Figure 3.18 shows a representative example of ray tracing results. Similar simulations have been conducted using profiles from previous experiments to explore experimentally accessible regimes. Typical correlation lengths for turbulence in DIII-D can range from $\sim 0.5-2$ cm in H-mode plasmas to $\sim 0.5-4$ cm in L-mode and Ohmic plasmas [64]. The narrow spacing between DBS-5 channels ($\sim 0.5-3$ cm, depending on the density gradient) allows detailed study of zonal flows, geodesic acoustic modes, radial electric field shear, turbulence correlation lengths, and the application of higher order statistical techniques. The radial spatial coverage provided by the multiple channels is suitable for studying the evolution and interaction of turbulence with larger structures such as tearing modes and sawteeth. By launching at angles far from normal, it is also possible to make local measurements of intermediate and small scale turbulence (up to $k_\perp \sim$ 15 cm^{-1}), probing the dynamics of trapped electron modes ($k_\perp \rho_i \lesssim 1$, where ρ_i is the ion gyroradius) and even into the electron temperature gradient mode range ($1 \lesssim k_\perp \rho_i \lesssim 10$) [187]. The finely spaced array can measure a local portion of the radial electric field profile with very high radial resolution. This allows experimental determination of the local electric field shear, a critical parameter when comparing experimental turbulence measurements to predictions from nonlinear gyrokinetic turbulence codes. By arranging for the launched beam to be normal to the cutoff surfaces, the diagnostic may also be used as a conventional reflectometer to probe low-k density fluctuations.

An additional cross-check on the data analysis procedure that can be done is to compare DBS measurements launched at different angles in the same plasma. Figure 3.19 shows the alignment and launch angles for the two DBS systems used to acquire data in shot 136721. Figure 3.19(a) shows ray tracing results for both DBS systems–the system at 60° was launched at 7.0° above horizontal and the system at 240° was launched at −5.1°–which were matched radially. Figure 3.19(b) shows a top view of DIII-D, with the two port locations annotated. Both the tokamak and neutral beams are depicted. In Fig. 3.20 shows a time series of data from both DBS systems for the same shot. Figure 3.20(a-b) show

the scattering position and wave number, respectively, as determined by using a time series of EFIT equilibria and density profiles. Figure 3.20(c) combines the information in Fig. 3.20(b) with the measured Doppler shift to determine the propagation velocity of the turbulence. As one would expect for radially aligned measurements, all 7 channels show a high degree of agreement. The variations of the measured flow velocity are due to a combination of neutral beam timing changes and sawteeth. Note that Fig. 3.20(a-b) and Fig. 3.20(c) are plotted for different times. The scattering wave number information is approximated by a spline fit, then interpolated at DBS measurement times–the extra time in the ray tracing results is to minimize boundary effects on the interpolation.

3.4.2 2D full wave simulations

The fast calculations enabled by ray tracing make its utility very high; however, to address certain questions more complete models must be used. A 2D full-wave, finite difference, time domain code has been used to investigate DBS physics and for simulations to approximate DBS for a synthetic diagnostic for gyrokinetic simulations. The code solves Maxwell's equations on a 2D grid, where the system is closed with a current equation derived from the equation of motion for electrons (*i.e.* cold plasma limit). The grid is discretized using the Yee lattice method. Microwave propagation is separated into X-mode and O-mode polarizations for efficiency, Perfectly Matching Layer (PML) boundary conditions are used, and the code runs on a graphical processing unit (GPU). An early version of the code is described in Ref. [188], with the most recent version detailed in Ref. [189]. Input grids are generated using equilibrium magnetic geometry from the EFIT code and from measured density profiles. The simulation antenna launches from the same location as in the experiment and is configured to produce a beam that focuses in the plasma and matches beam characteristics measured in the laboratory using a duplicate of the quasi-optical antenna system.

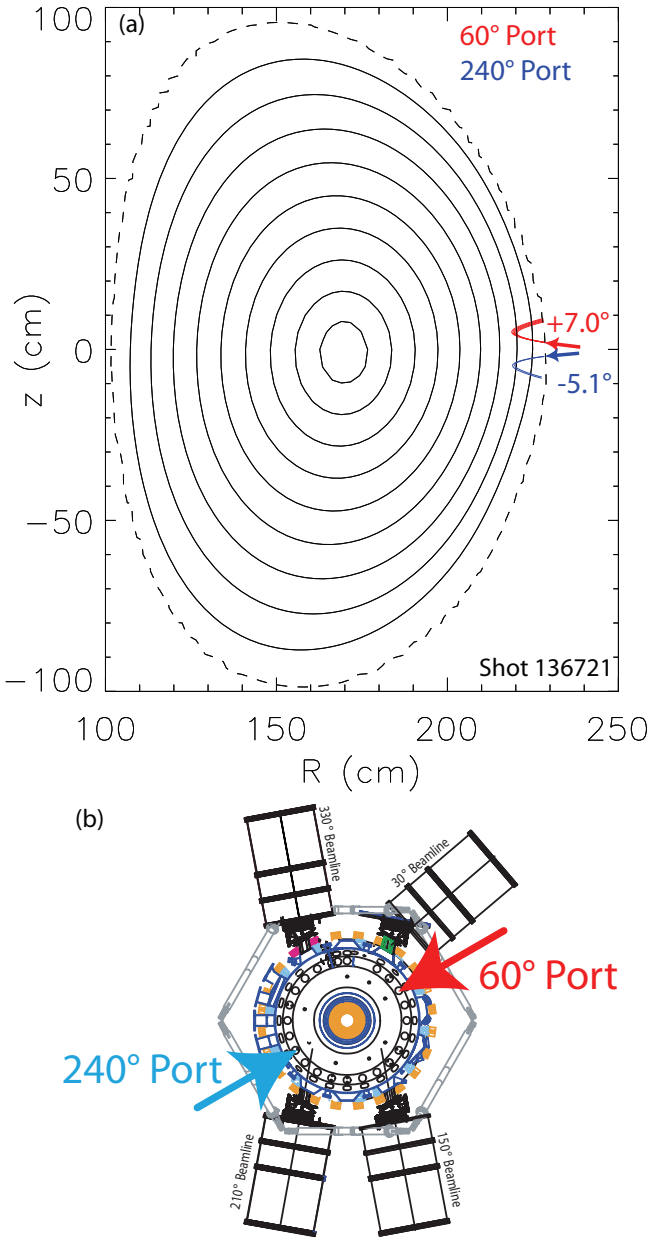

Figure 3.19: (a) Ray tracing results overlaid on EFIT equilibrium flux surfaces from two DBS systems. (b) Top view of DIII-D showing DBS port locations.

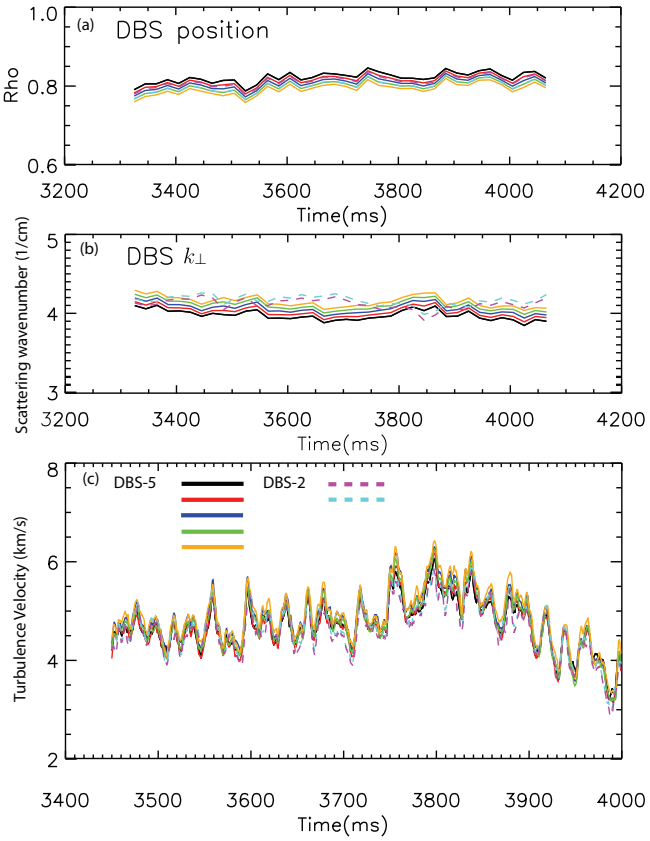

Figure 3.20: (a) Scattering position and (b) scattering wave number, determined by ray tracing using experimental profiles. (c) Propagation velocity of turbulence from measured Doppler shift and calculated wave numbers.

The equations solved by the code are

$$\nabla \times \mathbf{E} = -\frac{\partial \mathbf{B}}{\partial t} \tag{3.28}$$

$$\nabla \times \mathbf{B} = \mu_0 \mathbf{J} + \frac{1}{c^2}\frac{\partial \mathbf{E}}{\partial t} \tag{3.29}$$

$$\mu_0 \frac{\partial \mathbf{J}}{\partial t} = \frac{\omega_{pe}^2}{c^2}\mathbf{E} - \mu_0 \omega_{ce} \mathbf{J} \times \hat{\mathbf{B}}, \tag{3.30}$$

with a numerical damping term that can also be added. $\hat{\mathbf{B}}$ is the normalized magnetic field.

In the following section, results from the full wave code are incorporated in a synthetic diagnostic for Doppler backscattering, which has been used for direct comparisons between experimental DBS measurements and predictions from nonlinear gyrokinetic simulations.

3.4.3 Synthetic DBS for gyrokinetic simulations

Work in this section expands on Ref. [11]. Further gyrokinetic simulations of the experiment described in Ref. [9] were performed. To compare the DBS measurements of wave number-resolved density fluctuations directly to gyrokinetic simulation results required development of a synthetic diagnostic for DBS. Modeling of the experiment for the synthetic diagnostic is described in this section. The numerical implementation for GYRO is detailed in the Appendix of Ref. [10].

The approach described here was used to compare DBS measurements from a previous experiment [9] to a new set of gyrokinetic simulations, with physics results reported separately [10].

3.4.3.1 Introduction

Understanding the turbulent transport of particles, momentum, and energy is an important issue for magnetically confined plasmas. In the past decade, diagnostics and simulations have advanced to where, through synthetic diagnostics applied to simulation outputs, it is possible to make direct comparisons between experiment and theory at a fundamental level. Direct comparisons of fluctuation amplitudes, spectral shapes, the crossphase between

fluctuating fields, and more have been made between experimental measurements and nonlinear gyrokinetic simulations [16, 151–153, 155, 156, 190, 191]. This section describes work for the development of a synthetic Doppler Backscattering diagnostic for the quantitative comparison of wave number-resolved density fluctuation measurements to simulation predictions. These efforts are necessary to approach a validated, predictive capability for turbulent transport. The approach described here was used to compare DBS measurements from a previous experiment [9] to a new set of gyrokinetic simulations, with physics results reported separately [10].

Past synthetic DBS diagnostics have used different approaches: an estimate of the wave number sensitivity of DBS [151] and an analytical formalism for simple geometries [192] have been employed. Full wave finite difference, time domain (FDTD) methods are a powerful tool for the investigation and modeling of microwave and millimeter-wave plasma diagnostics−past work used similar simulations to investigate possible effects on DBS measurements [161, 163, 168, 193–196]. Full wave simulations have also been coupled to turbulence simulations to investigate conventional reflectometry [197].

3.4.3.2 Synthetic Diagnostic Description

The numerical implementation of the synthetic DBS diagnostic (detailed for GYRO in Ref. [10]) requires several inputs from modeling of the experiment: the scattering location (in the 2D poloidal plane); a central wave number, k_θ, and wave number sensitivity, Δk, for a Gaussian weighting function; and, optionally, a radial Gaussian weighting for global simulations (otherwise $k_r = 0$ is used).

As described in Ref. [6], the ray tracing code Genray [177] is used to determine the scattering location and k_θ.

For a Gaussian beam, with amplitude profile $E(r) \propto \exp(-r^2/w_0^2)$, where w_0 is the $1/e$ beam radius, one expects the wave number-weighting of the scattered signal to go as $\Psi(k) \propto \exp(-(k_\theta - k)^2/(\Delta k)^2)$. An approximation for Δk including the curvature of the

beam and of the cutoff layer, which broaden Δk [159, 198] is

$$\Delta k = \frac{2\sqrt{2}}{w_0}\left[1+\left(\frac{w_0^2 k_\theta}{R}\right)^2\right]^{1/2}, \tag{3.31}$$

where the effective radius of curvature is given by $R = R_{beam}R_{cutoff}/(R_{beam}+R_{cutoff})$. In a focusing beam's Rayleigh range, $R_{beam} \to \infty$, so $R \to R_{cutoff}$. This formulation has been used for antenna optimization for DBS systems [162, 180]; numerical simulations with a 2D full wave code have been found to qualitatively support Eqn. 3.31 [194]. A limitation of Eqn. 3.31 is that it neglects refraction of the beam, which can modify the effective spot size. This level of approximation may not be sufficient for incorporation in a synthetic diagnostic for quantitative turbulence validation studies.

A straightforward modification is to use the wave number and beam width in the plasma as the parameters in Eqn. 3.31, rather than vacuum estimates. That is accomplished here through use of ray tracing and 2D full wave simulations. The local cutoff curvature is determined from experimental equilibrium information. It was pointed out in Ref. [159] that for ideal circumstances, *e.g.* a slab model, refractive effects can be neglected and vacuum antenna properties can be used.

3.4.3.3 Full wave simulations

The full wave code used solves Maxwell's equations on a 2D grid, where the system is closed with a current evolution equation equivalent to the equation of motion for electrons (*i.e.* cold plasma limit), with a numerical damping term added. Propagation is separated into X-mode and O-mode polarizations, perfectly matching layer boundary conditions are used, and the code runs on a graphics processing unit (GPU). An early version of the code is described in Ref. [188], with the most recent version detailed in Ref. [189]. Input grids are generated using experimental magnetic geometry and measured density profiles. The simulation antenna is configured to produce a beam that focuses in the plasma and matches beam characteristics measured in the laboratory using a duplicate of the quasi-optical antenna system [8].

Figure 3.21 shows an example of a full wave calculation using experimental parameters

for an L-mode DIII-D [157] plasma with toroidal magnetic field B_T =2 T, plasma current I_p =0.8 MA (directed opposite to B_T), line-averaged density $\langle n_e \rangle \approx 2 \times 10^{19}$ m^{-3}, major radius R ≈1.7 m, and minor radius $a \approx 0.6$ m; detailed profile information is given in Ref. [9]. Input grids were typically about 2000 by 3000 grid points covering the subset of the 2D plane needed to capture the beam's propagation (grid spacing $\sim 1/10 - 1/20$ of vacuum wavelength), with 36 time steps per wave period to satisfy the Courant condition, a total of $\sim$ 20k − 30k time steps were used for each run. Simulations were run on nodes of the Hoffman2 cluster at UCLA equipped with Nvidia Tesla GPU cards and required ~ 5 minutes each.

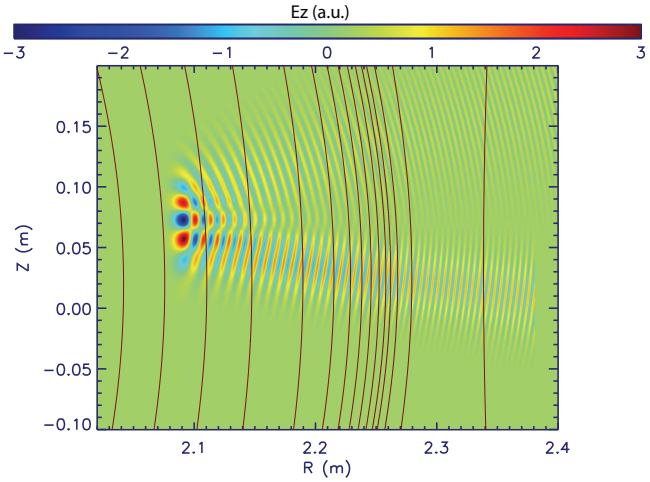

Figure 3.21: 2D full-wave contours of E_z for X-mode at 63.68 GHz, launched at 7°. Overplotted are contours of the X-mode right-hand cutoff.

The simulation is run for one additional wave period after completion, over which the beam's electric field is averaged. Both electric field components are used to calculate the RMS average, $E_{rms} = \sqrt{\langle E_Z^2 + E_R^2 \rangle}$ (for X-mode). Figure 3.22 compares the RMS beam electric field profile in vacuum and with plasma, taken along a vertical cut at the major radius of the maximum amplitude of the beam. The beam is launched at an amplitude of 1 a.u. There is a large increase in the electric field amplitude near the cutoff, which helps to localize the scattering region; additionally, refraction broadens the beam profile and shifts the beam vertically. In this example the local beam radius, w_{loc}, at the major radius of

maximum beam amplitude increases by about 40% from vacuum to plasma, from 2.42 cm to 3.42 cm.

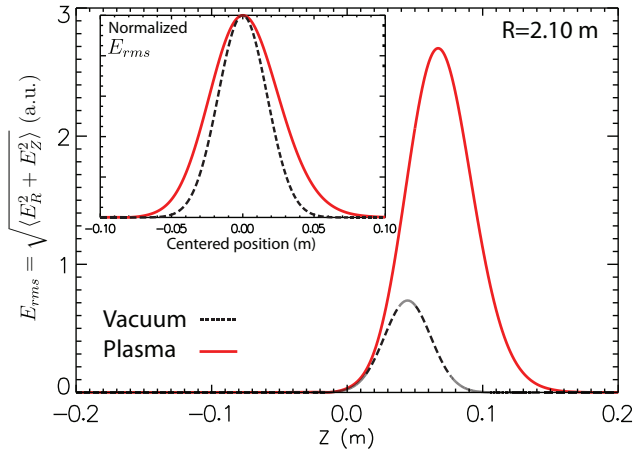

Figure 3.22: Vertical cuts of RMS beam profiles, in vacuum and with plasma. Inset, the same data is plotted, normalized and shifted to be centered at Z=0.0 m.

3.4.3.4 Application of synthetic diagnostic

An example of the application of the synthetic diagnostic, incorporating full wave modeling described in the previous section, is shown in Fig. 3.23. The full density fluctuation spectrum from GYRO is plotted along with the spectrum after convolution with the instrument function. The case corresponds to the 6 gyrotron, inner heating (high a/L_{T_e}) case in Refs. [9, 10], with experimental parameters for the synthetic diagnostic at $\rho = 0.6$.

For the parameters of that experiment, the effect of refraction determined by modeling was to increase the DBS beam waist by $\sim 20 - 50\%$ over the measurement radii (DBS frequencies were changed shot-to-shot), which narrowed Δk by $\sim 20 - 40\%$.

Figure 3.24 compares the frequency spectrum for the same data shown in Fig. 3.23, between the synthetic diagnostic output with Δk included and $k_\theta = 4$ cm^{-1} only. The primary effect is to change the magnitude of the spectrum, while the shape is altered little. The vacuum estimate for Δk would generate a result above the two plotted. The experiment in question had no external momentum input; for a strongly rotating case where the spectrum

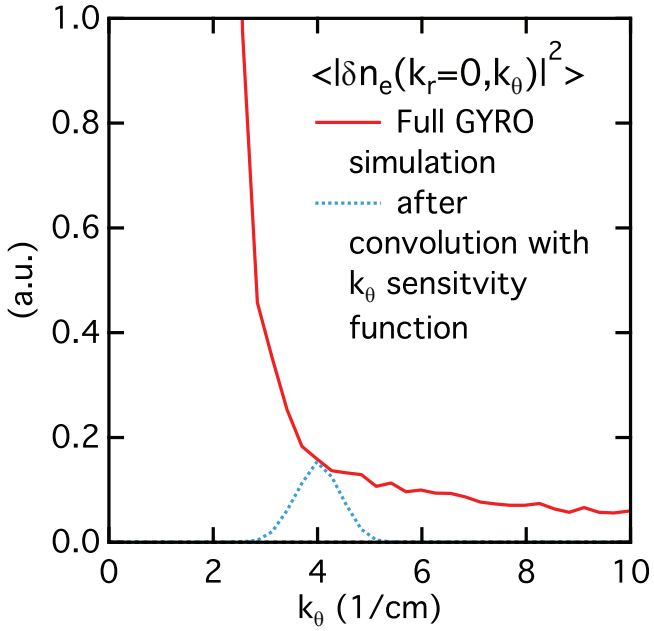

Figure 3.23: Full density fluctuation wave number spectrum from GYRO (solid red) and spectrum after convolution with k_θ sensitivity function (dashed blue).

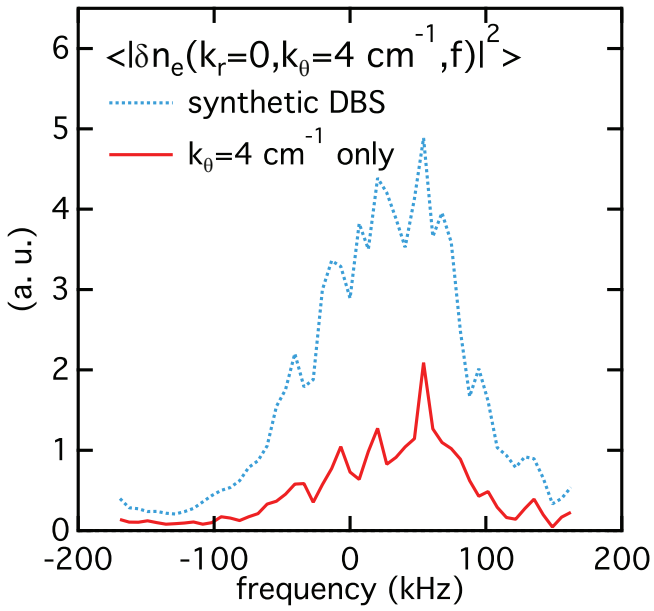

Figure 3.24: Synthetic diagnostic output (dashed blue) compared to fluctuations at $k_\theta = 4$ cm^{-1} only (solid red). Positive frequencies indicate propagation in the electron diamagnetic direction.

of the turbulence possessed a steep slope, *e.g.* at $k_\theta \sim 3$ cm^{-1} in Fig. 3.23, it may be that the synthetic spectrum would shift in frequency.

The approach described here enables further direct comparisons between DBS measurements and turbulence simulations, and the tools can be extended in future work to directly couple turbulence simulation output to full wave simulations.

3.5 Non-ideal effects in Doppler backscattering

The description of DBS in Sec. 3.3 leaves out a number of effects that can impact experimental measurements. Several of these non-ideal effects are investigated in this section.

3.5.1 Mirrored DBS signal due to mixer asymmetries

A low amplitude "image signal" can occur at the reflection across zero frequency of a Doppler shifted DBS signal due to mixer or amplifier asymmetries. Assume there are small phase and amplitude imbalances in a quadrature mixer, $\delta\varphi$ and δA, such that the "in-phase" and "quadrature" mixer outputs are $I(t) = A(t)\cos(\varphi(t) + \delta\varphi)$ and $Q(t) = (A(t) + \delta A)\sin\varphi(t)$, with the complex signal formed as $E(t) = I(t) + iQ(t)$. For $\delta\varphi = 0$ one finds

$$E(t) = A(t)e^{i\varphi(t)} + \delta A \sin\varphi(t). \tag{3.32}$$

Similarly, for $\delta A = 0$ and one finds

$$E(t) = A(t)\left(e^{i\varphi(t)} + \cos\varphi(t)\left(\cos\delta\varphi - 1\right) - \sin\varphi(t)\sin\delta\varphi\right) \tag{3.33}$$

Equations 3.32 and 3.33 clearly show that, in addition to the ideal Doppler shifted peak, $A(t)e^{i\varphi(t)}$, if asymmetries are present and are not treated numerically in post-processing, one can expect to see an image signal in spectral analysis of $E(t)$. Figure 3.25 compares spectrograms of DBS data with and without raw signal normalization to remove the artificial image signal created by asymmetries in the quadrature mixer or amplifier outputs. The large amplitude component at zero frequency in the figure is due to direct reflections

from mirrors and lenses. Note that cases exist where such a comparison results in no effect; non-localized scattering along the beam path, a second localized scattering region from propagation through a radial region with a sharp density gradient, tunneling through the right-hand X-mode cutoff with a second localized scattering region created at the left-hand cutoff, detection of the reflected signal, secondary antenna lobes, diffraction-like secondary scattering orders, or other effects may be important in such circumstances. Although phase imbalances can create a similar effect, the inherent phase offset for the quadrature mixers used is small and is not found to have a significant effect. Applying this data conditioning is a necessity when analyzing the DBS phase, particularly for data from the DBS-5 hardware, which, in a trade-off for flexibility in operation and due to the frequency modulation technique employed, is prone to amplitude asymmetries.

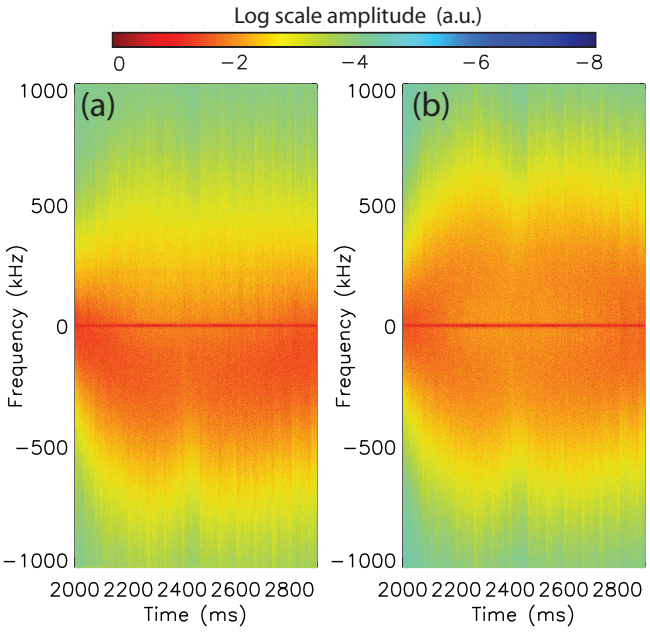

Figure 3.25: Spectrograms of DBS complex quadrature signal on a logarithmic scale. The only difference is that in (a), the raw data channels, $I(t) = A(t)\cos\varphi(t)$ and $Q(t) = A(t)\sin\varphi(t)$ are normalized. In (b), the amplitude of the raw data is not balanced and the signals are not normalized.

3.5.2 Microwave tunneling in steep gradients

The solution for 1-D O-mode reflectometry for a linear density gradient is an Airy function, where the incoming and reflected waves generate a standing wave pattern for frequencies above cutoff and an evanescent solution behind the cutoff. For X-mode propagation, there are two cutoffs and the upper-hybrid resonance–this raises the possibility that if the density gradient is large enough, that the evanescent portion of the solution could extend past the resonance into a second propagation region.

The tunneling effect is investigated here with the 2D full-wave code described in Sec. 3.4.2. X-mode propagation is used with a constant magnetic field, with 1-D density profiles, $n_e = n_e(R)$. Figure 3.26(a) shows a case with a steep gradient at $R = 2.0$ m due to a hyperbolic tangent density profile. The launched frequency is about 60 GHz and the density at the top of the `tanh` function is 1×10^{14} cm^{-3}, which is an experimentally relevant condition, similar to the H-mode pedestal. The constant magnetic field is 1.8 T. The contour scale is truncated to show the low amplitude tunneled wave; the launched amplitude, on the same scale, is 1.0. In Fig. 3.26(a), a few oscillations of the tunneled wave can be seen in the center of the plot, near R=2.0 m, Z=0.10-0.15 m.

To explicitly show the second propagation region, a pair of two hyperbolic tangent functions is used in 3.26(b), where, for the launched frequency, the right-hand cutoff and upper-hybrid resonance are located in the steep density region near R=2.1 m and the left-hand cutoff is in the second gradient region, near R=1.9 m. In between, a propagating wave can clearly be observed, which reflects off the left-hand cutoff, but is then mostly absorbed once the resonance is approached a second time.

In an experiment, a tunneling effect could result in two independent Doppler shifted peaks in a single spectrum–for instance, the small peak at slightly less than -100 kHz in Fig. 3.4, where the main Doppler peak is at about +400 kHz. Such an effect on measurements in an H-mode pedestal could generate two significantly different peaks due to the large velocity shear in that region. The results in this section can be taken as a proof-of-principle that

this effect could occur in an experiment; although, a *caveat* must be noted that the code simulates a cold plasma and that resonant absorption would be different in a real plasma.

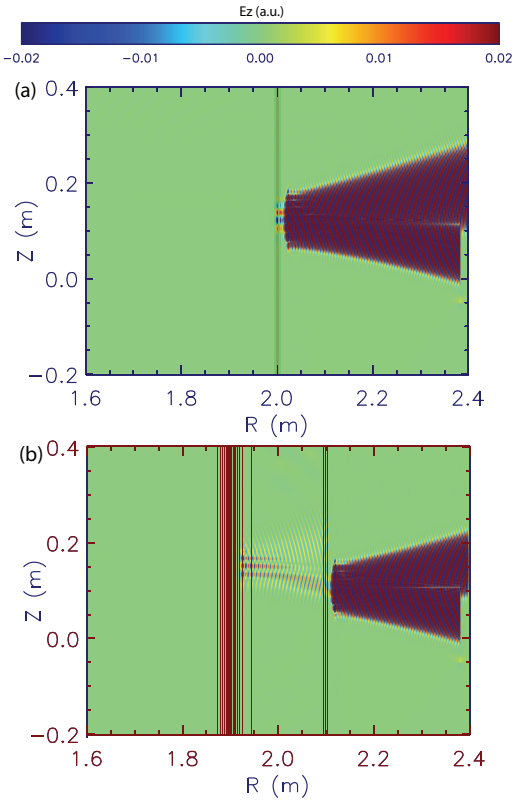

Figure 3.26: Contours of the Z-component of the beam electric fields for X-mode propagation. The vertical lines indicate contours of density. (a) Case with hyperbolic tangent density profiles. (b) Case with "staircase" of two hyperbolic tangent functions.

3.5.3 Assessment of additional plausible non-ideal effects

A number of other effects can impact DBS measurements. This section provides an overview of additional non-ideal effects that are plausible, with assessments of their importance for measurements at DIII-D.

3.5.3.1 Scattering along the beam path

The backscattering near the cutoff is of primary interest in the DBS technique, and due to the change in wave number along the beam path and the increase in electric field amplitude near the cutoff, it is highly localized. Small angle scattering along the beam path would still be expected to occur, even if its effect is negligible. Such effects have been investigated analytically and with full wave simulations. Small angle forward scattering from coherent modes was investigated in Ref. [199] for conventional reflectometry. The effect of multiple scattering events for DBS was investigated in Ref. [200], where it was found that for a combination of sufficiently large fluctuation amplitude and long path length the received scattered power is not linear with the fluctuation power at the cutoff. The criteria found for the nonlinear regime was

$$\gamma_{nl} = \tilde{n}^2 k_0^2 x_c L_c \ln \frac{x_c}{L_c} \gtrsim 1, \tag{3.34}$$

where $\tilde{n}$ is the density fluctuation level relative to the density at the cutoff, k_0 is the launch wave number, x_c is the path length through the plasma to the cutoff, and L_c is the correlation length of the turbulence. For comparison to typical DIII-D parameters, take $\tilde{n} = 0.01$, $k_0 = 12$ cm^{-1} (about 60 GHz), $x_c = 20$ cm (corresponding to $r/a \approx 0.7$ in DIII-D), and $L_c = 1$ cm (typical core L-mode value [64]). Equation 3.34 then results in $\gamma_{nl} \approx 0.85$. This puts core L-mode measurements near the limit of the linear regime. Due to lower fluctuation levels, H-mode plasmas are farther from the nonlinear regime. Measurements in large future experiments may be limited to the edge due to this effect; however, it should be noted that there has been no experiment validating the criteria.

3.5.3.2 Interferometer effect

In addition to direct scattering from equilibrium-scale instabilities (*e.g.* tearing modes), described in Ref. [199], Eqn. 3.13 suggests that an interferometer-type effect could impact DBS measurements, where oscillations of the path length result in measured phase oscillations. One can evaluate how large a path length difference would be required to be comparable to

the Doppler shift. For an example, take a GAM with typical $v_m \approx 1$ km/s and $f_m \approx 20$ kHz. To set a bound, assume the change in path length is localized near the cutoff, so that the magnitude of path length change can be approximated as $k_\perp \Delta x$, where Δx is the displacement of the cutoff. The wave number dependence cancels out and one finds $\Delta x \gtrsim 0.5$ cm for the Doppler shift and optical path length phases to be comparable. The node of the GAM m=1 density component occurs near the measurement location, so this effect would be expected to be negligible. The simplification of taking the wave number nearest the cutoff likely results in an overly pessimistic bound. The change in wave number along the path is localized to near the cutoff, so that approximation could realistically result in an order 1 underestimate of how large Δx would need to be. Equilibrium-scale instabilities, such as tearing modes, could cause a Δx of several centimeters, so DBS measurements in their presence may require detailed analysis to interpret. The velocity component of MHD or Alfvènic modes might also be smaller, reducing the bound on Δx. For the MHD-quiescent L-mode plasmas investigated in this dissertation, the interferometer effect can be neglected.

3.5.3.3 Pitch angle misalignment

In the limit where the frequency is much larger than the plasma frequency and cyclotron frequency, $\omega >> \omega_{pe}, \omega_{ce}$, the Born approximation can be used to calculate the scattered electric field for a beam incident on a volume of plasma with density fluctuations [201]. This has been investigated in detail [202, 203] for the measurement of density fluctuations in plasmas. This limit is not well satisfied for Doppler backscattering, where refraction of the probe beam is fundamental to the technique; however, similar processes would be expected to occur. There are also distortions of the beam that occur near the cutoff, in addition to simply being reflected [204, 205].

One relevant process is a dependence on the alignment of the probe wave-vector and the scattering wave-vector. The turbulence in tokamaks is essentially parallel to the magnetic field, $k_\parallel << k_\perp$, so for backscattering the probe beam should be arranged to minimize the parallel component of the scattered wave (or, equivalently, to match $k_\perp$). The pitch

angle of the magnetic field is given by, $\xi = \tan^{-1}(B_P/B_T)$; magnetic field lines in three dimensions take the form of helixes embedded in the flux surfaces. The variation of ξ has been used to spatially localize scattering measurements [206, 207]. The effect of pitch angle misalignment has been investigated for high-k scattering [208]. It was found that backscattering at $k_r \sim 35$ cm^{-1} is highly sensitive to misalignment, while at ~ 1 cm^{-1} there is little sensitivity. This was used to identify the measured signal with high-k fluctuations by varying the mismatch angle.

Although there are clearly significant effects not included in the formalism, it is informative to assess the impact of misalignment. From Ref. [203], the scattered power for each volume element along the path has the dependence

$$dI \propto dz n^2(\mathrm{k}^n, z) \exp\left(-\frac{\left(k_x^n - k_x^s\right)^2 a_x^2}{2}\right) \exp\left(-\frac{\left(k_y^n - k_y^s\right)^2 a_y^2}{2}\right), \tag{3.35}$$

where k^n is the wave-vector of the turbulence, z is the direction along the beam, x and y are the directions across the beam, k_j^n are the components of the turbulence wave-vector, k_j^s are the components of the scattered wave vector, n is the density fluctuation spectrum, and a_j are the beam radii. Assuming the turbulence is aligned with magnetic field lines, the arguments of the exponents are non-zero if, for backscattering, the angle between the beam and magnetic field differs from 90°. Assume the scattering is localized and take the x direction to be along the magnetic field line at that location. For DBS near cutoff the correspondences for z would be θ and for y would be the flux surface normal. Since for the turbulence, $k_\parallel << k_\perp$, take k_x^n to be negligibly small. For simplicity, take the mismatch to only occur due to the misalignment with the magnetic field (finite k_x^s) and ignore finite k_y^s. Also, take $a_x = a_y = a_0$. Define θ_m as the mismatch angle, where for $\theta_m = 0$ the arguments of the exponentials are zero; then, $k_x^s = k_s \cos(90° - \theta_m) = k_s \sin\theta_m$. To relate terms to the turbulence wave number, we then have from the Bragg relation for 180° backscattering $k_x^s = (k_{\tilde{n}}/2)\sin\theta_m$. Equation 3.35 then becomes

$$dI \propto dz n^2(\mathrm{k}^n, z) e^{-\frac{k_{\tilde{n}}^2 \sin^2\theta_m a_0^2}{4}}. \tag{3.36}$$

For significant scattered power (defined as $1/e$), we then have the criteria (for small θ_m):

$$|\theta_m| \lesssim \frac{2}{k_{\tilde{n}} a_0}. \tag{3.37}$$

For the conditions in Ref. [208], $k_{\tilde{n}} \approx 35$ cm^{-1} and $a_0 \approx 1.6$ cm; Eqn. 3.37 then gives $\theta_m \lesssim 2°$. This is in rough agreement with Fig. 9(a) of Ref. [208], where the measured and calculated $1/e$ point for the scattered power as a function of mismatch angle was found to be $\sim 1.5°$.

The ports at DIII-D are arranged to launch the beams in a vertical plane. Some experiments launch the beam at a slight toroidal angle to minimize the mismatch. For typical DIII-D DBS values of $k_{\tilde{n}} \approx 4.5$ cm^{-1} and $a_0 \approx 2.5$ cm; Eqn. 3.37 yields $\theta_m \lesssim 10°$.

For a standard tokamak, where the pitch angle is $\sim 10°$ or less (and that only near the edge), this should not be a large factor; however, for a spherical tokamak, the pitch angle can be $\sim 45°$. DBS measurements in a spherical tokamak may require an adjustable antenna system with an additional degree of freedom, to align the probe beam for measurements. Signal levels for large launch angles in DIII-D might be reduced by this effect.

3.5.3.4 Estimate of power-weighted average wave number

As noted in other sections, DBS measures density fluctuations over a finite wave number range. The power in the fluctuations themselves would also be expected to depend on wave number. The possibility then arises that there would be a shift of the effective, power-weighted average wave number due to this effect. This would result in a systematic error in the inferred propagation velocity of the turbulence when using the DBS wave number determined from ray tracing. This effect can be estimated.

Take the instrument function for DBS to be of the form

$$\Psi_{DBS}(k) = A_{DBS} e^{-\frac{(k-k_0)^2}{(\Delta k)^2}}. \tag{3.38}$$

Take the measurements to be performed over a range in wave numbers where the density fluctuations can be described by a power law:

$$\delta n(k)^2 = A_n (k_\theta \rho_i)^{-\alpha_p} \tag{3.39}$$

or by an exponential spectrum

$$\delta n(k)^2 = A_n exp(-2\alpha_e k_\theta \rho_i). \tag{3.40}$$

The measured spectrum will then be

$$\delta n_{meas}(k) = \delta n(k) \Psi_{DBS}. \tag{3.41}$$

The scattered power in the linear regime would be expected to be proportional to the fluctuation level squared. The power-weighted effective scattering wave number can then be written as

$$k_{eff} = \frac{\int k \delta n_{meas}(k)^2 dk}{\int \delta n_{meas}(k)^2 dk}. \tag{3.42}$$

This simplifies to (for a power law)

$$k_{eff} = \frac{\int k^{1-\alpha} e^{-2\frac{(k-k_0)^2}{(\Delta k)^2}} dk}{\int e^{-2\frac{(k-k_0)^2}{(\Delta k)^2}} dk}, \tag{3.43}$$

where to avoid the singularity, the integral is to be truncated at finite k (for experimentally relevant k_0 and Δk, the lower bound does not strongly affect the results). Clearly, for $\alpha_p = 0$ or $\alpha_e = 0$, $k_{eff} = k_0$. The question then becomes for what values of Δk and α_p or α_e would one expect k_{eff} to differ significantly from k_0.

Consider the experimentally relevant parameters $k_0 = 4$ cm^{-1} and $\Delta k/k = 0.3$. Experiments have found best fits to density fluctuation spectra in L-mode plasmas: for power laws $\alpha_p \approx 3 - 6$, with a transition at high-k [109] and for exponentials fits $\alpha_e \approx 1.45 - 1.7$ [5]. Numerical evaluation of Eqn. 3.43 over a range of experimentally relevant parameters ($\rho_s = 0.1 - 0.3$ cm, other parameter ranges as above) results in $k_{eff}/k_0 < 5\%$ for most cases, with $k_{eff}/k_0 \lesssim 10\%$ for worst cases. This systematic uncertainty is smaller, or at worst on the same order, as uncertainties from the density profile and magnetic equilibrium reconstruction.

3.5.3.5 Antenna issues

Real antennas have finite side lobes. Figure 3.13 shows the measured side lobs for one of the DIII-D antenna configurations. With a corrugated horn antenna the power in the side lobes is more than an order of magnitude less than the primary beam. Other types of horn antennas have larger side-lobes. Their use could result in the apparent detection of several Doppler shifted peaks in a DBS spectrum. If well separated in frequency, these could be used for diagnostic purpose–essentially measuring multiple locations (and wave numbers) simultaneously.

The launched beam for DBS is normally not detected. It simply reflects and continues to propagate elsewhere in the machine. For DBS measurements at small angles, or when a diverging beam is used, part of the reflected beam could be detected in addition to a significant backscattered contribution. Conventional reflectometry is concerned with detection and interpretation of the reflected beam. Detection of both may result in multiple peaks in the measured spectrum. Unlike side lobes, the reflected beam would not be expected to be Doppler shifted, and would be expected to show up near zero, as in conventional reflectometry. This complicates analysis and should be avoided.

3.6 Correlation electron cyclotron emission radiometry

In addition to the DBS system developed in the course of this work towards this dissertation, data from a previously developed correlation electron cyclotron emission radiometry system is used in subsequent chapters for measurements of relative electron temperature fluctuations and their crossphase with density fluctuations. The CECE system is described in detail in Ref. [3, 175]. The principles of ECE radiometry measurements and analysis as applicable to results presented in later chapters are briefly presented here for completeness. More detailed discussions can be found in Refs. [209–211]. A review of CECE methods can be found in Ref. [212]. A more complete description of the relevant radiation processes can be found in Ref. [201].

Predictions have been made that long wavelength temperature fluctuations should actually be invisible to the CECE technique [213]; however, those predictions have been clearly contradicted by experiment [110, 210, 214]. It is not clear whether this failure is due to the model ECE formulation or assumptions about the turbulence. If the latter, the formalism of Ref. [213] might yet provide insights.

3.6.1 Principles of ECE radiometry

A hot plasma emits and absorbs radiation at harmonics of the electron cyclotron frequency:

$$n\omega_{ce} = n\frac{eB}{m_e}. \tag{3.44}$$

In a tokamak, the magnitude of the magnetic field can be approximated as $B(r) = B_0R_0/R$, so that detection of a particular cyclotron frequency band localizes the measurement radially:

$$n\omega_{ce}(R) = n\frac{eB_0R_0}{m_eR}. \tag{3.45}$$

When the optical depth (an integral calculation of the emissivity and absorption that characterizes how many times emitted radiation is re-absorbed and re-emitted) is sufficiently high ($\tau \geq 4-5$), a slab of plasma will absorb all incident radiation and therefore radiates like a blackbody. In the classical limit (appropriate since $\hbar\omega/T << 1$), the emitted blackbody intensity is proportional to the electron temperature:

$$I_{BB}(\omega_{ce}) = \frac{\omega_{ce}^2 T_e}{4\pi^2 c^2} \tag{3.46}$$

Therefore use of a radiometer that produces a voltage proportional to the detected radiation intensity gives a measure of the temperature. The bandwidth of the recorded signal produced by the detector is referred to as the video bandwidth, B_{vid}. The bandwidth of the filter used to bandpass filter the signal is referred to as the IF bandwidth, B_{if}. Thermal noise fluctuations set a bound on the lowest fluctuation level that can be measured with a signal radiometer channel, which is given as [201]

$$\frac{\delta T}{T} = \sqrt{B_{vid}/B_{if}}. \tag{3.47}$$

The DIII-D correlation electron cyclotron emission (CECE) radiometer [3] uses IF filters with $B_{if} \approx 110$ MHz and amplifiers set $B_{vid} \approx 1$ MHz. The system detects 2^{nd} harmonic X-mode ECE radiation. The sensitivity limit given by Eqn. 3.47 is then $\sim 10\%$, which is about an order of magnitude larger than the RMS level of turbulent fluctuations measured in other fields in the core of tokamaks.

The approach taken with the CECE technique is to use two IF filters, which are closely-spaced, but do not overlap. Correlation techniques, documented in the next section, then allow the long wavelength temperature fluctuations to be separated from the thermal noise, which does not correlate when the filters do not overlap. An assumption in the following is that all the long wavelength temperature fluctuations correlate between the two locations.

3.6.2 CECE data analysis

Ignoring system noise temperature effects (which can be shown to be small [175]), a signal from a CECE channel can be represented as

$$S_i = c_i \left(\delta T_e + T_{e,0} \sqrt{\frac{B_{vid}}{B_{if}}} \right). \tag{3.48}$$

The symbol c_i is a calibration factor with unit of [Volts/eV]. For a single channel, the thermal fluctuations will dominate the temperature fluctuation component of the signal, so auto-correlation results in

$$\langle S_i S_i \rangle = c_i^2 T_{e,0}^2 \frac{B_{vid}}{B_{if}}. \tag{3.49}$$

Assuming the CECE filters are sufficiently close that all long wavelength temperature fluctuations correlate, but are not overlapped, so that no thermal fluctuations correlate:

$$\langle S_i S_j \rangle = c_i c_j \delta T_e^2, \ i \neq j. \tag{3.50}$$

For the normalized correlation coefficient function (definitions in Appendix A) at zero lag, we then have:

$$C_{ij}(\tau = 0) = \frac{\langle S_i S_j \rangle}{\sqrt{\langle S_i S_i \rangle} \sqrt{\langle S_j S_j \rangle}} = \frac{{\delta T_e}^2}{T_{e,0}^2 \frac{B_{vid}}{B_{if}}}. \tag{3.51}$$

The relative temperature fluctuation level is therefore

$$\frac{\delta T_e}{T_{e,0}} = \sqrt{C_{ij}(\tau = 0)}\sqrt{\frac{B_{vid}}{B_{if}}}. \tag{3.52}$$

A bias error, resulting in a systematic underestimate of $\delta T_e/T_{e,0}$, is introduced in Eqn. 3.49, since there is in principle a contribution to the autocorrelation from the turbulent temperature fluctuations. The impact of this will be assessed later.

It often desirable to calculate the spectrum of temperature fluctuations. Since the crosspower, $S_{xy}(f)$, is the Fourier pair to the correlation function, $R_{xy}(t)$, the temperature fluctuation level can be calculated from integration of the crosspower. For a calibrated signal:

$$\frac{\delta T_e}{T_{e,0}} = \sqrt{2\int S_{xy}(f)df}, \tag{3.53}$$

which in practice is calculated as a sum. Bias error from common pickup or noise can be corrected by calculating the crosspower of time-shifted (by more than the autocorrelation time of the turbulence) signals and subtracting it from the spectrum−this is done for analysis in later chapters, but the correction is typically much smaller than the sensitivity level of the diagnostic. Integration of the coherency spectrum will also be proportional to the relative temperature fluctuation level.

An issue that arises when employing Eqn. 3.53 is properly calibrating the signals. Absolute calibration factors can be determined in lab through use of noise sources, as was performed in Ref. [3]. Alternatively, it can be seen from Eqn. 3.49 that, given an independent measurement of T_e, the calibration factor can be determined from the autocorrelation or RMS value of the signal (neglected the previously noted bias error from neglecting autocorrelation of the turbulent fluctuations):

$$\sigma_i = \sqrt{\langle S_i^2 \rangle} = R_{ij}(\tau = 0) = c_i T_{e,0}\sqrt{\frac{B_{vid}}{B_{if}}}. \tag{3.54}$$

At DIII-D there is an independent, absolutely calibrated 40 channel array of ECE channels [215]. The temperature from this array can be used to determine the calibration factor

and to normalize each channel so that the relative fluctuation level can be calculated from integration of the crosspower spectrum.

If normalized to the local temperature and calibration factor, the unknown quantities drop out when Eqn. 3.54 is substituted into the expression, and we arrive at

$$\hat{S}_i = \frac{S_i}{c_i T_{e,0}} = S_i \frac{\sqrt{B_{vid}/B_{if}}}{\sigma_i}. \tag{3.55}$$

Time domain cross-correlation of Eqn. 3.55 is equivalent to cross-correlation of the raw signals; however, using the normalization with σ_i allows spectral calculations to be performed without recourse to independent measurements of T_e.

The sensitivity limit when the signal of interest is smaller in amplitude than other uncorrelated contributions to the signal is given for the CECE diagnostic as [3, 175, 210]

$$\left(\frac{\delta T_e}{T_{e,0}}\right)^2_{limit} \approx \frac{1}{\sqrt{N}} \frac{B_{vid}}{B_{if}}, \tag{3.56}$$

where N is the number of independent samples (the number of points in the time window for analysis). If the bandwidth of the fluctuation spectrum is known, B_{sig}, Eqn. 3.56 can be reduced by replacing B_{vid} with B_{sig}; otherwise, Eqn. 3.56 represents an overly conservative estimate since it essentially assumes the spectrum is flat. For instance, coherent modes can be easily visible in the spectrum and due to their narrow spectral width, the uncertainty of their amplitude is smaller.

All plotted values of electron temperature fluctuation power spectra and fluctuation levels in other chapters were determined by using a signal normalized as in Eqn. 3.55. This calculation was cross-checked against normalization to independent measurements of the electron temperature from the absolutely calibrated array and against the cross-correlation coefficient determination, Eqn. 3.52. In all cases in Chapter 5 (only chapter where CECE measurements are presented in this dissertation), the methods agreed to within the sensitivity limit given by Eqn. 3.56. In spite of the bias error introduced in Eqn. 3.55 by including the autocorrelations of both the thermal fluctuations and real plasma temperature fluctuations in σ_i, no systematic difference was observed in comparisons of that analysis with the

independent normalization from the ECE array. This indicates that bias error is significantly smaller than the radiometer uncertainty given by Eqn. 3.56, which *a posteriori* validates to limits taken to arrive at Eqn. 3.55 from Eqn. 3.48.

3.7 Conventional reflectometry

Port geometries with adjustable mirrors allow one of the DBS systems at DIII-D to be aligned for either Doppler backscattering or conventional reflectometry. The primary use of conventional reflectometry in this dissertation is through correlation with an ECE radiometer–the wave number sensitivity of the latter is set by the beam spot size and acts as the discriminating filter in the correlation, so none of the effects that have historically been issues for conventional reflectometry correlate. This may contribute to why the coherency between reflectometry and ECE has not been measured to be much higher than $\gamma = 0.3$ in DIII-D. The relatively low coherency might also be due to different wave number sensitivities of the diagnostics; for instance, fluctuations with short-scale radial wave numbers could contribute to the ECE signal, but not to the reflectometry signal. Nonetheless, a description of conventional reflectometry in included in this section for completeness.

The potential to use conventional reflectometry to diagnose plasma density fluctuations in tokamaks was realized long ago. Several now difficult to find works are referenced among the first experimental uses of microwave reflectometry [216–218], but quantitative studies were not routinely carried out until the late 1980's. An overview of references from that time is available in Ref. [219]. Multichannel reflectometers began to be deployed around the early 1990's that were used for correlation analysis [39, 219–221]. More detailed investigations of the physics of reflectometry and comparisons in conditions where other diagnostics were available to cross-check results were also conducted in the 1990's; several of these studies are referred to below.

In addition to measurements of density fluctuations and density profiles, reflectometry techniques have also be shown to be able to measure the magnitude of the magnetic field

through correlation of O-mode and X-mode [222, 223], temperature profiles when relativistic effects are important for the cutoffs [224], and magnetic pitch angle measurements through measurements of distortions of the beam profile [204, 205]. A variety of correlation techniques have also been applied to reflectometry analysis.

The hardware for conventional reflectometry is identical to that for DBS, as described in Sec. 3.3. In older work, many systems did not use quadrature mixers. Quadrature mixers allow both the phase and amplitude of the detected radiation to be determined. The nomenclature is that, individually, the two quadrature mixer outputs are often called "homodyne" signals. The traditional approach to reflectometry analysis focuses on the phase [169]. In an ideal sense, the cutoff surface can be thought of as a mirror into which the reflectometry beam is normally incident. Long wavelength fluctuations act to oscillate the position of the mirror, which results in optical path length fluctuations. Variations of the optical path length are then evident in the reflectometer phase. This approach is very powerful for global structures like tearing modes and Alfvèn eigenmodes [225]; however, for turbulence measurements it is often not possible to reconstruct the reflectometer phase.

Fluctuations of the reflectometer amplitude must be related to density fluctuations (ignoring magnetic fluctuations), but theoretical underpinning connecting those fluctuations to the real plasma fluctuations is lacking. What has been shown is that in simulations, the detected frequency spectrum for reflectometry bears little resemblance to the spectrum of fluctuations at the cutoff [226]. That is, the wave number sensitivity of the diagnostic has not been well described. As noted above, this is a non-issue for measurements of the crossphase angle between electron density and temperature fluctuations. It is also shown in Sec. 3.8.2 that when both the phase and amplitude can be recovered, cross-correlation with ECE gives the same crossphase angle. One can use either, but the phase of often not able to be recovered with high fidelity for turbulence measurements. Comparisons between between Langmuir probe measurements of fluctuation spectra and correlation lengths have found good agreement when using the reflectometer amplitude and homodyne signal [227–229].

Laboratory investigations focusing on recovery of the reflectometer phase have been con-

ducted [230], which were done to characterize microwave imaging reflectometry (MIR). The antenna arrangement for conventional reflectometry in Ref. [230] uses a diverging antenna pattern. The largest difference in the laboratory setup for the MIR tests was use of focusing optics, which were shown to improve the ability of the system to accurately recover the phase of the wave. Although the quasi-optical systems at DIII-D are used for conventional reflectometry, they do focus the probe beam. Many of the benefits attributed to MIR over conventional reflectometry can actually be achieved for the latter by focusing the probe beam.

Most recent new reflectometry efforts have still been focused on analysis of the phase. A thorough description of the sensitivity of the reflectometer phase and amplitude to plasma density fluctuations is yet to be developed and would be very valuable for transport model validation studies.

3.8 Measuring the crossphase between electron density and temperature fluctuations

The crossphase between electron density and temperature fluctuations was first measured in the stellarator Wendelstein 7-AS (W7-AS) [231], where it was found that phase between density and temperature fluctuations was close to zero. No detailed physics studies were performed with that initial realization of the measurement. Since the measurement became available at DIII-D, it has been used in numerous publications [15–17, 19, 175]. The W7-AS stellarator ceased operations in the year 2002; the $n_e T_e$ crossphase measurement at DIII-D is currently a unique capability, worldwide.

In this section we describe measurements of the crossphase between electron density and electron temperature fluctuations, α_{n_e,T_e}, made by arranging DBS-5 as a reflectometer and correlating its channels with ECE data from a radiometer-based CECE diagnostic [3]. The highest coherency between each pair of channels from the coupled reflectometer-ECE system is used in the results presented. The coherency is observed to decrease accross the DBS-5

array for a given ECE channel; this shows how indispensable the dense array of channels is for successfully obtaining and localizing the measurement. Previous literature has focused on using the reflectometer phase to reconstruct attributes of plasma turbulence, such as spectrum shapes and fluctuation levels. Issues that can arise when analyzing the reflectometer phase have been pointed out, with large aperture optical imaging systems suggested as the solution [226]. Past efforts to measure α_{n_e,T_e} also used the reflectometer phase [231]. An alternative approach that has received less attention is to use the reflectometer amplitude signal [16]. Although an analytical treatment of the amplitude is challenging, it has been demonstrated in both experiment [228, 229] and in 2D full wave simulations [232] that in many cases the homodyne or amplitude signals can be a better proxy for density fluctuations at the cutoff than the phase.

3.8.1 Coupled reflectometer and electron cyclotron emission radiometer

The n_eT_e crossphase is measured by correlating a channels from a correlation electron cyclotron emission radiometer [3] with channels from the DBS-5 system [6]. Typically, the CECE filters are set to the desired measurement location. The location is then attempted to be matched by the DBS-5 system, relying on between-shot ray tracing analysis. Figure 3.27 illustrates how the CECE and DBS-5 hardware are coupled. Both systems use a corrugated horn, which fills a collimating lens that directs the beams off a flat mirror, into a parabolic mirror, which focuses the beams in the plasma. The detected signals are combined using a WV-band diplexer (the CECE system is W-band, DBS-5 is V-band). The signals are then captured using D-TACQ digitizers, typically at 5 MHz. In the figure, the adjusted parabolic mirror is aligned so that DBS-5 functions as a conventional reflectometer. Annotations are given representing the right-hand cut-off layer and the 2^{nd} harmonic ECE layer, which determine the measurement locations for reflectometry and CECE, respectively. The depicted hardware arrangement has been used at the DIII-D 240° port during the years 2009-2012. During 2008 α_{n_e,T_e} measurements were made at the 60° port, where the plasma vertical position was adjusted so that the port geometry enabled reflectometry (the 60° is restricted to

launch angles $7° - 15°$ above horizontal).

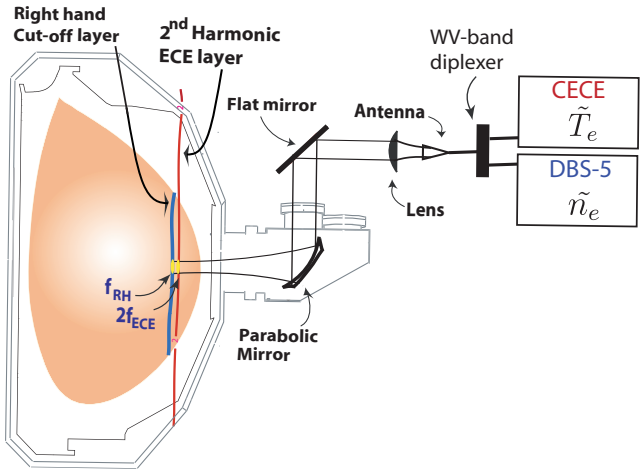

Figure 3.27: Illustration showing the arrangement of the CECE and DBS-5 hardware and quasi-optical components at the DIII-D 240° port. Optics not to scale.

3.8.2 On reflectometer phase versus reflectometer amplitude

The following measurements were obtained in an Ohmic plasma discharge with electron cyclotron heating (ECH) in the DIII-D tokamak. The DBS-5 and CECE diagnostics were diplexed together and shared the same quasi-optical antenna system, at the 60° Port. Both diagnostics are sensitive to low-k fluctuations ($k_\perp \rho_i \lesssim 0.5$). DBS-5 was aligned for reflectometry, and both the multiple reflectometry channels and adjustable channels from the CECE diagnostic were tuned to probe the same volume of plasma, at $\rho \approx 0.6$. By doing this, either the phase or the amplitude of the reflectometer channels can be correlated with the ECE channels. The plasma was optically thick ($\tau > 5$) at the measurement location, so no contribution of density fluctuations to the ECE signals would be expected. Figure 3.28 compares the coherency and crossphase attained by correlating each reflectometer signal with an ECE channel. Note that the value of the coherency is lowered by the thermal noise contribution to the ECE signal. Both reflectometer signal types show coherency, although the coherency with the amplitude is higher. This is a representative result—when the reflectometer phase can be recovered and correlates with ECE, the amplitude always does, and

with higher coherency. However, the correlation with the phase signal is often negligible, even when correlation with the amplitude is present. When both are present for a significant frequency range, the crossphase angle is the same, within statistical error measures. These observations are consistent with the amplitude being a better proxy for measuring local density fluctuations from turbulence.

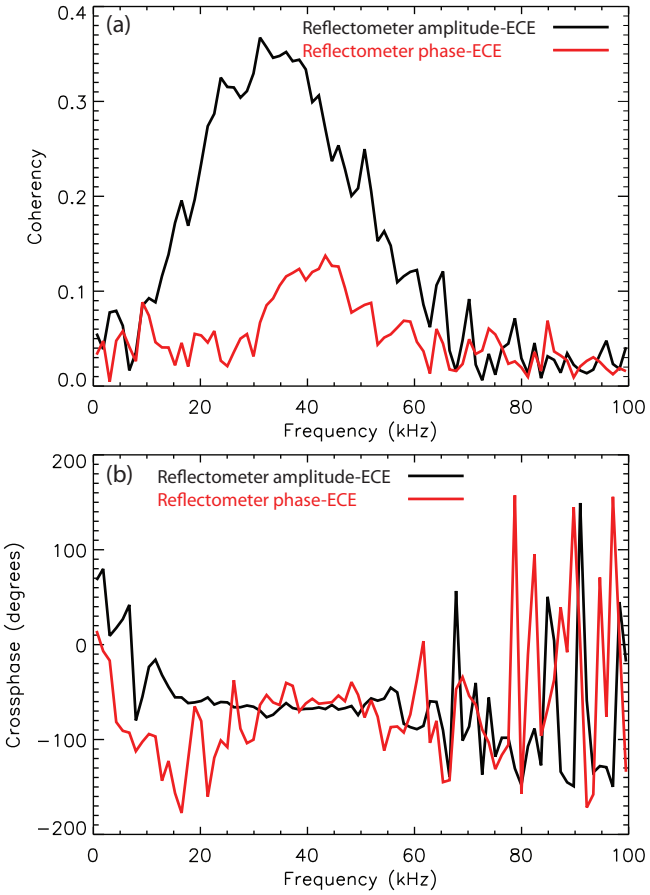

Figure 3.28: Comparison of cross-correlation of reflectometer phase and ECE data to the reflectometer amplitude from the same channel and the same ECE signal, ensemble averaged over 400 ms using 975 records. Error bars omitted for clarity. (a) Comparison of the coherency. (b) Comparison of the crossphase angle, α_{n_e,T_e}, using the reflectometer as the reference signal.

CHAPTER 4

On the geodesic acoustic mode and other zonal flows

4.1 Introduction

The geodesic acoustic mode (GAM) is a non-linearly driven zonal flow-like mode that is thought to play a role in setting the saturated level of turbulence in L-mode tokamak plasmas. An extensive experimental investigation of the GAM in DIII-D was conducted and published in Hillesheim *et al.* [20]. A smaller set of results on the GAM was included in Hillesheim *et al.* [15]. This chapter includes and expands on the results from both of those papers. See Sec. 2.3.2 for a review of existing work and background information on zonal flows and the GAM. Section 4.2 describes the experimental conditions for the discharges investigated in detail. Section 4.3 covers measurements of basic GAM characteristics, including mode frequency, toroidal correlation, radial structure, damping, and magnitude. Sections 4.4 and 4.5 present results related to non-linear characteristics of the GAM, with the former quantifying the intermittency of the GAM and the latter covering bispectral analysis results. In addition to the GAM at $\sim 15-20$ kHz, other low frequency zonal flows are also observed; Sec. 4.6 reports on investigations of these flows. Finally, conclusions are summarized and discussed in Sec. 4.7.

4.2 Experimental conditions

The GAM is observed in nearly every Ohmic and L-mode DIII-D plasma (exceptions are discussed later). In this section, the equilibrium parameters of several shots that are analyzed in detail in subsequent sections are recorded.

Shots with several different arrangements of DBS-2, DBS-5, and DBS-8 were used to acquire the data presented in the chapter. Specifics are described, where appropriate. Two discharges in particular were investigated in detail, with results presented in several sections. The hardware arrangement in those shots was DBS-5 at the 240° Port and DBS-8 at the 60° Port (see Sec. 3.3.4 for port location information); in several places the former is referred to as the P240° system and the latter as the P60° system.

Two L-mode DIII-D discharges, chosen for the observed GAM phenomenology they contain, are examined in detail in subsequent sections of this chapter. In both of these cases, toroidal correlation between P240° and P60° channels is observed. The most significant phenomenological difference is the observed coherence of the GAM: a weakly coherent GAM case ($\tau_{ac} f_{GAM} \sim 4$) and a more coherent GAM case ($\tau_{ac} f_{GAM} \sim 15$), where τ_{ac} is the autocorrelation time of the GAM. Additional shots are introduced and described below to illustrate brief points. In this section, the equilibrium parameters for the shots are described for the time periods over which the ensemble averages are performed.

Figure 4.1 shows spectrograms of the DBS phase, the Fourier transform of which is proportional to $v_{E\times B}$ for oscillatory modes, and the ensemble averaging window for each shot. The channels pictured for each shot display the level of consistency in the GAM frequency and amplitude. Although it would appear from Fig. 4.1 that longer intervals could have been used, the ensemble averaging windows were chosen as a compromise—both shots contain slow equilibrium changes that more prominently affect the GAM on other channels outside this window, preventing a longer interval from being used. As in Hillesheim et al. [15], the oscillation in shot 141958 can be identified as a GAM by the frequency scaling with the electron temperature pulses from sawteeth. The observed oscillation frequency is also roughly consistent with the expected GAM frequency, $\sim$ 20 kHz. Early heating was applied in shot 142121, which slowed the current diffusion so that the onset of sawteeth did not occur until after 2000 ms. The mode can be identified by looking later in the shot, shown in Fig. 4.2(b), when sawteeth are present. An equilibrium magnetic field shape change starts at 2000 ms, including a significant change to the elongation, κ, as depicted in Fig. 4.2(c).

The shape and resultant transport changes cause modifications to the equilibrium density profile and therefore to the DBS measurement locations, which is why the GAM switches between DBS channels in Fig. 4.2(a-b). There are also changes to the electron temperature profile, but they are insufficient to cause the $\sim 40\%$ change to the GAM frequency. This is consistent with previous experiments showing a scaling of $f_{GAM} \widetilde{\propto} 1/\kappa$ (Refs. [124, 125]) and theoretical expectations of $f_{GAM} \propto 1/\sqrt{1+\kappa^2}$ (Ref. [120]); however, investigation of the dependencies of the GAM frequency is not a focus and will not be pursued further.

Figure 4.3 shows equilibrium profiles for each shot. Electron temperature and density profile measurements are from Thomson scattering, averaged over the 500 ms windows shown in Fig. 4.1. Figure 4.3(c) shows the q-profile from EFIT [176] reconstruction using external magnetics data (no Motional Stark effect data was acquired during the time periods of interest). For shot 141958 the plasma current was 960 kA and the on-axis toroidal magnetic field was 1.8 T, with ~ 0.2 MW of ion cyclotron resonance heating (ICRH) and ~ 2.5 MW neutral beam power co-injected with the plasma current. A small caveat exists for this shot: during the time window of interest the gap between the plasma boundary and the wall at the outboard midplane was scanned, which resulted in small changes to elongation, major radius, minor radius, electron temperature, and coupled ICRH power; however, as can be seen in Fig. 4.1(a), the local changes do not have a large effect on the DBS measurements of the GAM. Ray tracing calculations for several times during the outer gap scan predict movements of the DBS scattering locations of $\Delta\rho \sim 0.02$ due to the equilibrium changes, which is less than estimations of systematic uncertainties, and the estimated relative change between scattering locations is about a factor of ten less. For 142121 the current was 1.2 MA and the on-axis toroidal magnetic field was 2.1 T, with 4.4 MW neutral beam power half co- and half counter-injected to the plasma current. For both shots the main ion species was deuterium, the major radius was $R_0 \approx 1.7$ m, and the minor radius was $a \approx 0.6$ m. Shot 141958 was a diverted plasma with a single upper null, and 142121 was inner wall limited.

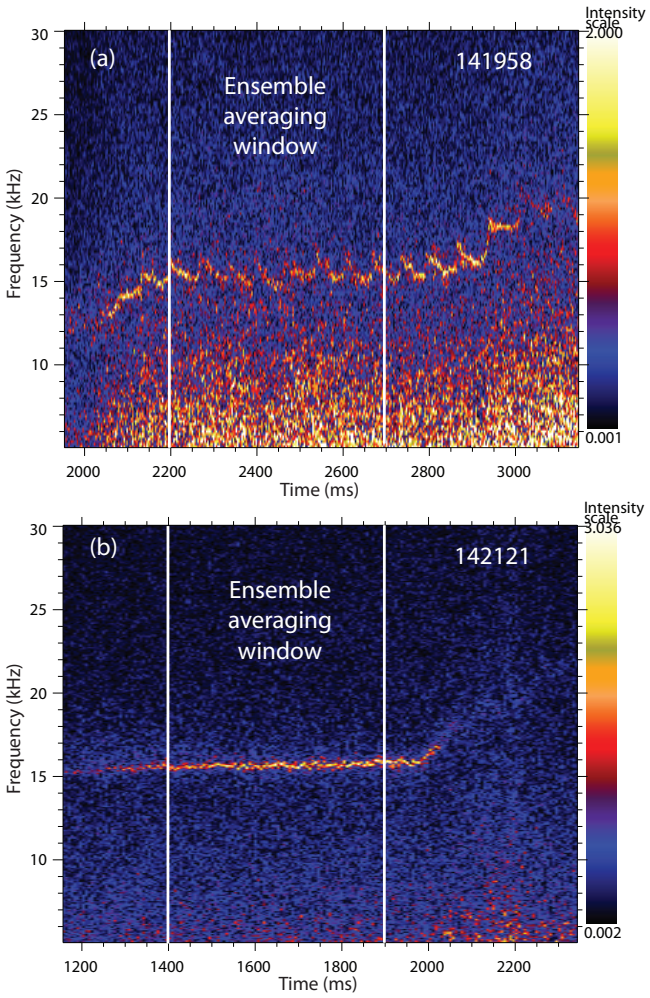

Figure 4.1: Spectrograms of DBS phase on a linear scale for DIII-D shots (a) 141958 (P60°, 57.5 GHz) and (b) 142121 (P60°, 72.5 GHz), from one DBS channel for each shot. Also denoted are the time windows taken for ensemble averaging: 2200-2700 ms for 141958 and 1400-1900 ms for 142121.

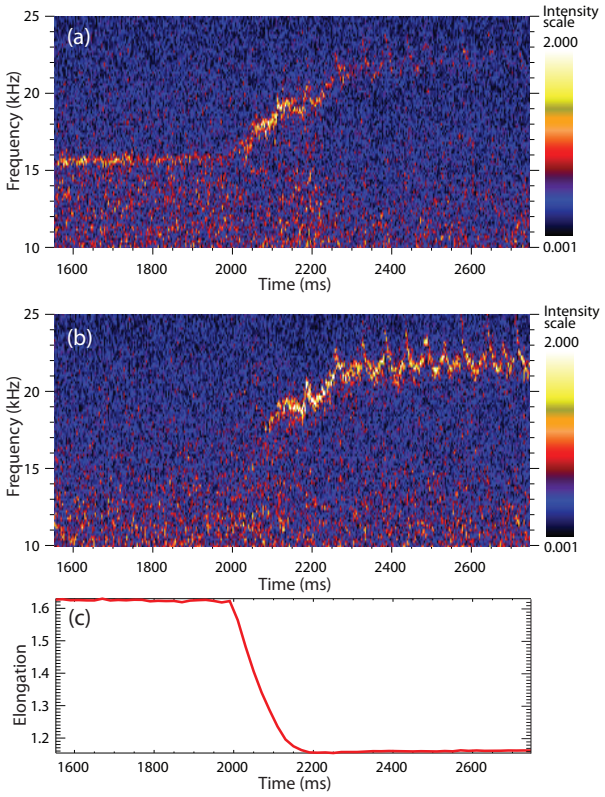

Figure 4.2: Spectrograms of DBS phase on a linear scale from two channels of shot 142121, showing the changing GAM dynamics across two DBS channels: (a) P60°, 70.0 GHz and (b) P60°, 67.5 GHz. (c) Magnetic equilibrium elongation at the separatrix.

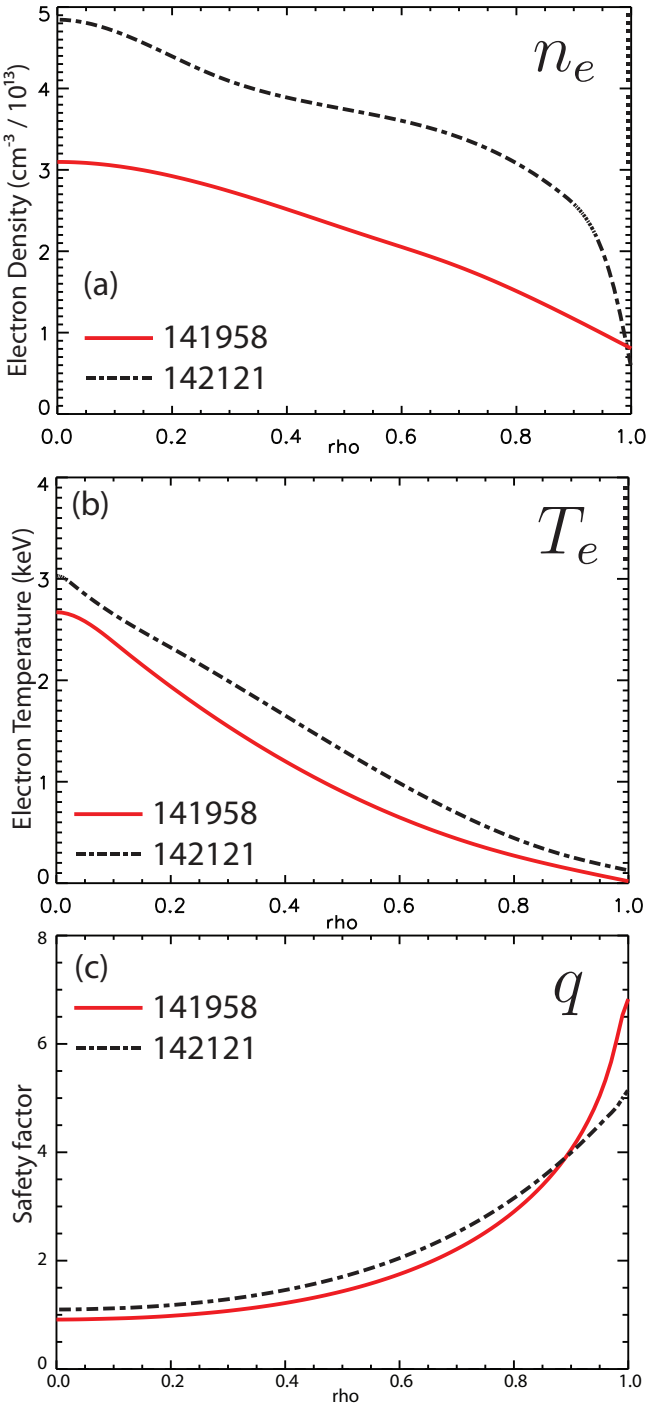

Figure 4.3: Equilibrium profiles of electron density (a) and electron temperature (b) averaged over the 500 ms window. (c) Safety factor profile at midpoint of 500 ms windows.

4.3 Basic GAM characteristics

4.3.1 GAM frequency

In the high safety factor, circular plasma, electrostatic limit, the GAM frequency becomes $\omega_{GAM} = \sqrt{2}c_s/R_0$. The sound speed is $c_s = \sqrt{\frac{T_e+\gamma_i T_i}{m_i}}$, with kinetic calculations yielding $\gamma_i = \frac{7}{4}$ for the GAM[119, 233]. Here, R_0 is the major radius, T_e is the electron temperature, T_i is the ion temperature, and m_i is the ion mass. Figure 4.4 shows a spectrogram of the DBS phase and the electron temperature from a profile ECE diagnostic [215] at nearly the same radial location as the DBS measurement in a neutral beam heated L-mode DIII-D discharge. There is nothing significant on the fast magnetic probes or in spectral analysis of the ECE at this frequency, so the DBS phase oscillation can be identified through Eqn. 3.14 as due to the local turbulence flow. Calculation of the GAM frequency using local plasma parameters produces about 20 kHz. The clear relationship between the electron temperature pulses from sawtooth crashes and the flow oscillation identifies the mode as a GAM.

4.3.2 Toroidal correlation of the GAM

Correlation analysis can be applied between the multiple DBS channels to extract more information about the GAM. The data in this section was acquired with DBS-5 at the 60° Port and DBS-2 at the 240° Port. Figure 4.5 shows the ensemble averaged coherency and crossphase, $\alpha_{v_{\mathrm{GAM}}}$, between the phase signal, φ_{DBS}, of two DBS channels at locations separated by 180° toroidally, but aligned within 1 cm radially at $\rho \approx 0.8$, where ρ is the square root of the normalized toroidal flux. The safety factor at the measurement location is about 2, lower than most previous observations, which have mostly been acquired at higher q, near the last closed flux surface. The width of the coherent peak is due mostly to the sawtooth oscillations. The high coherence at low frequencies is due primarily to the equilibrium component of the radial electric field. The channels are also offset poloidally by about 5° due to the port geometries, with DBS-5 probing slightly above the midplane and DBS-2 slightly below. The small phase difference between the two channels is consistent

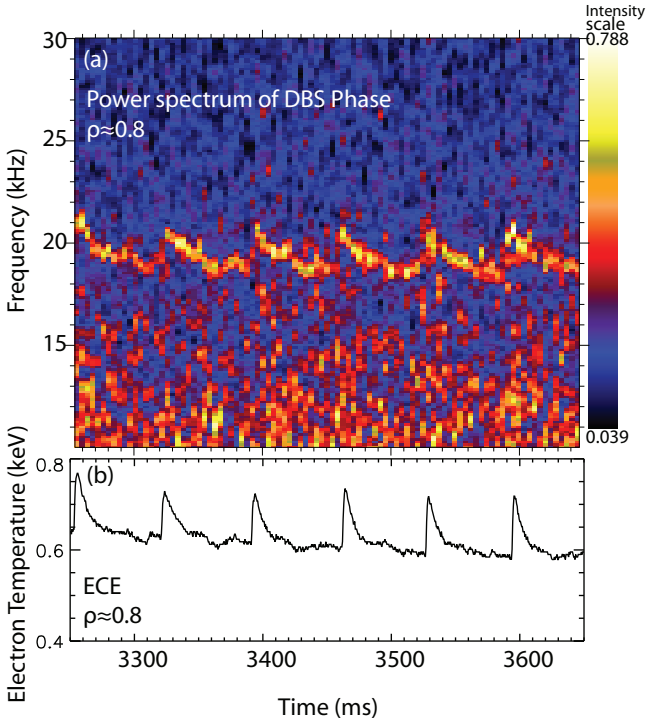

Figure 4.4: (a) Spectrogram of the DBS phase at $\rho \approx 0.8$, showing a flow oscillation from a GAM as the GAM's frequency is modulated by sawtooth heat pulses. (b) Electron temperature from ECE at the same radial location.

with the expected axisymmetric (m=0, n=0) flow structure for the GAM.

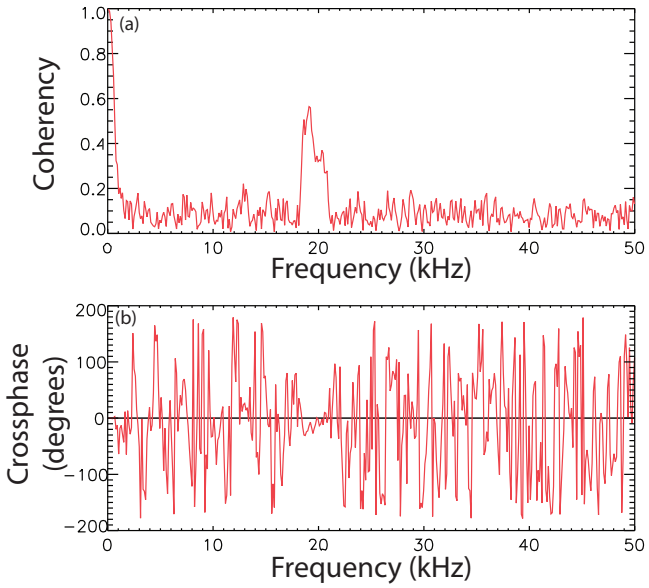

Figure 4.5: (a) Coherency of the DBS phase between two DBS channels at toroidal locations separated by 180°, radially aligned at $\rho \approx 0.8$, and ensemble averaged over 400 ms. (b) Crossphase between the same two channels.

4.3.3 Measured GAM radial structure

The background information on the GAM in Sec. 2.3.2.1 included discussion of the radial structure of the mode. Section 2.3.2.2 reviewed the original GAM derivation [112], which was done within the framework of magnetohydrodynamics. In MHD, the GAM exists independently on each flux surface, which leads to the prediction of a continuum of modes with frequencies that vary radially with local plasma parameters. Section 2.3.2.3 reviewed the derivation of the eigenmode GAM [138], where when kinetic effects are included, a radial eigenmode with a constant frequency is predicted. This section presents investigations of the experimentally measured GAM radial structure and radial propagation of the mode.

4.3.3.1 Radial propagation of the GAM

Figure 4.6 shows the crossphase among 7 DBS channels, using both DBS-5 and DBS-2, at the frequency of maximum coherency for the GAM, referenced to the middle channel of DBS-5. Assuming that the GAM potential is dominantly axisymmetric (m=0, n=0), which is consistent with Fig. 4.5, then, even though toroidally and poloidally separated channels are used, the change in crossphase is due to the difference in radial location. The ray tracing code GENRAY [177], using experimental equilibrium and density profiles, is used to determine the locations. The crossphase, $\alpha_{v_{\mathrm{GAM}}}(\rho)$, between the channels shows a linear increase outwards, consistent with outward radial propagation−for a standing wave one would expect 0° or 180°. Applying a linear fit to the data, a radial wavelength of $\lambda_{GAM} \approx 3$ cm is calculated. These observations are consistent with previous experiments on DIII-D [115, 124] and with experiments on other tokamaks [117, 136]. The error bars in Fig. 4.6 are purely statistical and do not account for systematic errors.

The $\rho \approx 0.80$ point from the 240° port appears to be inconsistent with the fit. This could in part be due to a low signal level for that channel. When there is a low signal level from the plasma, the backscattering signal competes with system noise and ambient pickup, potentially decreasing the coherency for uncorrelated noise and biasing the crossphase towards zero for coherent ambient pickup. A second explanation is that the radial wavenumber for the GAM is expected to depend on poloidal angle [113]; the two explanations cannot be distinguished with this data set.

4.3.3.2 More detailed structure measurements

Two independent, multichannel DBS systems (DBS-5 and DBS-8) were used to make simultaneous measurements at two toroidal locations and multiple radial locations. Figure 4.7 shows ray tracing results for shot 141958 at 2450 ms, overlayed on the EFIT equilibrium, showing the poloidal and radial separation of the measurement locations. Figure 4.8 shows the radial measurement location and wave number for both shots from ray tracing, which

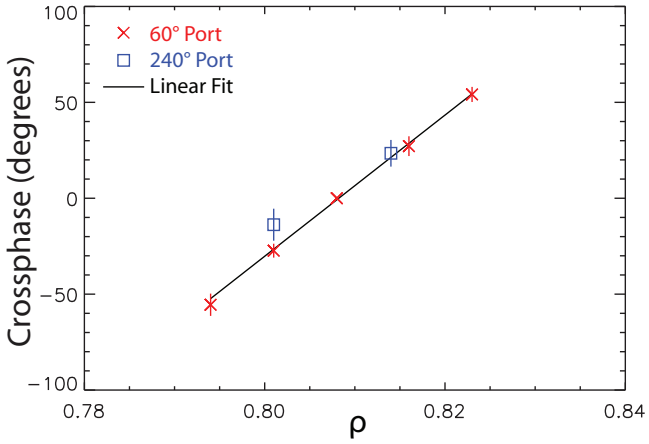

Figure 4.6: The crossphase, $\alpha_{v_{\mathrm{GAM}}}(\rho)$, among the phase of 7 DBS channels at the GAM frequency plotted against ρ, ensemble averaged over 400 ms, showing outward radial propagation of the GAM. The center channel of DBS-5 is the reference.

are used in calculations below. The flux surface label, ρ, is the normalized square root of the toroidal flux.

By cross-correlating the DBS phase between channels, the radial propagation of GAM phase fronts can be measured, assuming the GAM potential is in fact axisymmetric (m=0, n=0) [15]. Radially aligned measurements with toroidal and poloidal separation are consistent with an axisymmetric potential. Given that the measurement locations are radially, poloidally, and toroidally separated, little can be concluded from the change in the crossphase between channels without the axisymmetric assumption. More strictly, since the measurement locations are exactly 180° apart toroidally, the toroidal mode number can only be constrained by measurement to even values; also, due to the geometry of the poloidal locations and measurement uncertainties, a finite poloidal mode number cannot be definitively excluded. This analysis is applied to the two shots under consideration here, both of which exhibit toroidal correlation of the GAM.

In Fig. 4.9 the coherency and crossphase of the DBS phase, $\varphi_{DBS}(\omega) \propto v_{E\times B}(\omega)$, for P240° and P60° channels, referenced to the 55.0 GHz channel of P60° are plotted. The 500 ms time window referenced above is partitioned into 151 records. The vertical error bars

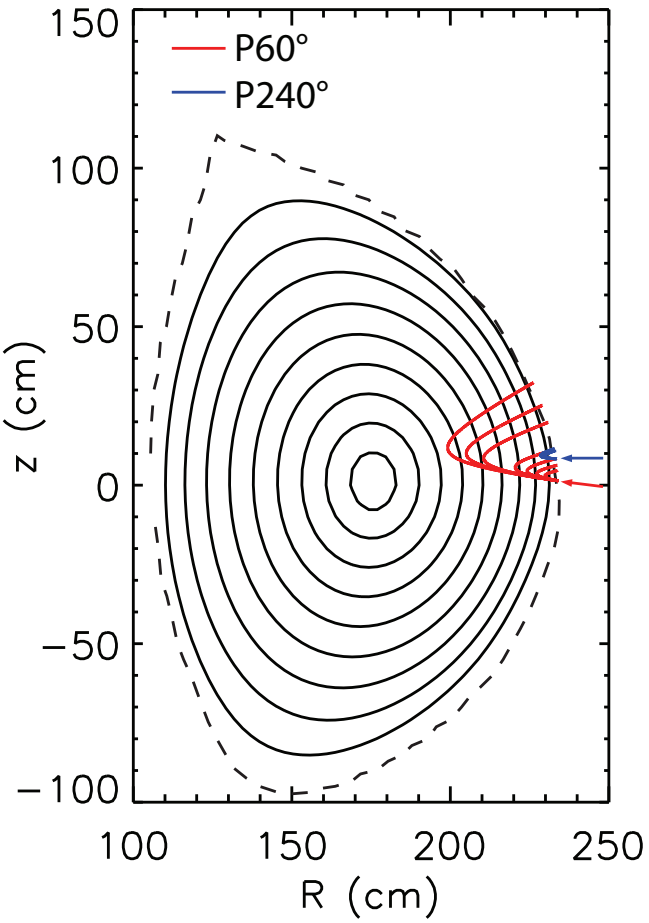

Figure 4.7: Ray tracing results from P60° at the 60° Port, launched at 7° to the horizontal (red) and from P240° at the 240°, launched parallel to the horizontal (blue) projected onto the equilibrium from EFIT from shot 141958; contours of ρ are plotted. Arrows indicate the starting trajectory of each set of rays.

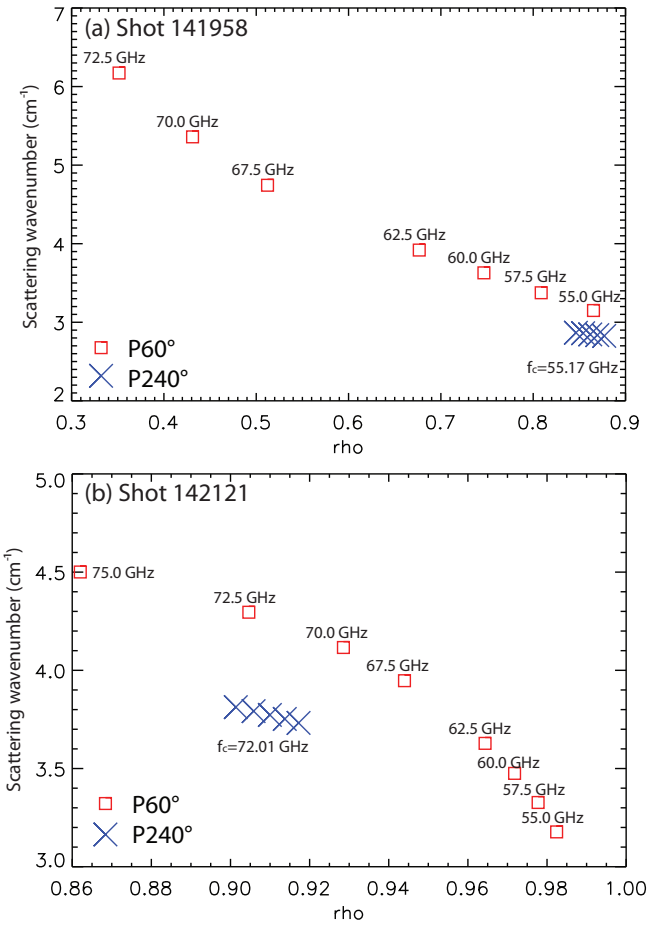

Figure 4.8: The measurement location and wave number for (a) shot 141958 and (b) shot 142121 for P60° channels (red squares) and P240° channels (blue Xs). Annotated are the frequencies of the P60° channels and of the center channel of the P240° array. The 75.0 GHz channel in 141958 is absorbed at the 2^{nd} electron cyclotron harmonic before reaching cutoff.

represent the statistical error. The primary source of systematic error is from uncertainty in the density profile and equilibrium. This systematic error can be estimated by performing the ray tracing calculations at several times within the 500 ms window. Note that this error affects the location of all of the channels, while the uncertainty of the relative distance between channels is much smaller, less than size of the symbols in the plot for a case like 141958 where the density gradient changes little between scattering locations. This estimated systematic error is represented by the horizontal error bar given for one point in the figure. Using the radial change in crossphase between the P240° channels, the radial wave number can be calculated−the sign of the change is consistent with outward radial propagation. Note that, due to refraction, the scattering region for each channel is at both slightly different radial and poloidal positions; also, as can be seen in Fig. 4.7, the measurement locations for the two toroidally separated DBS systems are poloidally separated. However, assuming the flow oscillation for the GAM is indeed m=0, n=0, then the measured change in crossphase is due only to radial propagation of the GAM phase fronts. Radially aligned channels, within uncertainties, *a posteriori* confirm this assumption.

Using the location of the center of the scattering region as determined by ray tracing, the distance between the channels is projected onto the normal to the flux surfaces to correct for the poloidal separation. This is a small correction for channels within P240°, typically $\sim 2-4\%$. The measured radial wave number of $k_r \approx 2.0 \pm 0.2$ cm^{-1} is determined by a linear fit to the P240° channels, weighted by the calculated statistical errors in the crossphases, giving a statistical uncertainty in the fit of $\sim 2-3\%$. A larger uncertainty arises when attempting to estimate the error by choosing a different reference channel: this approach produces an estimated error of $\sim 10\%$.

The process of examining alternate reference channels is nonetheless illuminating. First, using 180° toroidally displaced channels separates finite frequency zonal components of the flow−here, the GAM−from the equilibrium flow and from the ambient turbulence, which only has an effect on other measurements within a turbulence correlation length of the same magnetic field line. This is shown in Fig. 4.10, which compares the coherency spectra between

a reference channel from P60° to three other DBS channels: two P240° channels and one P60° channel. The effect of the different toroidal locations is clear in Fig. 4.10, where the broadband correlation is present only between channels at the same toroidal location. The radial separation between the channels results in the different values for the crossphase at the frequency of the GAM. Note that in an ensemble average, the measured crossphase from the ambient turbulence is close to being a uniform random variable, and so averages to zero; however, when a coherent mode is present, random phasing of the turbulence means that the measured crossphase is due only to the coherent mode. Since the presence of a GAM in a channel's autopower spectrum can be occluded by the ambient turbulence, using toroidal correlation is a useful way to detect its full radial extent. The significant level of broadband coherency between the two P60° channels in Fig. 4.10 plausibly has contributions from several sources: the equilibrium $E \times B$ flow, low frequency zonal flows, ambient turbulence, and non-ideal DBS effects like non-localized small angle scattering along the beam path.

There is an apparent inconsistency between Fig. 4.9(b) and Fig. 4.10(b), where different reference channels are used: a monotonic ordering of the relative crossphase puts the P60°, 55.0 GHz channel between P240°, 55.17 GHz and 54.82 GHz in the former, but in between P240°, 55.17 GHz and 55.52 GHz in the latter−this is based purely on an ordering of the relative crossphase when using a different reference channel and therefore is not affected by uncertainties in the equilibrium. The coherency is high in both cases ($\gamma_{xy}(f_{GAM}) \approx 0.8$) and there is a sufficiently large number of records ($n_d = 151$) that the difference cannot be attributed to statistical uncertainty ($\sigma_{\alpha_{xy}}(f_{GAM}) \approx 2.5°$). One explanation is that there is a contribution to the crossphase from the ambient turbulence that does not act as a uniform random variable, for instance, due to an average radial propagation; however, that should occur at all frequencies, which is not consistent with Fig. 4.10(b). Another possibility is that the discrepancy arises due to the poloidal variation of the radial wave number of the GAM, which would be expected in an elongated and up-down asymmetric plasma, since, while the GAM potential is constant on a field line, the radial distance between two given field lines varies poloidally; a more complete data set is required to assess this explanation.

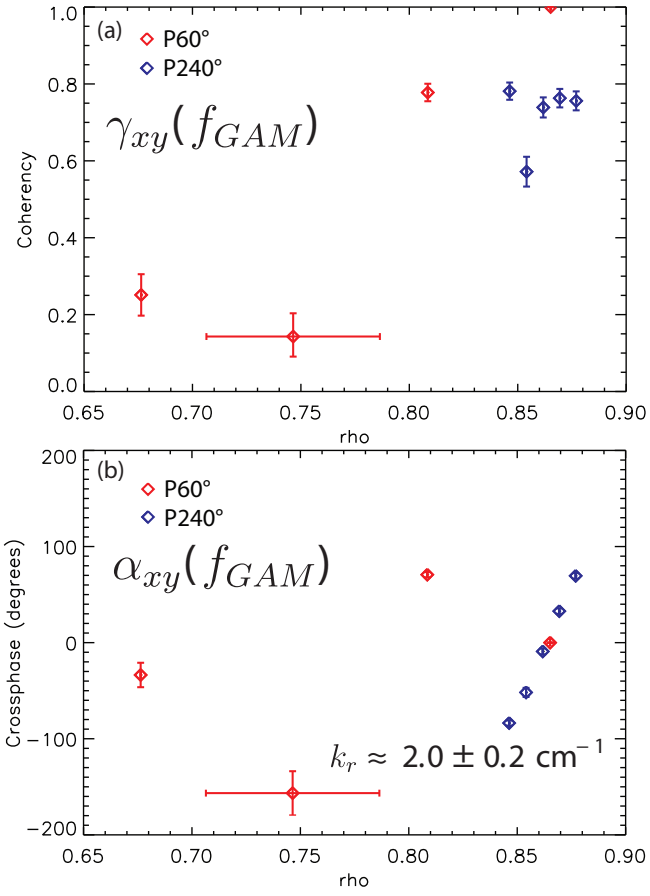

Figure 4.9: The 55.0 GHz channel of P60° is used as the reference to correlate with the other P60° channels and with the P240° channels, which are centered at 55.17 GHz and are toroidally separated by 180°. The ensemble-averaged (a) coherency and (b) crossphase for each pair, correlating the DBS phase, are plotted from shot 141958.

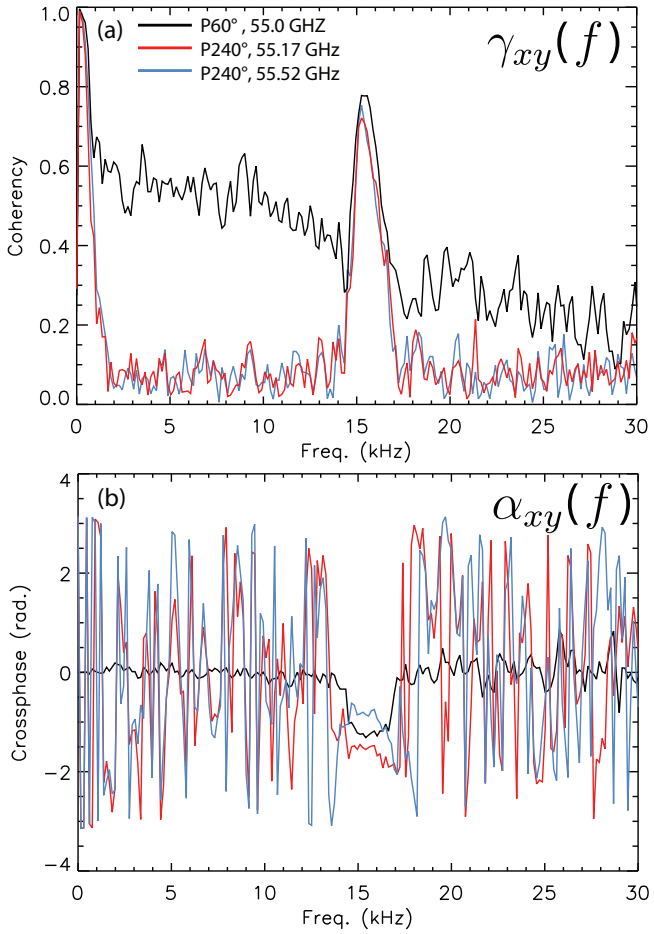

Figure 4.10: The ensemble-averged (a) coherency and (b) crossphase between the P60° 57.5 GHz channel and three other DBS channels, correlating the DBS phase, from shot 141958.

Figure 4.11 shows the same analysis described for Fig. 4.9 applied to DBS data from shot 142121. One notable difference is that since there is more curvature to the density gradient (large second derivative with respect to radius; not magnetic field curvature) at the measurement locations (see Fig. 4.3), there is a larger uncertainty in the relative locations of the measurements. That, in turn, leads to a larger estimated uncertainty in the determination of the radial wave number of the GAM, which is $k_r = 1.4 \pm 0.4$ cm^{-1}. The sign of the crossphase change is again consistent with outward propagation. Although there is a similar slope of the crossphase between the P240° and three outermost P60° channels, there is a noticeable offset. Due to differences in port geometry and launch angle, refractive effects are different for each beam path; the radial offset is within uncertainties from the density profile for this reason. Here, the GAM is detectable on the four highest frequency P60° channels, but not on the four lowest frequency channels. The GAM is not actually visible above the broadband turbulence in the autospectrum of the P60°, 67.5 GHz channel, but the radial change in crossphase across the P240° array can be extracted when using it as the reference; this is a consequence of the toroidal displacement of the channels.

One possible reason for the attenuation (low coherency) of the GAM at the outer locations is that, due to uncertainties in the density profile and equilibrium, those measurement locations are actually outside of the last closed flux surface, where the GAM cannot be supported. A second, potentially more interesting explanation, is that the GAM is exposed to a higher degree of damping in this region. In other work, the GAM has also been observed to attenuate before the last closed flux surface [124, 125]. The collisionless Landau damping would not be expected to change significantly between these radially adjacent locations. One factor that has not received significant attention in the literature is the effect of neutral damping, which could plausibly play a role, considering the mean free path of neutrals is typically on the order of a centimeter into the plasma. The ion-ion collisional damping may also become relevant as the ion temperature decreases. GAM damping is addressed more quantitatively in Sec. 4.3.5.

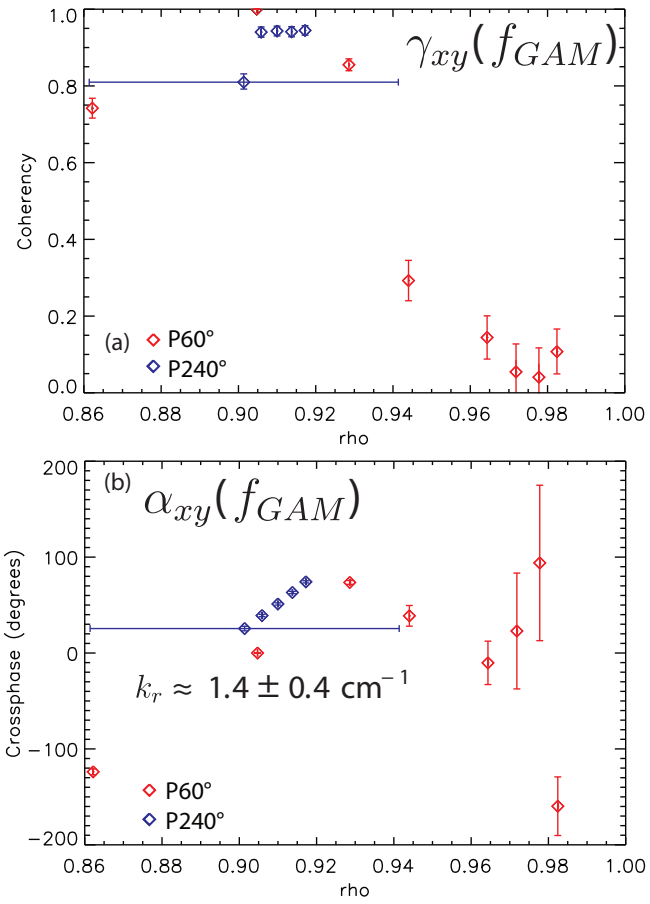

Figure 4.11: The 72.5 GHz channel of P60° is used as the reference to correlate with the other P60° channels and with the P240° channels, which are centered at 72.01 GHz and are toroidally separated by 180°. The (a) coherency and (b) crossphase of the DBS phase for each pair are plotted from shot 142121.

4.3.3.3 Extended radial correlation of the GAM

Looking at whether the radial propagation of the GAM between P240° channels can be measured by different reference channels of P60° gives a strong indication of the radial coherence of the GAM. Figure 4.12(a) shows the coherence of the DBS phase between the channels of P240°, referenced to 4 different channels of P60°, at the frequency of the GAM (error bars are suppressed for clarity). Note that the difference in the behavior of the P240° channel at $\rho \approx 0.855$ is explained by a lower signal level on this channel. This results in pickup from noise sources being of comparable magnitude to the received scattered power, whereas that contribution is negligible for the other channels. The radial change in crossphase from the propagation of the GAM can be detected when the reference is the 55.0, 57.5, or 60.0 GHz channel of P60°, but not when the reference is the 62.5 GHz channel. Figure 4.12(b) shows the two most radially separated channels exhibiting significant coherency at the GAM frequency; the high level of coherency at low frequencies ($f < 2$ kHz) is due to the equilibrium flow and is not present in the spectrum if the DBS phase derivative is correlated instead. Referring to Fig. 4.8, Fig. 4.12 indicates that the GAM is radially coherent over at least $\Delta\rho \approx 0.15$, with the outer bound determined by measurement limitations (no measurement locations $r/a > 0.9$). From variation of the magnetic field and the electron temperature profile, the ion sound radius, varies between $\rho_s \approx 0.1 - 0.2$ cm over the coherent region. This gives a radial correlation length for the GAM, determined using a radial projection of the DBS measurement locations as described above, of $L_{r,GAM} > 6$ cm, or, using the upper limit on ρ_s in the radial interval over which the GAM is coherent to arrive at a lower bound, $L_{r,GAM}/\rho_s > 30$. This is significantly larger than typically measured turbulence correlation lengths of $L_{r,turb}/\rho_s \sim 5 - 10$ [64], and demonstrates that the GAM can exist as a mesoscale structure smaller than the equilibrium scale, but larger than the turbulence correlation length.

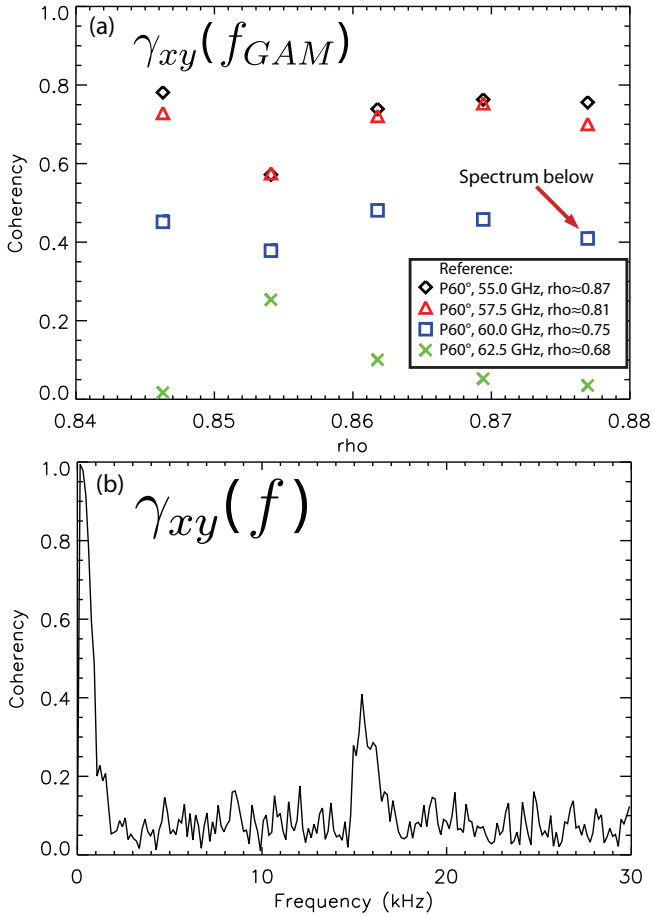

Figure 4.12: (a) The coherency of the DBS phase at the GAM frequency between the channels of P240° and four reference channels from the toroidally separated P60°, from shot 141958. (b) The coherency spectrum of the DBS phase between the two most radially separated channels showing significant coherency: P60°, 60 GH and P240°, 54.47 GHz.

4.3.4 Eigenmode GAM versus continuum GAM

One notable aspect of the GAM in Figs. 4.9, 4.11, and 4.15 is that the mode occurs at a constant frequency with radius. In fact, at a particular radial location, it is often possible to identify GAMs at two distinct frequencies, or to observe separate radial intervals over which the GAM occurs at different, but constant frequencies within each interval, *i.e.* a staircase of eigenmode GAMs. This is a different phenomena than peak splitting, which is also observed in some cases and appears to be due to interaction with low frequency flows. In previous work, similar observations have been made (*e.g.* Ref. [125, 136]); conversely, the GAM has also been observed to occur as a continuum of frequencies with radius (*e.g.* Ref. [234]). The latter case is the conventional picture of the GAM in the framework of magnetohydrodynamics, originating from Ref. [112]. In more recent work, the GAM has been shown to form radial Airy function-like eigenmodes when finite $k\rho_i$ effects are included [119, 138–140]. In DIII-D it appears that both regimes can be realized experimentally. Data indicates that the continuum GAM (low temperature, $k\rho_i \to 0$) occurs in Ohmic discharges and L-mode with little auxiliary heating, and the eigenmode GAM (high temperature, finite $k\rho_i$) occurs in L-mode discharges with additional heating.

To clearly demonstrate the radially extended structure, Fig. 4.13 shows a contour plot of DBS measured $v_{E\times B}$ fluctuations (calculated using the time derivative of the DBS phase) versus frequency and position from the P60° system, where interpolation is done between the 8 channels. The GAM is distinctly visible in the spectrum at ~ 16 kHz between $\rho \approx 0.86$ and $\rho \approx 0.94$, and is not observable in the autospectrum at larger radii. Referring to Fig. 4.3, the electron temperature changes from more than 300 eV at $\rho \approx 0.86$ to less than 200 eV at $\rho \approx 0.94$. The GAM in Fig. 4.13 plainly does not reflect the local temperature. Although there were no measurements acquired for $\rho < 0.86$ in this case, using ρ_s at $\rho = 0.86$, the lower bound on the radial correlation length of the GAM can still be found to be $L_{r,GAM} \gtrsim 15\rho_s$.

To illustrate the empirical differences in GAM behavior, P60° data from an additional plasma discharge, DIII-D shot 140437, is shown in Fig. 4.14. The data shows the GAM in the

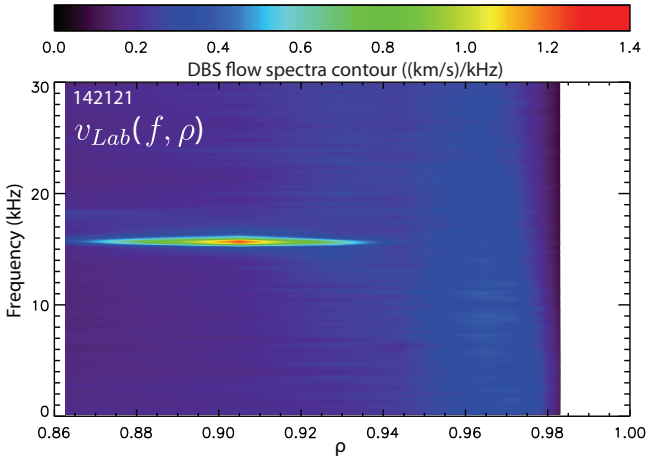

Figure 4.13: (Color online) Contour plot of DBS measured lab frame flow fluctuations versus frequency and flux surface from the 8 P60° channels in shot 142121 (points between the 8 channels are interpolated), ensemble-averaged over the period 1400-1900 ms.

early L-mode phase and leading up to an H-mode transition at $\sim$ 1290 ms after additional neutral beam heating is applied. At $\sim$ 500 ms the GAM appears on the 55.0 GHz channel of P60° at $\sim$ 17 kHz and also weakly on the 57.5 GHz channel at $\sim$ 18.5 kHz. This is consistent with the continuum GAM, where the frequency reflects local conditions at each radius. As time progresses the equilibrium profiles evolve, which results in the GAM appearing on different P60° channels, but there is a clear continuity of the mode's existence. At $\sim$ 1200 ms the GAM appears on both the 60.0 GHz and 62.5 GHz channels at $\sim$ 16 kHz, consistent with characteristics of the eigenmode GAM. Correlating the time derivative of the DBS phase between the 60.0 GHz and 62.5 GHz channels during the time period of 1100-1200 ms results in a coherency of $\gamma = 0.58 \pm 0.04$ at the frequency of maximum coherency, $\sim$ 15.9 kHz—as noted elsewhere, correlation analysis can extract information about the GAM even when it is not clearly visible in the autospectrum of individual channels. Although the plasma is not stationary for the time period—the line averaged density increases by $\sim$ 10%—ray tracing calculations using density profiles averaged over this time period indicate that the 60.0 GHz and 62.5 GHz channels are radially separated by $\sim 1.0 - 1.5$ cm. At the measurement location, $\rho_s \approx 0.1$ cm, so here $L_{r,GAM} \gtrsim 10 - 15\rho_s$, which further substantiates the GAM at

later times in the plot as an eigenmode GAM.

There are two additional interesting features of this data. First, the continuum GAM appears to have a broad spectral width, while the eigenmode GAM has a narrow spectrum. This is a representative result for observations of the GAM in each regime. Second, since the GAM is observed on at most two P60° channels simultaneously in Fig. 4.14, the GAM's radial extent is narrower than observed in Fig. 4.9; so, while the coherent radial extent of the GAM can be significantly larger than the correlation length of turbulence, that is not necessarily true in all cases−as noted above, the lower bound on the radial correlation length of the GAM between 1100 and 1200 ms in Fig. 4.14 is found to be $L_{r,GAM} \gtrsim 10 - 15\rho_s$, whereas $L_{r,GAM}/\rho_s > 30$ was found for the GAM in Fig. 4.9. In light of recent work on the GAM's role during the L-H transition at low densities [121], the implication illustrated by Fig. 4.14 is that it is the eigenmode GAM that may be important in such cases, not the continuum GAM. Looking at an additional set of shots, the difference between the eigenmode GAM and continuum GAM can be seen by viewing contours of flow spectra from DBS-8, which are included in Sec. 4.6 where characteristics of observed low frequency flows (including the GAM and other modes) are discussed.

4.3.5 GAM damping

The GAM is thought to be non-linearly driven by turbulence and linearly damped by collisionless ion Landau damping. A case where the damping rate could be experimentally inferred is compared to predictions in Sec 4.3.5.1. The GAM is also observed to be absent very near to the last closed flux surface. Collisional damping mechanisms are assessed in Sec. 4.3.5.2.

4.3.5.1 Measured GAM damping

Damping of the geodesic acoustic mode is thought to be an important limitation on the region where the mode can exist. Due to the e^{-q^2} dependence of the collisionless ion Landau

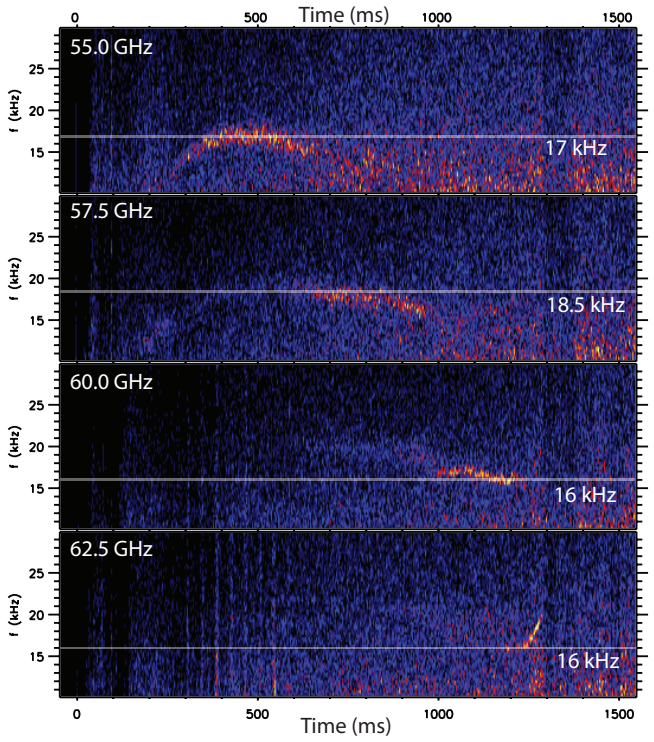

Figure 4.14: Spectrograms of DBS phase on a linear scale from four P60° channels showing the evolution of the GAM's frequency in shot 140437.

damping rate, the mode is strongly damped in the core. Collisional damping may come into play near the last closed flux surface.

Figure 4.15 shows ensemble averaged auto-spectra of the DBS phase at several locations from shot 142121, normalized to the amplitude at the GAM frequency. As discussed in more detail below, the observation that the same frequency occurs at several radii is consistent with descriptions of the GAM as a radial eigenmode. The long period of steady-state, sawtooth free plasma in shot 142121 allows the intrinsic width of the GAM spectra to be observed. Figure 4.15 shows that the spectra are quite narrow, consistent with the expectation of weak damping. The full-width at half-maximum of the peaks are $\sim 200 - 300$ Hz resulting in $\Delta f/f \sim 1 - 2$ %. If one assumes a damped exponential in time as the functional form determining the spectra, this puts an upper bound on the damping rate for the GAM in this case: $\gamma_{GAM} \lesssim 100 - 150$ Hz. There are additional factors that may account for a portion of the spectral width, such as temperature fluctuations—in similar conditions in DIII-D, electron temperature fluctuations have been measured to be ~ 1.5 % [110], which alone could account for a significant portion of the spectral width due to the GAM frequency dependence on the sound speed.

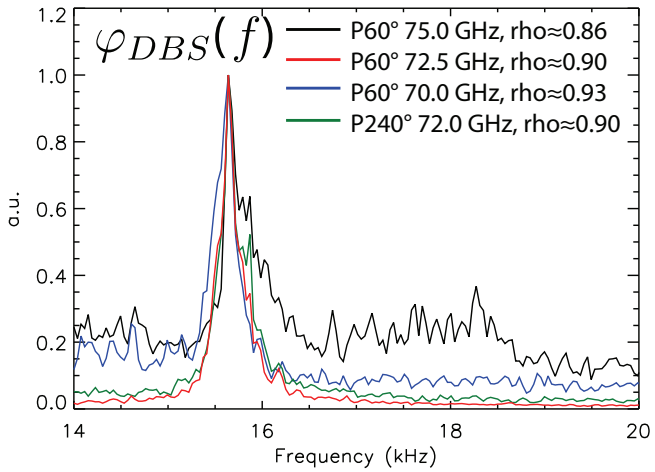

Figure 4.15: Four ensemble averaged DBS phase autospectra, normalized to the amplitude at the GAM frequency, from shot 142121.

A kinetic evaluation of the GAM damping rate for a low flow, circular plasma was con-

ducted in Ref. [119]. The collisionless damping rate found there was

$$\gamma_{GAM} = -i\frac{\sqrt{\pi}}{2}\frac{v_{ti}}{R_0}\frac{(R\omega_{GAM}/v_{ti})^6}{7/4 + T_e/T_i}q^5 exp\left[-\left(\frac{qR_0\omega_{GAM}}{v_{ti}}\right)^2\right], \tag{4.1}$$

where $v_{ti} = \sqrt{T_i/m_i}$ is the ion thermal velocity and $\tau = Z_i T_e/T_i$. The q-dependence arises due to the derivation using $k_\parallel = 1/(qR_0)$ for the parallel wave number. Evaluating Eqn. 4.1 for the conditions of Fig. 4.15 results in a damping rate of ~ 50 Hz. Given the statement in the previous paragraph regarding the potential for temperature fluctuations making a significant contribution to the bound of $\gamma_{GAM} \lesssim 100 - 150$ Hz, we conclude that, quantitatively, observations in the core of L-mode plasmas are not inconsistent with predictions for collisionless damping of the GAM.

4.3.5.2 Discussions of GAM damping near the last closed flux surface

In several experiments and with multiple diagnostics the GAM has been observed to peak in amplitude before the last closed flux surface and decay as the LCFS is approached. The collisionless damping of the GAM would be expected to become weaker and the amplitude of turbulent fluctuations increases towards the edge–from both those factors one would expect the opposite of the observations. As noted in the previous section, collisional damping may be a factor. The collisionlessly undamped zonal flow [65] (*i.e.* the Rosenbluth-Hinton residual flow) is thought to be damped by ion-ion collisions. In fluid plasma simulations, an ion-neutral damping term appears explicitly–along with ion viscosity, it damps zonal flows and affects the non-linear saturated state of the turbulence [235, 236] (separately, it also impacts linear growth rates). In simulations of partially ionized plasmas in the LAPD, zonal flows have been argued to be significantly affected by neutral collisions [237]. Both of these mechanisms can be quantitatively assessed for DIII-D conditions.

The ion-ion collision rate in Ref. [238] is

$$\nu_{ii} = 4.80 \times 10^{-8} Z_i^4 \mu^{-1/2} n_i \ln\Lambda T_i^{-3/2} \text{ Hz}, \tag{4.2}$$

where μ is the ion mass normalized to the mass of a proton and $\ln\Lambda$ is the well known

Coulomb logarithm. Evaluation of Eqn. 4.2 for conditions near $\rho = 1.0$ of a typical L-mode DIII-D plasma results in a damping rate of $\sim$ 2 kHz. This number is higher than the collisionless damping rate, but still only about 1/10 of the GAM frequency–notably, it is similar to the autocorrelation time of the GAM.

Estimation of the neutral damping rate for ions is slightly more involved. An important factor is that the neutral gas, which is the primary particle source at the edge, is not molecular deuterium when it is ionized. Pathways from molecular deuterium to ionization involve several collisions; for an overview of these processes see Ref. [239]. For instance, a relatively high likelihood pathway first involves a collision of an electron with D_2 that excites the D_2 into a higher vibrational energy level. The higher vibrational energy level significantly increases the collisional cross-section for another electron collision, which can elevate the D_2 to a metastable or repulsive state that results in dissociation. The products of the dissociated deuterium typically have energies ranging from ~ 0.3 eV to ~ 3 eV, with an average of $\sim$ 1eV. This energy is often referred to as the Franck-Condon energy due to the use of the Franck-Condon principle (separation of electronic and nuclear coordinates) to calculate changes to energy levels and cross-sections in elevated vibrational states.

For the energy range of interest, the Maxwellian averaged electron-neutral collision cross-section is about $\langle \sigma v \rangle \sim 10^{-8}$ cm^3/s. The neutral collision frequency is $\nu_{0e} = n_e \langle \sigma v \rangle$, which for the $n_e \approx 10^{13}$ cm^{-3} typical for L-mode DIII-D plasmas near the LCFS yields $\sim 10^5$ Hz–about five or six times the typical GAM frequency, which should be more than sufficient to damp the mode.

The mean free path of a neutral with velocity v_0 into a plasma is

$$\lambda_{mfp} = \frac{v_0}{n_e \langle \sigma v \rangle}. \tag{4.3}$$

For room temperature, $T \approx 0.025$ eV, $\lambda_{mfp} \approx 1$ cm, which could not explain the reduction in GAM damping starting at $\rho \approx 0.95$, which is a few centimeters into the plasma. Using the Franck-Condon energy of about 1 eV yields $\lambda_{mfp} \approx 7$ cm; however, that does not account for the increasing plasma density and should be considered an overestimate. Between the

evaluations of the neutral collision frequency and estimates of λ_{mfp} it can be concluded that damping due to neutral collisions is a plausible cause for the damping of the GAM in the region $0.95 \lesssim \rho < 1.0$.

The ionizing collisions with electrons result in ions with negligible momentum compared to the thermal plasma, which effectively constitutes a drag force. Another potential mechanism would be non-ionizing collisions between the thermal ions and neutrals.

4.3.6 GAM magnitude and $E \times B$ shear

One of the physical mechanisms that is invoked to explain the nonlinear interaction of the GAM with turbulence is $E \times B$ shear suppression [63]: the turbulence transfers energy to the GAM through three-wave interactions and the mode can grow sufficiently large for the $E \times B$ shear associated with the GAM to quench the growth of the unstable turbulent modes, saturating the turbulence.

The $E \times B$ shear associated with the GAM only can be separated from the equilibrium $E \times B$ shear by calculating the RMS velocity of the GAM, combined with knowledge of the radial wave number of the mode; an additional requirement for experimental extraction of the radial wave number is that the measurement is in a region where the GAM propagates (*i.e.* not in the Airy lobe of the radial eigenfunction). Figure 4.16 compares (a) the bandpass filtered (10-25 kHz) DBS phase derivative versus the same signal with a wider filter (10-100 kHz) and (b) the DBS derivative phase versus the Quadrature-FFT approach, both bandpass filtered (10-25 kHz). Comparison of the two methods gives some insight into uncertainties associated with the analysis. From Fig. 4.16(b) one can see that both approaches yield very similar results once higher frequency components (both real, from turbulence in the plasma, and artificial, introduced by the numerical derivative) are filtered out, although the DBS phase derivative resolves peaks with better granularity. In the filtered frequency range the GAM is dominant (similar to Fig. 4.15), which is the oscillation in the plots. One notable attribute is that the GAM's amplitude is not very constant in time; this intermittency is

quantified in Sec. 4.4. Figure 4.17 shows the RMS velocity of the GAM at each of the DBS measurement locations from shots 141958 and 142121 where the GAM is observable in the auto-spectrum, using both techniques. Generally, when there is a high signal to noise ratio, the two approaches are in good agreement, while for the cases where the GAM is on the same order as the turbulence or noise spectrum, the two calculations yield different results. In general, the DBS phase derivative calculation allows the full time resolution of the diagnostic to be used (200 ns here), but it is less robust to interference from turbulence and/or noise than the Quadrature-FFT approach. Note that the lower amplitude pair of points in Fig. 4.17(a) at $\rho \approx 0.85$ appears to be due to a low signal to noise level on that channel and is likely not physical, even though calculations using the same data presented elsewhere in this article appear robust to the same effects. The discrepancy between the points at the innermost radius in Fig. 4.17(a) has no clear explanation. The drop in magnitude in Fig. 4.17(b) at $\rho \approx 0.9$ appears to be real and to coincide with an increase in the magnitude of low frequency flow fluctuations, similar to Ref. [240]. Interestingly, the low frequency contribution appears absent in the spectra corresponding to the innermost point of Fig. 4.17(b), instead it is a case with two GAMs (two regions over which the GAM has a constant frequency can overlap, which has been previously observed [125]). This observation implies, at the very least, that there is not always a monotonic change in regime from GAM dominated at the edge to zonal flow dominated turbulence in the core. The largest systematic error likely arises from the influence of the uncertainty in the density profile and equilibrium on the scattering wave number; this can be estimated by calculating the scattering wave number at several times within the averaging window, the resulting variation is $\sim 10\%$. Rather than calculating statistical errors, the underlying distribution can be determined from the data. This is a more informative approach, since, as will be shown in the discussion of the probability distribution function of the GAM flow velocity, the distributions vary somewhere between Gaussian and sinusoidal. It is noteworthy that even though it will be shown below that the autocorrelation time varies by a factor of three to four between the two cases, the amplitude of the GAM is similar.

For these L-mode DIII-D discharges with $\sim 2.5-4.5$ MW auxiliary heating, the measured amplitude of the GAM $E \times B$ velocity is typically $v_{RMS,GAM} \approx 1$ km/s or less and the typical radial wave number is $k_r \approx 1-2$ cm^{-1}. This gives a typical local RMS $E \times B$ shear rate due to the GAM on the outboard of the tokamak as $\gamma_{E\times B,GAM} = k_r \sqrt{\langle v^2_{E\times B,GAM} \rangle} \lesssim 1-2\times10^5$ rad/s $\approx 16-32$ kHz. This is on the same order or larger than the equilibrium $E\times B$ shear in L-mode discharges: see for instance Refs. [16, 156]; although, due to its oscillatory nature, the GAM is predicted to be less effective at $E\times B$ shear suppression than equilibrium shear of the same magnitude [241]. This is also a somewhat larger figure for $\gamma_{E\times B,GAM}$ than previously reported on DIII-D [116]. For the magnitude of the GAM, a figure to compare to is the Mach number. The electron temperature over most of the measurement region is $T_e \approx 200-300$ eV. This puts the ion sound speed at $c_s = \sqrt{T_e/m_i} \approx 100$ km/s. Taking the radial electric field of the GAM to be balanced completely by a toroidal plasma flow and the ratio of the poloidal to total magnetic field to be about 1/10, a GAM $E \times B$ velocity of ~ 1 km/s yields a toroidal Mach number of at most ~ 0.1 for the flow associated with the GAM (by similar reasoning, assuming the flow is entirely poloidal yields a poloidal Mach number of at most ~ 0.01). This figure is further reduced if the ion temperature is included in c_s. Similarly, taking $v_{E\times B,GAM} = k_r\phi/B$, where ϕ is the electrostatic potential, yields $\phi_{GAM} \approx 10$ eV resulting in $e\phi_{GAM}/T_e \sim 0.05$. Both the Mach number and potential put the relative amplitude of the GAM at $\lesssim 5-10\%$ in normalized physical units. Although it may be possible for additional nonlinearities−for instance, secondary flow shear driven instabilities−to develop at these amplitudes, these figures are consistent with the picture that the two contributions to the GAM's amplitude are nonlinear interactions with turbulence and linear damping processes.

4.4 Quantification of GAM intermittency

In this section temporal characteristics of the GAM are investigated through calculation of the mode's autocorrelation function, autocorrelation time, and $E \times B$ velocity PDF.

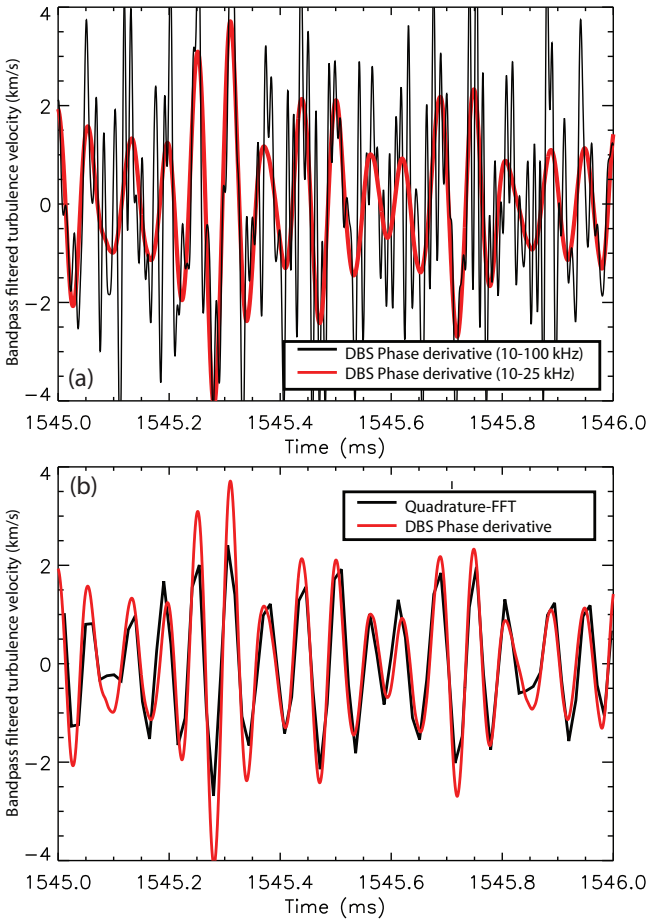

Figure 4.16: (a) Lab frame turbulence velocity obtained from the time derivative of the DBS phase, bandpass filtered 10-100 kHz (black) and 10-25 kHz (red). (b) Lab frame turbulence velocity, bandpass filtered 10-25 kHz, from both the DBS phase derivative (red) and Quadrature-FFT (black) calculations. Data is from P60°, 72.5 GHz channel, shot 142121.

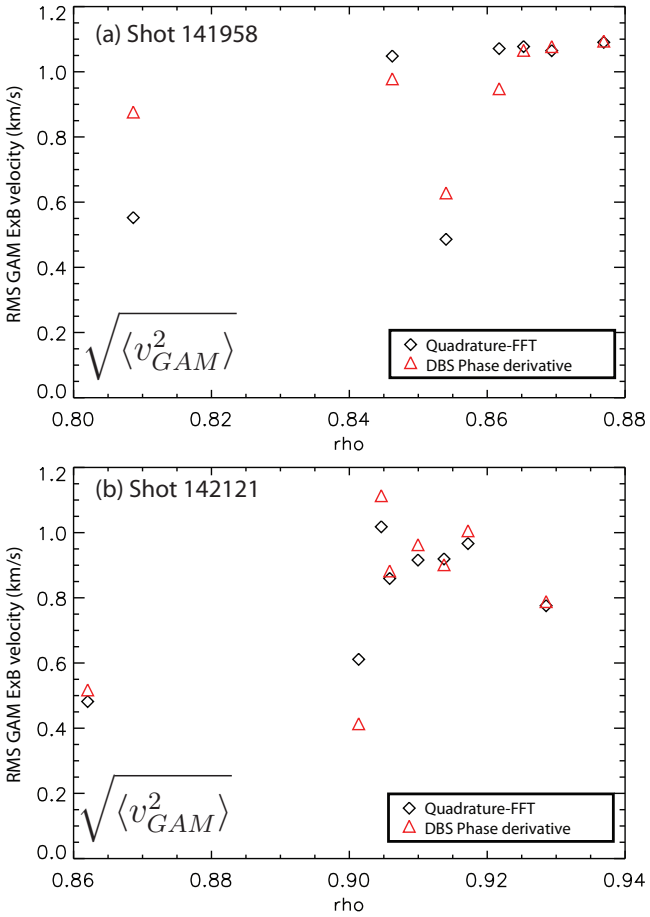

Figure 4.17: Root-mean-square velocity of bandpass filtered ($f_{GAM} \pm 5kHz$) $E \times B$ velocity from DBS in shows (a) 141958 (b)142121. Two approaches to the calculation are plotted: Quadrature-FFT (black diamonds) and DBS phase derivative (red triangles).

It has been observed in previous work that the GAM may have an intermittent character [123, 128, 132]. The intermittency observed in, for instance, Ref. [128] shows a "bursty" behavior, which is different from what is observed here. Here, it is observed that, although the GAM is continuously present (exhibiting neither "bursty" nor limit cycle behavior), it often possesses a relatively short coherence time; that is, the phase of the oscillation is not coherent for long times in comparison to the period of the mode. This can be quantified by a mode specific autocorrelation time, as defined in Appendix A. On first consideration, a short autocorrelation time is not consistent with the narrow spectra observed in Fig. 4.15; since, if the spectral width were due only to damping, then one would expect weak damping to entail a long correlation time, or for a short correlation time to accompany a broad spectrum. Indeed, if the autocorrelation time is estimated from the upper bound for the GAM damping rate arrived at in Sec. 4.3.4, the result is an order of magnitude too large. This can be resolved by considering the presumed drive for the GAM: turbulence. A narrow spectrum and a short autocorrelation time is consistent with a short coherence time for the drive, but weak damping for the GAM itself. This can be thought of as analogous to a simple driven and damped harmonic oscillator, where the driving force is intermittent.

Figure 4.18 shows the autocorrelation function for the lab frame turbulence velocity, computed using the DBS phase derivative, bandpass filtered around the GAM's frequency for DBS channels from shots 141958 and 142121. The autocorrelation is an even function of lag, so only positive values of lag are plotted. Similar to Fig. 4.17, either the Quadrature-FFT or DBS phase derivative methods can be used and yield similar results, only that the latter has significantly better temporal resolution. By definition, the autocorrelation at zero lag is equal to one; also, the autocorrelation near zero lag has contributions from the ambient turbulence, $\mathcal{O}(\tau_{ac,turb}) \sim 10$ μs. Since the oscillations are due to the GAM, fitting to peaks away from zero lag is done, to give the autocorrelation time of the GAM alone, which is what is of interest here, even though the effective autocorrelation at zero lag (A in Fig. 4.18) is not one. One notable aspect of the autocorrelation function is that there is a long tail visible: for long lag times the fall off of the autocorrelation function is slower than exponential for

both the case with short and long autocorrelation time. The short autocorrelation case, Fig. 4.18(a) also shows differences from an exponential falloff. There also appears to be a lower frequency modulation present. Note that since the signal is first bandpass filtered, this might indicate low frequency amplitude modulation of the GAM, similar to Ref. [118].

The presence of the slower than exponential tail and the implications of autocorrelation time compared to the GAM period ($\tau_{ac} f_{GAM}$) can be better quantified by viewing the probability distribution function of the turbulence velocity, bandpass filtered around the GAM frequency($f_{GAM} \pm 5$ kHz). Figure 4.19 shows the probability distribution functions (PDFs) for the GAM $E \times B$ velocity. Both Quadrature-FFT and DBS phase derivative methods are applied. The same calculation applied to frequency bands with only ambient turbulence result in PDFs that are very close to Gaussian, as one would expect. This is different even from the case with a short autocorrelation time, Fig. 4.19(a), where there is a slight flattening of the peak of the distribution as compared to a Gaussian fit. This distribution is a typical result for the PDF of the GAM velocity in cases examined. Figure 4.19(b) is an extreme result for a relatively large amplitude, very coherent GAM; significant departures from a Gaussian are observed in this case, although Gaussian-like tails are retained. The bulk of the distribution begins to resemble the PDF of a sinusoid. Plotted for comparison is the PDF of a Gaussian with the same RMS velocity as calculated for the GAM from the DBS phase derivative. These results show that even for cases when the GAM is continuously present, it has a very intermittent character in terms of its amplitude and phase coherence in time. This may have importance for understanding the nature and importance of the interaction between the GAM and turbulence, particularly if the interaction between the GAM and turbulence changes significantly between period of high and low amplitude GAM. This point will be investigated further in Sec. 4.5.

Figure 4.20 shows the autocorrelation time for the GAM from the DBS arrays in shots 141958 and 142121. Both Quadrature-FFT and DBS phase derivative methods are included for comparison. Generally, for relatively strong, coherent cases both approaches are in relatively good agreement. In cases where there are two GAMs present in the spectrum, or where

the amplitude of the GAM is only marginally larger than the ambient turbulence, it is difficult to justify calculation of an autocorrelation time due solely to the GAM; therefore, some of the higher frequency DBS channels in shot 141958 are omitted. The highest frequency channel in Fig. 4.20(b) has two GAMs in the autospectrum, but one is significantly higher amplitude, by a factor of ~ 2.5, so that point is displayed, although the Quadrature-FFT autocorrelation function envelope bears little resemblance to an exponential, resulting in the difference between the two methods for that radial location. Similarly, for the shorter correlation times in Fig. 4.20(a), the lower time resolution attained with the Quadrature-FFT method leads to erratic results when attempting to fit the GAM envelope in the autocorrelation function. Errors in the fits could be calculated, but are not plotted since there are larger sources of systematic error. First, as mentioned above in the discussion of Fig. 4.18(a), if there is a coherent amplitude modulation of the GAM, an exponential fit may be a poor assumption for the expected functional form of the autocorrelation function. Second, it cannot be guaranteed that there is not a significant contribution from the ambient turbulence within the passband.

There are two relevant points to extract from the plot. First, considering only DBS phase derivative points, the GAM autocorrelation time is quite constant with radius for both cases, which is consistent with the coherency measurements reported in Sec. 4.3.3.3 and the description of the GAM as a radial eigenmode rather than as a continuum of incoherent oscillations. The second is to note the factor of ~ 4 difference in the ratio between the autocorrelation time and the period of the GAM. This difference and the related changes to other statistical measures provide an avenue in future work for assessment of how well simulations reproduce the statistical steady-state of the system.

4.5 Interaction between the GAM and turbulence

In this section, bispectral analysis techniques are applied to investigate the interaction of the GAM with the ambient turbulence. The definitions used for the applied analyses can

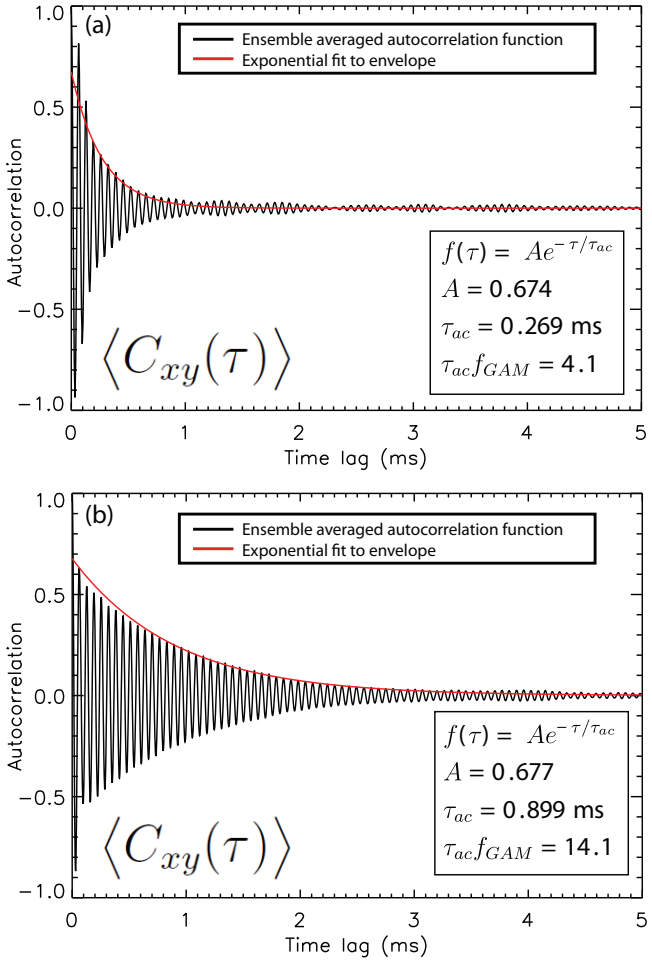

Figure 4.18: Ensemble averaged autocorrelation function of turbulence velocity, bandpass filtered about the GAM frequency ($f_{GAM} \pm 5$ kHz) with exponential envelope fit for (a) P60° 72.5 GHz channel, shot 142121, and (b) P60°, 72.5 GHz, shot 142121.

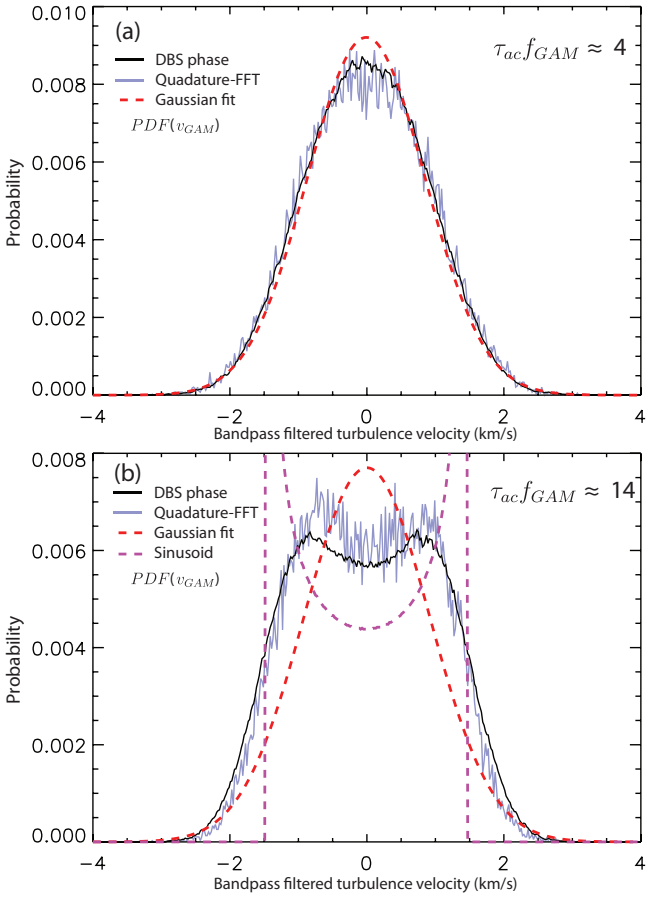

Figure 4.19: Probability distribution function of bandpass filtered ($f_{GAM} \pm 5$ kHz) turbulence flow as measured with (a) P240°, 54.82 GHz, shot 141958 and (b) P60°, 72.5 GHz, shot 142121. The solid black lines show the calculation using the time derivative of the DBS phase, the solid blue lines show the calculation using the Quadrature-FFT method, the dashed red lines are Gaussian fits to the DBS phase curves, and the dashed purple line shows the equivalent distribution for a sinusoid at the GAM frequency with the same RMS velocity as measured by the DBS phase ($v_{GAM,rms} \approx 1.1$ km/s).

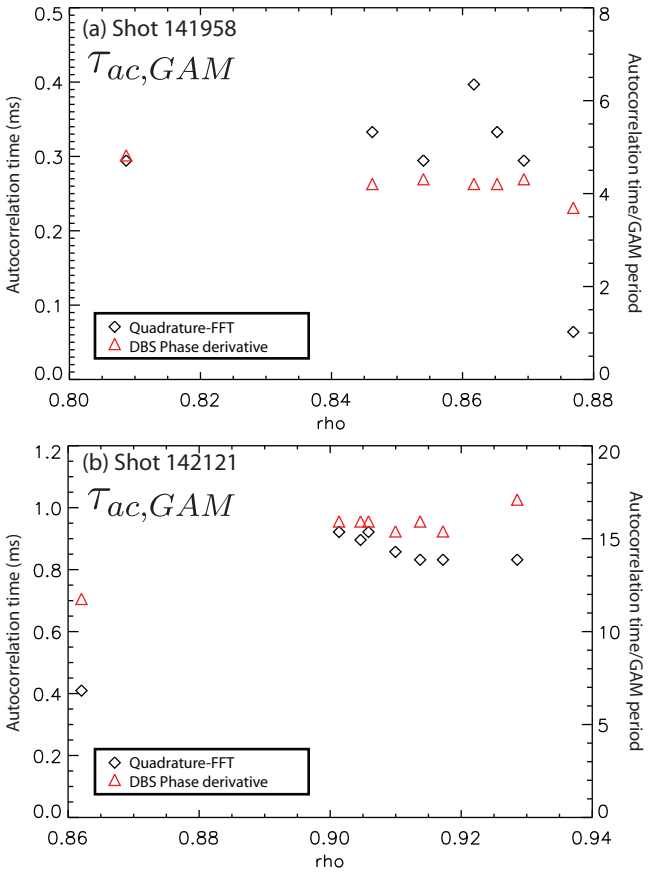

Figure 4.20: Autocorrelation time of the bandpass filtered ($f_{GAM} \pm 5$ kHz) as determined by both quadrature-FFT and DBS phase derivative methods for multiple radial channels in shots (a) 141958 (b)142121.

be found in Appendix A. Bispectral analysis is used to detect the presence of three wave coupling via quadratic nonlinearities. Strictly speaking, the presence of a significant level of auto-bicoherence indicates only the presence of three waves satisfying the relationship $f_1 + f_2 = f_3$ that have a definite phase relationship. Applying cross-bicoherence analysis can give further insight by removing the inherent symmetries of the auto-bicoherence spectrum.

Figure 4.21 compares the auto-bicoherence of the DBS measured turbulence velocity (using the DBS phase derivative method) from the P60°, 72.5 GHz channel from shot 142121 with the cross-bicoherence where f_1 and f_2 belong to P240°, 72.71 GHz and f_3 belongs to P60°, 72.5 GHz. 609 records are ensemble averaged; resulting in, for example, an estimated random error standard deviation of the squared bicoherence for $b^2(f_1, f_2) = 0.040$ of $\sigma_{b^2}(f_1, f_2) \approx 0.016$. Figure 4.21(a) shows a significant level of bicoherence at the GAM frequency, interacting over a broad spectrum with ambient turbulence. Indeed, this feature is retained in the bicoherence spectrum when the analysis is conducted out to higher frequencies than depicted in Fig. 4.21. This is reminiscent of Ref. [144] where it was observed in simulation that the GAM's three wave matching was satisfied by an unstable drift wave, the GAM, and a stable drift wave−not between the GAM and two unstable modes. This is significant because one would expect less spectrally coherent interaction were the latter case to be true due to poorer matching of the three-wave coupling condition. Figure 4.21(b) then shows the cross-bicoherence between toroidally separated DBS systems, demonstrating it is truly an interaction between a mode which is constant on a flux surface, the GAM, and local ambient turbulence. Note that in both Fig. 4.21(a) and (b) there is variation along the lines of significant bicoherence at the frequency of the GAM ($f_1, f_2, f_3 = f_{GAM}$), with the strongest peaks at low frequencies ($< f_{GAM}$). The difference between the plotted auto- and cross-bicoherence spectra can be understood by considering the definition of the bispectrum. There is no bicoherence along $f_1 = f_{GAM}$ or $f_2 = f_{GAM}$ in the cross-bicoherence since the other two waves in those cases belong to the ambient turbulence, each from a different toroidal location (on a different field line), and are therefore incoherent.

Exploring further, Fig. 4.22 shows the summed squared bicoherence for the two cases

displayed in Fig. 4.21, a calculation that compares the interaction at particular values of f_3 relative to other values. The variance of the summed bicoherence can be estimated as the sum of the variances of the summands, assuming the covariance at different frequency matchings can be neglected; for the presented data, this yields $\sigma_{b^2}(f_3) \approx 0.2$. Both summed auto- and cross-bicoherence show significant levels of interaction at the GAM frequency. The outcome of applying the same analysis to data from shot 141958 is not qualitatively different from the pictured results; quantitatively, the bicoherence is smaller.

Leveraging the relatively large data set available, it is possible to employ conditional averaging to further probe the GAM's interaction with turbulence. The condition used to partition the data records is the RMS value of the bandpass filtered ($f_{GAM} \pm 5$ kHz) turbulence velocity (DBS phase derivative method) for each record in the bispectral ensemble average. The cumulative probability distribution function for the condition is calculated for the ensemble, which is then split into three sub-ensembles, containing the top, middle, and bottom third of the distribution, respectively. Figure 4.23(a) shows the application of this partitioning algorithm to the P240°, 72.01 GHz channel from shot 142121. Figure 4.23(b) then shows the summed squared auto-bicoherence for each of the sub-ensembles. There exists a clear relationship between the amplitude of the GAM and the strength of its interaction with the ambient turbulence. The high amplitude ensemble possesses $b^2(f_3 = f_{GAM})$ approximately 70% larger than the low amplitude ensemble, which is larger than the estimated uncertainty of $\sigma_{b^2}(f_3) \approx 0.2$. This is not a general result, partially attributable to the estimated uncertainty of the summed bicoherence. For the examined data from shot 141958, where the GAM is less coherent, the typical result is that all three sub-ensembles are of comparble amplitude, within $\sigma_{b^2}(f_3)$. For other channels from shot 142121, there also exists cases where there is not as large of a difference between the ensembles, or where the two higher amplitude ensembles are comparable, but larger than the low amplitude ensemble. The analysis presented in Fig. 4.23 demonstrates a link between the amplitude of the GAM and its interaction with turbulence, but the lack of generality of the result implies additional complexities are at play; speculatively, the $E \times B$ shear from the GAM could be near a

marginality condition for suppressing a portion of the turbulent spectrum.

An additional calculation that can be done is the cross-bicoherence between the turbulence flow from the DBS phase, $\varphi_{DBS} \propto v_{E\times B}$, and the amplitude of intermediate wave number density fluctuations, as measured by the DBS amplitude, $A_{DBS} \propto \tilde{n}(k_\perp)$. This calculation yields an interesting comparison. Consider Fig. 4.8(b), where the two DBS systems measure different wave numbers at the same radial location. One expects the measured flow due to the GAM to be independent of the probed wave number, so channels can be used interchangeably for that purpose. Figure 4.24 compares the summed squared bicoherence between the 72.5 GHz P60° channel and the 72.01 GHz P240° channel in shot 142121; taking the flow from one channel and the amplitude of intermediate-k density fluctuations from the other, then switching which channel is used for each purpose. Although the probed wave number is not greatly different in the two cases, the summed bicoherence at the GAM frequency is significantly larger than other frequencies for the lower wave number case, while it is not for the higher wave number case. It should be noted that due to the width of the wave number resolution of the diagnostic, Fig. 4.24 does not indicate the GAM ceases to interact with turbulence between 3.8 cm^{-1} and 4.3 cm^{-1}. Using Eqn. 3.7 to approximate the wave number sensitivity of the diagnostic, the low-k side of the $1/e$ dependence $(k_\perp - \Delta k)$ is found to be 2.2 and 2.9 cm^{-1}, respectively−using local parameters, that corresponds to $k_\perp \rho_s \approx 0.54$ and 0.61, while $(k_\perp - \Delta k)\,\rho_s \approx 0.31$ and 0.41. This puts the measured wave numbers towards the upper end of what is typically considered the low-k range for turbulence in tokamaks. Previous work has demonstrated convection of low-k turbulence by the GAM [145] and modulation of low-k turbulence and of the particle flux at the GAM frequency [115, 137]. Taken together, these results indicate that the interaction of the GAM with turbulence takes place over a limited wave number range.

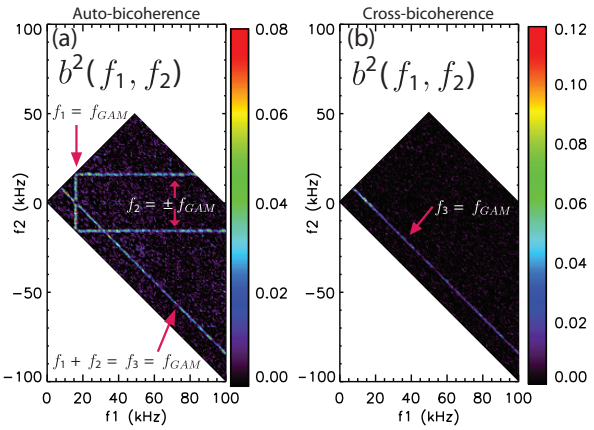

Figure 4.21: Ensemble averaged squared bicoherence of turbulence velocity from time derivative of DBS phase from shot 142121, using 609 records, showing significant bicoherence at the frequency of the GAM. (a) Auto-bicoherence using P60°, 72.5 GHz channel and (b) Cross-bicoherence between P60°, 72.5 GHz (f_3) and P240°, 72.71 GHz (f_1 and f_2). Annotations indicate the vertical and horizontal lines of significant bicoherence at $f_1 = f_{GAM}$ and $f_2 = \pm f_{GAM}$, respectively, as well as the diagonal along which $f_3 = f_{GAM}$.

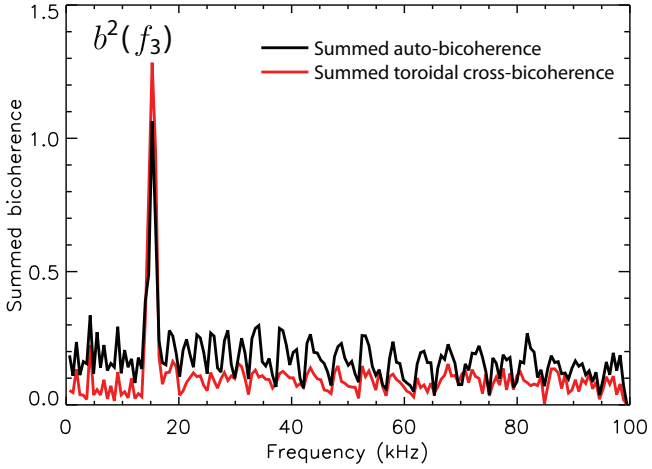

Figure 4.22: Summed auto-bicoherence using P60°, 72.5 GHz channel and summed cross-bicoherence between P60°, 72.5 GHz and P240°, 72.71 GHz, from shot 142121.

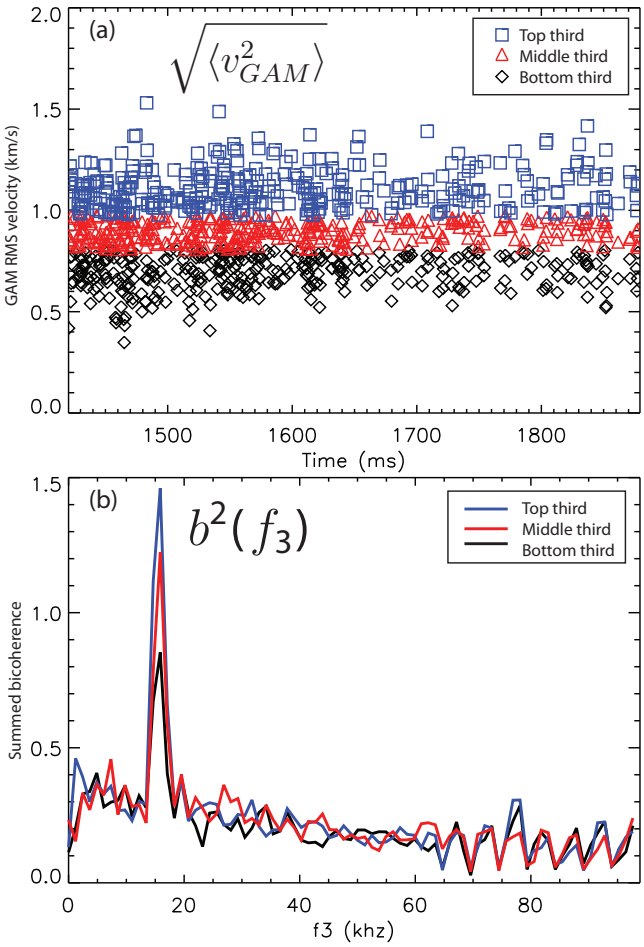

Figure 4.23: Conditionally averaged summed auto-bicoherence using P240°, 72.01 GHz channel, shot 142121. (a) Root mean square bandpass filtered ($f_{GAM} \pm 5$ kHz) velocity (DBS phase derivative method) for each record is used as the averaging condition. 1121 total records are split approximately into thirds, with the top third plotted as blue squares, the middle third as red triangles, and the bottom third as black diamonds. Each record time length is approximately 150 a/c_s. (b) Summed auto-bicoherence ensemble averaged using the three conditions, which the top third plotted in blue, the middle third in red, and the bottom third in black.

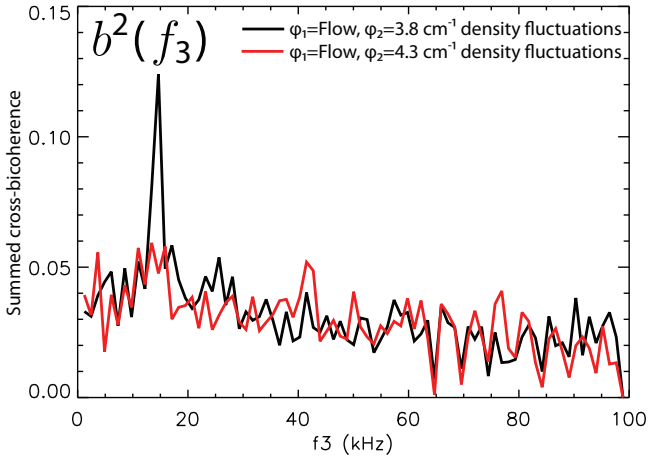

Figure 4.24: Comparison of summed squared cross-bicoherence between the flow and intermediate wave number density fluctuations using P60° 72.5 GHz and P240° 72.01 GHz in shot 142121. The black line uses the P60° channel for the flow and the P240° channel for density fluctuations, vise versa for the red line.

4.6 Characteristics of observed low frequency flows

In addition to the GAM at $\sim$ 20 kHz, additional finite frequency zonal flows are observed at lower frequencies, $\sim$ 500 − 3000 Hz in L-mode plasmas. These low frequency zonal flows (LFZF), like the GAM, occur at well defined frequencies, correlate toroidally, and possess long auto-correlation times. These are neither of the two widely investigated types of zonal flows: the GAM [112] and the Rosenbluth-Hinton residual flow [65]. In this section, characteristics and dependencies of measured flows are investigated. Note that the often invoked Rosenbluth-Hinton residual flow is zero frequency, and therefore difficult to separate from the equilibrium in experiment.

Figure 4.25 displays an overview of commonly observed low frequency flows in L-mode DIII-D plasmas. Figure 4.25(a) is a contour plot of the measured flow velocity versus frequency and minor radius from shot 142361, averaged over 2000-3000 ms from DBS-8. This data is from the High T_e/T_i condition of Ref. [19]. Visible in the plot are a "staircase" of GAMs: two overlapping eigenmode GAMS, as well as the GAM 2^{nd} harmonic at significant

amplitude, shown in Fig. 4.25(b). The peak peak amplitude of the GAM 2^{nd} harmonic occurs at a larger radii than the fundamental; this could be due to weaker collisional damping of the higher frequency mode. Note that due to averaging over the temperature perturbations from sawteeth, the apparent spectral width of the GAMs are broadened. At inner radii, $\rho \lesssim 0.6$, the GAM is not observed; instead, finite frequency flows at $\lesssim 3$ kHz are observed.

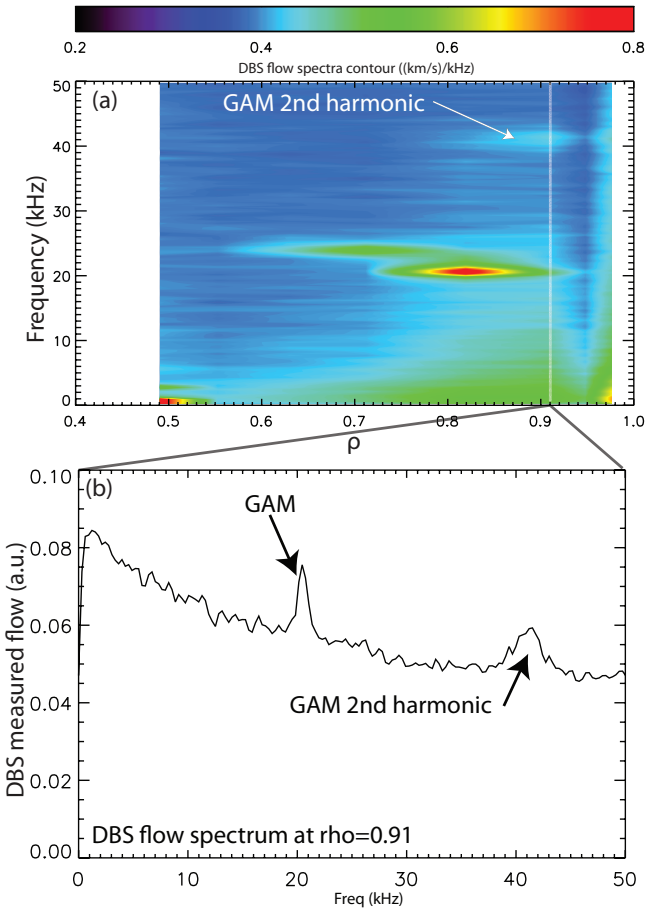

Figure 4.25: (a) DBS flow contour plot from shot 142361, averaged 2000-3000 ms. (b) DBS flow spectrum from one channel showing both the GAM and its 2^{nd} harmonic.

Figure 4.26 shows the coherency and crossphase between the flow from the innermost DBS channel in Fig. 4.25 and the flow from another DBS channel separated by 180°, but at close to the same radius, $\rho \approx 0.5$. Similar to the GAM, these low frequency flows exhibit very high toroidal coherency and are nearly in phase, consistent with a n=0, m=0 potential.

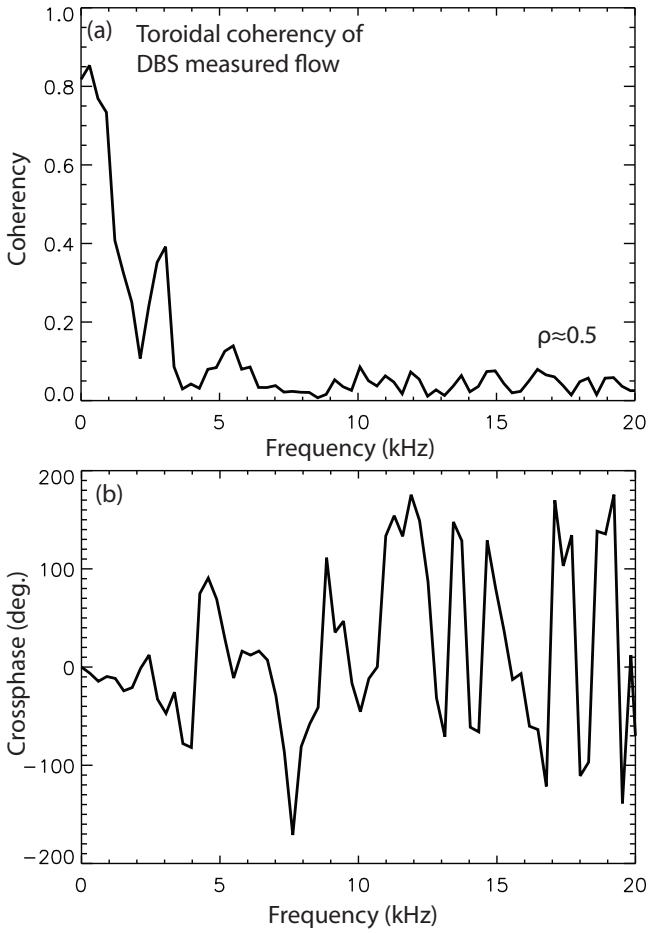

Figure 4.26: (a) Coherency and (b) crossphase between flow from DBS channels separated by 180° toroidally, both close to $\rho = 0.5$.

To complete this brief overview of flows in L-mode DIII-D plasmas, Fig. 4.27 shows a flow contour from another period of a shot from the experiment described in Ref. [19]; here, an ECH-heated L-mode plasma (no NBI heating during the averaged period). As opposed to the typically observed eigenmode GAM behavior, the plotted data shows behavior consistent with the continuum GAM, where the frequency varies with radius. Also visible, $0.7 < \rho < 0.8$, is a second GAM. In absolute terms, the GAM is much weaker in this shot, about half the amplitude of most shots analyzed in this thesis containing the eigenmode GAM. The distribution of the GAM frequency versus radius for the outer GAM in Fig. 4.27 is has qualitative similarites to Fig. 3(b) of Ref. [242], where in fluid simulations (which lack the kinetic effects that are necessary for the eigenmode GAM) GAM oscillations are observed at and above the local linear GAM frequency across the simulation radii. A consistent interpretation is that the GAM follows the fluid prediction of a continuum of frequencies, but still propagates radially outward.

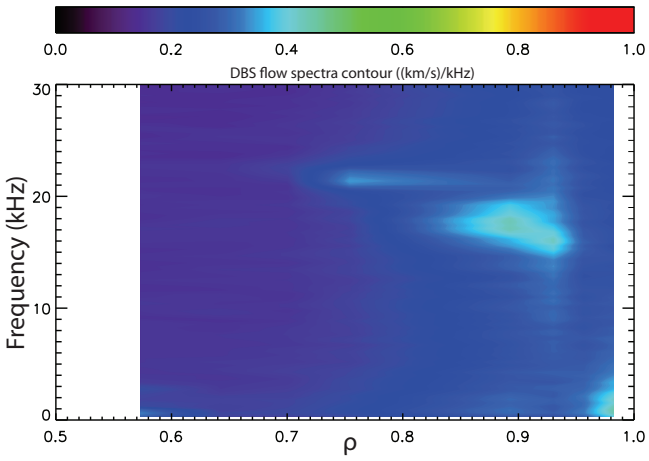

Figure 4.27: Flow contour from shot 142364, averaged 3100-4000 ms.

4.6.1 Dependence of low frequency flows on T_e/T_i

In this section and the next, dependencies of low frequency flows are demonstrated.

Figure 4.28 shows low frequency flow spectra contours from both the Low and High

T_e/T_i conditions of Ref. [19]. Notably, the GAMs are stronger in High T_e/T_i, but the broad spectral feature, $f < 15$ kHz, that is visible in the Low T_e/T_i condition is no longer present. Measured density profiles and EFITs are used for ray tracing to determined the scattering wave number and location for the DBS-8 channels. This information is used with $\partial\varphi_{DBS}/\partial t$ spectrum to produce the contour plots. Interpolation is performed radially between the 8 channels.

Theoretical comparison for these observations likely require global gyrokinetic simulations, which may occur in the future.

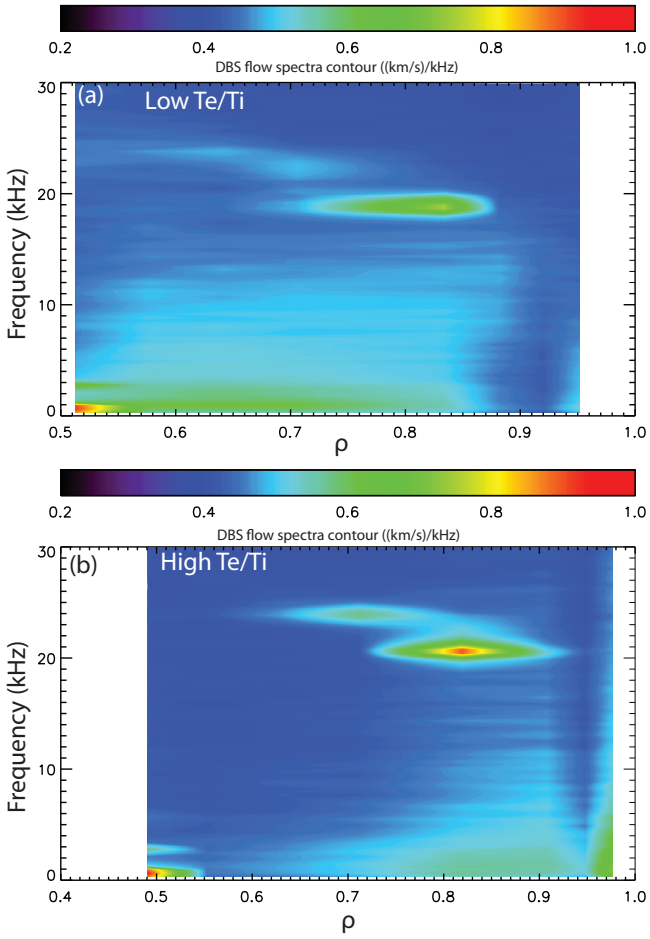

Figure 4.28: Averaged flow contours at (a) Low T_e/T_i and (b) High T_e/T_i conditions.

4.6.2 Dependence of the GAM and LFZF on rotation and Z_{eff}

The physics investigated in this section concerns the GAM and LFZF and belongs to this Chapter; however, the experiment the data comes from is studied in much more detail in Chapter 5–see there for detailed information alluded to in this section.

Figure 4.29 displays data from the experiment described in detail in Sec. 5.3. In particular, Fig. 4.29(a) shows a discharge with ECH and co-injected beams and Fig. 4.29(b) shows an otherwise nearly-matched discharge with counter-injected beams. Both shots have ECH arrangement (5, 0.5) (see Sec. 5.3 for explanation). While the former shows GAMs and LFZF similar to other shots in this chapter, in the latter, the amplitude of all low frequency flows is significantly smaller–they are almost completely gone.

The two major differences between the shots in Fig. 4.29 are the rotation and effective ionic charge, Z_{eff}. Z_{eff} is systematically higher in counter-injected plasmas. Possible explanations for the difference in Z_{eff} include the intuitive transport explanation, the electric field points inward in counter-injected discharges, which could have a large effect on high Z impurities. A second, source explanation, is the impact of the larger portion of direct loss orbits from counter beams (the initial gyro-motion of ions born from counter-beams is outward, for co-beam ions it is inward) results in sputtering from fast ions hitting the carbon tile walls.

While the reasons for a rotation dependence are not clear, a possible reason for a Z_{eff} dependence can be assessed. Ion-ion collisions are thought to be involved in zonal flow damping. The ratio between ion-ion and electron-ion collisions for heavy impurities, neglecting collisions with lighter ion species, can be expressed as

$$\frac{\nu_{ii}}{\nu_{ei}} = \frac{n_i Z_i^4}{n_e} \left(\frac{m_e}{m_i}\right)^{1/2} \left(\frac{T_e}{T_i}\right)^{3/2} . \tag{4.4}$$

In the counter-injection plasmas in question, the primary impurity is carbon ($\sqrt{m_e/m_i} \approx 150$) and $Z_{eff} \approx 3$, or $n_i/n_e \approx 0.5$. Assuming equal temperatures, this results in $\nu_{ii}/\nu_{ei} \sim 0.4$: the impurity-impurity collision rate approaches that of electron-ion collisions. Additionally, under these parameters, the carbon species accounts for $\sim 1/3$ of the mass density of the

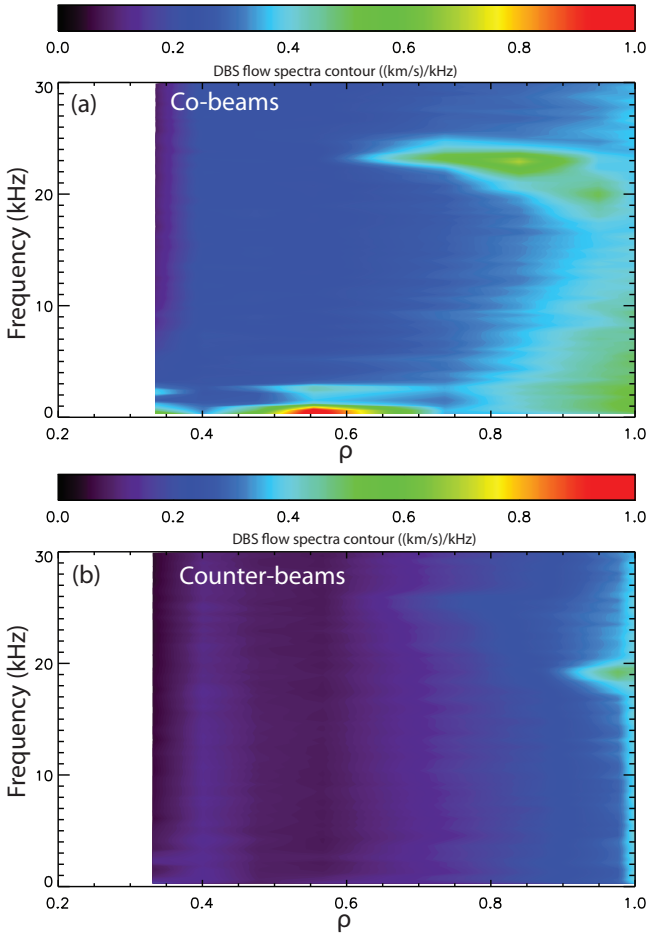

Figure 4.29: Averaged flow contours with (a) beams co-injected with plasma current and (b) counter-injected to the plasma current.

plasma. A hypothesis suggested by these observations is that the difference in Fig. 4.29 can be accounted for by ion-ion collisional quenching of the zonal flows.

The collisional zonal flow quenching hypothesis can be assessed by comparing otherwise similar discharges where Z_{eff} differs. Such circumstances serendipitously occurred in the same experiment as the shots in Fig. 4.29. Figure 4.30 compares the closest one-to-one comparison found in the data set in Chapter 5. The panels show the frequency spectrum of the low frequency flows as a function of minor radius. Both contours were ensemble averaged over ECH+Co-NBI periods with ECH arrangement (1, 4.5) in different shots. The time period in Fig. 4.30(a) followed an ECH-only period and the shot had no period with only counter beams. The time period in Fig. 4.30(b) followed a time period with only counter beams, which raised Z_{eff}. To put both plots on the same scale, the contours above 1.0 (km/s)/kHz are truncated. The difference is not as striking as Fig. 4.29; here, there is a slight, $\sim 20\%$ reduction in the amplitude of the GAM. There is also a shift of the broadband feature near the last closed flux surface at higher frequencies.

The Z_{eff} comparison in Fig. 4.30 suggests that collisional quenching of the low frequency flows cannot explain the result depicted in Fig. 4.29. The second certain equilibrium difference in Fig. 4.29 is the rotation. The panels in Fig. 4.31 show the intermediate-flow cases, ECH+Bal-NBI and ECH-only. The GAM in Fig. 4.31 is at lower frequency, consistent with the low ion temperature. The amplitude of the flows do appear to be bracketed by the high and low flow cases in Fig. 4.29, consistent with a dependence on rotation.

Another explaination for the difference could be a change in the characteristics of the dominant instability. However, it was noted about that both cases in Fig. 4.29 have ECH arrangement (5, 0.5). It will be argued in Chapter 5 that in both of these cases the dominant instability is ∇T_e-driven TEM.

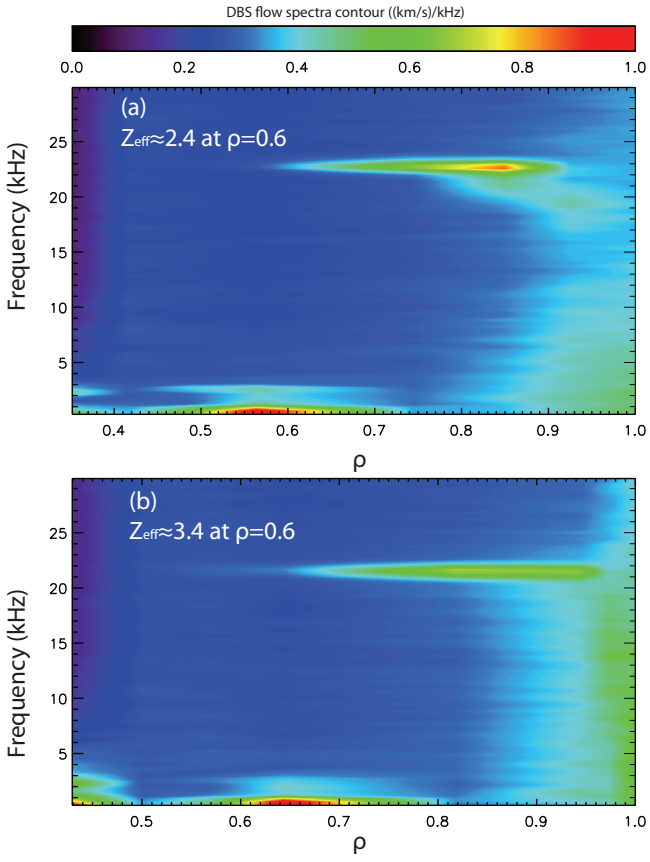

Figure 4.30: Averaged flow contours with beams co-injected with plasma current: (a) Lower Z_{eff} and (b) Higher Z_{eff}

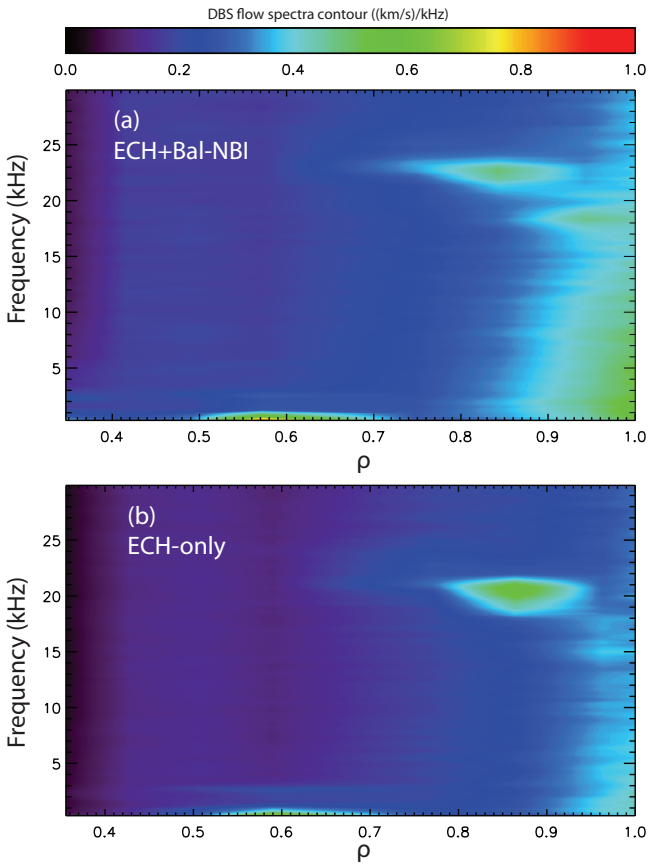

Figure 4.31: Averaged flow contours with (a) ECH+Bal-NBI and (b) ECH-only. Both cases have ECH arrangement (5, 0.5) and $Z_{eff} \approx 2.5$

4.6.3 Discussion of the LFZF

The low, finite frequency flows have no clear theoretical description in the literature. One candidate is what are briefly mentioned in Ref. [113] and termed therein "magnetic drift modes." They are described there as a modification to the GAM by the guiding center magnetic drift velocity (sum of ∇B and curvature drifts); qualitatively, the magnetic drift velocity can reinforce the m=1 density component of the GAM. This results in a mode with a larger proportion of its average energy in its pressure component than in its kinetic energy, compared to the standard GAM. It also has a lower frequency than the GAM.

Speculatively, another possibility is that they are not truly linear eigenmodes of the system, but are instead a non-linear limit cycle oscillation of the Rosenbluth-Hinton residual flow. Limit cycle oscillations zonal flow have been observed to play a role in slow L-H transitions [21] and have been observed in nonlinear plasma fluid simulations [235].

Further investigation is deferred to future work.

4.7 Conclusions

The results presented in this chapter show that the GAM interacts with turbulence in the outer core and edge region of the DIII-D tokamak ($r/a \gtrsim 0.75$) in L-mode plasmas, and, furthermore, that the characteristic spatial and temporal scales associated with the GAM can be significantly larger and longer than that of the ambient turbulence that drives both the GAM and transport of particles, momentum, and heat. In this section, these observations are discussed as they relate to the assumptions that underly turbulence models, and the relevance and generality of specific results are also summarized. Observations of the LFZFs, related work, and future directions are included.

It was shown in Sec. 4.3.3.3 that the GAM's radial correlation length can be $30\rho_s$ or greater, a factor of at least three to five larger than is typically ascribed to the radial correlation length of turbulence. Additionally, the GAM in the L-mode discharges examined

has a constant frequency with radius, not one that varies as the local temperature. This is an attribute consistent with descriptions of GAM eigenmodes when finite $k_r\rho_i$ effects are included. The form of the GAM eigenmode depends on the radial profiles of equilibrium quantities [119], and is therefore a nonlocal phenomenon. For situations where the GAM functions as an important nonlinear saturation mechanism for the drift wave turbulence and resides in the eigenmode GAM regime, simulations functioning in the local limit ($\rho^* \to 0$) may not accurately capture the dynamics of the GAM and its nonlinear interactions. It may also be necessary to examine the boundary conditions of global simulations and whether they have an effect on the GAM eigenmode. In addition to the difference in how frequency varies with radius, Fig. 4.14 also shows a qualitative difference in the spectra: the continuum GAM has a significantly broader spectrum than the eigenmode GAM. At this point, it is not clear in what other ways the regimes differ.

The autocorrelation time of the GAM is also found to be significantly longer than the ambient turbulence, $\sim 300 - 900$ μs for the former versus ~ 10 μs for the latter; however, the amplitude of the GAM is found to be quite intermittent in time. The range of autocorrelation times presented here, about 4 to 15 GAM periods, appears to be representative of L-mode conditions; other DIII-D plasmas examined fall within this range. Figures 4.19 and 4.23 show that the amplitude of the GAM can vary significantly in time, and that the interaction between the GAM and turbulence depends on the GAM amplitude. This points to an important comparison for future work: how well are variations within the steady-state reproduced in simulations? Given that each record in Fig. 4.23 is ~ 150 a/c_s, simulations may need to be run longer than is typically done to fully capture these dynamics. It was also shown that the interaction of the GAM and turbulence can depend on the wave number of the turbulence; a more complete set of measurements would allow a spectrally resolved comparison of the interaction between experiment and simulation.

In light of recent work questioning the physical mechanism for radial propagation of the GAM [143], the toroidal correlation measurements presented in Sec. 4.3.3.2 take on greater relevance. The measurements show, as has been observed in other experiments [15, 115, 136],

outward radial propagation of the GAM. As was also performed in Ref. [15], the toroidal correlation separates poloidally localized turbulence from oscillations that are constant on a flux surface. The experimental results showing high toroidal coherency ($\gamma > 0.8$) accompanied by radial change in crossphase are consistent with radial propagation of a mode that is constant on the entire flux surface−the GAM−not with radial migration of poloidally localized zonal jets that create illusory propagation of the GAM as described in Ref. [143]. Poloidally localized jets would be expected to follow magnetic field lines, and should therefore not correlate, which is in contradiction with measurements. The radial propagation of the GAM can be understood from the standpoint of the Airy function description of its eigenmode [119, 138–140]. An Airy function, $Ai(-x)$, describes a standing wave pattern for $x > 0$, created by interference between an incoming and outgoing wave, which reflects near $x = 0$. In other contexts where an Airy function solution arises, such as the 1-D description of O-mode reflectometry or the solution of the Schroedinger equation for a potential of constant slope, the source of the wave is at some distant location. The source is local for the GAM, spread out within the region of interest. Following this interpretation, once energy has been transfered to the GAM it either travels inward and reflects, or travels outward until the mode is collisionally damped or reaches the last closed flux surface and can no longer be supported. The nature of the source ensures net outward radial propagation for typical conditions (*i.e.* not in a regime where the propagation side of the Airy function is inward radially), although additional factors likely necessary for a complete description.

In addition to the above comments, several more specific experimental observations−all pertaining to the GAM in the regime where $k\rho_i$ effects are significant−are worth noting:

- In Sec. 4.3.5.1, a long steady-state, sawtooth free period was leveraged to experimentally put an upper bound on the GAM damping rate in those conditions. The bound found was $\gamma_{GAM} \lesssim 100-150$ Hz. This figure is not inconsistent with the expected weak damping of the GAM, which evaluates to ~ 50 Hz for the measurement conditions, since temperature fluctuations may contribute to the spectral width and the actual damping rate may be smaller than the determined bound.

• The spatial variation of the amplitude of the GAM RMS $E \times B$ velocity and its associated shear was investigated in Sec. 4.3.6. In L-mode conditions in DIII-D, the RMS value of $v_{E\times B,GAM}$ generally appears to be about 1 km/s or less and k_r is typically $1 - 2$ cm$^{-1} \approx 0.1 - 0.2\ k_r\rho_s$; the resulting shearing rate is $\lesssim 100 - 200$ krad/s.

• The autocorrelation function and probability distribution function of the GAM $E\times B$ flow were studied in Sec. 4.4. In both long and short autocorrelation time cases, the autocorrelation function shows deviations from an exponential fall-off: both show evidence of a long tail and the short $\tau_{ac,GAM}$ case shows low frequency modulation of the GAM. The long tail appears to be a typical characteristic for the GAM and is consistent with the weak collisionless damping. The two $\tau_{ac,GAM}$ cases show markedly different behavior in the PDF of the GAM $E \times B$ flow, with the long $\tau_{ac,GAM}$ approaching a sinusoidal PDF.

• It was shown in Sec. 4.5 that there is significant bicoherence between the GAM and ambient turbulence and that it persists even in the cross-bicoherence between the toroidally displaced DBS systems. The bispectral analysis also showed that the strength of the nonlinear interaction varies with the amplitude of the GAM and that there is a wave number dependence to the interaction.

The issues pointed out above motivate an important issue for future work; namely, direct, quantitative comparison of the nonlinear interactions of GAMs, and more generally zonal flows, with turbulence between simulation and experiment, as well as comparison of the statistical steady-state and other characteristics of the nonlinear saturated state such as correlation lengths, autocorrelation functions, and spectra shapes. Additional avenues for future work include the interplay between the various damping mechanisms for the GAM near the last closed flux surface, and interaction between the GAM and zonal flows.

Section 4.6 presented observations of observed low frequency zonal flows in L-mode plasma. Both the GAM and LFZF were observed to be almost completely suppressed in counter-injected plasmas. Comparing similar discharges in an experiment showed that the

suppression could not be explained by a change in the dominant instability and could only partially be explained by increased impurity ion-ion collisions due to higher Z_{eff} in counter-injected plasmas. By elimination, it is the rotation itself that appears to be important. This result motivates investigations of the Mach number dependence of the GAM.

Similar analyses to those in this chapter were also used to investigate the role of zonal flows during low L-H transitions in DIII-D [21]; there is was found that the plasma edge first transitions out of L-mode into a limit cycle phase. During that phase the ion pressure gradient increases, with the radial electric field shear from the ion pressure gradient eventually overtaking the zonal flow shear, whereupon the plasma transitions fully to H-mode. Unlike Ref. [121], where the GAM was observed to play a role, in DIII-D the GAM disappears during the limit cycle phase. Reasons for this difference remain unanswered. Also, although it is shown in Ref. [21] that the transition from L-mode to the limit cycle phase correlates with a decrease in the autocorrelation time of the turbulence, the causal relationship in not clear. For instance, it could be that the GAM ceases to be supported by the plasma and is replaced by the lower frequency zonal flows, which more effectively suppress the turbulence, causing the transition from L-mode to the limit cycle phase. Several experiments have investigated the role of zonal flows during the L-H transition [21, 121, 243–246]. Further theoretical work is needed for comparisons to the experimental results and for predictions for future experiments, like ITER.

CHAPTER 5

Study of fluctuations in multiple fields with systematic variation of a/L_{T_e} and rotation

5.1 Introduction

An extensive set of local turbulence measurements were acquired during an experiment where the inverse electron temperature scale length, $L_{T_e}^{-1} = -\nabla T_e/T_e$, and toroidal rotation were systematically varied in steady-state L-mode DIII-D plasmas. A key new result is the observation of a critical gradient threshold for electron temperature fluctuations: below a critical value they do not change within uncertainties and above they rapidly increase. A critical value was also determined for the electron thermal diffusivity, which is in quantitative agreement with the threshold value for electron temperature fluctuations. Above this threshold, the electron heat flux and stiffness (which parameterizes the incremental increase in flux for an incremental increase in gradient) increase–the clear inference being that the electron temperature fluctuations play a direct, causal role for the increased transport and stiffness. Although the increased temperature fluctuations are concluded to play at least a partial role for the increased transport, other mechanisms are discussed that could also contribute. These measurements also provide the first direct, systematic evidence for critical gradient behavior–and therefore for linear instability of gyroradius-scale turbulence–in the core of a tokamak.

Furthermore, both measurements of the electron temperature fluctuations and the mean gyrofluid growth rate calculations, as determined by the Trapped-Gyro-Landau-Fluid code (TGLF), show threshold behavior at $\eta_e = L_{n_e}/L_{T_e} \approx 2$. This provides substantiation for the

description of plasma turbulence arising from linearly unstable gyroradius scale modes. A wide variety of measurements will be shown to be individually consistent with ∇T_e-driven trapped electron mode turbulence above the threshold, which is also supported by gyrofluid calculations. The totality of the accumulated evidence strongly favors identifying ∇T_e-TEM as the cause of the critical gradient. In contrast to ion stiffness studies [247, 248], the electron temperature fluctuations and transport show little sensitivity to toroidal rotation.

Measurements of the crossphase angle between electron density and temperature fluctuations were also acquired. These measurements are consistent with ∇T_e-TEM above the threshold. Below the threshold, the crossphase measurement imply that different instabilities are dominant, depending on the NBI configuration.

Also presented are measurements of density fluctuations from Beam Emission Spectroscopy (BES) and Doppler Backscattering (DBS), including DBS measurements showing frequency-localized changes to spectra that correlate with $L_{T_e}^{-1}$

This Chapter is organized as follows: Sec. 5.2 describes initial measurements of the crossphase angle between electron density and temperature fluctuations in DIII-D plasmas and includes a brief review of relevant previous work; Sec. 5.3 presents results from the experiment, including description of the experimental approach, of equilibrium profiles, of transport analysis, and of the extensive turbulence measurements; Sec. 5.4 presents results from gyrofluid and gyrokinetic codes and compares the results to experimental measurements; and, Sec. 5.5 concludes the Chapter with a discussion of the results.

5.2 Initial measurements of α_{n_e,T_e} in DIII-D Ohmic and ECH only plasmas

5.2.1 Experimental conditions

The first measurements of the crossphase between electron density and temperature fluctuations at DIII-D were made in 2008, using a coupled CECE-reflectometer diagnostic (Sec. 3.8

contains diagnostic details). Standard statistical analysis procedures are adopted throughout this chapter (see Appendix A). The first implementation of the crossphase measurement [231] used an *ad hoc* definition for the coherency–that alternate approach is applied in Appendix E. Port geometry at the time necessitated the plasma to be vertically displaced to align DBS-5 for reflectometry. This was done with an Ohmic target discharge in the DIII-D tokamak. Electron cyclotron heating power was added to the core of the Ohmic target discharge in three power steps. Fluctuation diagnostics were aimed at a sequence of radii during repeat discharges. Crossphase measurements were acquired at $\rho \approx 0.6$. The dominant effect of the ECH power steps at this radial location was to increase T_e/T_i and to decrease the normalized electron collisionality, $\nu_{ei}/(c_s/a)$–these effects would be expected to favor the instability of trapped electron modes. For detailed equilibrium information and further analysis of this experiment, refer to Ref. [17].

Although high quality turbulence measurements were acquired during the experiment, the vertical displacement had a deleterious effect on equilibrium profile measurements. For this reason, quantitative comparisons to nonlinear gyrokinetic simulations were not pursued for this experiment.

5.2.2 Initial α_{n_e,T_e} measurements

A sequence of times with different amounts of ECH power occurred in the same discharge. By applying correlation analysis to a steady-state time period during each ECH power step, a clear trend in the crossphase appears, which is shown in Figure 5.1. The effect of the ECH is to increase both the electron temperature and electron temperature scale length by roughly equivalent amounts, making the scan primarily consist of concurrent changes to the temperature ratio between ions and electrons and to the collisionality when non-dimensional quantities are considered. There are also small changes to the density and density gradient during the scan, the effects of which are not captured in Fig. 5.1.

The results in Fig. 5.1 were published in Hillesheim *et al.* [15], along with the diagnos-

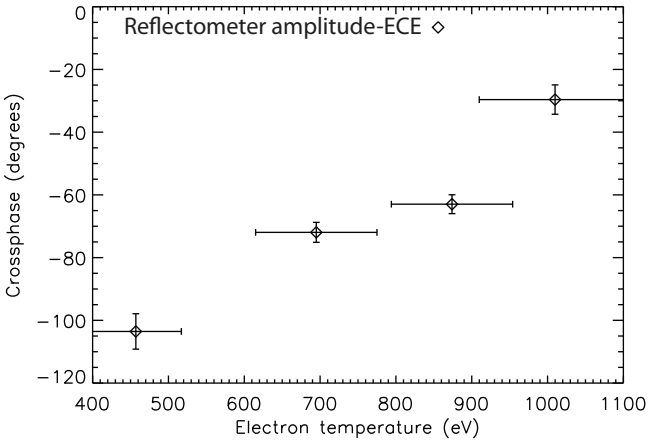

Figure 5.1: The changes to the crossphase between electron density and temperature fluctuations, α_{n_e,T_e}, with increasing electron temperature at $\rho \approx 0.6$, calculated with reflectometer amplitude correlated with an ECE channel. The frequency at which the maximum coherency occurs for each pair is used to calculate the crossphase and error bars.

tic development results presented in Sec. 3.8.2. The same results, along with additional turbulence measurements were investigated in more detail in Wang et al. [17].

5.2.3 Relevant previous work performed in the DIII-D tokamak

The experimental results in Sec. 5.3 build upon a series of transport model validation experiments performed in the DIII-D tokamak. Portions of three of these experiments are particularly relevant and are briefly discussed here. The first two relate to measurements of the crossphase between electron density and temperature fluctuations. The third relates to investigation of instabilities and transport driven by the electron temperature gradient.

The first publication of nT crossphase, α_{n_e,T_e}, results from DIII-D was White *et al.* [16]. Presented therein were α_{n_e,T_e} measurements at three radial locations in L-mode plasmas with co-injected NBI heating only and in plasmas with NBI and core ECH heating. In terms of dimensionless parameters, the ECH significantly increased T_e/T_i and decreased the normalized collisionality, $\nu_{ei}/(c_s/a)$. At all three radial locations for the NBI-only case α_{n_e,T_e} was measured to be in the range $\sim -130°$ to $-100°$. At all three locations α_{n_e,T_e} became less

negative with the added ECH, measured to be in the range $\sim -90°$ to $-60°$. Additionally, the electron temperature fluctuation level increased while long wavelength density fluctuations measured with BES did not change within uncertainties. These changes were attributed to a change in the dominant instability from ITG to TEM. The measured α_{n_e,T_e} frequency spectrum was directly compared to the output from the nonlinear gyrokinetic code GYRO using a synthetic diagnostic for one of the cases. Quantitative agreement for the crossphase between the experiment and the synthetic diagnostic were found over the frequency range where significant coherency was experimentally measured.

Another comparison of NBI heated L-mode plasmas with and without core ECH, which resulted in large changes to T_e/T_i and $\nu_{ei}/(c_s/a)$ was reported in Ref. [19]. For two more cases α_{n_e,T_e} measurements were directly compared to synthetic diagnostic results from GYRO; in both good quantitative agreement was found. Additionally, synthetic density and temperature fluctuation spectra were directly compared. In these two previous experiments, it was argued that TEM were destabilized due to the T_e/T_i and $\nu_{ei}/(c_s/a)$ changes, while $L_{T_e}^{-1}$ changed much less. This is in contrast to the experiment investigated in detail in this chapter, where large changes to $L_{T_e}^{-1}$ were made, but T_e/T_i and $\nu_{ei}/(c_s/a)$ locally changed little.

A third directly relevant experiment was described in Ref. [9], which presented the experimental results and initial gyrokinetic simulations. Further simulations are presented in Ref. [10], where the synthetic DBS diagnostic described in Sec. 3.4.3 was employed. The experiment examined L-mode DIII-D plasmas with only off-axis ECH heating. ECH gyrotrons were aimed at two closely spaced radial locations. The gyrotrons aimed at each location were modulated 180° out of phase with a 50% duty cycle with the goal of modulating the electron temperature gradient. A broad set of fluctuation measurements were acquired and presented in Ref. [9]. One conclusion from analysis and simulations of the experiment was that the plasma appeared to be near marginality for ∇T_e-driven trapped electron mode turbulence. However, with only two pairs of values of the inverse gradient scale length to compare, a systematic experiemental investigation was not possible–systematically varying the inverse gradient scale length was motivated by this work and is reported in Sec. 5.3.

As a constraint on the phase relationship between two different fluctuating fields, α_{n_e,T_e} provides a strong challenge to simulations. The quantitative agreement found in Refs. [16, 19] provided ground for further investigation of these measurements; namely, the new results that are presented in Sec. 5.3.

5.2.4 Previous work investigating critical gradients and thermal transport stiffness

A major issue for magnetic confinement fusion devices is the transport of particles, momentum, and heat by gyroradius-scale turbulence in the core of the plasma. This turbulence is widely thought to arise due to linear instabilities; this differs from the (neutral) hydrodynamic view, where turbulence arises while the system is linearly stable. Many of these modes are expected to exhibit a critical gradient threshold in the equilibrium gradient providing free energy for the instability, where the mode is linearly stable below the threshold and unstable above [25]. Indirect evidence supporting the existence of critical gradients has been reported in tokamaks for both electron and ion thermal transport through transport analysis and comparison to model predictions [94, 247, 249–251]. Direct, systematic observation of instability has been related to critical gradient criteria in linear experiments [252–254]; although, no previous work exists in the core of a confined high-temperature plasma. Many experiments in tokamaks have related fluctuation levels monotonically to driving gradients or input power, or investigated transient measurements—see Ref. [27] for a review—but controlled, steady-state observations demonstrating threshold behavior for a gradient in a systematic experiment have proven elusive.

There is a set of tangentially related work (mostly occurring after the publication of Ref. [27]), from NSTX, where investigations of electron temperature gradient (ETG) turbulence were made by examining transient changes in equilibrium plasma parameters. Ref. [96] reported transient changes to small scale ($k_r\rho_i \sim 10$) density fluctuations, which were attributed to ETG mode turbulence through support by linear gyrokinetic calculations. In subsequent works, it was argued that the ETG fluctuations could be suppressed by large $E \times B$

flow shear [97], negative magnetic shear [98], and the electron density gradient [99, 100]. Although the breadth of the work presents compelling evidence, a few *caveats* separate the new results presented in this chapter from this set of results, in terms of being interpreted as direct evidence for linear instability. First the NSTX high-k scattering system [255] is primarily sensitive to the radial wave numbers of fluctuations, k_r. Normally linear calculations are performed for modes with $k_r = 0$ at the outboard midplane and finite k_θ. These radially elongated modes are broken up non-linearly, which is usually attributed to zonal flows–the k_r spectrum should therefore be thought of primarily as a non-linear property of the turbulence. Increases to small scale k_r density fluctuations had been observed on other experiments [256]. Attribution of the turbulence in tokamaks to linear instabilities should focus on measurements sensitive to k_θ, which is the wave number directly related to theoretical predictions. Furthermore, NSTX plasma are constantly evolving and do not reach a steady-state. The NSTX publications referenced all pertain to transient observations, while the new results presented below are from long (500-800 ms) steady-state time periods. The diagnostics used below are also sensitive to the same k_θ values as the instabilities being studied.

A phenomenon related to critical gradients is stiff transport. Qualitatively, stiffness is the incremental change in flux for an incremental change in gradient. A consequence of stiff transport (*i.e.* high stiffness) is little change to equilibrium profiles with additional source input. Since fusion power in a magnetically confined plasma is proportional to pressure squared, the diminishing returns enforced by stiff heat transport could present an issue for the efficiency of future reactors [257]. The observations presented here relate to electron temperature fluctuations and profile stiffness and are relevant to scenarios with strong electron heating, such as would be expected by alpha particles in burning plasmas.

Stiff heat transport has been previously observed for both ions [247] and electrons [94]; however, both of these studies lacked direct measurements of fluctuations. It was observed that stiffness for ion heat transport could be ameliorated with the combination of high toroidal rotation and low magnetic shear [248]. Previous studies of the stiffness of electron

heat transport did not investigate dependence on rotation or flow shear.

5.3 Measurements of fluctuations in multiple fields with systematic variation of a/L_{T_e} and rotation

5.3.1 Experimental conditions

The fluctuation measurements presented in the chapter were obtained in one of a series of experiments conducted in the DIII-D tokamak during 2011 to investigate profile stiffness and critical gradients [12]. Plasmas were in L-mode, MHD-quiescent, upper single null diverted, with plasma current $I_p = 0.8$ MA, minor radius $a \approx 0.6$ m, major radius $R_0 \approx 1.7$ m, $B_0 = 2$ T toroidal magnetic field (directed opposite to I_p), and had line-averaged density of $\sim 2 \times 10^{13}$ cm^{-3}. At $\rho = 0.6$, the gyrokinetic expansion parameter, $\rho^* = \rho_s/a_0$, was about 1/300. Feedback control was used to maintain constant line-averaged density. The resonance locations of six gyrotrons used for electron cyclotron heating (ECH) were re-steered shot-to-shot between $\rho = 0.5$ and $\rho = 0.7$, which scanned $L_{T_e}^{-1}$ at $\rho = 0.6$. In addition to ECH-only cases, neutral beam injection (NBI) was employed to create $L_{T_e}^{-1}$ scans at three rotation states: two co-injected (to I_p) NBI sources (ECH+Co-NBI), two counter-injected NBI sources (ECH+Ctr-NBI), and balanced injection with one of each (ECH+Bal-NBI). Combinations of NBI and ECH were held in steady-state for 500-800 ms, these time periods were used to average equilibrium profiles and turbulence data. One ECH source was modulated at 50% duty cycle for transient heat pulse analysis; this had a neglible effect on the turbulence measurements, which will be demonstated below through conditional averaging of turbulence measurements on the modulated ECH source. There was ~ 3 MW ECH power in all shots. NBI shots had ~ 2 MW of beam power in addition to the ECH, for a total of ~ 5 MW. The thermal temperatures for both ions and electrons where much less than the neutral beam energy, ~ 80 keV, so the beam fast ions predominatly heated the electrons [1].

Figure 5.2 shows the effect of scanning the gyrotron resonance locations on the electron

temperature and inverse electron temperature gradient scale length for the ECH-only conditions. There are several notable features of the plots. At the target radii, $\rho = 0.6$, where fluctuation diagnostics were aimed, $L_{T_e}^{-1}$ was systematically scanned. Reasonably small radial variation of $L_{T_e}^{-1}$ in the neighborhood of $\rho = 0.6$ was attained for each ECH arrangement. Furthermore, the edge T_e profiles show little change for $\rho > 0.75$, which minimized the impact of boundary condition effects. While $L_{T_e}^{-1}$ was scanned by about a factor of 3, the variation of T_e at $\rho = 0.6$ was only $\sim 10\%$ about its average value accross all gryotron conditions–most of the change to $L_{T_e}^{-1}$ was from the electron temperature gradient itself. The plotted temperature profile data was acquired with the 40 channel ECE system [215]. The long steady-state periods allowed the random error uncertainty for measurements to be made much smaller than estimates of systematic errors, which are estimated to be $\sim 25\%$ for $L_{T_e}^{-1}$. In addition to noting measurements by local gradient scale length values, the short hand "Shot (m,n)" is used, where "Shot" is the shot number, m is the number of ECH gyrotrons as $\rho = 0.5$, and m is the number of gyrotrons at $\rho = 0.7$. In all cases, one of the $\rho = 0.7$ gyrotrons was modulated at 50% duty cycle; this is rounded up in the (m,n) notation in several places in the chapter.

The systematic errors arise from effects like ECE calibration factors and the magnetic equilibrium reconstruction: there were inconsistencies near the magnetic axis, where ECE channels at the same flux surface at $R > R_0$ and $R < R_0$ did not match. This indicates that one or both of the mentioned systematic errors were present, the likely source being the equilibrium reconstruction, since only external magnetics data was used due to the lack of NBI for motional Stark effect measurements in ECH only plasmas. However, errors in correctly reconstructing the magnetic axis position (*i.e.* accurately accounting for the Shafronov shift), would not be expected to have a large effect on flux surfaces (and therefore gradients) at $\rho = 0.6$–this approximation has been used previously in similar experiments [9], where reasonable agreement was found between low-k fluctuation measurements and nonlinear simulation predictions [10]. Additionally, such errors should be highly correlated, resulting in, perhaps, a different value being identified for a critical gradient, but having no

effect on the qualitative identification of the existence of such a phenomenon.

In later sections, the local values of $L_{T_e}^{-1}$ and other parameters are used for each measurement, as determined from equilibrium information and using methods described in Chapter 3.

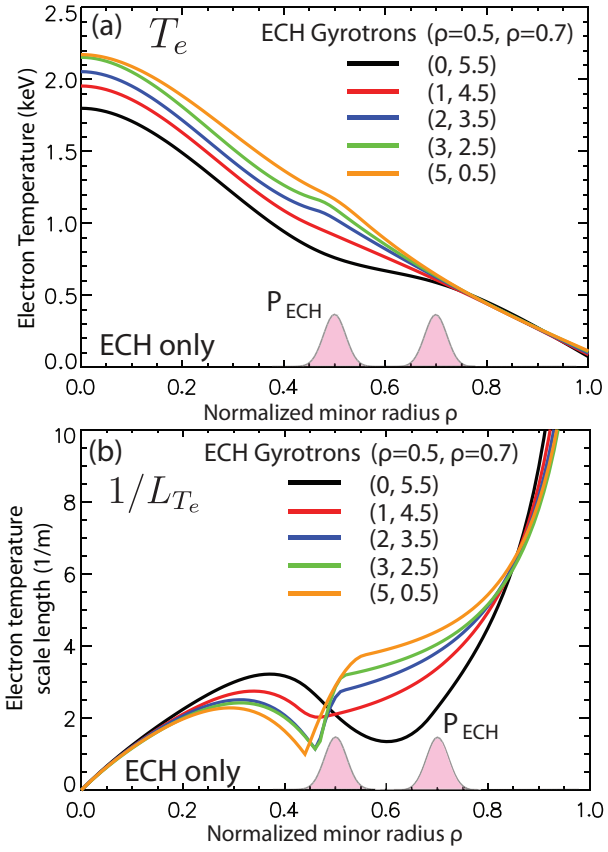

Figure 5.2: Equilibrium profiles of (a) electron temperature and (b) inverse electron temperature gradient scale length for the ECH-only plasmas. Annotated are indications of the ECH power deposition profiles at $\rho = 0.5$ and $\rho = 0.7$.

The other source that was systematically scanned in the experiment was the momentum input from neutral beam injection. The toroidal rotation was measured with the Charge Exchange Recombination spectroscopy (CER) diagnostic at DIII-D. Short 10 ms beam blips were used to acquire measurements during the ECH-only and ECH+Ctr-NBI conditions. For ECH+Co-NBI and ECH+Bal-NBI, the CER beams were interlaced into the beam timing for the entire time period. Figure 5.3 shows the effect of NBI on toroidal rotation and rotation shear. The toroidal rotation velocity, shown in Fig. 5.3(a), was varied from 10 ± 6 km/s for

ECH+Ctr-NBI to 58 ± 4 km/s for ECH+Co-NBI (given values are average plus or minus the standard deviation for all ECH arrangements), with the two other cases in between. Plotted in Fig. 5.3(b) are the normalized toroidal rotation profiles, the toroidal Mach number,

$$M_\phi = \frac{\Omega_{tor} R_0}{c_s}, \tag{5.1}$$

where the sound speed is taken to be $c_s = \sqrt{T_e/m_D}$ (m_D for the mass of deuterium) and Ω_{tor} is the toroidal rotation frequency, which is a flux function (unlike the toroidal velocity). Instead of the local major radius, the major radius on axis is used in the definition of M_ϕ (annotated in the figure), so that is is also a flux function. It can be observed that the Mach number profiles are significantly flatter than the toroidal rotation profiles, which is due to the variation of the T_e profiles. Notable is that an intrinsic rotation source in the Co-NBI direction must be invoked to explain the rotation profiles in Fig. 5.3(a-b): there is finite rotation even with no net momentum input and at $\rho = 0.6$, the rotation is slightly in the Co-NBI direction, even when all momentum input is in the opposite direction in the Ctr-NBI case. Also, even though there is not strong beam heating, in a normalized sense, the rotation is appreciable, with $M_\phi \approx 0.2 - 0.3$ for 3 of 4 cases near the radius of interest. Neutral beams inject a fixed ratio of heat and momentum, so NBI-heated plasmas with very different temperatures and confinement properties will often have similar Mach numbers. Figure. 5.3(c) shows the normalized flow shear,

$$\frac{\gamma_E}{c_s/a} = \frac{\rho}{q(c_s/a)} \frac{\partial \Omega_{tor}}{\partial \rho}. \tag{5.2}$$

The important feature of Fig. 5.3(c) is the flow shear (several definitions for flow shear exist; the one plotted corresponds to the input parameter many gyrokinetic codes use) is small, $\gamma_e < 0.05 c_s/a$, for all cases. Growth rate calculations, to be shown later, generate values several times higher. Flow shear stabilization effects do not appear to have a strong influence in this experiment.

More description of equilibrium profiles is available in Ref. [12]. Briefly, the n_e profiles and T_e profiles for $\rho > 0.5$ were well-matched for all conditions (T_e was higher in the core with beam heating); although, the minimum value of $L_{T_e}^{-1}$ for cases with NBI were higher.

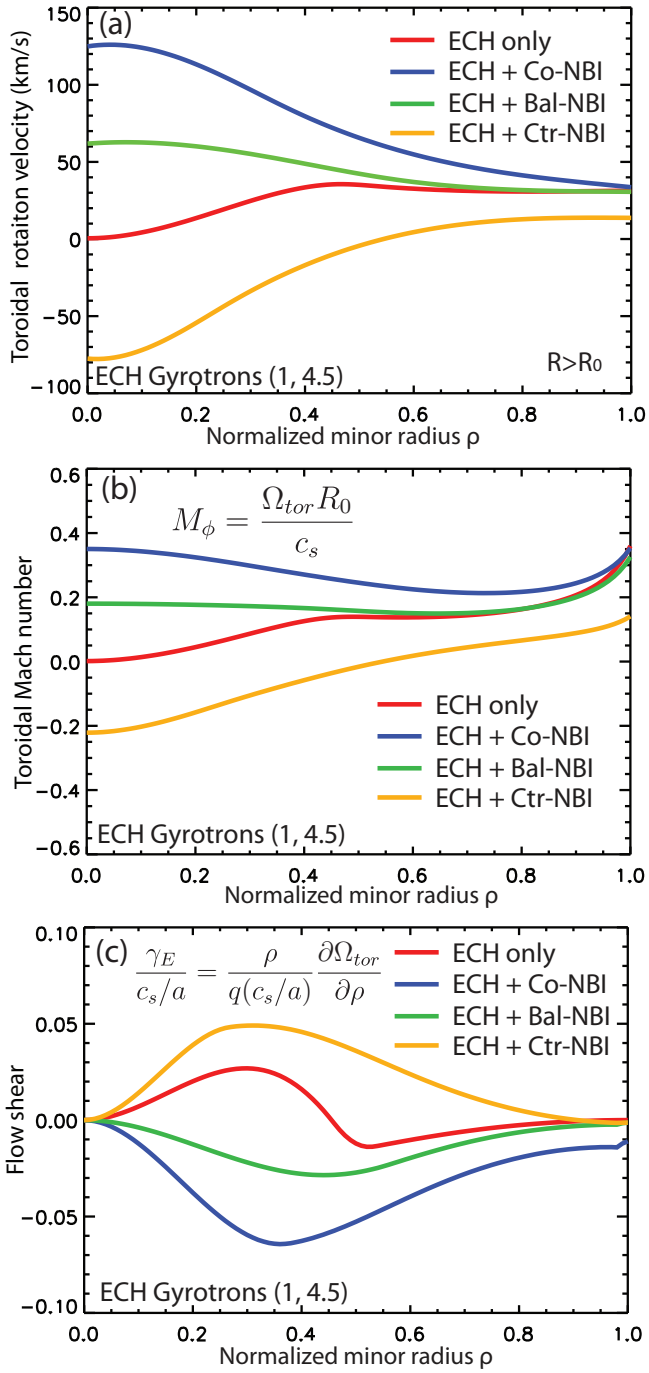

Figure 5.3: Equilibrium profiles of (a) toroidal rotation profiles (near outboard mid-plane, low-field side), (b) toroidal Mach number, and (c) normalized flow shear for the 4 rotation cases with 1 gyrotron at $\rho = 0.5$ and the rest at $\rho = 0.7$ (1, 4.5).

The T_i profiles were well matched for cases with NBI, but were uniformly lower for ECH-only. The effective ionic charge at $\rho \approx 0.6$ for most of the discharges was $Z_{eff} \approx 2.3 - 2.8$, but was systematically higher for shots with ECH+Ctr-NBI, where $Z_{eff} \approx 2.9 - 3.2$. The main ion species was deuterium and the dominant impurity was carbon. It was found that although there was random variation of profiles–other than the electron temperature profile–with ECH deposition location, none of the variations were systematically correlated with ECH location; the variations were order $\sim 10\%$.

Two parameters that will impact later arguments are the temperature ratio and Z_{eff}. Both impact growth rate calculations, with the latter coming in through collisions. Figure 5.4(a) shows Z_{eff} profiles from cases with the same ECH arrangement in the 4 rotation states. Z_{eff} was one of the parameters that did exhibit significant variations among shots. Although Z_{eff} at $\rho = 0.6$ is well-matched in the figure, the variation across the profile, $\rho < 0.8$, between the 3 non-Ctr-NBI cases was typical of the shot-to-shot variation at $\rho = 0.6$. The value of Z_{eff} was systematically higher for shots with Ctr-NBI, typically $\sim 30\%$ higher. The likely reason for this is due to a larger proportion of direct loss orbits for the counter beams: the initial gyro-orbit for Co-beams is radially inward while for Ctr-beams it is radially outward. This may result in fast ion orbits hitting the walls, which are made out of carbon tiles at DIII-D, sputtering material into the plasma. Figure 5.4(b) shows the temperature ratio in the 4 rotation cases. Due to the lower ion temperature, T_e/T_i was $\sim 50\%$ higher at $\rho = 0.6$ for ECH-only plasmas. The influence of T_e/T_i on trapped electron modes will be discussed later.

Linear gyrokinetic and gyrofluid results are presented in Sec. 5.4. The large number of experimental conditions renders a list of all input parameters for each case prohibitively prolix. Instead, Table 5.1 lists the average and standard deviation for a number of local quantities at $\rho = 0.6$ for each of the rotation scenarios. The quantity scanned in each scenario, $L_{T_e}^{-1}$, is omitted from the table. The reference length scale a is chosen to be ρ_{max} for consistency with other work. The is done because the gradient scale lengths are defined as $L_j^{-1} = \rho_{max}^{-1} j^{-1} \partial j / \partial \rho$ (also for consistency with other work from DIII-D); the radial

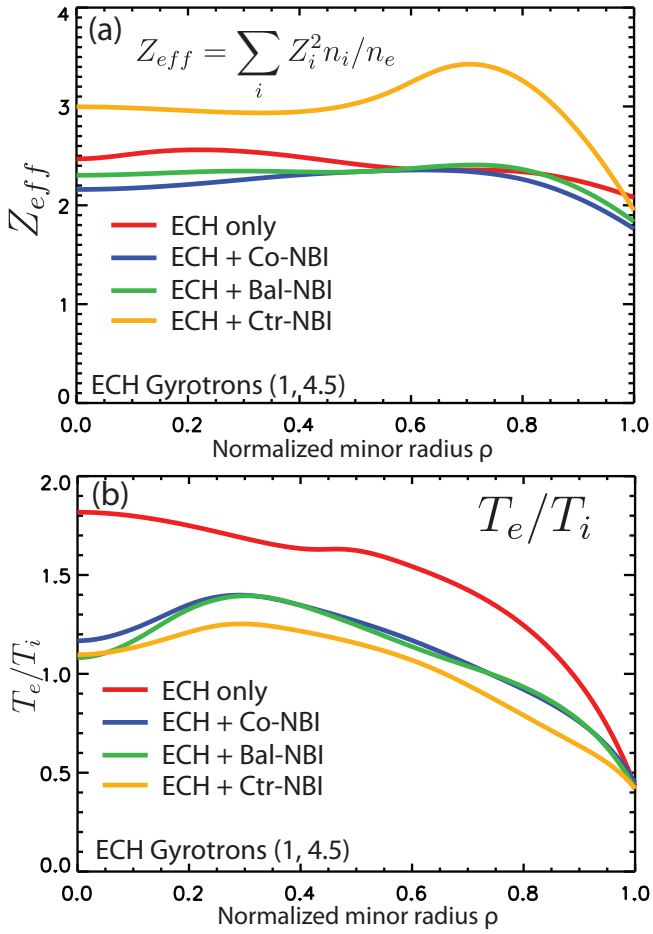

Figure 5.4: Equilibrium profiles of (a) effective ionic charge and (b) temperature ratio for the 4 rotation cases with 1 gyrotron at $\rho = 0.5$ and the rest at $\rho = 0.7$.

Parameter	ECH-only	ECH+Co-NBI	ECH+Bal-NBI	ECH+Ctr-NBI
c_s/a (kHz)	250 ± 12	260 ± 5	264 ± 7	261 ± 10
a/L_{T_i}	1.50 ± 0.08	1.51 ± 0.13	1.45 ± 0.03	1.26 ± 0.13
a/L_{n_e}	1.09 ± 0.06	1.26 ± 0.11	1.26 ± 0.16	1.17 ± 0.15
a/L_{n_C}	1.20 ± 0.07	1.19 ± 0.10	0.92 ± 0.07	0.59 ± 0.14
a/L_{n_D}	1.05 ± 0.09	1.07 ± 0.21	1.22 ± 0.28	1.38 ± 0.48
$a/L_{n_{fast}}$	0	5.53 ± 0.31	5.56 ± 0.16	5.34 ± 0.42
Z_{eff}	2.57 ± 0.11	2.66 ± 0.42	2.66 ± 0.28	3.05 ± 0.17
n_{fast}/n_e	0	0.036 ± 0.004	0.035 ± 0.003	0.030 ± 0.007
T_e/T_i	1.65 ± 0.12	1.06 ± 0.16	1.05 ± 0.12	1.16 ± 0.10
$\nu_{ei}/(c_s/a)$	0.18 ± 0.04	0.16 ± 0.02	0.15 ± 0.01	0.16 ± 0.03
M_ϕ	0.13 ± 0.01	0.23 ± 0.02	0.14 ± 0.01	0.04 ± 0.02
$\gamma_E/(c_s/a)$	0.012 ± 0.005	0.049 ± 0.004	0.023 ± 0.003	-0.029 ± 0.006
q	2.45 ± 0.08	2.31 ± 0.03	2.34 ± 0.03	2.45 ± 0.09
$\hat{s}$	1.51 ± 0.09	1.67 ± 0.09	1.62 ± 0.06	1.54 ± 0.13
β_e	$0.13 \pm 0.01\%$	$0.15 \pm 0.01\%$	$0.15 \pm 0.01\%$	$0.15 \pm 0.01\%$

Table 5.1: Average local plasma parameters for $L_{T_e}^{-1}$ experiment at $\rho = 0.6$

coordinate, ρ, is the square root of the normalized toroidal flux and $\rho_{max} = \sqrt{\Phi/(\pi B_0)}$, where Φ is the toroidal flux within the last closed flux surface. The reference length is chosen to be ρ_{max} so that the normalized scale lengths do not include a ratio of two different definitions for the reference scale length. Physically, ρ_{max} is the diameter of a circular plasma with the same enclosed flux as the real, shaped plasma. The normal definition of minor radius, a_0, is half the minor diameter at the mid-plane. Global parameters, which do not change significantly, are listed in Table 5.2. Additional experimental details such as shot times and analysis periods can be found in Appendix C.

Parameter	Value
I_p	0.8 MA
B_t	-2.05 T
R_0	1.70 m
a_0	0.62 m
ρ_{max}	0.79 m
q_{95}	6.3
κ	1.6

Table 5.2: Global plasma parameters for $L_{T_e}^{-1}$ experiment

5.3.2 Transport analysis

The primary result of the experiment was that a critical gradient was observed for electron temperature fluctuations. Above this critical gradient, the electron heat flux increased non-linearly, with stiffness increasing. The focus of this chapter is on the turbulence measurements and comparisons of those measurements to model predictions. To provide a more complete picture of the impact of the changes in the turbulence on the transport and confinement properties of the plasma, the electron heat flux inferred from power balance and a summary of the results in Ref. [12] are included in this section.

The electron heat flux, in gyro-Bohm units ($Q_{GB} = n_e T_e c_s (\rho_s/a)^2$), at $\rho = 0.6$ for the complete data set is shown in Fig. 5.5 as a function of $L_{T_e}^{-1}$. The heat flux was inferred from power balance calculation using the ONETWO model [258]. There is a fast increase in the electron heat flux with $L_{T_e}^{-1}$, with stiffness (the incremental increase in flux for an incremental increase in gradient) clearly increasing. Furthermore, little sensitivity to toroidal rotation or other NBI-case dependent parameters is observed. While the normalized heat flux increases by about a factor of 10, the actual heat flux increases by a larger factor, due to the temperature dependence of the normalization, $Q_{GB} \propto T_e^{5/2}$.

As discussed above, due to the long time periods, the normalized random errors for

equilibrium quantities are thought to be small compared to systematic errors. In addition to systematic measurement and equilibrium reconstruction issues for profile measurement, inference of the heat flux has further sensitivities. For example, the source terms for NBI and ECH are calculated using models that are yet to be completely experimentally validated. To quantify an estimate of the random error contribution, about 100 fits were produced for n_e, T_e, T_i, and v_{tor} profiles, where the measurement points were varied within their uncertainties. This ensemble of fits were used as the input to the transport code ONETWO. The resulting estimate of the random error was typically a few percent for the electron heat flux, at most about 5%. This error is quite small due since the flux must be highly-constrained by the heat source inputs. As noted about, there might be difficult to quantify systematic errors in the source modules. For instance, it is known that the fast ion distribution can be broaden due to transport by gyroradius-scale turbulence [259]. Systemic issues like this would be highly-correlated and are very unlikely to change the interpretation of any presented results.

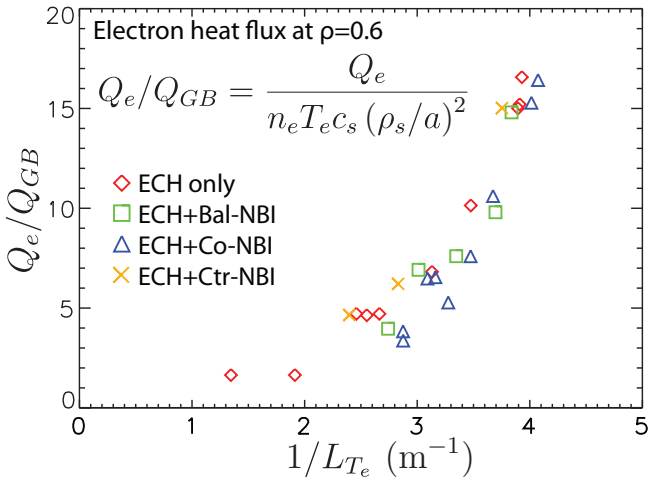

Figure 5.5: Electron heat flux, normalized to gyro-Bohm units, at $\rho = 0.6$ for the complete data set as a function of $L_{T_e}^{-1}$.

The modulated ECH gyrotron was used to perform heat pulse analysis in Ref. [12]. To summarize the results, a critical gradient was found for the electron thermal diffusivity, χ_e, at a value of $L_{T_e}^{-1} = 3.0 \pm 0.2$ m^{-1} in ECH-only plasmas. The definition for stiffness (here, for example, for electron heat flux dependence on the electron temperature gradient)

is usually $S = (\nabla T_e/Q_e)(\partial Q_e/\partial(\nabla T_e))$. Analysis indicated that the stiffness parameter, S, increased above the critical gradient, consistent with Fig. 5.5. For quantification of stiffness see Ref. [12]–the focus of the work presented here are the turbulence measurements and comparisons of those measurements to predictions.

5.3.3 Fluctuation measurements

A broad array of turbulence measurements were acquired during the experiment. The long steady-state periods were used to average the data, resulting in relatively smooth spectra and small statistical errors. The experiment was run with a low plasma current to reduce the size of sawteeth. Long wavelength ($k_\theta \rho_s \lesssim 0.5$) electron temperature fluctuations measured with the correlation electron cyclotron emission (CECE) diagnostic [3] can be found in Sec. 5.3.3.1. Quantitative assignment of a critical gradient value for electron temperature fluctuations is described in Sec. 5.3.3.2. Long wavelength ($k_\theta \rho_s \lesssim 0.4$) density fluctuation measurements acquired with Beam Emission Spectroscopy [260] (BES) are presented in Sec. 5.3.3.3. Intermediate-scale ($k_\theta \rho_s \sim 0.8$) density fluctuations measured with a Doppler Backscattering (DBS-8) system [7] are shown in Sec. 5.3.3.4. Results from conditionally averaging the turbulence data on NBI and ECH timing are presented in Sec. 5.3.3.5. The CECE system was coupled to a reflectometer array [6] to measure the crossphase angle between electron density fluctuations and electron temperature fluctuations; those measurements can be found in Sec. 5.3.3.6. Investigations of the probability distribution function of the crossphase measurements are in Sec. 5.3.3.7. Low frequency flows were also measured with DBS, which are discussed in Sec. 5.3.3.8.

5.3.3.1 Electron temperature fluctuation measurements

The CECE system was arranged to measure temperature fluctuations at two radii, with two channels at $\rho \approx 0.55$ and two channels at $\rho \approx 0.61$. For general hardware and data analysis details, see Sec. 3.6.

Figure 5.6 shows electron temperature power spectra measured with CECE at $\rho = 0.61$ for each rotation case. In all rotation cases there is a an increase (and for ECH-only apparent saturation) of the temperature fluctuation power spectra with $L_{T_e}^{-1}$. In all cases there appears to be a low frequency ($f < 10$ kHz) feature. The feature is also present during earlier portions of the shots with no ECH and clearly shows dependence on plasma parameters–it does appear to be a real feature of the spectrum. Such a feature could arguably be seen in previous work [110]; however, the steady-state time periods in that work did not result in sufficiently small uncertainties for the feature to be unambiguously identified. The differences in the frequency distribution of the fluctuation power observed in the spectra are explainable by a Doppler shift induced by the equilibrium $E \times B$ shift. There is finite intrinsic rotation in the two cases with close to zero net momentum injection, Fig. 5.6(a-b), where a feature in the spectra is observed at $\sim 50 - 70$ kHz. For the ECH+Co-NBI cases in Fig. 5.6(c), the spectrum is Doppler shifted to higher frequency and widened, with a fairly flat spectrum for 50 kHz $> f >$ 150 kHz. The last case, ECH+Ctr-NBI in Fig. 5.6(d), is the lowest rotation case. The two features in the spectrum overlap, resulting in higher values at low frequencies for the highest $L_{T_e}^{-1}$ condition.

To determine the temperature fluctuation level, spectra like those in Fig. 5.6 are integrated over the range 0-400 kHz. The result, for both $\rho = 0.55$ and $\rho = 0.61$, is plotted in Fig. 5.7. There is observed to be a threshold in $L_{T_e}^{-1}$: below the threshold fluctuations are unchanged within uncertainties and above they abruptly increase. Furthermore, the thresholds show little indication of dependencies on rotation. There are cases at $L_{T_e}^{-1} \approx 3.2$ m^{-1} that are outside of uncertainties at similar values of $L_{T_e}^{-1}$–this will be shown later to depend on the density gradient scale length, not rotation directly. The increase in temperature fluctuations in Fig. 5.7 directly correlates with the increased electron heat flux and transport stiffness depicted in Fig. 5.5. The growth rates for ∇T_e-driven trapped electron modes are expected to be proportional to the electron temperature gradient scale length [90]. Additional dependencies are discussed below.

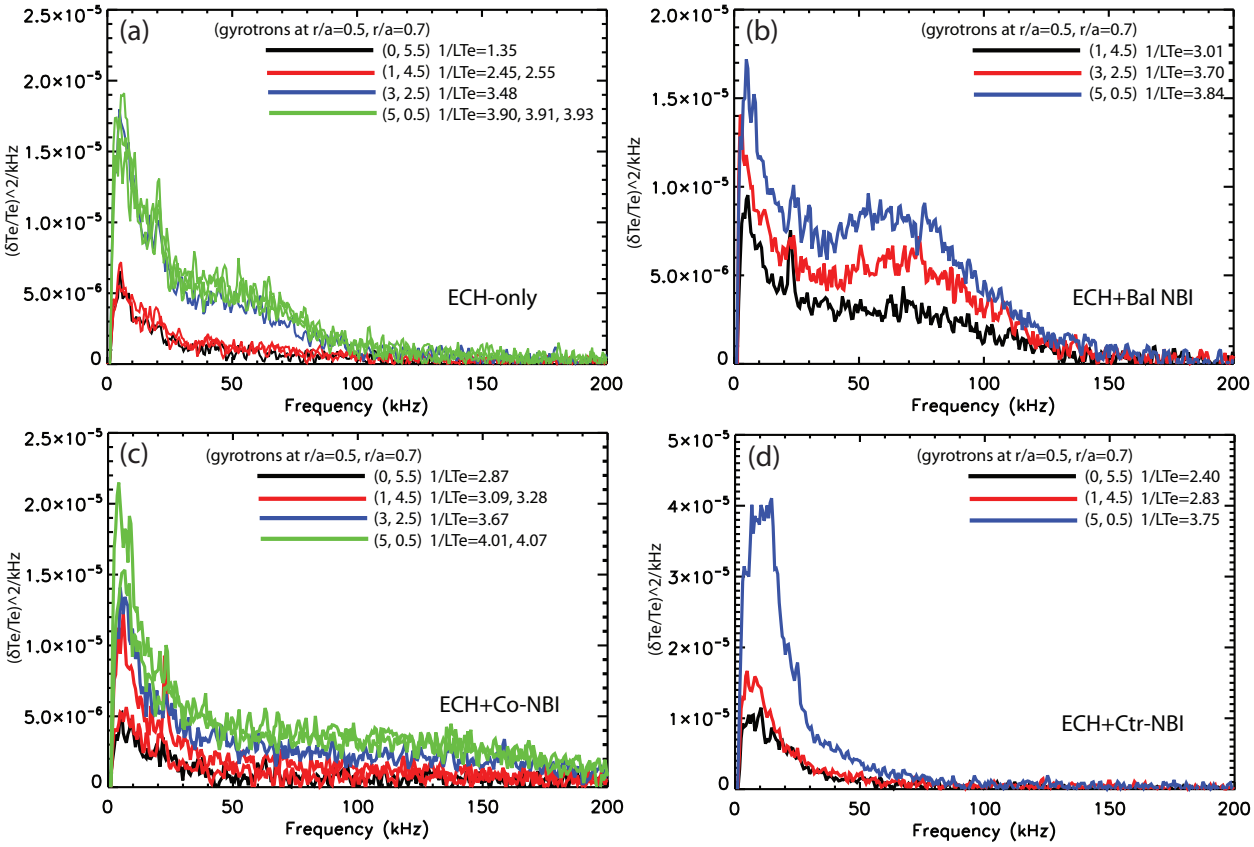

Figure 5.6: Electron temperature power spectra in (a) ECH-only, (b) ECH+Bal-NBI, (c) ECH+Co-NBI, and (d) ECH+Ctr-NBI at $\rho \approx 0.61$. Annotated in legends are the local values of $L_{T_e}^{-1}$ for each measurement.

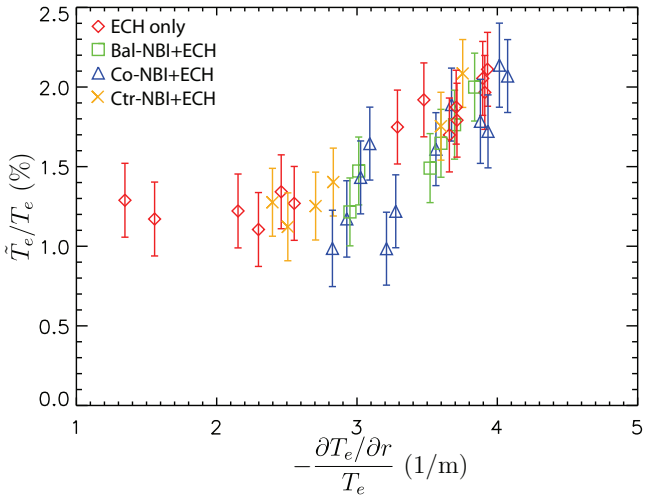

Figure 5.7: Electron temperature fluctuation levels as a function of $L_{T_e}^{-1}$, for the 4 rotation cases.

5.3.3.2 Determination of $\delta Te/Te$ critical gradient value

The measurements of electron temperature fluctuations in Fig. 5.7 exhibit critical gradient behavior. In this section, that behavior is quantified. To do this, several model equations were fit to the data in Fig. 5.7. The simplest choice of model is a piecewise linear fit with two segments. A Monte Carlo approach was taken, varying the data points within uncertainties and taking the mean and standard deviation of fit parameters–large ensembles were used, with 50,000 or more minimum χ^2 fits. The piecewise linear model yielded poor results, with about half the fits finding the best fit to be with the critical gradient to one side of the complete data set–clearly a poor description of the results.

Predictions for the dependence of the electron thermal diffusivity on a critical gradient can be found in Ref. [261]. The best fit, as defined by the minimum mean χ^2 for the ensemble of fits, was found by assuming $\chi_e \propto (\delta T_e/T_e)^2$ and using the model equation

$$(\delta T_e/T_e)^2 = c_0 + c_1 \left(L_{T_e}^{-1} - L_{T_e}^{-1}|_{crit}\right)^{\ell} H\left(L_{T_e}^{-1} - L_{T_e}^{-1}|_{crit}\right), \tag{5.3}$$

where $H(x)$ is the Heaviside function. The mean and standard deviation of the parameter of primary interest was $L_{T_e}^{-1}|_{crit} = 2.8 \pm 0.4$ m^{-1}. The mean reduced χ^2 for the ensemble of fits was 1.4. Results for the other parameters were $c_0 = 1.4 \pm 0.2$, $c_1 = 2.1 \pm 0.9$, and $l = 1.4 \pm 0.8$.

The resulting best fit is shown in Fig. 5.8. The four parameter fit is not well constrained by the data, with c_1 and l both possessing significant variation–essentially either can account for the slope of the data above the critical gradient. The model put forward in Ref. [261] had an additional parameter; the extra parameter was similarly poorly constrained by the data. On the other hand, a three parameter fit, with $c_1 = 1$, lacked sufficient flexibility to fit the data, resulting in a higher mean χ^2.

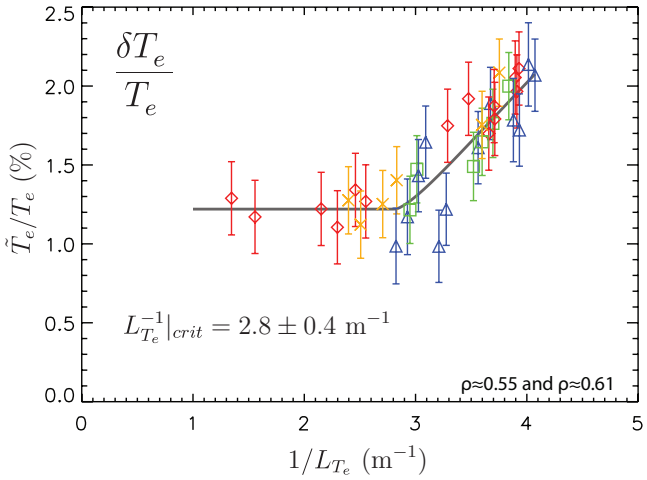

Figure 5.8: Electron temperature fluctuation levels as a function of $L_{T_e}^{-1}$, with best fit. Critical gradient value annotated.

Non-linear simulations of ∇T_e-driven TEM turbulence have found no evidence of a non-linear upshift of the critical gradient [92, 93]. This is in contrast to simulations of ITG [84] and ∇n_e-driven TEM [92] turbulence which have found non-linear upshifts. The shift is often referred to as the "Dimits shift" and occurs in simulations due to zonal flow dominated states in between the linear critical gradient and the non-linear critical gradient. The predicted absence of a Dimits shift for ∇T_e-driven TEM implies that the linear and non-linear critical gradients should be the same. It is therefore well-posed to compare linear ∇T_e-TEM predictions to experimental measurements.

Analytical predictions for the critical threshold for trapped electron modes have been investigated, which can be calculated from equilibrium parameters and compared to the mea-

sured value for temperature fluctuations. The Weiland advanced fluid model predicts [262]

$$\left.\frac{R}{L_{T_e}}\right|_{crit} = \frac{20}{9K_t} + \frac{2}{3}\frac{R}{L_n} + \frac{K_t}{2}\left(1 - \frac{R}{2L_n}\right)^2, \tag{5.4}$$

where $K_t = f_t/(1-f_t)$ and f_t is the fraction of trapped particles. Evaluating Eqn. 5.4 over the entire data set at $\rho = 0.6$ results in a mean and standard deviation of $L_{T_e}^{-1}|_{crit} = 1.7 \pm 0.2$ m^{-1}, which is significantly lower than the value of $L_{T_e}^{-1}|_{crit} = 2.8 \pm 0.4$ m^{-1} found for electron temperature fluctuations. Since Eqn. 5.4 lacks accurate description of kinetic electrons, collisions, shaping, and other effects, disagreement is perhaps not surprising.

Another formula for the ∇T_e-TEM is given in Ref. [263]; there, parameter scans of linear gyrokinetic simulations with quasilinear flux calculations were performed at a value of $L_{T_e}^{-1}$ around twice the critical value, with extrapolation assuming a linear dependence between flux and gradient to determine $L_{T_e}^{-1}|_{crit}$. The result was

$$\left.\frac{R}{L_{T_e}}\right|_{crit} = \frac{0.357\sqrt{\epsilon} + 0.271}{\sqrt{\epsilon}}\left[4.90 - 1.31\frac{R}{L_n} + 2.68 + ln\left(1 + 20\nu_{eff}\right)\right], \tag{5.5}$$

where ϵ is the inverse aspect ratio, $\hat{s}$ is the magnetic shear, and $\nu_{eff} = 0.1 n_e^* Z_{eff}/T_{ek}^2$, where n_e^* is the electron density in units of 10^{19} m^{-3} and T_{ek} is the electron temperature in units of keV. Evaluating Eqn 5.5 for the data set at $\rho = 0.6$ yields $L_{T_e}^{-1}|_{crit} = 4.6 \pm 0.2$ m^{-1}, also in quantitative disagreement with the experiment; although, given that the electron heat flux in Fig. 5.5 increases faster than linearly, it is qualitatively consistent that one would expect Eqn. 5.5 to over-predict the critical gradient value. Similarly to Eqn. 5.4, Eqn. 5.5 includes no shaping effects. It is notable that in other work it has been argued that Eqn. 5.5 did accurately describe the experimentally observed gradient over a range of minor radii in QH-mode DIII-D plasmas [5]. It is not clear why agreement was found there, but disagreement is found for the L-mode plasmas here–this motivates future work to clarify the discrepancy.

Given the significant quantitative disagreements found for analytical predictions, later sections will focus only on comparisons to more complete models, which are realized through initial value code calculations.

5.3.3.3 Long wavelength density fluctuation measurements

Measurements of long wavelength density fluctuations were acquired with Beam Emission Spectroscopy during the ECH+Co-NBI cases only. Other cases used NBI sources that did not allow BES measurements. Figure 5.9 shows both the electron temperature and density fluctuation levels at long wavelength. The BES measurement is from radial position $\rho \approx 0.58$. The diagnostics are sensitive to slightly different wave number ranges, with BES measuring $k_\theta \rho_s \lesssim 0.5$ and CECE measuring $k_\theta \rho_s \lesssim 0.4$. There is a $\sim 25\%$ increase in the low-k density fluctuations from the lowest value of $L_{T_e}^{-1}$, but the fluctuations then do not change significantly in amplitude. This is consistent with past work where changes to electron temperature fluctuations levels were observed, but there was little change to density fluctuations, increased electron mode growth rates were attributed the cause in those cases also [16, 17, 89]. The ratio $(\delta T_e/T_e)/(\delta n_e/n_e)$ clearing increases with the inverse gradient scale length in Fig. 5.9– this is also consistent with a transition to TEM dominated turbulence [89]. The random error in the BES measurements is about 4-5%, which is smaller than the BES symbols in Fig. 5.9.

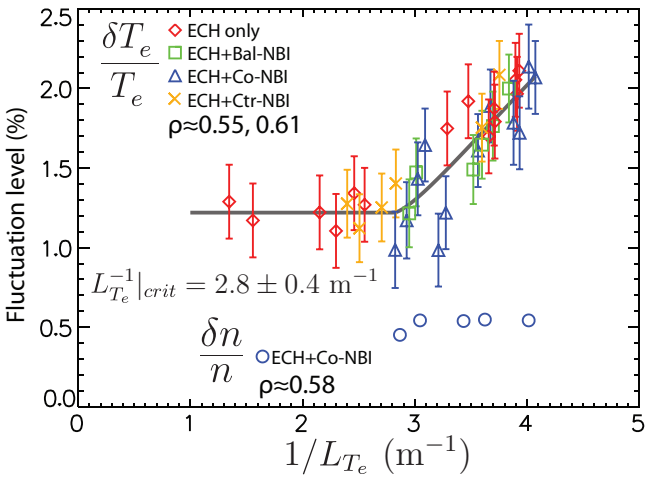

Figure 5.9: Electron temperature and density fluctuation levels as a function of $L_{T_e}^{-1}$. Critical gradient value annotated.

5.3.3.4 Intermediate-scale density fluctuation measurements

Measurements of intermediate scale ($k_\theta \rho_s \sim 1$) density fluctuations were acquired during the experiment with DBS-8. It is possible to build up a wave number spectrum of the turbulence with DBS, as was done in Ref. [5]; however, due to the changing conditions shot-to-shot in this experiment, it was decided to get density fluctuation measurements at one wave number for the entire data set. One of the DBS channels (67.5 GHz) was located at $\rho \approx 0.6$ and measured density fluctuations at $k \approx 4$ cm^{-1} or $k_\theta \rho_s \approx 0.8$. The DBS measured Doppler shift is given by

$$\omega_{DBS} = k_\theta v_{E\times B} + k_\theta \tilde{v}, \tag{5.6}$$

where $v_{E\times B}$ is the piece of the lab frame velocity due to the equilibrium $E \times B$ drift and $\tilde{v}$ is the plasma frame velocity of the turbulent structure. The trapped electron mode is expect to propagate in the electron diamagnetic direction, which should be apparent in the DBS spectrum (assuming there are not also significant changes to the equilibrium radial electric field) and might be able to be identified when an independent measurement of the equilibrium radial electric field is available.

Figure 5.10 displays the concurrent changes to the long wavelength electron temperature fluctuations and intermediate-scale density fluctuations for ECH-only plasmas. Plotted in Fig. 5.10(a) are the quadrature DBS spectra. The spike at close to zero frequency is due to direct reflections from lenses and windows. The electron diamagnetic direction is in the negative direction. The spectra clearly shift towards the electron diamagnetic direction above the critical $L_{T_e}^{-1}$, consistent with expectations for ∇T_e-TEM. There is no change in momentum input, therefore the change in the spectrum must be due to the turbulence: either $\tilde{v}$ changes due to a change in the phase velocity of the turbulence or the equilibrium E_r changes due to a change in momentum transport (or both). The CER measurements during the ECH-only phase were accomplished through short neutral beam blips, which introduces difficult to quantify systematic errors and limits reduction of random errors compared to the other conditions. Another facet of the DBS spectra to note is that they are not highly Gaussian,

as was shown in Fig. 3.4, implying the measurements take place in the rotation range where both the instrumental Δk and the turbulent $\Delta\tilde{v}$ contribute to the spectral shape. Other effects, such as distortion of the DBS spectrum due to the shape of the density fluctuation wave number spectrum would be expected to shift and skew the spectrum, not widen it, as is observed below the critical gradient in Fig. 5.10. It is notable that the spectra in Fig. 5.10(a) below the threshold are wider than a Gaussian, which would be consistent with two instabilities being present. Above the threshold, the spectra narrow, which would be consistent with one of the modes weakening and the other getting more unstable. Opposite dependencies on $\eta_e = L_{n_e}/L_{T_e}$ are expected for ∇n_e-TEM and ∇T_e-TEM (see, for instance, Fig. 2 of Ref. [92]). Figure 5.10(b) shows the electron temperature fluctuation power spectra, with the integrated fluctuation levels inset. Similar to the DBS spectra, there is a significant change between values above or below the threshold, but little change within the two groups. The temperature fluctuation power spectra increase across the full frequency range, but the higher frequency feature, $f \sim 50$ kHz, increases more than the low frequency feature, consistent with a new mode at stronger amplitude above the threshold.

Figure 5.11 shows the DBS spectra from the other case with close to zero net momentum input, ECH+Bal-NBI (beam power was matched, but there was a small net momentum input). The spectra are ensemble averaged over ~ 800 ms, with a normalized random error of less than 2%. The spike at zero frequency due to reflections has been ommitted (can be slightly oberved at $f = 0$ kHz). There is a clear increase in the amplitude of fluctuations on the electron diagmagnetic side of the spectra as $L_{T_e}^{-1}$ increases. Automated CER analysis (and ray tracing for the scattering wave number) place the expected Doppler shift from the equilibrium $E \times B$ velocity as, for instance, about 250 kHz for the black case and 220 kHz for the red and blue cases (using E_r from CER and k_θ from ray tracing). Further analysis to reduce uncertainties for equilibrium quantities is under way. The frequency-localized increase to the spectrum appears to correlate more strongly with $L_{T_e}^{-1}$ than with η_e, unlike the low-k temperature fluctuation measurements. All the gradient values are the local values for each channel, determined by profile fitting and ray tracing analysis. That explains why $L_{T_e}^{-1}$ is

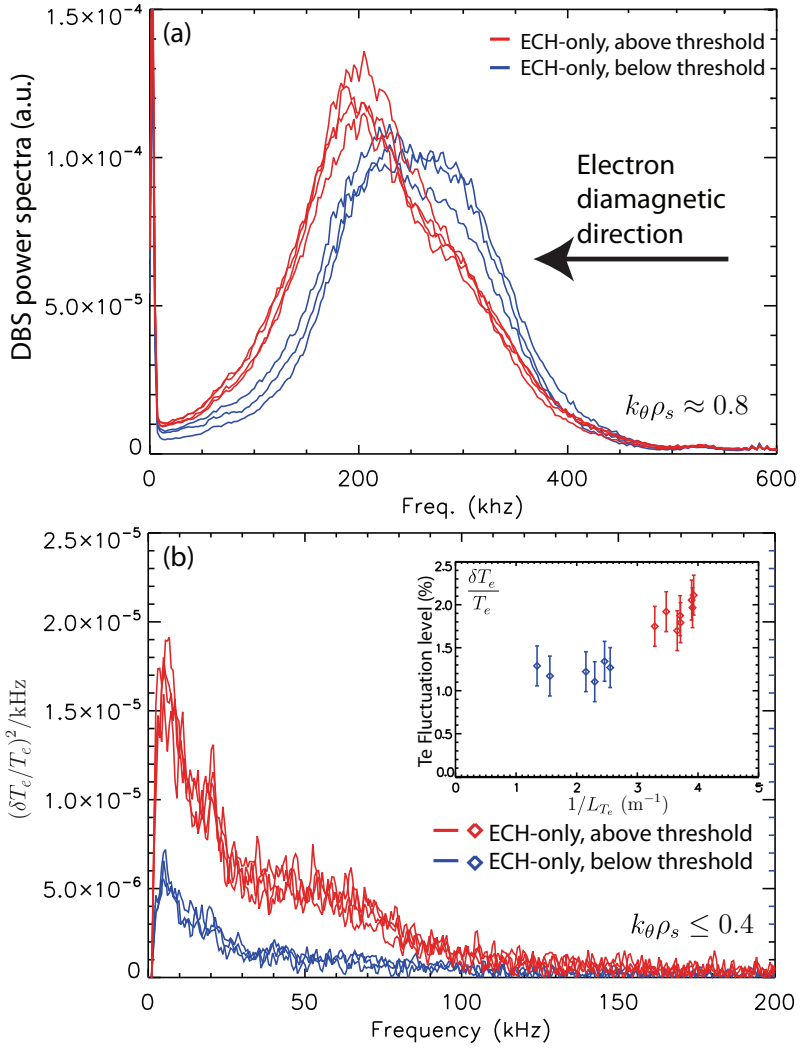

Figure 5.10: (a) DBS density power fluctuation spectra and (b) CECE electron temperature fluctuation spectra for ECH only plasmas. Inset in (b) are the integrated $\delta T_e/T_e$ levels. Symbols and lines are color-coded with blue indicating data below the critical gradient threshold and red about it. Negative direction is the electron diamagnetic direction.

higher in the (3,3) ECH arrangement case than in the (5,1) case, which is consistent with the DBS measurements and instills some confidence in the integrated methods necessary to determine the local gradient values; although, the stilted correlation between $L_{T_e}^{-1}$ and the DBS spectra does raise some questions. It is somewhat surprising that although there is a significant difference between $L_{T_e}^{-1}$ for the (2,4) case and the (5,1) case, the DBS spectra are almost identical, while the small change in $L_{T_e}^{-1}$ to (3,3) results in a large change to the spectra. This will be investigated further in Sec. 5.4 to see whether the changes to multiple parameters results in growth rate predictions consistent with the measurements and to see how mode frequency predictions compare to the measurements.

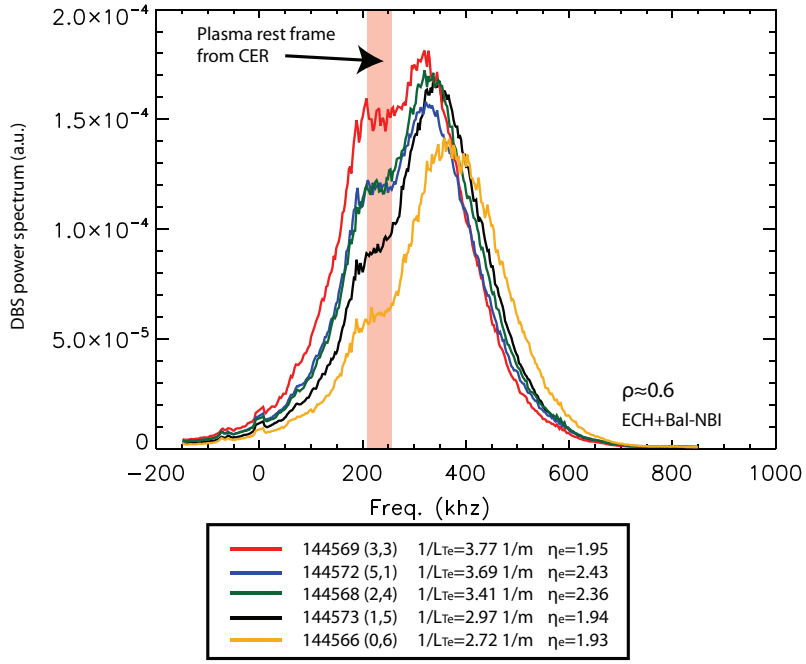

Figure 5.11: DBS density fluctuation quadrature power spectra ECH+Bal-NBI plasmas. Annotated are local values for $L_{T_e}^{-1}$ and η_e for each case. Also annotated is the plasma rest frame from CER. Negative direction is the electron diamagnetic direction.

Neither ECH+Co-NBI nor ECH+Ctr-NBI show qualitative behavior in the shape of the spectra consistent with a second mode coming in. The spectral width for DBS increases with rotation, but the mode frequency in the plasma rest frame should stay constant (assuming there are no finite flow effects or changes to flow shear, etc.). At high rotation the spectral

width from Δk becomes much larger than the mode frequency and obscures any impact of the turbulence spectrum on the measured quadrature spectrum. The spectra in ECH+Co-NBI are sufficiently Doppler shifted such that they are very nearly Gaussian, similar to Fig. 3.4. The spectra in ECH+Ctr-NBI are narrow and show no qualitative indications of two modes.

One would expect the mean frequency of the DBS spectrum to shift towards the electron diamagnetic direction with increasing $L_{T_e}^{-1}$ if ∇T_e-TEMs are being destabilized and the dominant instability below the critical gradient is ITG. Figure 5.12 shows the power-weighed mean frequency for each case in the data set, with the mean frequency at the lowest $L_{T_e}^{-1}$ (for each of the four rotations, respectively) subtracted to account for the differences in toroidal rotation. In three of the cases–ECH-only, ECH+Bal-NBI, and ECH+Co-NBI–the mean frequency shifts in the electron diamagnetic direction, consistent with expectations for ∇T_e-TEM. The trend is the opposite for ECH+Ctr-NBI, with the frequency going towards the ion diamagnetic direction. It will be pointed out later that the preponderance of the data is consistent with ∇T_e-TEM at high $L_{T_e}^{-1}$ in all four cases. It will also be shown that the crossphase measurements are consistent with a different instability dominating at low $L_{T_e}^{-1}$ in ECH+Ctr-NBI than in the other cases. An interpretation of Fig. 5.12 consistent with that data would be that the instability below the threshold in ECH+Ctr-NBI propagates in the electron diamagnetic direction faster than the ∇T_e-TEM at high $L_{T_e}^{-1}$.

The total scattered power, which is proportional to the square of the density fluctuation level (in the linear regime), can be analyzed for DBS in several ways. From the quadrature mixer outputs, $A_{DBS}\sin\varphi_{DBS}$ and $A_{DBS}\cos\varphi_{DBS}$, the amplitude of the signal, A_{DBS}, can be directly determined. The absolute density fluctuation level for DBS cannot be easily determined due to the complex scattering geometry. It is possible to cross-calibrate DBS channels using a mirror in the lab, which was done to normalize the signals to produce fluctuation spectra in Ref. [5]. Similarly, a single channel can be used to examine differences due to modifications of local plasma conditions, which is the assumption underlying the previous analysis in this section. Using the DBS-8 channel near to $\rho = 0.6$, the mean and standard deviation of A_{DBS} was calculated for the data set. The result is shown in Fig. 5.13,

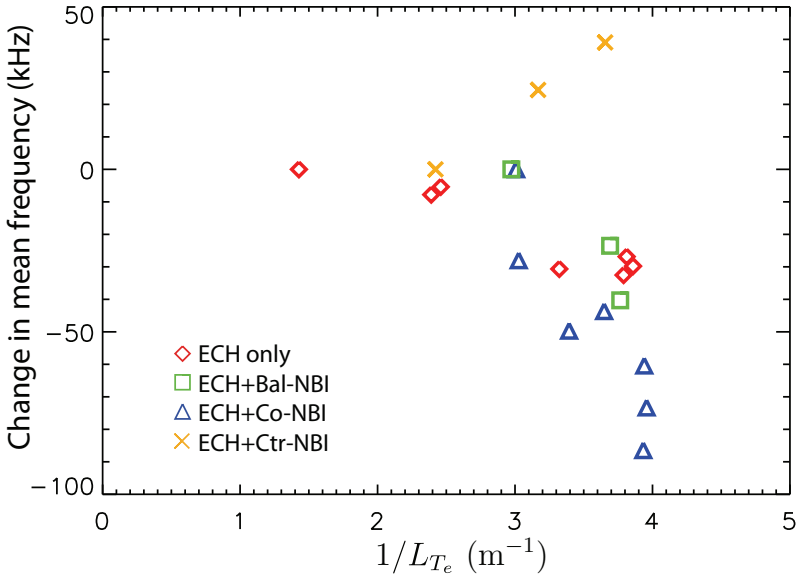

Figure 5.12: Change to power-weighted mean frequency of DBS spectra from lowest value of $L_{T_e}^{-1}$ for each NBI case. Negative direction is the electron diamagnetic direction.

where the standard deviation of A_{DBS} is used for the error bars. There are $\sim 10\%$ differences in the mean values, but overall there are no changes within the error bars.

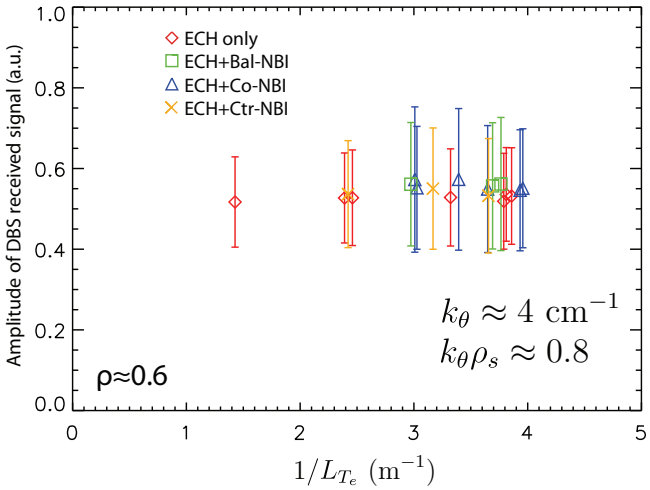

Figure 5.13: Amplitude of 67.5 GHz DBS-8 channel for complete data set. Error bars indicate standard deviation of signal.

Although there are no significant changes to the total received signal, there are clearly significant changes to frequency-localized portions of the DBS spectrum, for instance in

Figs. 5.10 and 5.11. A better estimate of the measured DBS fluctuation level is obtained taking the square root of the integrated quadrature spectrum (FFT of $S = A_{DBS}\cos\varphi_{DBS} + iA_{DBS}\sin\varphi_{DBS}$) over the frequency range of the Doppler shifted peak, omitting non-plasma related signals like the direct reflection peak at zero frequency and other noise pickup. For instance, for the ECH+Bal-NBI cases in Fig. 5.11, the spectrum is integrated from $f = -150$ kHz to $f = 850$ kHz. The result of performing this analysis for the complete data set for the same data used for Fig. 5.13 is plotted in Fig. 5.14. Figure 5.14 is consistent with Fig. 5.13 under the interpretation that the variations in the latter are muted due to the inclusion of non-plasma related information (reflections, the LO, etc.) in the analysis. Due to the large number of records, the normalized standard error is very small–smaller than the symbols. Similarly, any systematic or bias errors should have a highly correlated effect on all of the data points and not affect the observed trends. Instead, the standard deviation of the integrated spectrum over the ensemble are used for the error bars.

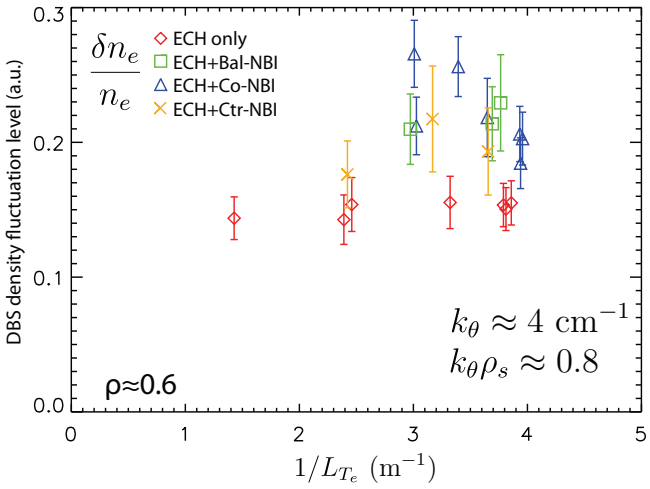

Figure 5.14: Relative amplitude of density fluctuations measured with th 67.5 GHz DBS-8 channel for complete data set. Error bars indicate standard deviation of integrated spectrum over the ensemble.

For the ECH-only points in Fig. 5.14, there is little change in amplitude despite the changes in the shape of the spectra shown in Fig. 5.10. The frequency-localized changes to the ECH+Bal-NBI spectra in Fig. 5.11 also result in little change to the integrated spectra–

the points are however within error bars of the ECH+Co-NBI points. The ECH+Co-NBI case starts higher, then arguably decreases, approaching the ECH-only level. The ECH+Ctr-NBI case is within error bars of ECH-only below $L_{T_e}^{-1}|_{crit}$ and within error bars of the ECH+Co-NBI points above $L_{T_e}^{-1}|_{crit}$. The density profiles for all cases are well-matched, but there is no core particle source in the ECH-only case, while for the other three cases there must be, due to the NBI. Since there is no particle source other than at the edge in ECH-only and the profiles are steady-state, one would expect the total particle transport to be zero. For the NBI cases, particle transport must be increased to account for the beam source–the increased intermediate-scale density fluctuations for the beam cases would consistent with higher particle transport. BES measurements were only acquired in ECH+Co-NBI plasmas and provide no information on this point.

Rather than the quadrature spectrum, the DBS amplitude spectrum can also be calculated. Figure 5.15 shows the DBS amplitude spectrum for the same cases the quadrature spectra where plotted in Fig. 5.11. There are three peaks in the spectra (ignoring zero frequency). The peaks around 400 kHz appear to be related to leakage of the Doppler shift information, which can occur, for instance, do to mixer asymmetries. The peaks around 200 kHz appear to be related to pick-up noise–those are visible throughout the shot and change little. The interesting peak occurs at about 60 kHz and appears to be directly correlated to the frequency-localized increase seen in Fig. 5.11. This will be compared to predicted mode frequencies in Sec. 5.4.1.7. More comparisons of DBS quadrature, amplitude, and phase spectra are presented in Appendix F.

5.3.3.5 Conditional averaging of intermediate-scale density fluctuation measurements

Further insight is gained into the turbulent dynamics by conditionally averaging DBS power spectra during the ECH+Bal-NBI conditions. The method used to realize balanced injection was to interlace injection from sources at different duty cycles–the total power was kept constant, but the momentum input was changing on the time scale of the beams. One

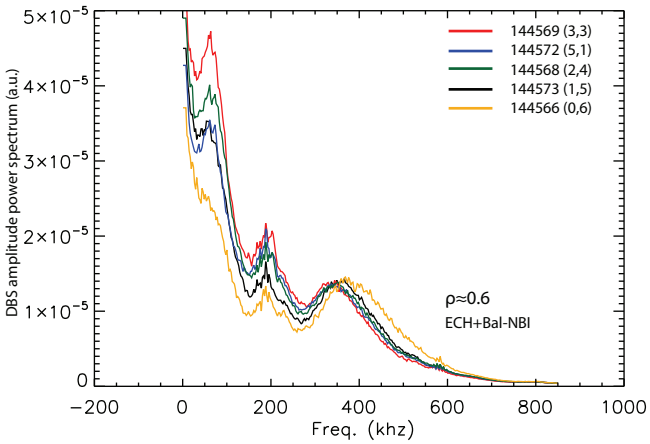

Figure 5.15: DBS amplitude power spectra for ECH+Bal-NBI plasmas.

counter-injected source, from the 210° beamline, was applied 10 ms on, 10 ms off. To acquire CER measurements of both the toroidal and poloidal plasma velocities two co-injected sources were required: a 30° source and a 330° source were each used 10 ms on, 30 ms off. Conditional averaging on the beam timing leads to two differences in the DBS spectra.

Figure 5.16 shows the result of conditionally averaging the DBS spectra on four different NBI timing conditions. The large total sample time period left normalized random errors of only $\sim 3\%$, even for the sub-ensembles for the beams with 25% duty cycle. One point to be made with Fig. 5.16 is that there is no significant difference observed between the cases using only the 30° source, only the 330° source, or the sub-ensemble using both. This means that there should be no systematic error introduced by taking the toroidal and poloidal CER measurements from different time periods. The second point is that there are two differences in the spectra during the counter-injected beam. First, the spectrum is shifted in the counter-direction by $\sim 10 - 15$ kHz–which corresponds to a $\sim 300 - 400$ eV/m change to E_r if the shift is completely due to the equilibrium radial electric field. The second is an increase in the amplitude of the spectrum over $\sim 200 - 250$ kHz, the same frequency range shown in Fig. 5.11 to monotonically increase with $L_{T_e}^{-1}$.

These two changes–frequency shift and frequency-localized amplitude increase–are seen

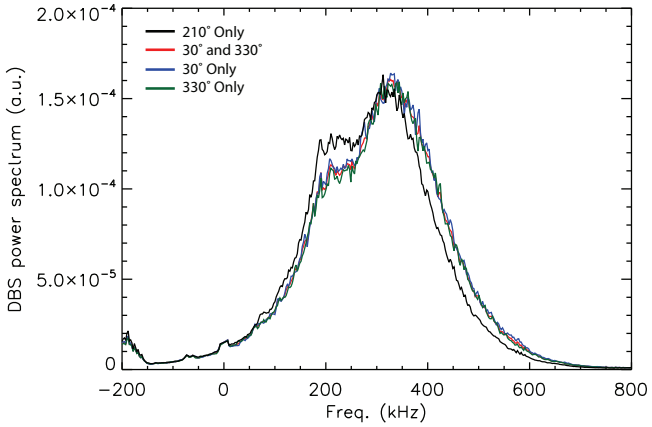

Figure 5.16: Conditional averaging of DBS spectra on NBI timing. Negative direction is the electron diamagnetic direction.

systematically for the ECH+Bal-NBI plasmas. This is shown in Fig. 5.17 three of the cases in Fig. 5.11 (same colors are used), which have been conditionally-averaged to create two sub-ensembles: the first while the counter-injected beam is on and the second while either one of the co-injected beams are on. The annotated average values of $L_{T_e}^{-1}$ refer to the average over the complete time period. The frequency shift and frequency-localized amplitude increase are observed for all cases.

Only three of the five cases are shown as only those cases had profile reflectometry data, which allows the density gradient to also be conditionally averaged. The profile reflectometry and ECE data were conditionally averaged on the beam timing. In all three cases, $L_{n_e}^{-1}$ increased by about 1% in the counter-beam periods and $L_{T_e}^{-1}$ decreased by about 1%–the exact opposite of what one would expect for the observed trend to be attributed to η_e. The small magnitude of the change also raises questions. For instance, consider the black lines. The change in $L_{T_e}^{-1}$ over the entire time window from the black case to the blue case is about 20%, while the changes to the spectra due to the conditional averaging are similar to the change between the black case to the blue case. It seems highly unlikely that the condtional averaging of the DBS spectra can be related to the $\sim$ 1% modifications to the equilibrium gradients. The other obvious parameter to consider would be the rotation or its shear; however, both CER beams are Co-beams, so there is not an independent measurement

for the Ctr-beam time periods. Furthermore, the DBS-8 channels are too sparse–the three closest channels are at $\rho \approx 0.5$, 0.6, and .7–for a reliable measurement of the radial electric field shear to be determined. DBS-5 was aligned for reflectometry and cannot be used to determine the shear either. Attributing the change to radial electric field shear would also be somewhat surprising, since that parameter was concluded to be relatively unimportant for the low-k and transport analysis. We lack the measurements to make a definative conclusion regarding the explanation for the conditionally-averaged DBS spectra.

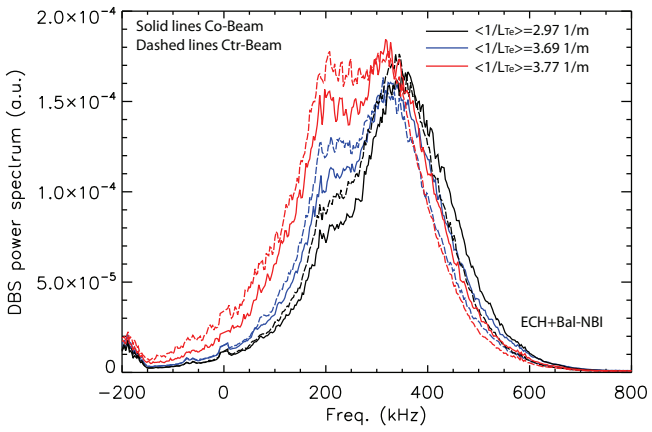

Figure 5.17: Conditional averaging of DBS spectra on NBI timing for three average values of L_{Te}^{-1} in ECH+Bal-NBI plasmas. Solid lines are during co-injection and dashed lines are during counter-injection. Negative direction is the electron diamagnetic direction.

One of the six ECH gyrotrons was modulated at 50% duty cycle–50 ms on, 50 ms off–so a question that could be raised is whether the changes in Fig. 5.17 are actually due to coincident phase locking to the ECH modulation. This does not appear to be the case. The result of conditionally averaging the same DBS spectra on the modulated gyrotron is shown in Fig. 5.18. Very little change is observed to be correlated with the ECH modulation for any of the three ECH+Bal-NBI cases.

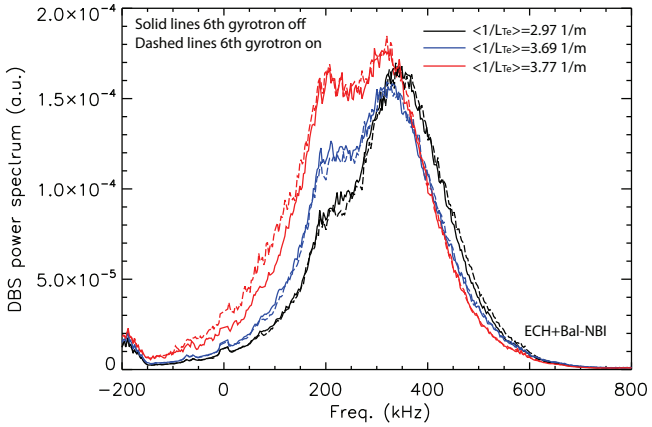

Figure 5.18: Conditional averaging of DBS spectra on ECH modulation for three average values of $L_{T_e}^{-1}$ in ECH+Bal-NBI plasmas. Solid lines are while the modulated gyrotron is off and dashed lines while it is on. Negative direction is the electron diamagnetic direction.

5.3.3.6 α_{n_e,T_e} measurements

Measurements of the crossphase between electron temperature and density fluctuations, α_{n_e,T_e}, were acquired simultaneously with the $\delta T_e/T_e$ measurements by coupling the CECE system to a tunable reflectometer array, see Sec. 3.8 for more details. The reflectometer array, DBS-5, was launched at about $-1.5°$ to the horizontal, which run-day ray tracing calculations indicated was normal incidence at $\rho \approx 0.6$. Although the intention was to overlap DBS-5 with the CECE channels at $\rho \approx 0.6$ most shots also showed significant coherency with the CECE channels at $\rho \approx 0.55$. Presented in this section are the results from the closest pair of DBS-5 and CECE channels to each location in each time period. Appendix D has additional analysis, showing results from various combinations of the 5 reflectometry and 4 CECE channels within time periods.

Figure 5.19(a) shows the electron temperature fluctuation power spectra for the ECH+Bal-NBI case. Figure 5.19(b-c) show the coherency and associated crossphase determined by cross-correlating the reflectometer and CECE channel closest to $\rho = 0.6$. As noted before, the $\delta T_e/T_e$ power spectrum monotonically increases with $L_{T_e}^{-1}$. At the same time, the coherency, γ_{n_e,T_e}, also increases. Since the auto-power of an ECE channel is dominated

by statistical fluctuation associated with the mean T_e, while only real plasma fluctuations would be expected to correlate with density fluctuations, one would expect γ_{n_e,T_e} to increase if $\delta T_e/T_e$ increases, all else the same. Over the frequency range where significant coherency is measured, a relative constant crossphase is observed. The measured crossphase also monotonically changes with $L_{T_e}^{-1}$. This may imply two physically meaningful changes. First, the crossphase between fluctuating fields is a fundamental characteristic of instabilities–its measurement acts as a 'fingerprint' for the dominant instability in the plasma. Second, change to α_{n_e,T_e} implies that the directly transport related crossphases, $\alpha_{n_e,\varphi}$ and $\alpha_{T_e,\varphi}$, may also change.

To determine a single value for the crossphase in each condition, the α_{n_e,T_e} frequency spectra were averaged over the frequency range where γ_{n_e,T_e} was 0.8 times or greater than its maximum value in each case. The results for the complete data set is plotted in Fig. 5.20

For the $L_{T_e}^{-1}$ scan in ECH+Co-NBI and ECH+Bal-NBI, the trends, and values, in crossphase are remarkably similar to previous experiments [15–17, 19]; there it was concluded that the trend in crossphase was associated with a change in the dominant instability, from ion temperature gradient (ITG) or mixed ITG/TEM at low (more negative) values of α_{n_e,T_e} to dominant TEM at higher values. In those experiments, ECH was added near the axis of Ohmic and NBI-heated L-mode plasmas, which had large effects on T_e/T_i and collisionality, but caused a comparatively small change to $L_{T_e}^{-1}$. Here, with targeted off-axis ECH, large changes to $L_{T_e}^{-1}$ were induced. Either set of parameter changes would be expected to favor ∇T_e-TEM instability.

The ECH-only points in Fig. 5.20 exhibit a reduced slope in comparison to ECH+Co-NBI. The different trend may be consistent with ∇n_e-driven TEM below the $L_{T_e}^{-1}$ threshold rather than ITG, which was also suggested for ECH only plasmas in Refs. [9, 12]. The narrowing of the spectrum in Fig. 5.10 may be consistent with the explanation, as one would expect opposite dependencies of the two TEM branches on η_e.

The crossphase data from ECH+Ctr-NBI is non-monotonic, higher-valued at low $L_{T_e}^{-1}$, and exhibits radial dependence not observed for the other cases. The two points with $\alpha_{n_e,T_e} \approx$

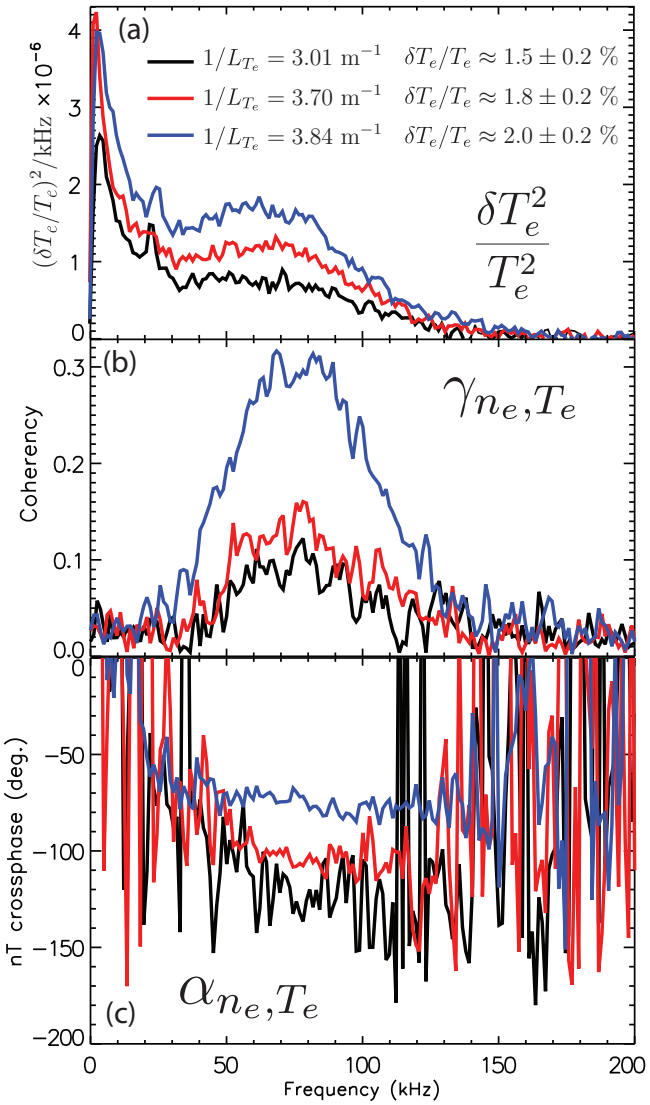

Figure 5.19: For ECH+Bal-NBI plasmas: (a) electron temperature fluctuation power spectrum with values of $L_{T_e}^{-1}$ for measurements and integrated fluctuation levels annotated, (b) coherency between closely reflectometer and correlation electron cyclotron emission channel, and (c) crossphase associated with each coherency.

$+50°$ are both from $\rho \approx 0.55$ in different shots. The pairs of points at $L_{T_e}^{-1} \approx 2.5$ m^{-1} and 2.8 m^{-1} that differ by $\sim 100°$ are from different locations in the same discharges. The higher Z_{eff} in ECH+Ctr-NBI may play a role. Higher Z_{eff} would be expected to dilute the main ion species and have a stabilizing effect on ITG; however, at high Z_{eff} additional instabilities can become relevant, such as a Carbon-ITG [107]. The information in Table 5.1 shows that with Z_{eff} higher in ECH+Ctr-NBI cases, the carbon density scale length is reduced by about a factor of two in comparison to ECH+Co-NBI, which is what one would expect for a Carbon-ITG to be destabilized; that is, η_i for carbon increases. Ref. [107] also discussed another instability, which occurs for oppositely directed main ion and impurity density gradients even when all temperature gradients are zero. Little work has been done on the toroidal versions of these modes. Speculatively, it might be that oppositely directed density gradients are sufficient, but not necessary for the instability, and that what is also sufficient is a large enough difference between the gradients. The existence of a different mode (or as is discussed later, modes at different wave numbers) in ECH+Ctr-NBI is supported the observation in Fig. 5.12 of an opposite trend in the mean frequency of the DBS spectrum with increasing $L_{T_e}^{-1}$.

At high $L_{T_e}^{-1}$, the cases in Fig. 5.20 converge, consistent with ∇T_e-driven TEM turbulence in all four.

In Sec. 5.4 a number of the hypotheses suggested by the data concerning dominant instabilities in the various regimes are tested.

The unusual result in ECH+Ctr-NBI plasmas at low $L_{T_e}^{-1}$ warrants further analysis. Figure 5.21 shows the coherency and crossphase between the four CECE channels and a DBS-5 channel that is approximately at the midpoint between the two CECE locations, in ECH+Ctr-NBI (1, 4.5) shot 144575. Using a reflectometry channel in between the CECE locations minimizes any bias introduced by using different radial separations between the correlated channels and is why the coherencies in Fig. 5.21(a) are all of similar value. The difference in radial location for ECH+Ctr-NBI plasmas was mentioned above in the discussion of Fig. 5.20. Figure 5.21 shows the difference in the crossphase spectra themselves.

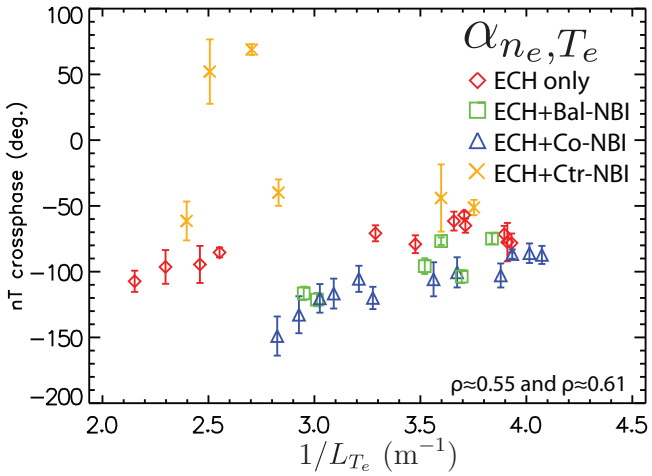

Figure 5.20: Mean α_{n_e,T_e} for complete data set from both $\rho \approx 0.55$ and $\rho \approx 0.61$.

The crossphase spectra for the channel pair at each radial location are very similar, as would be expected. There are two significant difference between the radial locations: one, the inner location has positive crossphase values, which have not been observed under any other conditions; and, two, there is a definite slope to the crossphase with frequency at the outer location, which is also not observed under other conditions. This data, where density fluctuations at one radial location show significantly different crossphases with temperature fluctuations at different radial locations will provide a strong test of non-linear gyrokinetic simulations in future work.

5.3.3.7 α_{n_e,T_e} probability distribution function

The probability distribution function of the crossphase between turbulent fields can yield information about the nonlinear dynamics of the turbulence [264]. In particular, it has been examined in recent studies of damped eigenmodes in plasma turbulence [61]. A quasilinear estimate of the flux would use a single value of the crossphase for each unstable mode. It was argued in Ref. [61] that, in nonlinear simulations, energy transfered to damped eigenmodes not only broadened the crossphase PDF, but resulted in average transport phases that drove more transport, in comparison to the single quasilinear crossphase.

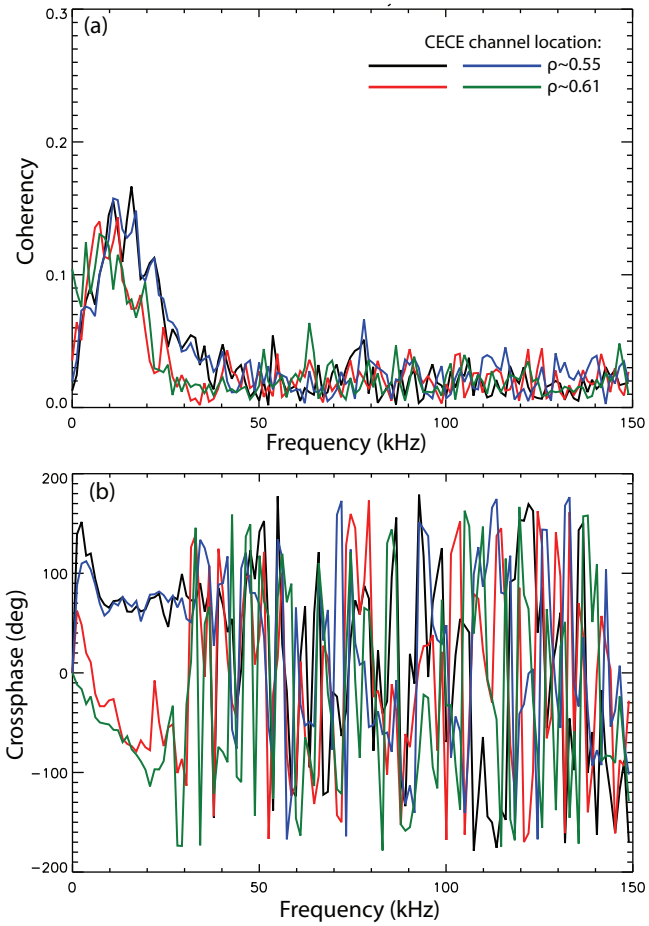

Figure 5.21: (a) Coherency and (b) crossphase from correlation between each of the four CECE channels and a DBS-5 channel approximately equidistant from the CECE channel pairs.

The crossphase trends for all but ECH-only in Fig. 5.20 indicate significant changes to the dominant instability. The natural place to look for signs of changes similar to Ref. [61] is the ECH-only scan. The PDFs of the crossphase for three values of $L_{T_e}^{-1}$ are shown in Fig. 5.22. Note that at the highest $L_{T_e}^{-1}$, PDF values above 0.08 are truncated to keep all plots on the same scale. Averaging over the frequency range with significant coherency actually results in little change to the normalized width of the PDFs; however, a qualitative change in evident. From Fig. 5.20(a) to (c) more area in frequency-angle space is found to be at higher amplitude. Twenty bins are used, so the expected value for a uniform random variable is 0.05. Since probability is conserved, for it to rise somewhere it must fall elsewhere (*i.e.* the noise floor is lowered, but the integrated PDF must always be equal to unity for each frequency)–this is the explanation for the changes at positive frequencies.

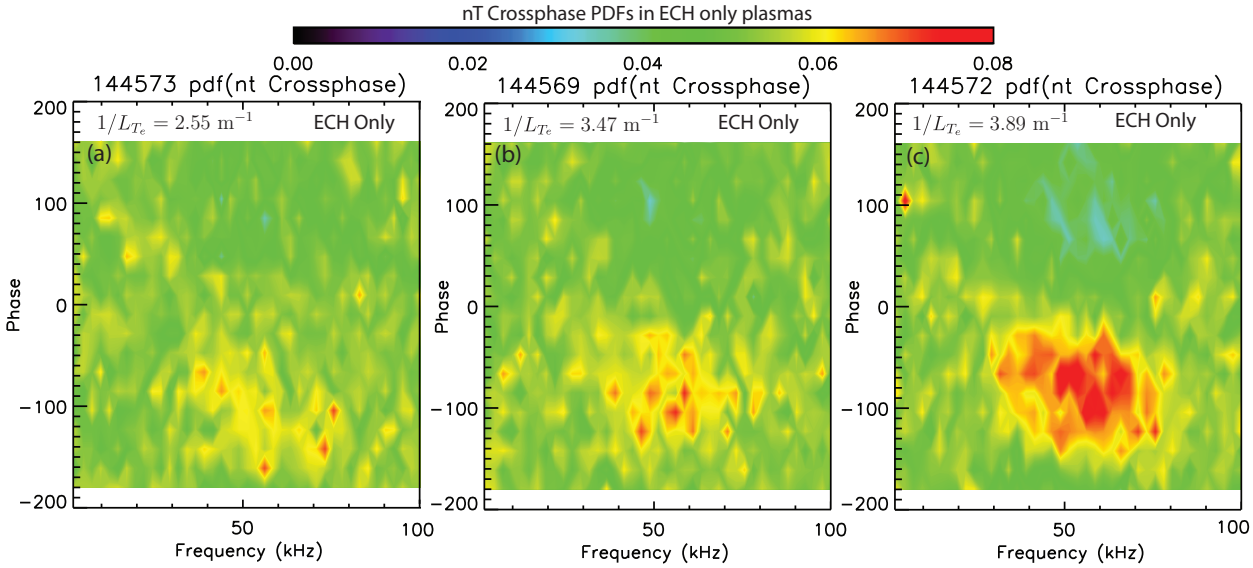

Figure 5.22: Probability distribution of α_{n_e,T_e} in ECH-only plasmas at (a) $L_{T_e}^{-1} = 2.55$ m^{-1}, (b) $L_{T_e}^{-1} = 3.47$ m^{-1}, and (c) $L_{T_e}^{-1} = 3.89$ m^{-1}.

Figure 5.23 shows the crossphase PDF analysis performed for three values of $L_{T_e}^{-1}$ in the ECH+Bal-NBI scan. Note the different scale for Fig. 5.23. The same qualitative feature of stronger distribution over an area of frequency-crossphase space is present. The analysis

artifact of the depletion of the PDF for positive frequencies is more pronounced. Figure 5.24 shows the data in Fig. 5.23 averaged over 50-100 kHz and normalized, with the minimum subtracted. Consistent with Fig. 5.20, the mean crossphase changes value with $L_{T_e}^{-1}$. As noted in the discussion for the crossphase PDF plots for ECH-only, there does not appear to be a significant broadening of the frequency-averaged spectrum. The qualitative feature of stronger PDF over an area of frequency-crossphase does not appear to broaden the crossphase spectrum. The expectation that the crossphase spectrum should broaden nonlinearly in Ref. [61] considered comparisons of quasilinear versus nonlinear conditions. More recent work has argued that damped eigenmodes play an important role in a wide variety of plasma conditions [62, 265] and has argued they are responsible for turbulence induced magnetic stochasticity [105, 266, 267]; however, work concerning expectations for nonlinear behavior under different drive strengths–the relevant comparison for the data presented–is lacking.

5.3.3.8 Low frequency flow measurements

Low frequency flow measurements were also acquired with DBS-8 during the experiment. The dependence of these flows on co- versus counter-NBI was already described in Sec. 4.6.2. Briefly, the result shown there was that both the GAM and the other low frequency flows in the tokamak core were significantly weaker–almost completely gone–in counter-injected plasmas. It was argued that a direct dependence on rotation was most consistent with the data and that indirect dependencies through the NBI sources, such as differing Z_{eff}, or other hypothesizes were not sufficient to explain the observations.

5.4 Comparison to gyrofluid predictions

The fluctuation measurements detailed in Sec. 5.3 are compared in this section to predictions from linear gyrofluid calculations. These models are described more thoroughly in Sec. 2.2. The main result from Sec. 5.3–the observation of a critical gradient for electron temperature fluctuations that was directly correlated with increased electron heat flux–is also seen in

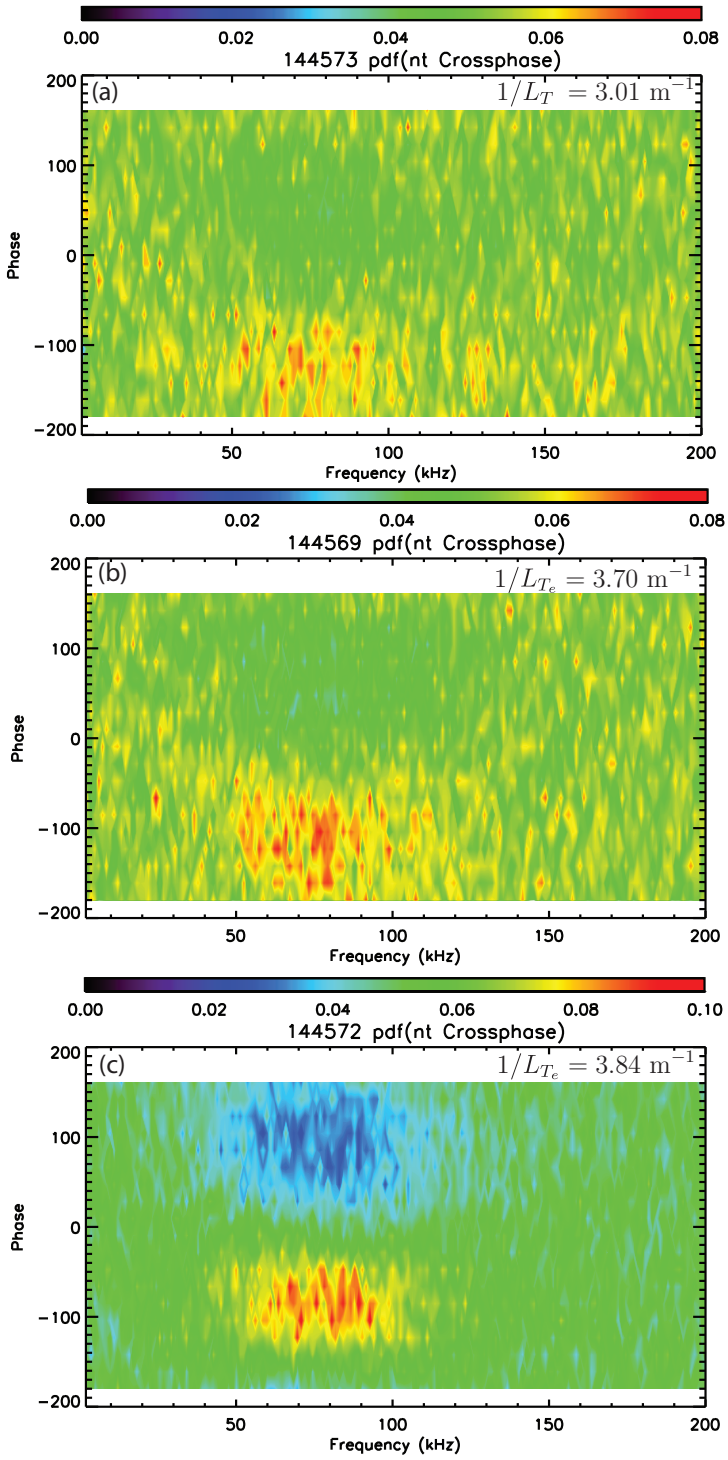

Figure 5.23: Probability distribution of α_{n_e,T_e} in ECH+Bal-NBI plasmas at (a) $L_{T_e}^{-1} = 3.01\ \mathrm{m}^{-1}$, (b) $L_{T_e}^{-1} = 3.70\ \mathrm{m}^{-1}$, and (c) $L_{T_e}^{-1} = 3.84\ \mathrm{m}^{-1}$.

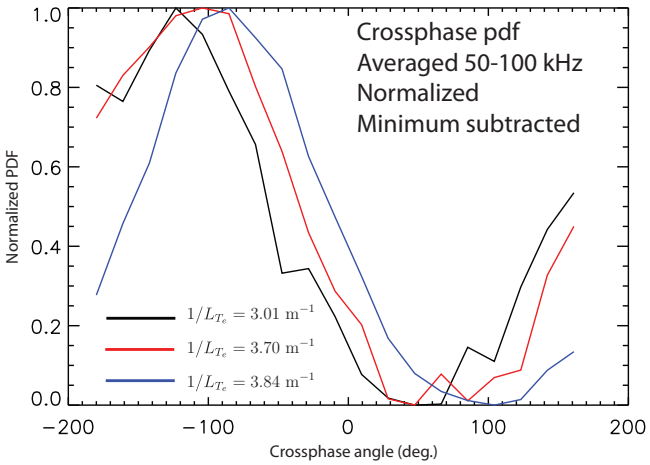

Figure 5.24: Frequency-averaged, minimum-subtracted probability distribution of α_{n_e,T_e} in ECH+Bal-NBI plasmas.

model predictions. Furthermore, linear calculations indicate that the instability threshold is governed by the dimensionless parameter $\eta_e = L_{n_e}/L_{T_e}$ more so than by $L_{T_e}^{-1}$ alone. Both linear gyrofluid calculations and the electron temperature fluctuations measurements exhibit a sharp increase at $\eta_e \approx 2$.

More detailed information about input setups and analysis is provided in Appendix C.1. Linear gyrokinetic calculations were also attempted; results are briefly discussed in Appendix C.

5.4.1 Comparison to gyrofluid predictions from TGLF

The Trapped-Gyro-Landau-Fluid code (TGLF) [57] is used in this section to compare to experimental measurements. Version 1.93 of the code was used, which includes the most recent collision model [59]. The collision model is for electron-ion pitch angle scattering only. No energy diffusion terms are included.

5.4.1.1 Identification of critical gradient

Figure 5.25 shows linear gyrofluid growth rate calculations from TGLF at $\rho = 0.6$ for the data set. The fastest growing mode propagating in the electron diamagnetic direction is plotted for each wave number. The calculations were performed over the wave number range $0.0 \leq k_\theta \rho_i \leq 1.0$, which explains the variation of the highest plotted values for $k_\theta \rho_s$. The ion temperature changes significantly for ECH-only plasmas, whereas the electron temperature was better matched for the data set, which is why it was chosen to plot the growth rates as a function of $k_\theta \rho_s$. The general trend is observed that the growth rate spectrum increased with $L_{T_e}^{-1}$. The spike in the dark blue line, which is actually the lowest value of $L_{T_e}^{-1}$, appears to be due to an ITG mode propagating in the electron direction: if $L_{T_i}^{-1}$ is increased by 20% the mode propagates in the ion direction and the blue line flattens (see Sec. 5.4.1.6).

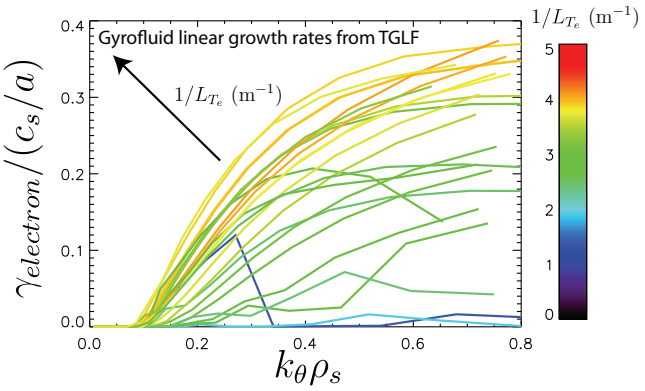

Figure 5.25: Linear gyrofluid growth rates for the fast growing mode propagating the electron diamagnetic direction for the complete data set at $\rho = 0.6$. Lines are color-coded by value of $L_{T_e}^{-1}$.

To compare to the electron temperature fluctuation measurements, the growth rates in Fig. 5.25 are averaged over the approximate wave number sensitivity range of the CECE diagnostic, this averaged growth rate is denoted by brackets: $\langle \gamma_{electron}/(c_s/a) \rangle$. The CECE beam waist diameter has been measured to be about 3.8 cm. To leading order, this corresponds to a wave number range for the experiment of $0.0 \leq k_\theta \rho_s \leq 0.4$. Averaging the growth rates in Fig. 5.25 over that wave number range and plotting the result as a function of $L_{T_e}^{-1}$

yields Fig. 5.26. The lowest value of $L_{T_e}^{-1}$ corresponds to the dark blue line in Fig. 5.25 (ITG case). There is a general feature of the plot that the average growth rates quickly increase above $L_{T_e}^{-1} \approx 2.5$ m^{-1}; however, additional dependencies affect the calculation, leading to scatter of the data points.

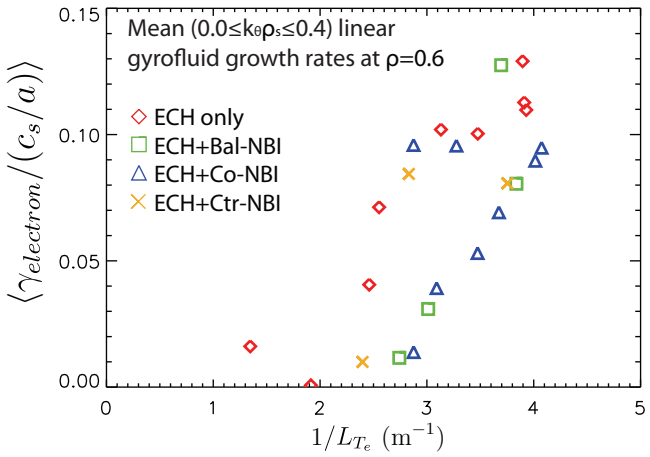

Figure 5.26: Linear gyrofluid growth rates averaged over $0.0 \leq k_\theta \rho_s \leq 0.4$ as a function of $L_{T_e}^{-1}$.

The dimensionless quantity $\eta_e = L_{n_e}/L_{T_e}$ shows a better defined transition for the electron temperature fluctuation levels and the averaged electron-direction growth rates. This is shown in Fig. 5.27, where $\langle \gamma_{electron}/(c_s/a) \rangle$ calculations and $\delta T_e/T_e$ measurements are plotted as a function of η_e. Vertical dashed lines are annotated at $\eta_e = 1.9$ and a horizontal dashed line in Fig. 5.27(b) is annotated at 1.5%. The lowest $L_{T_e}^{-1}$ point in Fig. 5.27(a) is again attributed to an ITG mode. In both Fig. 5.27(a) and (b) there is a rapid increase near $\eta_e = 2$, with a better defined abrupt change observed for the CECE measurements at about $\eta_e = 1.9$. One can see that the lines at $\eta_e = 1.9$ and 1.5% in Fig. 5.27(b) effectively segregate the data into two quadrants. For the most part outside of uncertainties, $\delta T_e/T_e < 1.5\%$ for $\eta_e < 1.9$ and $\delta T_e/T_e > 1.5\%$ for $\eta_e > 1.9$, with nearly step function-like behavior in the neighborhood of $\eta_e = 1.9$. The sharp increase is consistent with the onset of a linear instability. The consistency between the linear calculation and experimental results for the critical gradient indicate that there is no non-linear upshift of the critical gradient, which is

consistent with the simulation results referenced above.

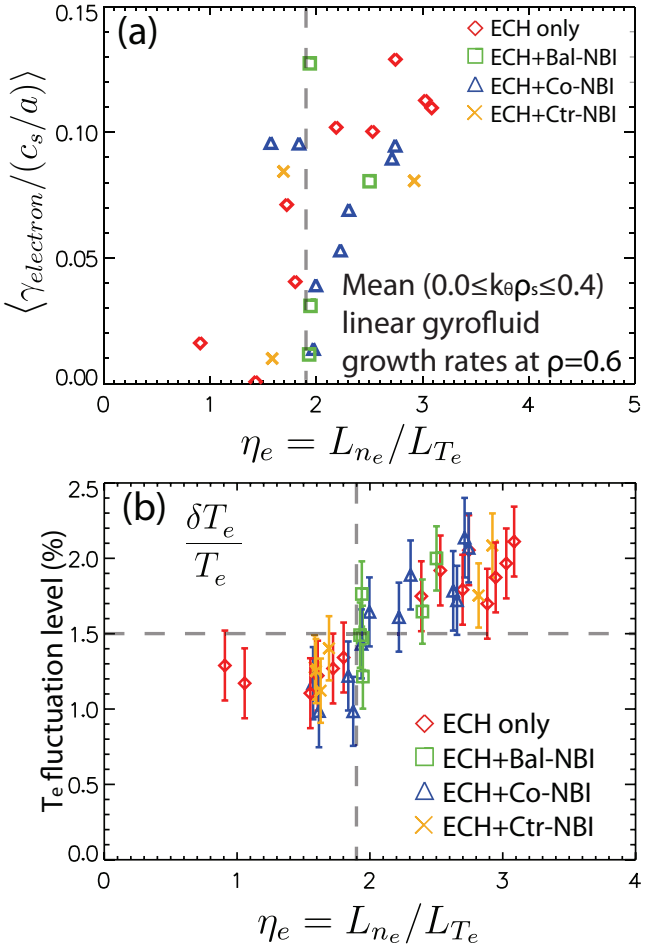

Figure 5.27: (a) Linear gyrofluid growth rates averaged over $0.0 \leq k_\theta \rho_s \leq 0.4$ and (b) $\delta T_e/T_e$ measurements as a function of η_e. Dashed lines annotated for reference.

5.4.1.2 TGLF predicted change to the ratio $(\delta T_e/T_e)/(\delta n_e/n_e)$

It was written in Sec. 5.3.3.3 that it has been argued in past work that an increase in the ratio $(\delta T_e/T_e)/(\delta n_e/n_e)$ is an indication of a transition to TEM dominated turbulence. The argument in Ref. [89] relied on comparing experimental measures showing an increase in that ratio to linear growth rate calculations for ITG and TEM. That calculation is performed here for the ECH+Co-NBI plasmas, where both BES measurements of long wavelength density fluctuations and CECE measurements of long wavelength electron temperature fluctuations

were acquired. Take $\hat{\gamma}$ to be defined as

$$\hat{\gamma} = \frac{\langle \gamma_{electron} \rangle_{CECE}}{\langle \gamma_{ion} \rangle_{BES}}. \tag{5.7}$$

The brackets indicate that the mean growth rate over the approximate sensitivity for each diagnostic was used. For CECE $0.0 \leq k_\theta \rho_s \leq 0.4$ and for BES $0.0 \leq k_\theta \rho_s \leq 0.5$. $\gamma_{electron}$ are growth rates of modes propagating in the electron diamagnetic direction and γ_{ion} the ion direction. The result for all of the ECH+Co-NBI time periods is shown in Fig. 5.28. Except for one point, the ratio $\hat{\gamma}$ generally increases with the stability parameter η_e found in Sec. 5.4.1.1; that is, the ratio $(\delta T_e/T_e)/(\delta n_e/n_e)$ is consistent with an increase of the ratio between TEM and ITG growth rates.

The point that does not agree with the trend is interesting to note, since there are two cases in the plot that had the exact same heating applied: Co-NBI beams and ECH (0, 5.5). Those two shots were 144577 and 144566. One significant difference is Z_{eff}, which was about 3.1 for 144577 and about 2.2 for 144566. Figure 5.9 has data only from 144566 and *not* 144577, so the aberrant point in Fig. 5.28 does not contradict Fig. 5.9 or conclusions drawn from it. Explanations for the outlier include the possibility that, like one of the ECH-only points, the fast growing ITG could be propagating in the electron diamagnetic direction, complicating the comparison. The frequency of the fastest growing mode propagating in the ion direction is $\lesssim 0.01\ c_s/a$ for $k_\theta \rho_s \lesssim 0.4$. It could be those are not actually the fastest growing ITG modes, leading to the aberrant point.

5.4.1.3 Instability dependencies beyond η_e

The spread in the data points in Fig. 5.27 and outlying points like the 144577 case in Fig. 5.28 imply that there may be additional physical parameters affecting mode stability beyond $L_{T_e}^{-1}$ and $L_{n_e}^{-1}$.

Figure 5.29 shows the averaged electron direction growth rates ($0.0 \leq k_\theta \rho_s \leq 0.4$) plotted as a function of (a) $L_{T_e}^{-1}$, (b) η_e, (c) $\eta_a \rho_{max}/L_{n_D}$, and (d) $\eta_a \nu_{ei}/(c_s/a)$. The outlying point in Fig. 5.29(a-c) for the lowest abscissa for each plot is the ITG case that propagates slightly

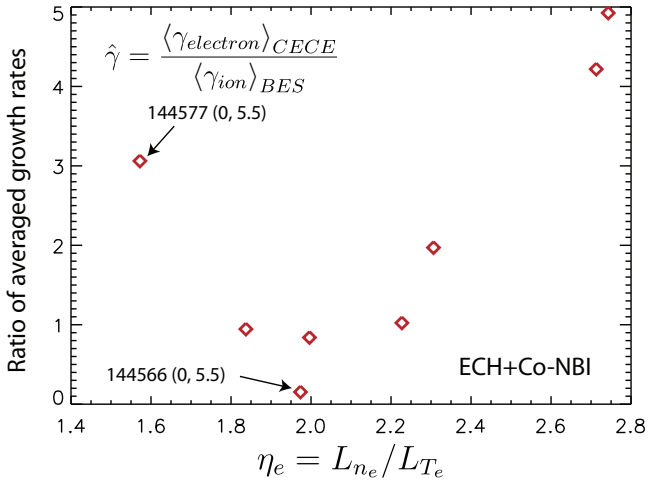

Figure 5.28: Ratio of averaged electron direction and ion direction linear gyrofluid growth rates as a function of η_e. Arrows indicate two cases of interest that are discussed in text.

in the electron diamagnetic direction (see Sec. 5.4.1.6). The plots as a function of $L_{T_e}^{-1}$ and η_e were discussed earlier and are included for reference.

Two composite parameters were found that qualitatively reduce the scatter in the plots. Fig. 5.29(c) is plotted against $\hat{\eta} = \eta_e \rho_{max}/L_{n_D}$ (ρ_{max} is used instead of a_0 for consistency with other plots; for reference $a_0 \approx 0.6$ m and $\rho_{max} \approx 0.79$ m), where $L_{n_D}^{-1}$ is the inverse deuterium density scale length. The two densities that are directly measured are electrons and carbon. The outlying point at $\hat{\eta} \approx 4$ is significantly different from the other cases for another parameter, the inverse carbon density scale length, $L_{n_C}^{-1}$. That point has both the lowest $L_{n_C}^{-1}$ of the data set, less than 1/10 of the mean $L_{n_C}^{-1}$, and the highest $L_{n_D}^{-1}$, 60% higher than the data set mean.

The second composite parameter found to reduce the scatter is $\tilde{\eta} = \eta_e \nu_{ei}/(c_s/a)$, which is the abscissa in Fig. 5.29(d). The plot as a function of $\tilde{\eta}$ reduces the scatter for all but about 5 data points, which align vertically at $\tilde{\eta} \approx 1.7$. The result shown in Fig. 5.29(d) should be considered odd for at least two reasons: first, the electron direction ITG point aligns with the rest of the points; second, TEM growth rates should decrease with increasing collisionality, as is shown in Fig. 5.38 (although η_e and $\nu_{ei}/(c_s/a)$ are not independent parameters). Other than the fact that it reduces the scatter and therefore hints at additional dependencies, no

further conclusions are drawn. Just as it is later shown that complications exist for simple expectations for ITG modes (*e.g.* direction of propagation), these results show that using the real measured profiles for inputs reveals dependencies not expected by over-simplified theory.

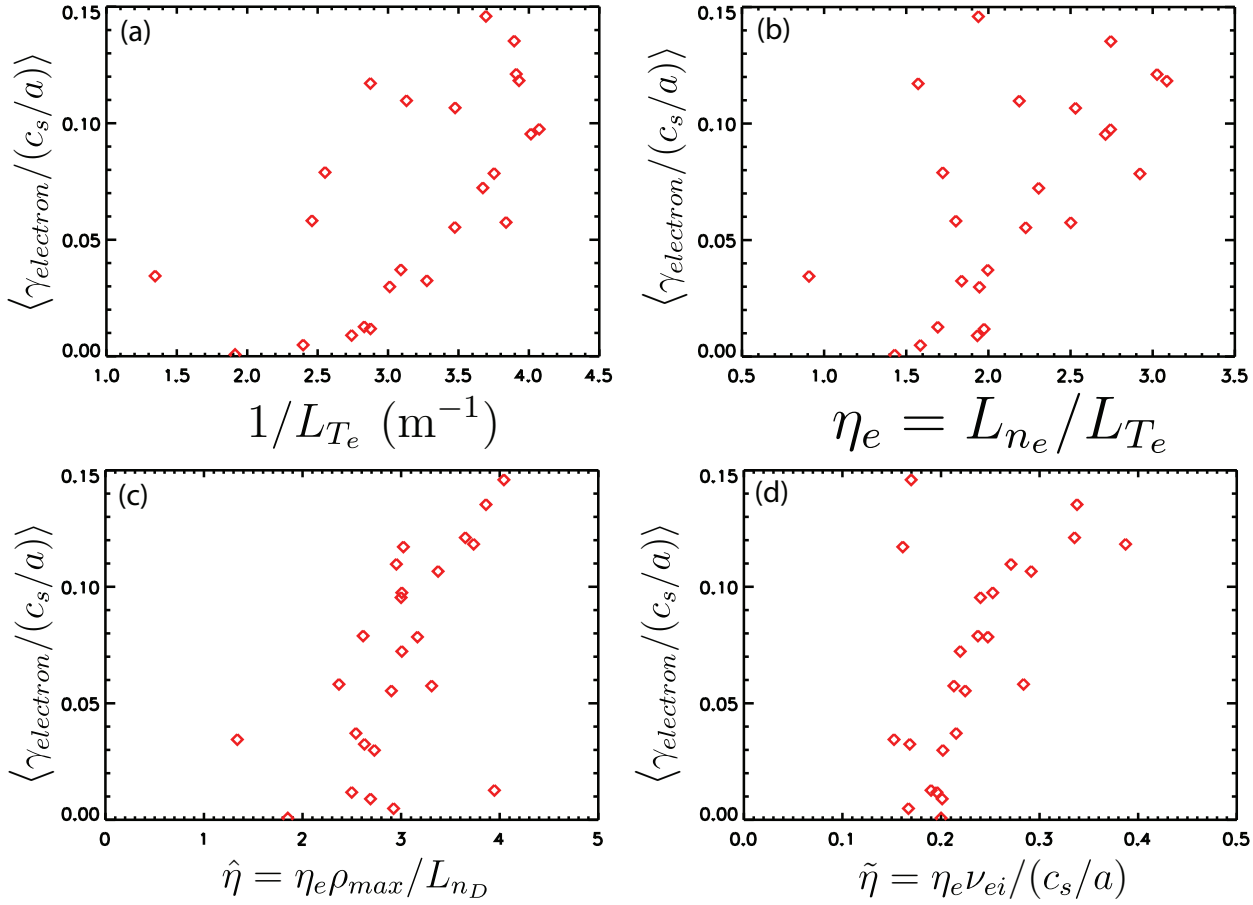

Figure 5.29: Averaged linear gyrofluid growth rates of fastest propagating mode in the electron direction as a function of (a) $L_{T_e}^{-1}$, (b) η_e, (c) $\eta_a \rho_{max}/L_{n_D}$, and (d) $\eta_a \nu_{ei}/(c_s/a)$.

5.4.1.4 TGLF predictions for α_{n_e,T_e}

In addition to growth rates, TGLF can calculate the linear crossphase angle between quantities. The calculations are done for each wave number, which makes direct comparisons with experimental results difficult; however, interpretations of data can be tested.

One interpretation given in Sec. 5.3.3.6 was that the dominant mode for ECH+Co-NBI plasmas below the critical gradient was ITG. The crossphase angle between electron density and temperature fluctuations for the fastest growing mode propagating in the ion diamagnetic direction (ITG modes) as a function of wave number is plotted for several ECH+Co-NBI cases in Fig. 5.30. The portion of the $1/L_{T_e} = 2.88$ 1/m line at exactly zero degrees is due to those modes having exactly zero growth rates. Curves of the same color indicate plasmas with the same ECH arrangement. There is a general trend that the crossphase starts near $-90°$ at low-k and gradually decreases until the two fields are out of phase. The rate at which the crossphase changes with wave number increases with $L_{T_e}^{-1}$. The lines are constructed from a finite number of wave numbers, which results in the large vertical changes visible where the values cross 180°. None of the curves have data points in the region $-90° \lesssim \alpha_{n_e,T_e} \lesssim 170°$. The attribution of the low $L_{T_e}^{-1}$ points from ECH+Co-NBI in Fig. 5.20, where α_{n_e,T_e} was about $-150°$, is consistent with the TGLF predictions for the ITG crossphase in Fig. 5.30 over the measured wave numbers.

Considering the average crossphase over measured wave numbers ($0.0 \lesssim k_\theta \rho_s \lesssim 0.4$), the slope changes in Fig. 5.30 would result in the average crossphase decreasing as $L_{T_e}^{-1}$ is increased. That would be the opposite trend from what was measured experimentally and plotted in Fig. 5.20, which would contradict an explanation attributing the experimental trends to ITG alone.

The qualitative features of the ion direction modes are generally the same for the other three rotation cases.

Figure 5.31 show the crossphase for the fastest growing modes propagating in the electron diamagnetic direction (TEMs) for the same cases the ion modes were shown in Fig. 5.30. The portions of curves at low-k at exactly zero degrees are again due to those modes being stable (zero growth rate). Generally, the TEM crossphases start at about $-70°$ and increase with wave number until about $+70°$ is approached.

The ITG modes in Fig. 5.30 and the TEM in Fig. 5.31 have different characteristic crossphases. For the most part the TEM crossphases are in the range $-70° < \alpha_{n_e,T_e} < 70°$,

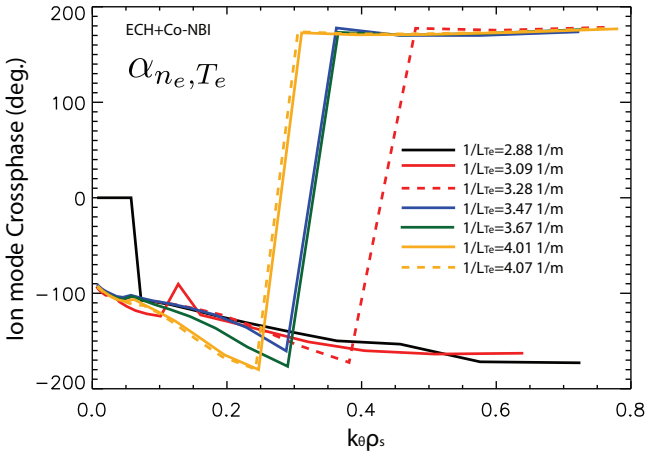

Figure 5.30: Crossphase angle of fastest growing mode propagating in the ion diamagnetic direction as a function of $k_\theta \rho_s$ for ECH+Co-NBI plasmas. Calculations at $\rho = 0.6$.

which shares no overlap with the ITG crossphase values. The experimentally observed increase is consistent with a transition to TEM dominated turbulence. The experimental crossphase values in Fig. 5.20 converge around $-70°$ to $-90°$ at high $L_{T_e}^{-1}$, which are similar values to the lowest wave number (with finite growth rate) TEM crossphase values in Fig. 5.31. A consistent explanation for the convergence of the experimental points is that they become dominated by the longest wavelength unstable TEM.

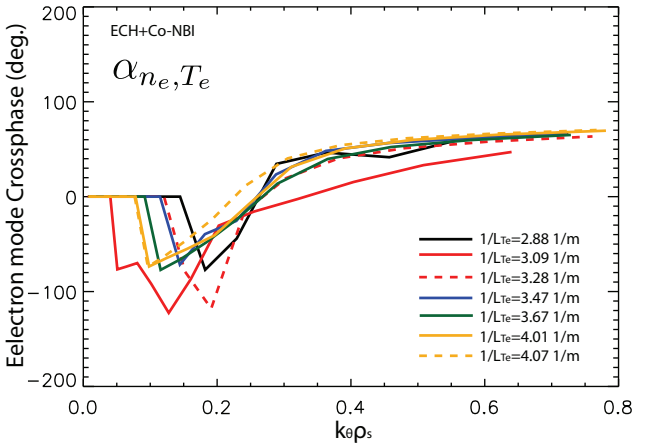

Figure 5.31: Crossphase angle of fastest growing mode propagating in the electron diamagnetic direction as a function of $k_\theta \rho_s$ for ECH+Co-NBI plasmas. Calculations at $\rho = 0.6$.

The ECH-only crossphase measurements exhibited a different trend than the ECH+Co-NBI plasmas. The reduced heating of the ions in ECH-only in comparison to the cases with NBI leads to generally reduced ITG growth rates, which can make ITG negligible even at low $L_{T_e}^{-1}$. Figure 5.32 shows the crossphase for the fastest growing mode propagating in the electron diamagnetic direction (TEM) as a function of wave number for the ECH-only plasmas. The case with an ITG mode propagating in the electron direction is omitted. The curves are generally similar to Fig. 5.31, but differ slightly in the details, with a slower increase in crossphase with wave number and smaller differences in terms of at what wave number growth rates become positive. The crossphase values generally increase with $L_{T_e}^{-1}$.

The ECH-only measurements began at about $-100^\circ \pm 10^\circ$ and increased to about $-70^\circ \pm 10^\circ$ as $L_{T_e}^{-1}$ increased. Assessing the approximate value of the TGLF predicted crossphase of the longest wavelength unstable TEM, that value increases from about -105° for $L_{T_e}^{-1} = 1.91$ 1/m and $L_{T_e}^{-1} = 2.46$ 1/m (ignoring the $L_{T_e}^{-1} = 1.91$ 1/m point above which growth rates return to zero) to about -55° for the highest $L_{T_e}^{-1}$ case. The changes to the measured values of crossphase for the ECH-only and the value of the crossphase for the longest wavelength unstable TEM predicted by TGLF for the same plasmas are similar.

The electron direction crossphase values predicted by TGLF for the remaining two rotation cases, ECH+Bal-NBI and ECH+Ctr-NBI, are qualitatively similar to ECH+Co-NBI. TGLF makes no predictions at $\rho = 0.6$ unambiguously consistent with the measured positive values of crossphase angle in ECH+Ctr-NBI plasmas. Additional TGLF runs were performed at radial locations $0.5 \leq \rho \leq 0.6$. This resulted in small changes to the details of the growth rate, frequency, crossphase spectra, but no significant qualitative differences.

The only prediction from TGLF consistent with the measured positive crossphase values in low $L_{T_e}^{-1}$ ECH+Ctr-NBI plasmas are for TEM at high $k_\theta \rho_s$. This could occur if, speculatively, the low-k is suppressed by $E \times B$ shear, leaving the lowest-k that is unstable in the nonlinear system to be one of the wave numbers with positive crossphase. However, the $E \times B$ shear was fairly small in all cases in the experiment. Furthermore, reviewing Table 5.1, the magnitude of the flow shear in ECH+Ctr-NBI was about 40% less than ECH+Co-NBI.

Alternatively, the crossphase as a function of wave number in Fig. 5.31 does not change as much with $L_{T_e}^{-1}$ as the growth rates do. Without invoking $E \times B$ suppression, a simpler explanation would be that positive growth rate measurements are from higher-k TEM because growth rates at lower wave number are too small to produce measureable fluctuations.

More assumptions would have to be added to explain why the positive crossphase was not measured for low $L_{T_e}^{-1}$ in ECH+Co-NBI plasmas For instance, the higher Z_{eff} in ECH+Ctr-NBI plasmas could have a dilution effect on the deuterium, resulting in less energy in the fluctuations from ITG. From Table 5.1, a/L_{T_i} is lower and a/L_{n_D} is higher for ECH+Ctr-NBI, which lowers η_i for deuterium and therefore has a stabilizing effect on ITG. However, η_i is also higher for carbon, which is consistent with an impurity ITG explanation–which could be present even if it is sub-dominant.

Further investigation awaits comparison to non-linear simulations.

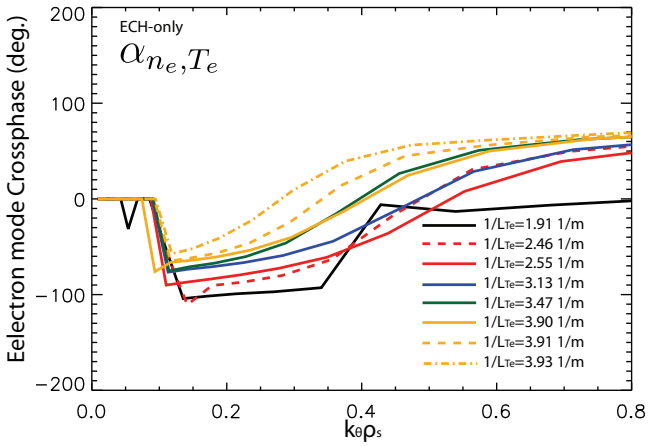

Figure 5.32: Crossphase angle of fastest growing mode propagating in the electron diamagnetic direction as a function of $k_\theta \rho_s$ for ECH+Co-NBI plasmas. Calculations at $\rho = 0.6$.

5.4.1.5 High wave numbers

Although the turbulence measurements presented were all at low-k and intermediate-k, a clear questions that arises is whether high-k (ETG scale) instabilities would be expected

to also increase in amplitude. Figure 5.33 expands the calculations in Fig. 5.25 to ETG scales, showing plots of the fastest growing modes propagating in the electron diamagnetic direction, color-coded by $L_{T_e}^{-1}$. One can see that there are two features in the spectra: an intermediate-k feature peaking $k_\theta \rho_s \sim 1-2$, consistent with TEM, and a high-k feature that starts $k_\theta \rho_s \sim 3-4$ and peaks $k_\theta \rho_s \sim 10-20$, consistent with ETG. Qualitatively, the trend that the growth rate spectra increase with $L_{T_e}^{-1}$ appears to hold less strongly for the high-k feature than the intermediate-k feature, with more cases where there are lower high-k growth rates at higher values of the normalized gradient.

The growth rates at high-k are higher, but the scale is much smaller. A rough estimate of the transport can be made by comparing the quasi-linear diffusion coefficient, $D \sim \gamma/k^2$, for the two ranges. For some of the cases, the growth rates for the high-k feature are 5 times the low-/intermediate-k feature, but the spatial scale is more than 10 times smaller. One would then estimate that $D_{low}/D_{high} \gtrsim 20$, which can be taken as a lower bound on that estimated ratio. Direct calculation of γ/k^2 for the spectra results in peaks at $k_\theta \rho_s < 0.5$, with no significant increase at high-k. These simple estimates do omit any influence of the non-linearly generated radial streamers observed in simulations of ETG turbulence. Further investigation is deferred to future work, which is to include comparisons to nonlinear simulations.

High-k measurements can be made at DIII-D [208] and have been observed to change with ECH power input [256]. Figure 5.33 motivates future work using the $L_{T_e}^{-1}$ scan technique to try to identify ETG in a standard ratio tokamak.

5.4.1.6 Sensitivity studies for mode identification

Several sensitivity studies using TGLF code are presented in this section. These runs are performed by using experimentally measured parameters for the reference and changing specific parameters to test their dependencies. All calculations are done for $\rho = 0.6$, unless otherwise noted.

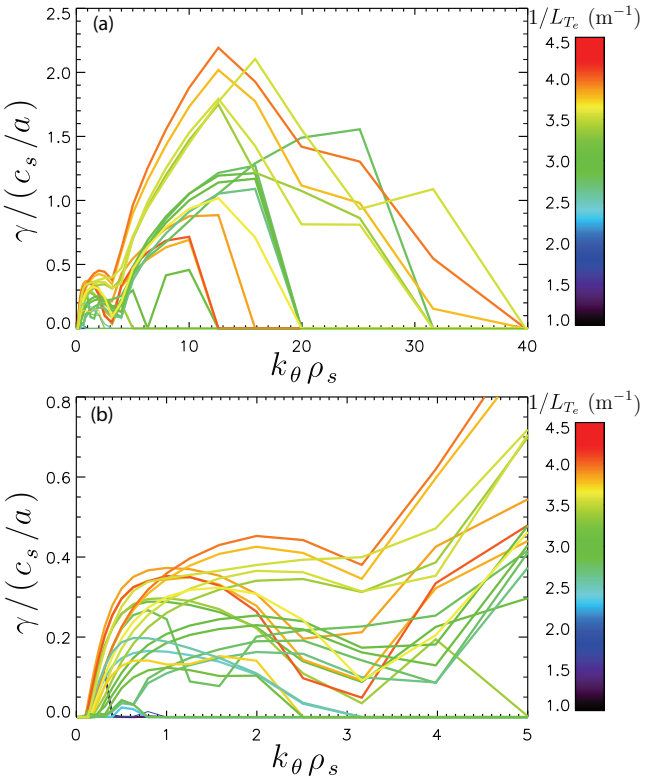

Figure 5.33: Linear gyrofluid growth rates for fastest growing mode propagating in the electron diamagnetic direction for (a) $0 \leq k_\theta \rho_s \leq 40$ and (b) $0 \leq k_\theta \rho_s \leq 5$

The "Base case" in Fig. 5.34 is the lowest $L_{T_e}^{-1}$ case in the averaged growth rate plots; plotted are the fastest growing mode propagating in both the electron and ion diamagnetic direction for the base case and for cases with ∇T_i (for both deuterium and carbon) increased by 10% and 20% (in terms of code parameters a/L_{T_i} is changed but T_i/T_e is not changed). Consider the base case. A plot of the fastest growing mode regardless of direction would produce an unbroken curve (the jumps at $k_\theta \rho_s \approx 0.1$ and $k_\theta \rho_s \approx 0.3$ are due to the sparseness of the data points). That would be consistent with a single mode, the real frequency of which happens to cross zero. The same can be seen to occur for the $\nabla T_i + 10\%$ case. As ∇T_i is increased, the ion direction growth rates generally increase, consistent with ITG. At $\nabla T_i + 20\%$ the electron direction mode growth rates in the CECE wave number region are all less then 0.01 c_s/a, which would put the corresponding point in Fig 5.27 (this is the point reference several times in the text) near zero. For the base case, the real frequency is indeed near zero over the region where the spike in the electron direction growth rate occurs, there it is less than 0.02 c_s/a. Overall Fig. 5.34 substaniates the explanation that the lowest $L_{T_e}^{-1}$ point in Fig. 5.27 is due to an ITG mode with near zero frequency, which happens to be propagating slightly in the electron direction for some wave numbers.

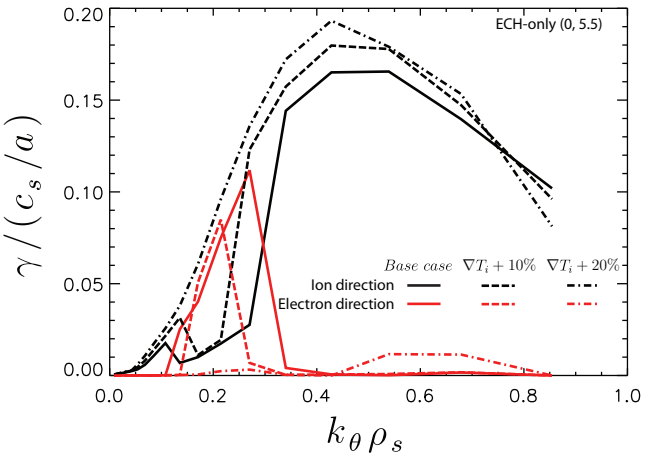

Figure 5.34: Linear gyrofluid growth rates from TGLF. Dependence of ion and electron direction modes on ∇T_i.

To investigate the dependencies of the fastest growing mode above $L_{T_e}^{-1}|_{crit}$ we go to a

ECH+Co-NBI case with ECH arrangement (5, 0.5), shot 144570. We choose a case with all Co-NBI due to the more complete diagnostic coverage with that beam timing. Z_{eff} is also relatively low for the chosen case, with $Z_{eff} \approx 2.3$. We have shown a threshold at $\eta_e \approx 2$ for electron temperature fluctuations. ∇T_e-TEM growth rates are expected to increase with η_e and to be stabilized at high electron-ion collision rates. Although ∇T_e-TEM increases with η_e, at sufficiently high $L_{n_e}^{-1}$, ∇n_e-TEM should be destabilized. We test TGLF predictions against these expectations by varying the code parameters a/L_{T_e}, a/L_{n_e}, and $\nu_{ei}/(c_s/a)$.

Figure 5.35 shows the dependence of the growth rate of the fastest growing mode for each wave number in the ion and electron direction to variations of ∇T_e for one of the ECH+Co-NBI cases at high $L_{T_e}^{-1}$. One result to glean from the plots is that for $k_\theta \rho_s > 0.15$ the electron direction propagating mode has increasingly larger growth rates. The larger electron mode growth rates is consistent with the interpretation of the experiment that the plasmas are TEM dominated at high $L_{T_e}^{-1}$. Also, the electron mode growth rates increase monotonically with ∇T_e, which is consistent with expectations for ∇T_e-TEM. There are also slight changes to the ion direction growth rates, with the opposite trend.

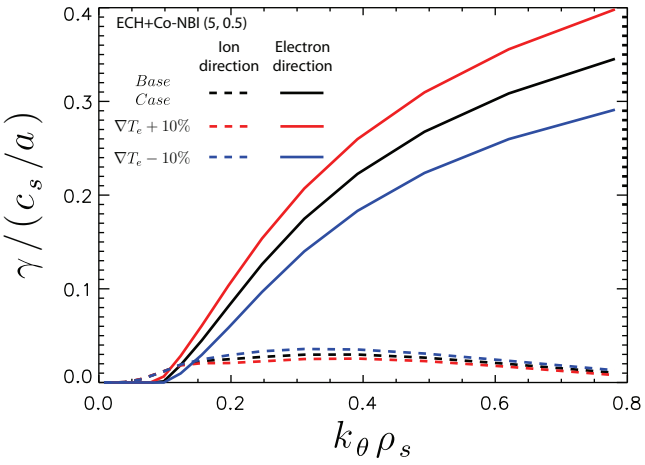

Figure 5.35: Linear gyrofluid growth rates from TGLF. Dependence of ion and electron direction modes on ∇T_e.

Figure 5.36 shows the response of the linear gyrofluid growth rates to small changes of the code parameter a/L_{n_e}. The electron direction growth rates decrease with increasing a/L_{n_e},

consistent with the expected η_e dependence for ∇T_e-TEM. Small changes are also calculated for the ion direction modes.

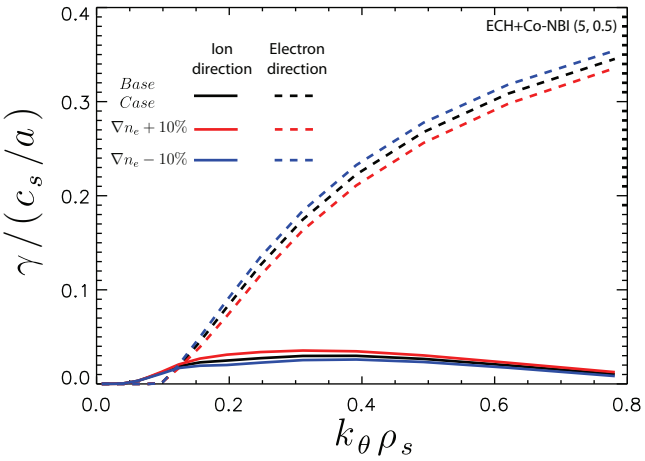

Figure 5.36: Linear gyrofluid growth rates from TGLF. Dependence of ion and electron direction modes on small changes of ∇n_e.

The ∇n_e-TEM has been argued to be of importance for saturating internal transport barriers [91, 92]. From Fig. 1 of Ref. [92] one would expect that increasing a/L_{n_e} further than shown in Fig. 5.36 would eventually destabilize ∇n_e-TEM. Modifying the ECH+Co-NBI (5,0.5) Base case by increasing a/L_{n_e} to as high as 20 shows no evidence for instabilities with growth rates larger than 0.1 c_s/a. The growth rate spectra decrease with a/L_{n_e} until completely stable. A subset of these calculations are shown in Fig. 5.37. For reference the Base case corresponds to $\eta_e = 2.67$, so that the $\nabla n_e \times 2.67$ corresponds to $\eta_e = 1$. Note that only a/L_{n_e} is scanned, so the calculations are not entirely self-consistent–in principle some combination of the deuterium, carbon, and fast ion density gradient must also change. The expected destabilization of ∇n_e-TEM is not observed. It might be that other existence conditions that are not satisfied, *e. g.* low collisionality or T_e/T_i. Multiple parameter scans are not performed here.

Figure 5.38 shows a code parameter scan for the normalized electron-ion collision frequency, $\nu_{ei}/(c_s/a)$. For the Base case $\nu_{ei}/(c_s/a) \approx 0.11$. As expected for dissipative ∇T_e-TEM, the growth rates of the fastest modes propagating in the electron diamagnetic direction

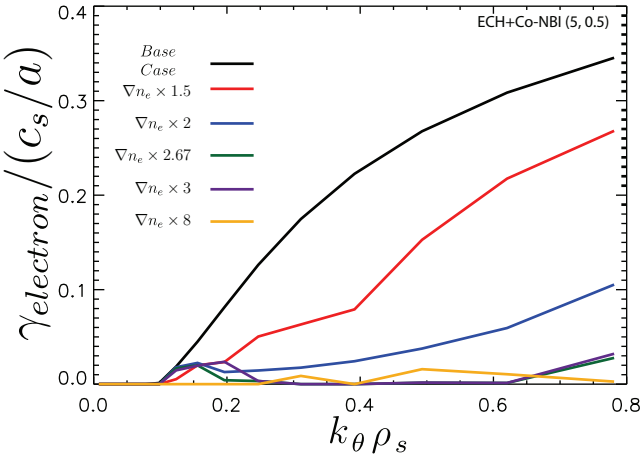

Figure 5.37: Linear gyrofluid growth rates from TGLF. Dependence of electron direction modes on larges changes of ∇n_e.

decrease with increasing $\nu_{ei}/(c_s/a)$. The ion direction growth rates at first increase by a small amount with $\nu_{ei}/(c_s/a)$. For the $\nu_{ei}/(c_s/a) \times 4.0$ and $\nu_{ei}/(c_s/a) \times 6.0$ cases, the ion direction growth rates are also decreased below $k_\theta \rho_s \approx 0.25$. It is interesting to note that as $\nu_{ei}/(c_s/a)$ increases, the fastest growing mode for long wavelengths eventually becomes the ion direction mode. This is consistent with the attribution of the linear Ohmic confinement to saturated Ohmic confinement transition to a switch from dominant TEM to ITG [86].

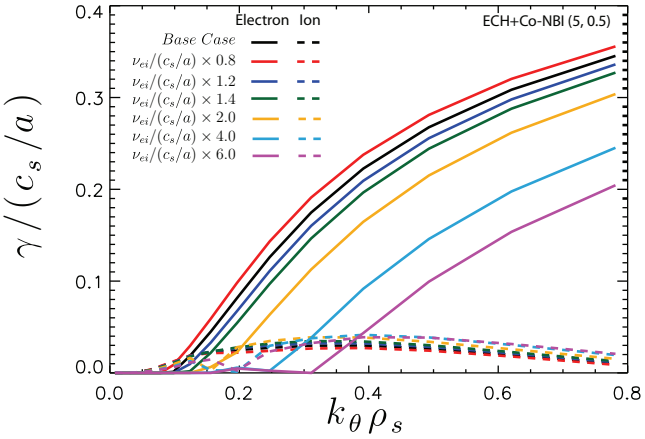

Figure 5.38: Linear gyrofluid growth rates from TGLF. Dependence of ion and electron direction modes on $\nu_{ei}/(c_s/a)$.

To test the hypothesis that ∇n_e-TEM was the dominant instability below the critical

gradient for the ECH only case, ECH-only (1, 4.5) is chosen as the base case for the scans. The (1, 4.5) case is chosen instead of (0, 5.5) to avoid the apparent issue with electron direction ITG in (0, 5.5). For the chosen case $Z_{eff} \approx 2.4$ (shot 144575). The expectation for ∇n_e-TEM is that growth rates should increase with $L_{n_e}^{-1}$.

The code parameter a/L_{n_e} is systematically varied in Fig. 5.39. The growth rates for the fastest growing mode propagating in the electron direction display interesting behavior. Growth rates at low wave numbers, $k_\theta \rho_s \lesssim 0.3$ slightly decrease when ∇n_e is decreased, but at higher wave numbers, the growth rates increase. At high wave numbers, $k_\theta \rho_s \gtrsim 0.7$, growth rates monotonically decrease with increasing ∇n_e–the same trend seen for ∇T_e-TEM in Fig. 5.35. However, at low wave numbers, growth rates increase monotonically with ∇n_e, consistent with expectations for ∇n_e-TEM. The co-existence of two modes with similar growth rates is qualitatively consistent with the DBS spectra below the threshold in Fig. 5.10. ∇n_e-TEM at low wave numbers and ∇T_e-TEM at high wave numbers would be consistent with Fig. 1 of Ref. [92]. The ion direction modes also exhibit changes in response to the electron density gradient.

There are only a few parameters that could explain why ∇n_e-TEM is observed for ECH-only in Fig. 5.39, but apparently cannot be destabilized for ECH+Co-NBI in Fig. 5.37. Reviewing Table 5.1 shows that differences in normalized collision frequency are unlikely to account for the difference. There is however a significant alteration to T_e/T_i, which is known to affect TEM stability boundaries [262]. Additionally, the difference in T_e/T_i in the ECH-only plasmas in comparison to the plasmas with NBI could influence the critical gradient; although, the TGLF results would be consistent with T_e/T_i having a much larger impact on ∇n_e-TEM than ∇T_e-TEM. The toroidal Mach number also different by about a factor of two.

Varying a/L_{T_e} results in a plot similar to Fig. 5.35, where the spectrum changes monotonically with ∇T_e. That is consistent with the picture that the ∇T_e-TEM is sub-dominant at low-k, but quickly becomes dominant at all wave numbers as $L_{T_e}^{-1}$ is increased.

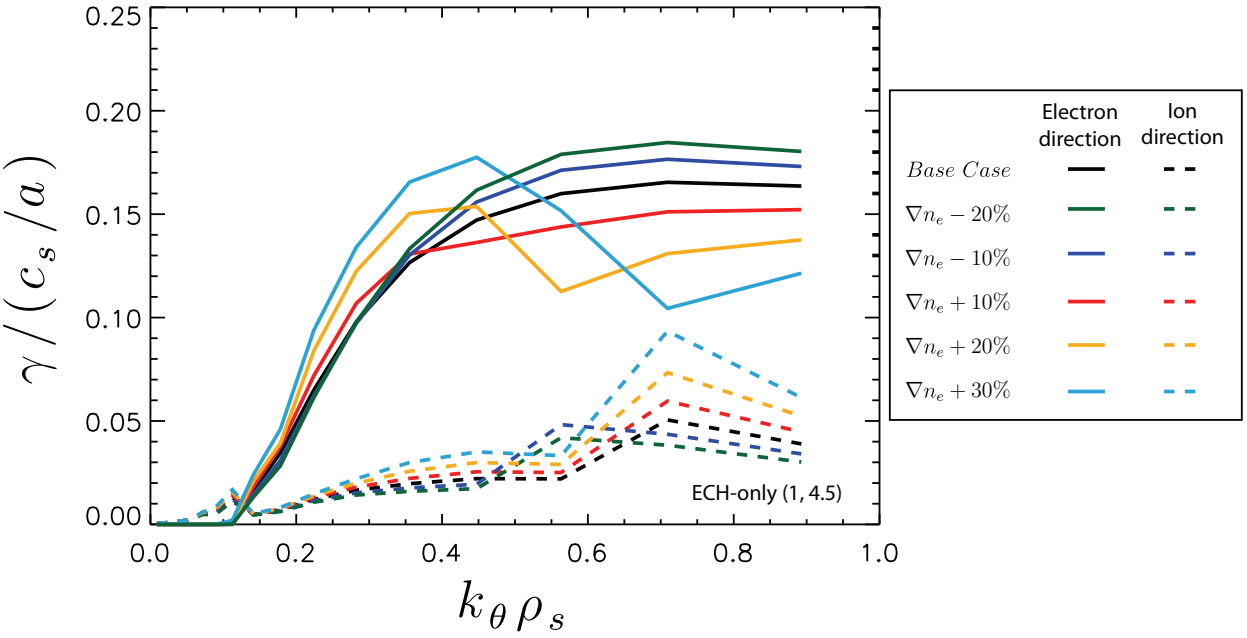

Figure 5.39: Linear gyrofluid growth rates from TGLF. Dependence of ion and electron direction modes on a/L_{n_e}.

5.4.1.7 Comparisons to DBS spectra

The frequency-localized changes to DBS spectra presented in Sec. 5.3.3.4 motivate comparisons to code predictions. Comparisons to linear predictions from TGLF are reported in this section.

Figure 5.40 shows the linear gyrofluid frequencies and growth rates at $\rho = 0.6$ for the same ECH+Bal-NBI plasmas the DBS spectra were shown in Figs. 5.11 and 5.15. The plots here are as a function of quantities in physical units. The binormal wave number (perpendicular to both the direction of the magnetic field and flux surface normal) is labeled as ky. The DBS measurement wave number was about 4 cm^{-1} (center of Gaussian instrument function). The growth rates show the same general trend as the DBS spectra, increasing with $L_{T_e}^{-1}$. Although all the TGLF calculations are from $\rho = 0.6$, the (3,3) case has the highest TEM growth rates, just as the (3,3) case had the most power out of the DBS spectra. The ion growth rates generally decrease as the electron growth rates increase.

In Fig. 5.11 the (2,4) and (5,1), and in Fig. 5.15 the (1,5) and (5,1) had nearly the same magnitude at the frequencies that responded to the $L_{T_e}^{-1}$ scan. The growth rates show that (1,5) and (5,1) cases are similar at 4 cm^{-1}, with the (2,4) cases slightly higher–the same trend seen in Fig. 5.15.

The frequency at 4 cm^{-1} falls between 50-80 kHz in 4 of the 5 cases, in reasonably good agreement with Fig. 5.15, where the increase in the DBS amplitude peaked at about 60 kHz. The outlier, the (5,1) case, has a frequency of about 150 kHz in the gyrofluid calculation–the measured spectra is not consistent with that; it also shows the increase near 60 kHz. The ITG frequencies range from 0 to about 60 kHz at 4 cm^{-1}, with 4 out of 5 cases in the range 0 to 20 kHz. The difference between the large peak in the spectra in Fig. 5.11 and the frequency range that increases with $L_{T_e}^{-1}$ is about 100 kHz, which is roughly consistent with the difference predicted by TGLF.

The combination of the DBS spectra, plasma rest frame from CER (with ray tracing for the DBS wave number), and the TGLF calculations appear to not be consistent; the plasma rest frame is at too low a frequency. One or more of the following must be true: the CER measured E_r is inaccurate, the wave number from ray tracing in inaccurate, or the spectra are more complicated than simple expectations from linear calculations. The simple expectation would be that the ITG peak should occur at the rest frame frequency plus the ITG frequency and the TEM peak should occur at the rest frame frequency minus the TEM frequency. This might not be correct for the non-linear system, *e.g.* the intermediate-scale measurements could be getting modulated by larger scales. It is also not obvious why the presumed ITG peak has a larger amplitude than the presumed TEM portion of the spectrum. A definite conclusion will require comparison to non-linear simulation.

The dependence of the TEM frequency on wave number could explain the trend observed in ECH+Ctr-NBI plasmas where the mean frequency moved towards the ion diamagnetic direction as $L_{T_e}^{-1}$ was increased. A possibility suggested in Sec. 5.4.1.4 for the measurements of positive crossphase was that those measurements occurred due to TEM growth rates increasing, while the crossphase for each wave number changed little, moving the power-

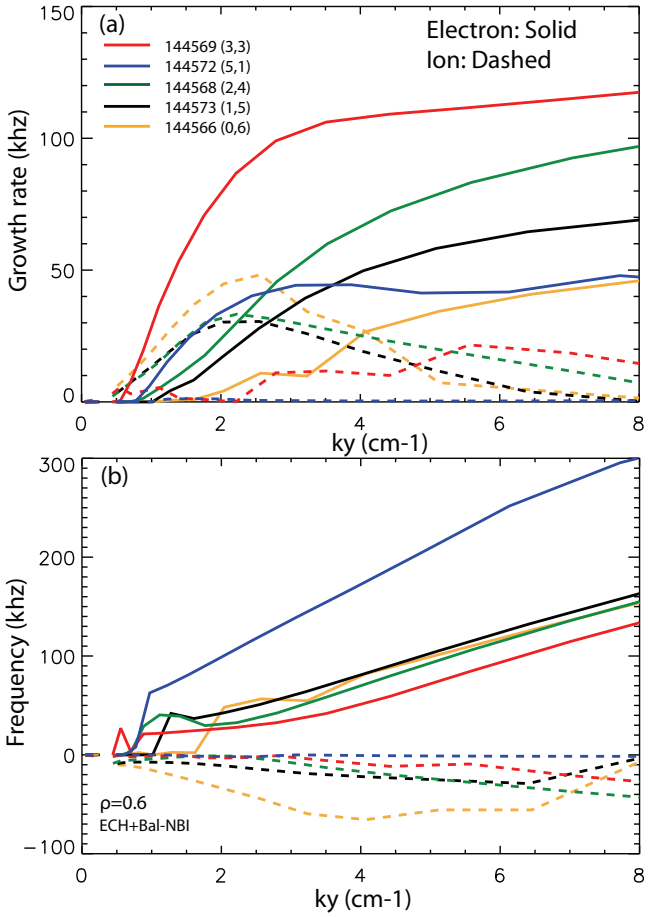

Figure 5.40: Linear gyrofluid (a) frequencies and (b) growth rates from TGLF in ECH+Bal-NBI plasmas. Modes propagating in the electron diamagnetic direction have solid lines, ion direction is dashed lines.

weighted crossphase to a lower wave number. A similar explanation could account for the change in frequency. The DBS measurements are at about 4 cm^{-1} with a Δk of about 1 cm^{-1}. If the lower wave numbers are initially stable or at small amplitude, then increase with $L_{T_e}^{-1}$, it could decrease the power-weighted wave number, which would correspond to a movement in frequency toward the ion diamagnetic direction.

5.5 Discussion and conclusions

The primary result is the observation of a critical gradient threshold for electron temperature fluctuations. The critical gradient value for electron temperature fluctuations is within uncertainties of the critical value for electron thermal diffusivity found from heat pulse analysis. Above the critical $L_{T_e}^{-1}$, temperature fluctuations, electron heat flux, and stiffness also increase.

The dimensionless parameter η_e was found to describe both the electron temperature fluctuation threshold and a threshold found in linear gyrokinetic simulations, with both increasing abruptly at $\eta_e \approx 2$. It is notable that the experimental threshold matches predictions for *linear* instability–this is consistent with the prediction from simulations that there is no significant Dimits shift for ∇T_e-TEM turbulence. There are a number of pieces of evidence consistent with the destabilization of ∇T_e-driven trapped electron modes:

- Threshold behavior was observed for the related quantities $L_{T_e}^{-1}$ and η_e.

- Sensitivity studies showed that the mode responsible for the critical behavior in linear gyrofluid simulations is consistent with ∇T_e-TEM: growth rates increase with $L_{T_e}^{-1}$, decrease with $L_{n_e}^{-1}$, and decrease with $\nu_{ei}/(c_s/a)$.

- Changes to the ratio between low-k electron temperature fluctuations and density fluctuations correlated with the increase in the ratio between TEM and ITG growth rates (over measured wave numbers).

- Measurements of intermediate-k density fluctuations showed frequency-localized in-

creases as $L_{T_e}^{-1}$ increased, which is evidence of a new mode being driven.

- The intermediate-k density fluctuation spectrum shifted to the electron diamagnetic direction with increasing $L_{T_e}^{-1}$, except in ECH+Ctr-NBI plasmas.

- At high $L_{T_e}^{-1}$ measurements of the crossphase between electron density and temperature fluctuations where consistent with linear gyrofluid predictions for TEM in all heating scenarios.

- $\beta_e \lesssim 0.2\%$ and $\nu_{ei}/(c_s/a) \sim 0.2$ are in a TEM relevant regime

Although it is concluded that ∇T_e TEM was responsible for observations above the critical gradient in all four rotation cases, observations below the critical gradient are consistent with different linear instabilities. It was shown that linear growth rate calculations were consistent with the co-existence of ∇T_e TEM and ∇n_e TEM in ECH-only plasmas, which is consistent with changes to the measured intermediate-k spectra and lack of change to the measured crossphase. ECH+Co-NBI plasmas were consistent with ITG below the critical gradient. The most cogent explanation for ECH+Ctr-NBI below the critical gradient is that the most unstable mode was ∇T_e-TEM at higher wave numbers that were destabilized above the low-k critical gradient. Plasma parameter changes also increased η_i for carbon, which would be expected to favor the instability of a Carbon-ITG, but no indications of such a mode were observed in linear calculations; however, the sub-dominant existence of such modes cannot be ruled out.

The electrostatic turbulent cross-field electron heat flux can be written as [24]

$$\widetilde{Q}_e = \frac{3 n_e T_e}{2B} \sum_{k_\theta} k_\theta \left(\frac{|\widetilde{n}_e|}{n_e} |\tilde{\varphi}| \gamma_{n_e,\varphi} \sin \alpha_{n_e,\varphi} + \frac{|\widetilde{T}_e|}{T_e} |\tilde{\varphi}| \gamma_{T_e,\varphi} \sin \alpha_{T_e,\varphi} \right), \tag{5.8}$$

where the sum is taken over the fluctuations associated with each k_θ. The α_{n_e,T_e} measurements indicate a more subtle picture than the $\delta T_e/T_e$ measurements alone. Simulations of similar plasmas found that the conductive term $(\widetilde{T}_e, \widetilde{\varphi})$ dominated, accounting for $\sim 90\%$ of $\widetilde{Q}_e$ [10]. Here, while $\widetilde{Q}_e/(n_e T_e)$ increases by more than $10\times$, $\delta T_e/T_e$ only increases by $\sim 2\times$. Changes to α_{n_e,T_e} give reason to infer that the transport related crossphases, $\alpha_{n_e,\varphi}$ and $\alpha_{T_e,\varphi}$

(where φ is the electrostatic potential), might also change in such a way that the turbulent heat flux increases. Other possibilities include additional transport from higher k_θ's than are measured (in past work from DIII-D high-k density fluctuations, $k_r \sim 35$ cm^{-1}, did increase [17, 256] and intermediate-k density fluctuations, $k_\theta \sim 4$ and 8 cm^{-1}, did change [9]), a modifcation to the average wave number of the low-k fluctuations, and non-local transport.

Two plausibility checks on the crossphase explanation can be accomplished briefly (taking high-k and other contributions to be negligible). First, by contradiction, if one assesses only the conductive term and assumes that the coherency and crossphases between fluctuations *do not change*, then $\tilde{\varphi}$ would have to increase by $\sim 5\times$. One would expect such a change to be reflected in the particle transport (unless $\sin\alpha_{n_e,\varphi} \approx 0$), which was not the case. Second, the required potential fluctuations to drive the observed $\widetilde{Q}_e/(n_eT_e)$ can be assessed. At high $L_{T_e}^{-1}$, $\widetilde{Q}_e/(n_eT_e) \approx 45$ m/s and $\delta T_e/T_e \approx 2\%$. To set a bound, take $\gamma_{T_e,\varphi} = 1$ and $\alpha_{T_e,\varphi} = 90°$. Also take the average poloidal wave number to be $\langle k_\theta \rangle = 1.5$ cm^{-1} ($k_\theta \rho_s \approx 0.3$). One then finds that for the conductive term to account for $\widetilde{Q}_e/(n_eT_e) = 45$ m/s at low-k would require $e\tilde{\varphi}/T_e \approx 2.5\%$, a level similar to the measured $\delta T_e/T_e$−the conclusion being it is indeed plausible; although, potential fluctuations five times the level of density fluctuations might be surprising.

Another argument that can be made is that for the ECH-only plasmas the particle flux in the core must be negligible, since the profiles are not changing and there is no source in the core. If that is true, then $\sin\alpha_{n_e,\varphi} \approx 0$, which implies $\alpha_{n_e,\varphi} \approx 0°$ or 180°. The measured α_{n_e,T_e} would then be directly related to the transport phase $\alpha_{T_e,\varphi}$. At high $L_{T_e}^{-1}$, the α_{n_e,T_e} measurements converge around −90°. For $\alpha_{n_e,\varphi} \approx 180°$, this would imply the phasing between turbulent fluctuations is such that the conductive term of Eqn. 5.8 is maximized. This description changes if opposing transport mechanisms are present: for instance an inward collisional pinch and outward diffusion, or outward diffusion at low-k balanced by inward diffusion at high-k.

A simple interpretation of how the crossphase measurements relate to linear calculations can explain many of the observations. The interpretation is that the measured crossphase

is dominated by the lowest wave number at a sufficiently high growth rate. The sufficiently high qualifier is difficult to quantify since the TGLF model is derived for strongly unstable modes and calculations at $\gamma \lesssim 0.05\ c_s/a$ might not be accurate [1]. Following that interpretation leads to reasonable agreement between the measured crossphase values above the critical gradient and linear calculations, as well as consistency with the ITG crossphase values for ECH+Co-NBI plasmas. It presents a resolution to the two puzzling results for ECH+Ctr-NBI plasmas: positive crossphase values and a DBS spectra that moves towards the ion diamagnetic direction as $L_{T_e}^{-1}$ is increased. The resolution occurs if the typical TEM crossphase values like those in Fig 5.31 and the frequencies like those in Fig. 5.40 change little with $L_{T_e}^{-1}$ in comparison to how much the growth rates change. The increased growth rates then lower the power-weighted mean wave number of the measured fluctuations, which could simultaneously move the crossphase from positive to negative values in Fig 5.31 and corresponds to lower frequencies in Fig. 5.40.

There are a number of future directions motivated by this work. In Sec. 5.3.3.2 significant disagreement was found between the measured critical threshold for electron temperature fluctuations and analytical predictions; however, one of the analytical formulas was found to agree with experiment in past work. The disagreement was found in L-mode DIII-D plasmas and the agreement in QH-mode DIII-D plasmas–discovery of the reason for the discrepancy might be revealing.

Another idea suggested by the data for future work are the results in Sec. 5.3.3.5 where conditionally averaging DBS spectra on the NBI timing revealed large changes to the spectra, which were presumably related to TEM. Conditionally averaging profile data resulted in only $\sim 1\%$ changes to the gradient scale lengths, which would be unlikely to cause the measured changes–the profile modifications would also have been expected to slightly stabilize TEM, where increases in the spectra were observed. The interesting possibility, which was not possible to assess with any real accuracy with the acquired data, is that the local $E \times B$ shear is changing due to, for instance, slightly different deposition profiles for the beams

[1] G.M. Staebler, *personal communication*

or differences in fast ion orbits. A future experiment could be designed to use DBS-5 for DBS rather than reflectometry, so that the local electric field shear could be conditionally averaged. In this way it might be possible to validate the isolated effect of $E \times B$ shear suppression in a carefully controlled experiment.

Predictions exist for differences in the wave number dependence of density fluctuation spectra for ITG dominated versus TEM dominated plasmas [108]. It is in principle possible to build up an experimental spectrum with DBS measurements, which could be compared to this prediction. For this experiment, it was decided to measured one wave number in all the different conditions. The only impediment to these measurements is run time.

Similarly, the gyrofluid calculations for the experiment showed that ETG scale fluctuations, $k_\theta \rho_s \sim 10$, would be expected to be destabilized during the $L_{T_e}^{-1}$. There is a high-k backscattering system in place that can measure fluctuations at that scale at DIII-D, which was not used during the experiment, but could have been.

Further comparisons of measurements to non-linear gyrokinetic simulations are underway. Several measurements will be particularly interesting to compare to the simulations. Given previous work concerning the impact of damped eigenmode on the crossphase PDF in simulations, the measurements of the crossphase PDF will be able to be compared to simulation results. The simulation results can be decomposed into the stable and unstable modes–this could give insight into the nature of the turbulent transport above the critical gradient, where there is high stiffness; that is, how much of the transport is due to damped modes? Does high stiffness correlate with more energy in the damped modes? If the relationship is significant, then can transport be affected by changing the damped mode spectrum, even if there is no change to the dominant instability? The frequency-localized changes to the measured DBS spectrum will also be able to be directly compared to simulation output, using the synthetic diagnostic described in Sec. 3.4.3.

In burning plasma conditions, the fusion alphas would be expected to primarily heat electrons. Although fluctuations in the core of current tokamaks have been observed to be reduced in H-mode plasmas, this can be attributed to strong $E \times B$ shear from NBI

heating. Neutral beams will not penetrate deeply into the core of large tokamaks, like ITER. Intrinsic rotation has also been observed to scale inversely with machine size [268], which projects poorly to ITER. The worst case, due to strong electron heating and low rotation, would be extremely high stiffness in the electron channel for ITER, similar to the observations presented here for L-mode plasmas–studies have shown this leading to reduced fusion performance [257]. Therefore ways to reduce the stiffness of electron heat transport is an important avenue for future work.

CHAPTER 6

Summary and Conclusions

This chapter summarizes the major conclusions from Chapters 3, 4, and 5 and discusses future directions motivated by the results.

6.1 Diagnostic development

Chapter 3 discussed the development and laboratory tests of a novel multichannel millimeter-wave diagnostic system (DBS-5) that has been used for Doppler backscattering and conventional reflectometry. The novel aspect of the hardware implementation of the diagnostic–simultaneous launch of multiple frequencies–was implemented through other approaches in subsequent systems (DBS-8). The measurement capabilities enabled by these multichannel systems have lead to a number of results and publications. Furthermore, situation of these systems at toroidally separated ports on the DIII-D tokamak have allowed correlation analysis identifying key characteristics of collective plasmas oscillations, such as geodesic acoustic modes and low frequency zonal flows.

Data analysis and interpretation were also discussed, including numerical modeling of DBS using ray tracing and full wave calculations. The latter was used in the implementation of a synthetic DBS diagnostic for nonlinear gyrokinetic simulations, which enabled the direct comparison of DBS measurements to simulation predictions. Data analysis approaches under-utilized in past work (analysis of the DBS phase) and several non-ideal effects were also discussed. Several further novel approaches to DBS analysis are presented in Appendix F, which could lead to new uses of DBS measurements in future work.

Data was presented showing that correlation of either the amplitude or phase of a conventional reflectometer channel produce the same crossphase when correlated with data from an electron cyclotron emission radiometer. Although the understanding of information in the reflectometer phase is better understood (when it can be accurately recovered), these results showed that the reflectometer amplitude must be sensitive to the same density fluctuations. The observation that the reflectometer-ECE correlation is always higher for the reflectometer amplitude than for the reflectometer phase is consistent with past work concluding that the former is often a better representative of density fluctuations.

These activities have moved DBS and the density-temperature crossphase diagnostics further into the category of routine, widely-accepted measurements for use in future work. The synthetic DBS diagnostic can also be used in future work for further comparisons and the approach taken can be extended to directly couple the output of nonlinear simulations to full wave simulations; this activity could lead to a verified reduced synthetic DBS diagnostic for use in transport and turbulence model validation studies.

6.2 Geodesic acoustic mode and low frequency zonal flows

A number of results from investigations of the geodesic acoustic mode and other low frequency zonal flows were reported in Chapter 4.

Correlations between toroidally separated DBS systems demonstrated long range correlations of the GAM and other low frequency flows in the core of L-mode plasmas, which were consistent with the predicted axisymmetric (toroidally and poloidally symmetric potential) structure expected for zonal flows.

Simultaneous measurements with the multiple radially separated DBS channels were used to study the radial propagation and radial structure of the GAM. The GAM was found to propagate radially outward, consistent with predictions, with a radial wave number of $k_r\rho_s \approx 0.1 - 0.2$, which is the range expected for zonal flow type modes. It was also shown that the GAM in DIII-D can exist either has a continuum mode (as would be predicted by

MHD), with a frequency that varies with radius, reflecting the local dispersion relation; or, as an eigenmode (as predicted when finite gyroradius effects are taken into account), with a frequency that is constant with radius. The former occurs in lower temperature Ohmic and L-mode plasmas, while the latter is observed in L-mode plasmas with significant auxiliary heating. This is significant as it implies that it is the kinetic, eigenmode GAM that might be important during L-mode periods (during the current ramp) and for the L-H transition of future reactors. Measurements were also presented demonstrating that the eigenmode GAM can be radially coherent over several dozen gyroradii–more than the correlation length of the turbulence. This categorizes the GAM in this regime as a meso-scale structure and breaks the local assumption ($\rho^* \to 0$) made in many turbulence simulations.

Damping of the GAM was also studied. It was concluded that in the core of L-mode plasmas, the damping rate inferred from experimental measurements was not inconsistent with the weak collisionless damping expected for the GAM. Differences between the measured damping and calculated damping rate could be attributable to temperature fluctuations or due to effects not included in the theoretical calculation (*e.g.* shaping effects). It was concluded that the GAM might be susceptible to collisional damping effects near the last closed flux surface.

Intermittency of the GAM had been reported in the past, but for the first time it was quantified. It was shown that the autocorrelation time of the GAM is much shorter than one would infer from the damping rate, which can be attributed to the presumed energy source for the GAM, the ambient turbulence. It was also observed that the probability distribution function of the GAM can vary quite significantly between nearly Gaussian to approaching a sinusoidal distribution.

Bispectral analysis of the GAM was also reported. It was shown that the GAM exhibits significant bicoherence with ambient turbulence, which persists in toroidal correlations, and is measured over a broad frequency range. Furthermore, conditional-averaging of the bicoherence on the amplitude of the GAM showed the bicoherence varies with the amplitude of the GAM. The measured bicoherence between the GAM flow and ambient turbulence was

also showed to depend on wave number.

Low frequency flows (a few kilohertz) were also reported to be observed in the core of L-mode plasmas and to correlate toroidally. These flows are consistent with neither of the commonly discussed zonal flow types (the GAM and the Rosenbluth-Hinton residual flow). Measurements were also presented showing that the radial distribution and amplitude of the GAM and the low frequency flows depends on T_e/T_i (which could be indirect, due to T_e/T_i dependence of the ambient turbulence). The flows were also seen to depend on the direction of momentum input from neutral beam injection, with both the GAM and LFZF nearly gone in counter-injected plasmas. Both toroidal rotation and Z_{eff} typically changes in counter-injected plasmas. An otherwise similar pair of cases with co-injected beams was found with significantly different Z_{eff}, where the GAM and LFZF were of marginally different amplitude (about 20%), but much less difference than the co- vs. counter- comparison. These results indicate a direct rotation dependence for the GAM and LFZF.

Several directions are motivated for future work. The first is that measured characteristics of the GAM and its interaction with turbulence should be directly compared to nonlinear gyrokinetic simulations. This could lead to direct evidence validating (or contradicting) the widely-held view of the role of zonal flows. Furthermore, the observed changes to the radial structure of the GAM could be used to validate global simulations. Although a prediction exists for a radially extended GAM eigenmode, no predictions exist that explain the often-observed "staircase" of eigenmode GAMs. Validation of GAM damping near the edge could also lead to a better understanding of the role of the GAM during the L-H transition and the dependence of the L-H transition on density.

6.3 Study of fluctuations in multiple fields with systematic variation of a/L_{T_e} and rotation

An extensive set of fluctuation measurements and their dependence on systematic variation of the local electron temperature gradient scale length and toroidal rotation were presented

in Chapter 5.

The principal result was the observation of a critical gradient threshold for electron temperature fluctuations. A threshold was observed in $L_{T_e}^{-1}$ below which electron temperature fluctuations did not change within uncertainties, and above which they steadily increased. The value of the critical gradient was within uncertainties of a critical gradient found for the electron thermal diffusivity from heat pulse analysis, above which stiffness also rapidly increased. The dimensionless parameter η_e was found to describe both the temperature fluctuation threshold and an increase in linear gyrofluid growth rates from TGLF over the wave numbers where the temperature fluctuations were measured. Sensitivity studies showed that the fastest growing mode in the linear gyrofluid calculations above the critical gradient was consistent with the ∇T_e-driven trapped electron mode. This evidence is consistent with the measured threshold being due to ∇T_e-TEM, which results in increased electron temperature fluctuations that play a causal role in the increased electron heat flux and stiffness. It is also notable that the *linear* calculations for the critical gradient were in agreement with measurements of the temperature fluctuations: this provides evidence consistent with past simulations where no Dimits shift was observed for ∇T_e-TEM.

A number of further measurements and gyrofluid calculations were presented, which substantiated this picture and provide further information about the instabilities active below the critical gradient. Long wavelength density fluctuations changed little during the $L_{T_e}^{-1}$ scan. An increase in the ratio between electron temperature fluctuations and density fluctuations has been argued in the past to be an indication of TEM turbulence; this past result was reproduced for this data set, supported again by gyrofluid calculations.

Measurements were also acquired of intermediate-scale density fluctuations with DBS. The $L_{T_e}^{-1}$ scans in two of the rotation cases correlated with frequency-localized changes to the DBS spectra, consistent with a new mode being driven. TGLF calculations also predicted an increase to linear growth rates for the measured wave numbers. The mean frequency of the DBS spectra shifted toward the electron diamagnetic direction in 3 of the 4 cases, consistent with the expectation for TEM.

Conditional-averaging of the DBS spectra on NBI timing revealed further discoveries, with the spectral increase attributed to TEM systematically being higher during the counter-NBI injection periods of ECH+Bal-NBI plasmas than during the co-NBI periods. Conditional averaging of profile information indicated that changes to density and temperature profiles could not explain the DBS measurements. Measurements were lacking to fully assess whether the changes could be attributed to local changes to the $E \times B$ shear, but do motivate future work, where it might be possible to isolate and directly validate turbulence suppression by equilibrium $E \times B$ shear in the core of a tokamak.

Measurements of the crossphase between electron density and temperature fluctuation indicated a more subtle picture than the temperature fluctuations alone. The crossphase measurements were consistent with different instabilities active in the different NBI configurations and implied plausible changes to the directly transport relevant crossphases. Estimates of the electron heat flux that could be driven by the measured electron temperature fluctuations were concluded to require a plausible level of potential fluctuations (which were unmeasured) to drive a flux close to the magnitude of those inferred for the experiment. The probability distribution function of the crossphase measurements were broad and showed changes with the strength of the drive of the turbulence, which can be investigated in future work through comparisons to nonlinear simulations.

The evidence for different instabilities below the critical gradients consists of several pieces of evidence. First, consider the ECH-only plasmas. The density-temperature crossphase measurements changed little (from low to high values of L_{Te}^{-1}) compared to the ECH+Co-NBI plasmas. The changes were roughly consistent with changes to the crossphase for the longest wavelength mode with finite growth rate propagating in the electron diamagnetic direction in TGLF calculations. Sensitivity studies with TGLF were consistent with the concurrent existence of both ∇n_e-TEM and ∇T_e-TEM, which would also explain the changes to DBS spectra, where it appeared that there were two modes below the threshold and one above it.

The ECH+Co-NBI (the ECH+Bal-NBI cases were similar) were consistent with ITG or mixed ITG/TEM below the critical gradient and TEM dominated turbulence above.

The TGLF calculations for ITG and TEM showed that the density-electron temperature crossphases characteristic of the two modes cover different ranges of crossphase values, with little overlap. The measurements of the crossphase below the critical gradient were consistent with the ITG range of crossphases from TGLF and with the TEM range above it. As noted above, the change in the ratio of fluctuation levels correlated with the change in growth rates and was consistent with a transition to TEM dominated turbulence, where BES measurements of density fluctuations were acquired only during ECH+Co-NBI shots. The measured DBS spectra also shifted towards the electron diamagnetic direction for both ECH+Co-NBI and ECH+Ctr-NBI, consistent with a change from ITG to TEM. The DBS measurement in ECH+Bal-NBI plasmas showed a frequency-localized increase in spectral power with $L_{T_e}^{-1}$ on the electron diamagnetic side of the DBS Doppler-shifted peak.

The description most consistent with measurements during the $L_{T_e}^{-1}$ scan in ECH+Ctr-NBI plasmas differs slightly from the other cases. Two unusual measurements were acquired in ECH+Ctr-NBI: the density-temperature crossphase was measured to be positive at some radii and the DBS spectra shifted towards the *ion* diamagnetic direction with increasing $L_{T_e}^{-1}$. TGLF calculations provided an explanation that would account for both observations if ∇T_e-TEM was responsible for observations both above and below the observed critical gradient, but the power-weighted wave number of the measurements shifted to larger scales as $L_{T_e}^{-1}$ increased. Since TGLF showed that the crossphase increased to positive values at higher wave numbers and the ∇T_e-TEM frequency increased with wave number, it could explain both measurements since the crossphase and frequency are much less sensitive to $L_{T_e}^{-1}$ than the growth rates, as a function of wave number. This explanation also requires the higher Z_{eff} to be invoked as having a dilution effect on the deuterium species, weakening ITG. Parameter changes during ECH+Ctr-NBI would also be consistent with destabilization of impurity modes, like a Carbon-ITG, which could have been sub-dominant. Future comparisons to nonlinear simulations will be able to further test these explanations.

The principal result, the direct observation of a critical gradient for electron temperature fluctuations, is also the first observation of critical gradient behavior for *any* locally

measured turbulent quantity in the core of a high temperature plasma in a systematic experiment. This is important, as it provides direct evidence for the widely assumed nature of turbulence in fusion experiments as arising from linear instabilities. This evidence proved elusive in past work for a number of reasons. First, it is simply often difficult to realize experimental conditions below a critical gradient; the circumstances of multiple instabilities in the experiment was actually a necessary requirement to observe the critical gradient at all. The second is the combination of local heating and diagnostics that made the experiment and measurements possible.

Since any burning plasma experiment, like ITER, or future reactor would be expected to have strong electron heating from alpha particles and low rotation, these results might in fact be similar to what one would expect in a reactor. Although these measurements were acquired in L-mode, typical H-modes in current tokamaks are often achieved with strong NBI heating, which drives strong rotation and equilibrium $E \times B$ shear, which can suppress the turbulence. Neutral beams cannot penetrate deep into larger devices (instead larger devices must rely on microwave or radio frequency heating, which do not drive strong rotation), so the same mechanism to reduce core turbulence cannot be relied upon. Furthermore, intrinsic rotation has empirically been observed to scale inversely with machine size, which would similarly result in slowly rotating plasmas. This points to an important need in future work to assess why ∇T_e-TEM turbulence appears to be so stiff and whether this can be controlled.

The future work directly following from these results is to include direct comparisons to nonlinear simulations. The breadth and depth of the systematic changes to measured turbulence characteristics will provide a strong constraint on future validation exercises.

APPENDIX A

Statistical analysis definitions

A number of higher order statistical measures are used in this dissertation to quantify measurements. For concreteness, definitions are stated here. More detailed information is available in the literature, for example Refs. [269, 270]. Given a long, steady-state data set, one can break the data into shorter records so that a statistically significant sample size can be attained for use in an ensemble average. In the following, such an ensemble average is denoted by brackets, $\langle ... \rangle$. The cross-correlation function for two records, $x(t)$ and $y(t)$, is given by

$$R_{xy}(\tau) = \frac{1}{T}\int_0^T x(t)y(t+\tau)dt. \tag{A.1}$$

The normalized cross-correlation coefficient function (called simply the correlation function in other sections, for brevity), assuming the time records have zero mean, is then given by

$$C_{xy}(\tau) = \frac{R_{xy}(\tau)}{\sqrt{R_{xx}(0)R_{yy}(0)}}. \tag{A.2}$$

Given an autocorrelation function, $R_{xx}(\tau)$, its Hilbert transform, $\tilde{R}_{xx}(\tau)$, and envelope function can be calculated, $A_{xx}(\tau) = [R_{xx}^2(\tau) + \tilde{R}_{xx}^2(\tau)]^{1/2}$. A general definition of the autocorrelation time is

$$\tau_{ac} = \frac{\int_0^\infty A_{xx}(\tau)d\tau}{A_{xx}(0)}. \tag{A.3}$$

This definition of the autocorrelation time gives a measure of the decorrelation rate of all contributions to the measured signal. For a particular oscillatory component of a signal, one can define the autocorrelation time as $C_{xx}(\tau_{ac}) = C_{xx}(0)e^{-1}$, where the exponential is fit to the envelope of the decaying oscillatory component of the autocorrelation coefficient function. The cross-correlation coefficient is defined as $C_{xy}(\tau = 0)$. Comparing the cross-correlation coefficient between multiple measurement points, a correlation length, L_r, can be

defined as the point where the cross-correlation coefficient drops to $1/e$. The cross-spectrum is the Fourier transform pair to the cross-correlation function:

$$S_{xy}(\omega) = \int R_{xy}(t) e^{i\omega t} dt. \tag{A.4}$$

Numerically, it is more efficient to calculate the cross-spectrum from the Fourier transforms of the individual records, as described in Ref. [270]. With cross- and auto-spectra in hand, one can then calculate the ensemble averaged coherency

$$\left\langle \gamma_{xy}^2(f) \right\rangle = \frac{\left| \langle S_{xy}(f) \rangle \right|^2}{\left| \langle S_{xx}(f) \rangle \right| \left| \langle S_{yy}(f) \rangle \right|} \tag{A.5}$$

The coherency can also be written as

$$\gamma_{xy}(f) = |\gamma_{xy}(f)| e^{i\alpha_{xy}(f)}, \tag{A.6}$$

where $\alpha_{xy}(f)$ is the crossphase. The coherency gives a measure of the linear relationship between the two correlated quantities. The interpretation of the crossphase depends on the quantities being correlated. It can arise, for instance, due to propagation between spatially disparate points, as in experimental sections of this dissertation; or, it can give insight into fundamental properties of the turbulence, such as the phase relationship between different fluctuating fields [15, 16, 231]. An alternate definition for a correlation length can be defined as the distance where the coherency at a particular frequency, or the average coherency over a frequency interval, falls to $1/e$. The spectral definition is often used since the calculation is significantly faster than for the time domain definition. For calculation of Fourier transforms, Hanning windows and 50% overlap of records are used in this thesis. The random error estimates of the standard deviations, $\sigma_{\gamma_{xy}^2}$ and $\sigma_{\alpha_{xy}}$ (in radians), are given by

$$\sigma_{\gamma_{xy}^2}(f) = \frac{\sqrt{2}|\gamma_{xy}|(1-\gamma_{xy}^2)}{\sqrt{n_d}} \tag{A.7}$$

and

$$\sigma_{\alpha_{xy}}(f) = \frac{\sqrt{1-\gamma_{xy}^2}}{|\gamma_{xy}|\sqrt{2n_d}}. \tag{A.8}$$

The symbol n_d is the number of independent discrete records.

Bispectral analysis is a powerful technique that can be used to experimentally quantify the strength of quadratic nonlinearities. The bicoherence is a measure of this nonlinear coupling. Strictly speaking, the presence of significant bicoherence indicates only that, on average, three different waves satisfying the frequency relation $f_1 + f_2 = f_3$ and that possess a definite phase relationship exist. In principle this could be due to either phase-locked co-generation or nonlinear energy transfer; although, as discussed in Ref. [269], some forms of co-generation that cannot be determined from the power spectrum alone can be demonstrated with bispectral analysis. Diagnosis of nonlinear energy transfer relies on interpretation and comparison to models. For two time series of data, $\phi_1(t)$ and $\phi_2(t)$, define the ensemble averaged bispectrum, $B(f_1, f_2)$, as

$$B(f_1, f_2) = \langle \phi_1(f_1)\phi_1(f_2)\phi_2^*(f_1 + f_2 = f_3) \rangle \,, \tag{A.9}$$

where $\phi_j(f_i)$ is the Fourier transform of $\phi_j(t)$.The bicoherence, $b^2(f_1, f_2)$, is then

$$b^2(f_1, f_2) = \frac{|B(f_1, f_2)|^2}{\langle |\phi_1(f_1)\phi_1(f_2)|^2 \rangle \, \langle |\phi_2(f_3)|^2 \rangle}. \tag{A.10}$$

The summed bicoherence, $b^2(f_3)$, is a measure of the amount of coupling at one frequency, relative to all others:

$$b^2(f_3) = \sum_{f_1 + f_2 = f_3} b^2(f_1, f_2). \tag{A.11}$$

Analogous to the crossphase for the coherency and cross-spectrum, the biphase is associated with the bicoherency and bispectrum; the biphase can be determined from the bispectrum:

$$\langle \phi_1(f_1)\phi_1(f_2)\phi_2^*(f_3) \rangle = A e^{i\alpha_{\phi_1,\phi_2}} \Rightarrow \alpha_{\phi_1,\phi_2}. \tag{A.12}$$

The meaning of the biphase depends on the quantities being examined and the model used to interpret the results; its value can arise, for instance, due to radial propagation or nonlinear energy transfer [145, 271]. The standard deviation due to random error for the bicoherence can be approximated by

$$\sigma_b(f_1, f_2) = \frac{1}{\sqrt{n_d}} \sqrt{1 - b^2(f_1, f_2)}, \tag{A.13}$$

which allows a bound of $1/\sqrt{n_d}$ to be set on the statistical random uncertainty of the bicoherence.

APPENDIX B

Fluctuation diagnostic pointnames

Data from the DBS/reflectometry diagnostic usually referred to as "DBS-5" in the text and detailed in Chapter 3 is stored on General Atomics servers and can be accessed through MDSplus. After first being installed in May 2008, the pointnames where the data is stored have changes several times. For completeness and to enable future replication of presented results, this information is included here, along with the same information for other fluctuation diagnostic data that is analyzed in Chapters 4 and 5.

Initially, DBS-5 had only 4 channels: bandpass filters at 3.75, 4.45, 4.80, and 5.15 GHz. The 4.10 GHz filter and associated amplifiers and mixers were active beginning Dec. 2009. The LO can be either above or below the launched frequencies, depending on the chosen setting. This flips the sign of the resulting Doppler shift. To determine the correct sign either check logbooks or compare against experimental signatures, *e.g.* the change in sign caused by co-injected neutral beams. Table B.1 lists the DBS-5 pointnames from 2008-2012. Logbooks need to be checked for the frequency setting(s) and mirror angles for any particular shot.

DBS-8 was active starting Dec. 2009. The eight static launch frequencies are 55.0, 57.5, 62.5, 67.5, 70.0, 72.5, and 75.0 GHz. These launch frequencies correspond to pointnames `d1a` & `d1b`, `d2a` & `d2b`,...`d8a` & `d8b`, respectively.

CECE data was normally stored to `ecrf1`, `ecrf2`, `ecrf3`, and `ecrf4`. Logbooks need to be checked for LO and filter selection. Starting Dec. 2009, the pointnames `dbsxa` & `dbsxb` were most often used to digitize signals from fast magnetic pickup loops (B3 and B4); although, these channels were at times re-appropriated for other diagnostics. DBS-2

Shots	133277-133739
Filter Frequency	Pointname
5.15 GHz	`refl1` & `refl2`
4.80 GHz	`refl3` & `refl4`
4.45 GHz	`refl5` & `refl6`
3.75 GHz	`refl7` & `reflmn`

Changes as of shot	133740
3.75 GHz	`refl7` & `refl8`

Changes as of shot	140378 (Dec. 2009)
3.75 GHz	`dbs1a` & `dbs1b`
4.10 GHz	`dbs2a` & `dbs2b`
4.45 GHz	`dbs3a` & `dbs3b`
4.80 GHz	`dbs4a` & `dbs4b`
5.15 GHz	`dbs5a` & `dbs5b`

Table B.1: DBS-5 MDSplus pointnames

pointnames vary: check logbooks.

APPENDIX C

Additional information for a/L_{T_e} experiment

This appendix contains additional information and details about the experiment investigated in Chapter 5.

A number of profile diagnostics were used to compile the information summarized in Table 5.1. The long steady-state time periods were used to average data. Electron density profiles were constrained by profile reflectometry, Thomson scattering, and interferometer chords. Ion temperature, impurity density, and toroidal rotation were measured by CER. The fast ion density was determined by modeling with Monte Carlo methods from a module of the ONETWO transport code [258]. Radiated power measurements from bolometer chords were included in the ONETWO calculations. The deuterium density was inferred from the electron, carbon, and fast ion profiles–this information was then used to calculate Z_{eff}. In effect, the reported Z_{eff} is a lower bound, neglecting high Z impurities. The EFITs used in the analysis presented used only external magnetics data for equilibrium reconstruction.

Figure C.1 shows time series of heating and equilibrium parameters for one of the shots in the experiment. Neutral beam heating is applied early in the shot, before 1000 ms, to raise the central temperature, which slows current diffusion and delays the onset of sawtooth oscillations in the center of the plasma. The experimental approach was to change the ECH locations shot-to-shot (as described in Sec. 5.3.1), while changing NBI within each shot. There were three time periods of interest in each shot that were used to average the turbulence measurements. These are shown for shot 144569 in Fig. C.1. Each shot had an ECH-only period, an ECH+Co-NBI period, and either a ECH+Bal-NBI or a ECH+Ctr-NBI period. Feedback control was used to keep the line-averaged density constant. During NBI

periods the neutral beams were interlaced in 10 ms intervals to gather data for different diagnostics. Neutral beam power was matched in the three NBI setups, which meant for ECH+Bal-NBI there was a slight offset in momentum input, with +2.1 Nm during the co-injection periods and -2.0 Nm during counter-injection periods.

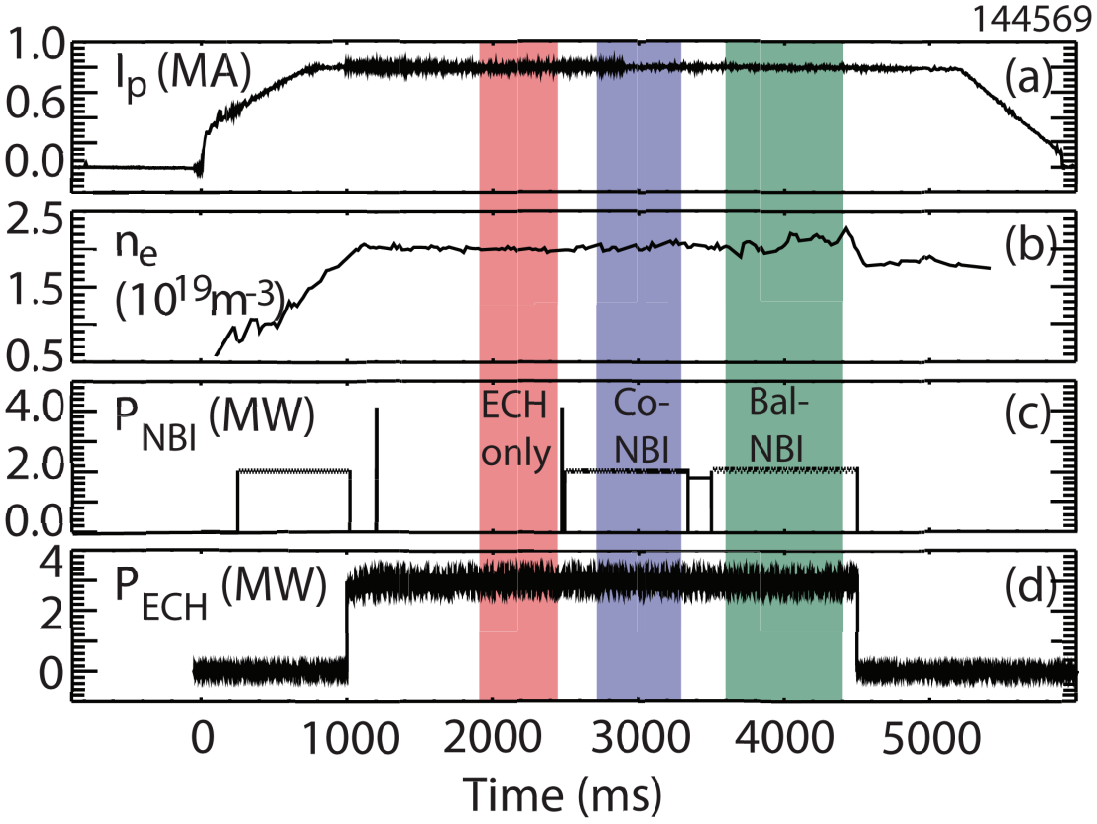

Figure C.1: (a) Plasma current, (b) line-averaged density, (c) neutral beam heating power, and (d) electron cyclotron heating power for shot 144569. Time periods of interest are shaded.

Table C.1 lists the good shots and time periods for the experiment. Glitches such as gyrotrons or beams dropping out are the cause of most of the shortened time periods; several of the early shots in the sequence also briefly entered H-mode. The 240° Port shutter was

ECH(in,out)	Shot	ECH-only	ECH+Co-NBI	ECH+Bal-NBI	ECH+Ctr-NBI
(0,6)	144566	1900-2470	2950-3350	3850-4200	
(1,5)	144567	1900-2470	2600-2960		
(2,4)	144568	1900-2470	2700-3300	3600-4400	
(3,3)	144569	1900-2470	2700-3300	3600-4350	
(5,1)	144570	1900-2470	2700-3040		
(5,1)	144572	1900-2470	2700-3300	3600-4400	
(1,5)	144573	1900-2470	2700-3300	3600-4400	
(1,5)	144575	1900-2470	3800-4400		2700-3500
(0,6)	144577	1900-2470	3900-4400		2700-3500
(5,1)	144579	1900-2470	3800-4400		2700-3500

Table C.1: Good shots and times for $L_{T_e}^{-1}$ experiment. Times are in ms.

kept closed until that behavior ceased, since one of the heating gyrotrons is at the same port location. If the plasma goes into H-mode and becomes over-dense, it could reflect $\sim 10^9$ times more power into the diagnostic hardware than it is designed to receive. This might result in equipment failure, so care is taken to avoid such circumstances. Shot 144568 was the first shot that did not briefly transition into H-mode, so it was only from 144569 onward that the 240° Port diagnostics (DBS-5 and CECE) were able to acquire data. The shutter at the 255° Port for the profile reflectometry system was also only open for 144569 and later. The time periods in the table were used for the ensemble averages of the turbulence spectra.

C.1 Calculation details

A number of results from the TGLF code were presented in Chapter 5. The version of TGLF used, v1.93, is set up to directly read one of the outputs from the ONETWO transport code, the `iterdb` file. The information stored in that file includes all profile information, as well as the Miller parameterization of the equilibrium, and transport calculations such as sources

and fluxes. This approach avoids issues regarding input normalizations and formatting. TGLF runs output a file with all input parameters, named `tglf_overwrite`. The values in this file can be modified and used as the input for subsequent runs. This was done for the parameter scans presented in Sec. 5.4.

In addition to linear gyrofluid results from TGLF, gyrokinetic calculations using the code GS2 were attempted. GS2 allows experimental equilibria from EFIT to be used directly, in addition to being able to use several analytical models. Unfortunately this module is not widely used and issues were encountered. Using the numerical equilibria with collisions resulted in all modes being linearly damped, while collisionless runs yielded reasonable looking results, *i.e.* frequency and growth rate spectra similar to TGLF results for TEM. Code authors were informed of the issues.

APPENDIX D

Additional analysis of γ_{n_e,T_e} and α_{n_e,T_e} measurements

In the main text of the thesis, correlations from typically only one pairing of a reflectometry channel and a CECE channel were presented for each time period and radii of interest. For instance, the data presented in Sec. 5.3.3.6 were all from the pair of channels closest to a particular radial location in each time period. Due to shot-to-shot changes to the launched DBS-5 frequency (attempts were made to assure the systems were overlapped) and due to small changes in the density profile, much of the presented data comes from different pairs of channels. There are a large number of possible correlations that can be calculated–5 reflectometry channels and 4 CECE channels–for each time period. Presented here are results from analyzing correlations with multiple channels during the same time period.

Figure D.1 shows analysis of one the ECH+Bal-NBI (5,0.5) time periods of the experiment covered in detail in Chapter 5. One CECE channel, `ecrf4`, is sequentially correlated with each of the DBS-5 channels. The CECE channel filter was centered at 91.55 GHz and the center of the DBS-5 array was launched at 66.82 GHz. Ray tracing (using measured density profiles and EFITs) indicated that the closest pair of channels were `ecrf4` and `dbs1`, with the 91.55 GHz (`ecrf4`) 2^{nd} ECE harmonic radiation originating from $\rho = 0.614$ and the X-mode cutoff for 66.12 GHz (`dbs1`) at $\rho = 0.609$–a separation of less than 0.5 cm. The radial separation between `ecrf4` and the DBS-5 channels increases with channel number. This is reflected in Fig. D.1(a) by the reduced coherency as the radial separation increases (`dbs2` is somewhat of an outlier–that is the fifth channel that was added after the system was originally constructed and has slightly different hardware components, with slightly more noise). Figure D.1(b) shows that the measured crossphase is almost identical for `dbs1`, `dbs2`,

and dbs3. This is consistent with the synthetic diagnostic results of Ref. [16], where it was concluded that radial separation between channels should reduce the measured coherency, but not affect the crossphase. For dbs4 and dbs5, the two most radially separated channels, there does appear to be a small change to the measured crossphase. For the results in Sec. 5.4.1.4, the change is toward crossphase values associated with ITG modes, and away from values associated with TEM. A consistent explanation would be that while the conclusions of Chapter 5 are valid–TEM is the dominant instability–that both ITG and TEM are unstable, with the TEM at higher-k than ITG. The increase in the radial separation can then be understood as a radial wave number filter, with TEM excluded as the radial separation is increased. The way the synthetic diagnostic is implemented for GYRO is that the reflectometry and CECE volumes are separately specified. Direct comparison to data like Fig. D.1 might provide an interesting comparison for validation studies. A possible explanation for why this radial wave number filter effect was not observed in the tests in Ref. [16] is that those simulations runs were local, radially periodic runs; global runs with radial domains much larger than the correlation length of the turbulence might be needed. A simpler alternate explanation might be that the tests in Ref. [16] were completely dominated by a single type of instability and that mixed mode turbulence is necessary to see the effect.

Figure D.2 shows another example of the difference in the correlations between one CECE channel, here ecrf1, and the five DBS-5 channels used for reflectometry. This example is from a ECH+Ctr-NBI (5, 0.5) plasma from Chapter 5. Ray tracing indicates that the closest two channels were ecrf1 at 93.39 GHz, $\rho = 0.545$ and dbs3 at 67.83 GHz, $\rho = 0.542$–almost perfectly overlapped. The correlation showing the maximum coherency is actually dbs4, but the differences between the peak coherency for dbs3, dbs4, and dbs5 are within statistical uncertainties. Unlike the ECH+Bal-NBI case, there is a significant slope to the crossphase (this was only observed for ECH+Ctr-NBI plasmas). Again the channels most radially separated and showing the lowest coherency exhibit measured crossphase values closer to those associated with ITG modes. Since the channels are almost exactly overlapped and the measurement geometry is almost exactly the same as the ECH+Bal-NBI case above, it

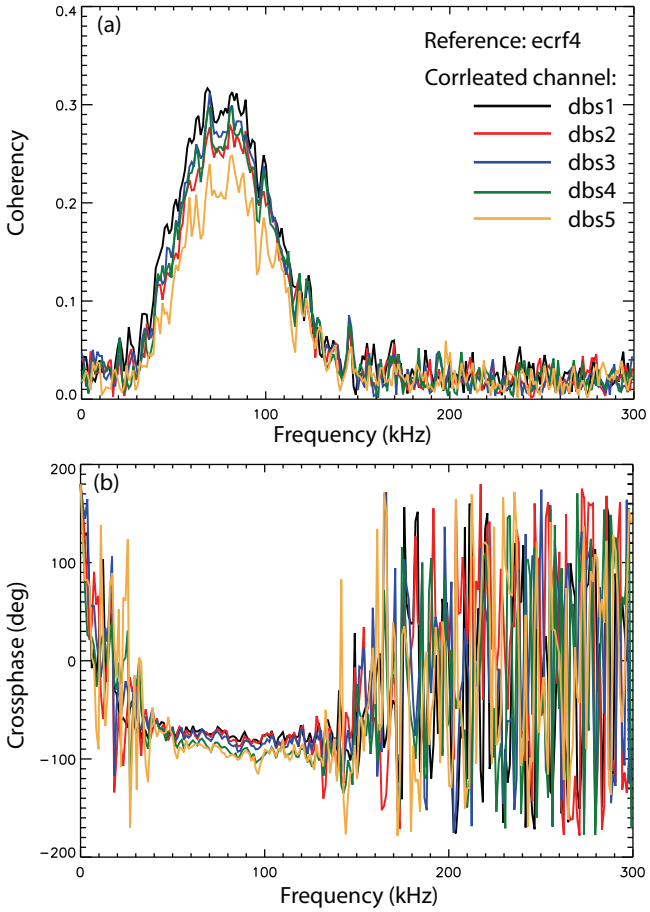

Figure D.1: (a) Coherency and (b) crossphase with one CECE channel and five different reflectometry channels. Shot 144572 3600-4400 ms.

is unlikely that the measured slope to the crossphase can be attributed to poloidal offset between the channels–which was shown to generate just such a slope in Ref. [16]–otherwise it should have been observed for ECH+Bal-NBI also. The reason a poloidal separation would be expected to introduce a slope to the crossphase would be due to rotation of the plasma. The ECH-Ctr-NBI plasma had the *lowest* rotation of any of the cases, so one would expect the effect to be smallest there. A possible explanation would be that in this case there was direct correspondence between each frequency and an unstable mode at a different wave number. The crossphase slope might then be attributed to a physical change in the crossphase between the temperature and density, as a function of wave number. This can be tested in future work through comparison to synthetic diagnostic output from gyrokinetic simulations.

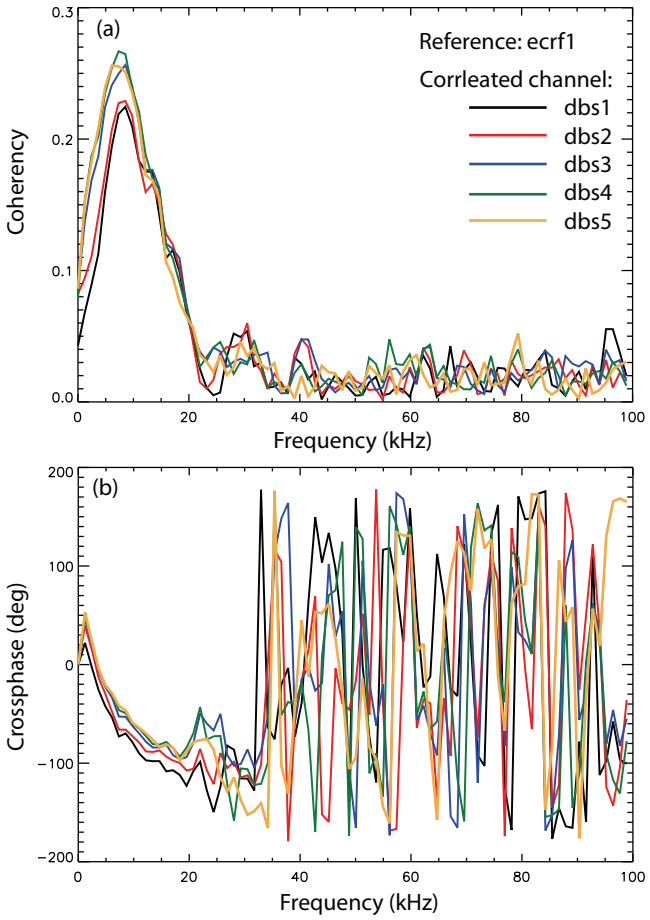

Figure D.2: (a) Coherency and (b) crossphase with one CECE channel and five different reflectometry channels. Shot 144579 2700-3500 ms.

APPENDIX E

Alternate calculation of γ_{n_e,T_e}

The measured coherency between reflectometry and CECE measurements at DIII-D have always been fairly low, $\gamma_{n_e,T_e} \lesssim 0.4$. Heuristically, for a reflectometry signal S_{refl} and an ECE signal S_{ECE}, the coherency is

$$\gamma_{nT} = \frac{S^*_{refl} S_{ECE}}{\sqrt{|S_{refl}|^2}\sqrt{|S_{ECE}|^2}}. \tag{E.1}$$

Recalling Sec. 3.6, Eqn. E.1 is clearly not the same as the coherency between density and temperature fluctuations: the thermal noise contribution should have zero correlation with the reflectometry signal in the numerator, but the ECE autocorrelation in the denominator will be dominated by it–this is why, as mentioned elsewhere, one expects γ_{nT} to increase if the temperature fluctuation level increases, all else the same. Reflectometry only effects could also contribute. The approach taken in the first realization of the crossphase measurement [231] was to use an *ad hoc* definition for the coherency, where instead of an auto-correlation for the ECE channel in the denominator, the crosspower between two CECE channels was used instead, which inflates the coherency (and one is no longer guaranteed that $\gamma \leq 1$):

$$\hat{\gamma}_{nT} = \frac{S^*_{refl} S_{ECE,1}}{\sqrt{|S_{refl}|^2}\sqrt{S^*_{ECE,1} S_{ECE,2}}}. \tag{E.2}$$

Figure E.1 shows the result of using the second definition for DIII-D data. The alternate definition for the coherency does not change the crossphase, for the same ECE channel used for the crosspower in the numerator (although one could argue for changes to the estimated error in the crossphase). In Fig. E.1(a-b), $S_{ECE,1} =$ `ecrf4` and $S_{ECE,1} =$ `ecrf2` (referring to Eqn. E.2) and in Fig. E.1(c-d) $S_{ECE,1} =$ `ecrf2` and $S_{ECE,1} =$ `ecrf4`. The frequencies for the

CECE channels are `ecrf4` at 91.55 GHz and `ecrf2` at 91.38 GHz. As would be expected, the crossphase spectra show negligible differences. The coherency spectra result in several differences from the standard definition. First, although the vertical axis in the plots are truncated, there are actually coherency values greater than unity. This must be occurring due to the crosspower $S^*_{ECE,1}S_{ECE,2}$ yielding very small values for some frequencies. Second, above $f \sim 150$ kHz, where the standard coherency definition yields consistently small values, the *ad hoc* definition exhibits noisy behavior, with large variations in coherency and a higher average noise floor. Third, the *ad hoc* coherency over the frequency range where the standard coherency was also significant, 40 kHz $\lesssim f \lesssim$ 150 kHz , using one of the CECE channels for the crosspower term $S^*_{refl}S_{ECE,1}$ results in lower values of coherency, but using the other CECE channel results in higher values.

Given the differences in coherency in Fig. E.1(a,c) one might question how the standard coherency is impacted by using different CECE channels from near the same radial location (*i.e.* using the other CECE channel that is used for the temperature fluctuation measurements). This comparison is shown in Fig. E.2, where the standard coherency is used to correlate DBS-5 with two different CECE channels. The result is small differences.

The coherency values in Fig. E.1(a,c) and Fig. E.2(a,b) imply that the differences observed in the *ad hoc* coherency values must be related to the ratio between the autopower in the individual CECE channels. That is, there is a diagnostic effect where the ECE calibration enters into the coherency. There is a hardware difference between the channels. There are four CECE channels: two fixed filter channels and two tunable filter channels. In past work [16, 110] the usual approach was to tune the two tunable channels to be near each other, for calculation of the temperature fluctuation level. In Chapter 5 each of the tunable channels were arranged to be near one of the fixed channels, for two measurements of the temperature fluctuation level per shot, so that there is a mixed set of filters at each radial location. For a measure that is supposed to normalize out such diagnostic effects, this is obviously a bad characteristic. Furthermore, allowing coherency values greater than unity and the increased noise floor are also clearly undesirable.

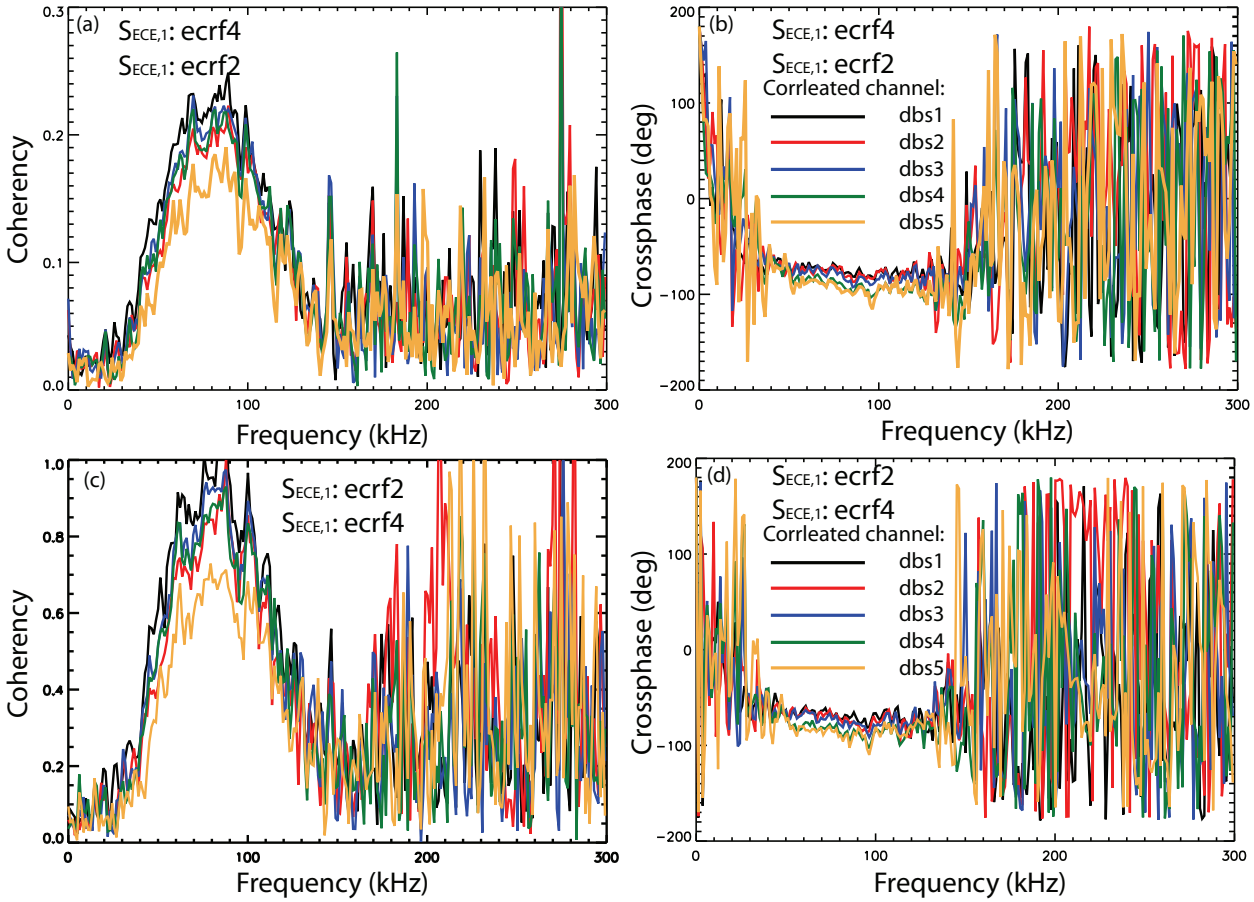

Figure E.1: (a,c) Coherency and (b,d) crossphase from 144572 3600-4400 ms between DBS-5 and CECE. (a,b) use $S_{ECE,1}$ =ecrf4 and $S_{ECE,1}$ =ecrf2. (c,d) use $S_{ECE,1}$ =ecrf2 and $S_{ECE,1}$ =ecrf4.

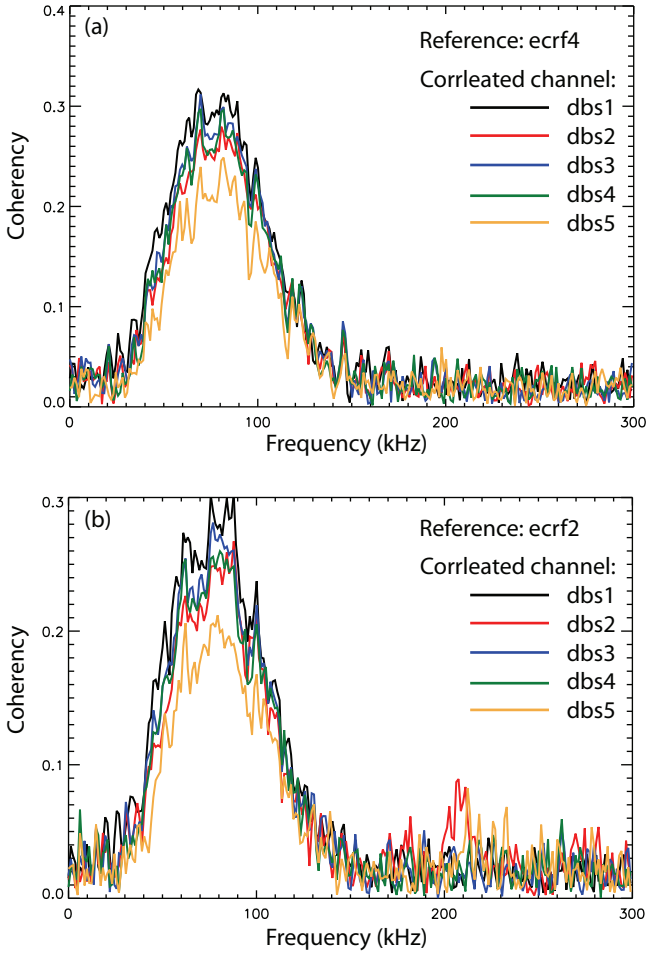

Figure E.2: Reflectometer-CECE coherency from 144572 3600-4400 ms. (a) uses ecrf4 for the CECE channel and (b) uses ecrf2 for the reference channel.

One of the three shortcomings of the *ad hoc* coherency can be addressed by using calibrated CECE channels (see Sec. 3.6 for details). The result of using calibrated ECE channels on the *ad hoc* coherency is depicted in Fig. E.3, for the two CECE channels as the reference channel with each channel of DBS-5. Both coherency values are larger than the standard coherency definition yields, as one would expect. The coherency values are also in reasonable agreement. The increased noise and possibility of $\gamma > 1$ persist, however. If a comprehensive description of how the reflectometer amplitude relates to density fluctuations is completed in the future, it might be possible to use the *ad hoc* approach to make an argument for relating the measured reflectometer-CECE coherency to the physical density-temperature coherency. Lacking that, the approach should be avoided. It should also be noted that in simulations, the coherency is always close to one–it is not clear that measurements of that quantity would actually be useful; it is the amplitude and phasing of the fluctuations that matter. The measured coherency must simply be sufficiently high for a meaningful measurement.

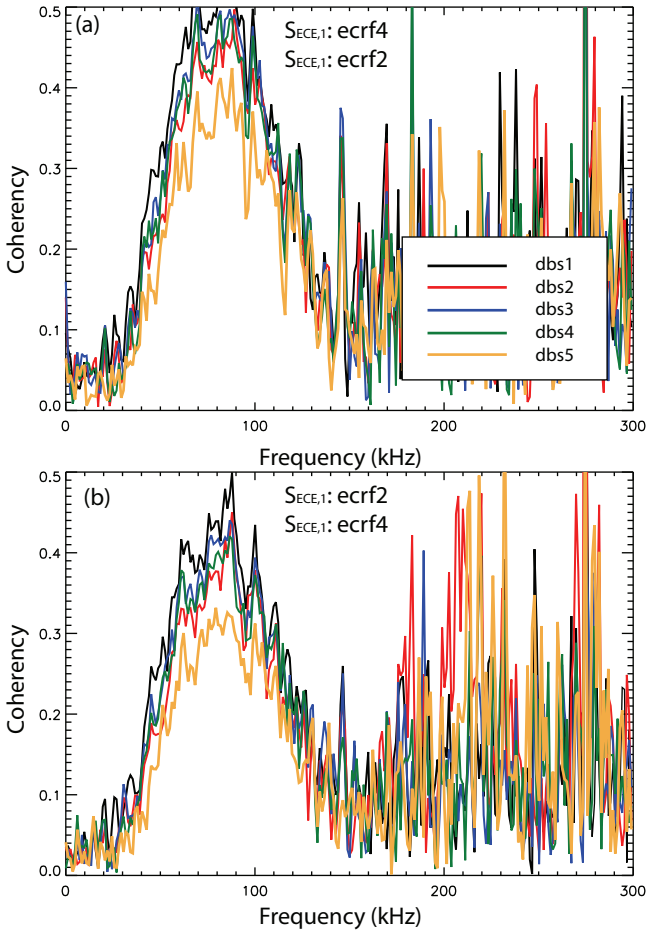

Figure E.3: Reflectometer-CECE coherency from 144572 3600-4400 ms, with calibrated CECE channels. (a) Uses $S_{ECE,1}$ = ecrf4 and $S_{ECE,1}$ = ecrf2. (b) Uses $S_{ECE,1}$ = ecrf2 and $S_{ECE,1}$ = ecrf4

APPENDIX F

Novel Doppler Backscattering analysis

A number of approaches to analyzing DBS data were attempted during the course of work on this dissertation that were not fully explored. In this section, several of these forays into novel analyses are documented.

F.1 DBS when $v_{E\times B} = 0$

Continuing the reasoning from Sec. 3.3.1.1, there are two possibilities for what is expected to occur when $v_{E\times B} = 0$. The question is how $v_{E\times B} = 0$ relates to the minimum width of the spectrum and to when the measured Doppler shift is zero. Clearly, the minimum Doppler shift should occur when the lab frame propagation velocity of the turbulence is zero, that is $v_{\tilde{n}} = 0$, which implies $v_{phase} = -v_{E\times B}$. One possible expectation is that the width of the DBS spectrum should be at a minimum at the same time. Heuristically, if one extends expressions for the spectral width to include the distribution of the phase velocity of the turbulence, it can be written that

$$\Delta\omega_{DBS} = \Delta k v_{E\times B} + \Delta k \left\langle v_{phase} \right\rangle + k_{\perp} \Delta v_{phase}, \tag{F.1}$$

neglecting the combined effect of Δk on the velocity distribution, symbolically denoted by Δv_{phase}. From this point of view, one would expect the second two terms on the right-hand-side of Eqn. F.1 should essentially be a constant and that the minimum spectral width should therefore occur when the first term vanishes. The arguments then hinges on asserting that $\Delta\omega_{DBS}$ is at a minimum when $v_{E\times B} = 0$. The minimum spectral width then corresponds when $v_{E\times B} = 0$, not $v_{\tilde{n}} = 0$.

The data in Fig. 3.3 can be used to discriminate between the two expectations. Figure F.1 shows analysis of two DBS channels from shot 134024, Fig. F.1(a) shows the standard deviation of the DBS quadrature spectrum and (b) shows frequency of the Doppler peak as functions of time. It is clear that the minimum spectral width occurs at a different time than when the Doppler shift is at zero frequency−this could not be true if the spectrum were at a minimum when $v_{\tilde{n}} = 0$. We therefore accept Eqn. F.1 as qualitatively correct and interpreted the minimum standard deviation of the spectrum as when $v_{E\times B} = 0$. It should be noted that there are additional complications: although the total heating power can be kept constant while $v_{E\times B}$ is swept through zero by changing the direction of momentum injection, other parameters that would be expect to have an effect on the turbulence, such as the shear of the radial electric are changing at the same time. It is assumed that in the neighborhood of $v_{E\times B} = 0$, these transient effects are negligible. With these *caveats*, we note from Fig. F.1 that the minimum spectral width occurs when $f_{Doppler} \approx 50$ kHz, consistent with the general expected frequency range for drift wave turbulence. For the scattering wave number from ray tracing of ~ 4.8 cm^{-1}, we then infer a phase velocity for the turbulence of about 650 m/s in the electron diamagnetic direction. These numbers would be generally consistent with the expectations for trapped electron mode turbulence.

F.2 Cross-correlation of DBS with CECE

When a Doppler Backscattering system is aligned for its beam to normally approach a cutoff surface it acts as a conventional reflectometer. Correlations between reflectometry and CECE have been explored in detail and used for physics studies in Secs. 3.8, 5.2, and 5.3.3.6 and have been featured in several publications. An immediate question that arises is whether DBS and CECE can be correlated, and, if so, what is the interpretation of the results.

First we look at a coherent mode, the GAM. Data from the a/L_{T_e} experiment in Chapter 5 is used, where correlations are performed between CECE at the 240° Port and DBS-8 at the 60° Port. The data in Fig. F.2 is from an ECH+Co-NBI (5,1) plasma. The outermost of

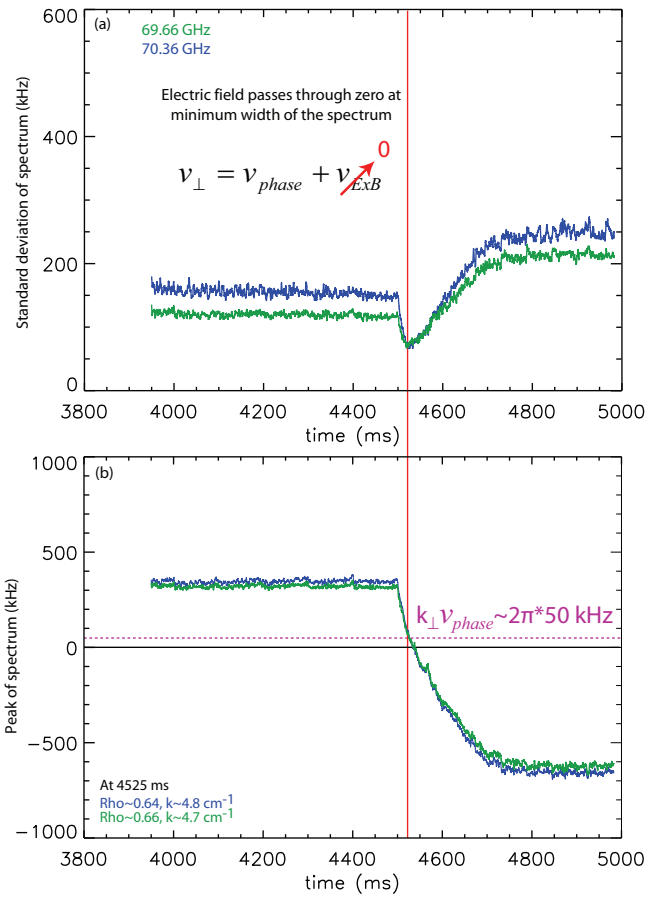

Figure F.1: (a) Shows the standard deviation of two DBS channels from shot 134024, and (b) shows the channel's peak frequency. In (b), the solid black line indicates zero frequency. The solid vertical line and dashed horizontal lines are added to help guide the eye.

the four CECE channels, `ecrf2` is correlated with the derivative of the phase (proportional to the local flow velocity) from 4 DBS-8 channels. There is a clear peak at about 25 kHz, consistent with a GAM. The CECE channel is at $\rho \approx 0.6$, with the highest frequency DBS channel, `d4`, at $\rho = 0.75$. The coherency drops as the radial separation increases. The frequency of the peak is consistent with the frequency in the flow contour plots in Sec. 4.6.2. There is a peak at the GAM frequency in several of the CECE spectra in Fig. 5.6. The toroidal correlation in Fig. F.2 shows the peak is indeed due to the GAM. Oscillations at the frequency of the GAM in ECE signals have been noted in previous work [115]. The changes in crossphase in Fig. F.2 are consistent with the radial propagation of the GAM; there are large changes between the 2.5 GHz separation between the DBS-8 channels. The GAM in this case is also evidently radially coherent over about 1/3 of the minor radius. The correlation is also present for φ_{DBS} (instead of $\partial\varphi_{DBS}/\partial t$), but not for the DBS amplitude, $A_{DBS} = \sqrt{I^2 + Q^2}$. This is consistent with the interpretation that it is the GAM $E \times B$ flow that is being correlated with a temperature component of the GAM. Since the temperature fluctuations correlate, but not density, it appears that the temperature component of the GAM is not m=1, like the density.

The correlation of the GAM motivates investigation of DBS-CECE correlations of turbulence. Figure F.3 shows the coherency and crossphase between a CECE channel and a DBS-5 channel aligned for reflectometry in an NBI-heated L-mode plasma (no ECH), with measurements at $\rho \approx 0.72$. The result that the reflectometer phase and amplitude yield the same crossphase, shown in Sec. 3.8.2, is reproduced.

The following shot was a essentially a repeat, but the DBS-5 angle was changed from $-1.5°$ for reflectometry in 145181 to $-5.0°$ for DBS in 145182. The same launch frequency was used, DBS-5 center frequency at 70 GHz, but the radial position of the measurement was shifted slightly outward, to $\rho \approx 0.75$, according to ray tracing. The scattering wave number was about 5 cm^{-1}. Figure F.4 shows the coherency and crossphase between a CECE channel and the amplitude, A_{DBS}, of 5 DBS-5 channels, aligned for DBS. Similar values are obtained for both the broadband feature, $\sim 50 - 200$ kHz, for both coherency

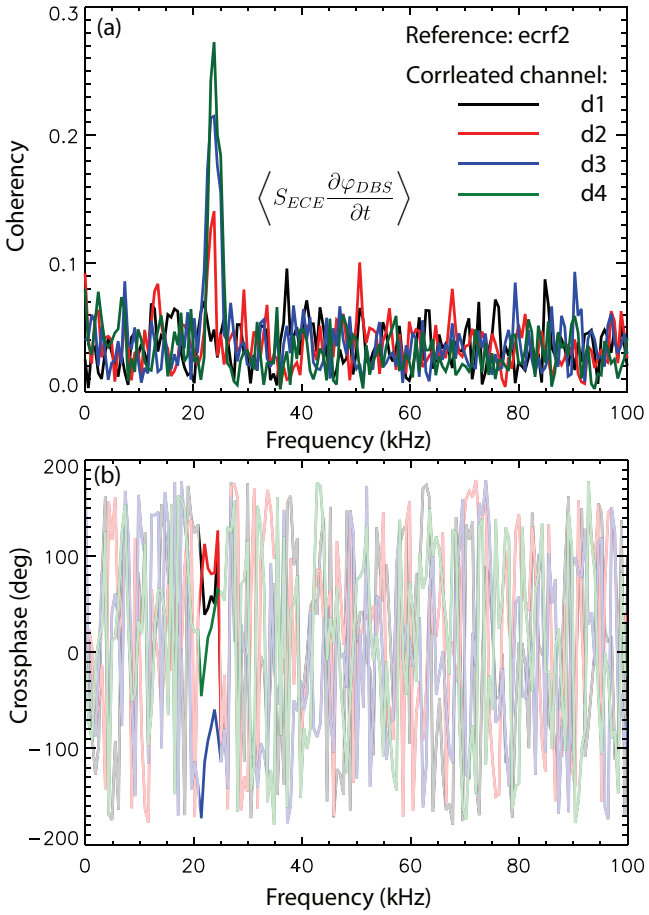

Figure F.2: (a) Coherency and (b) crossphase between a CECE channel and $\partial\varphi_{DBS}/\partial t$ from 4 DBS channels at a toroidally separated location. Shot 144579 3800-4400 ms.

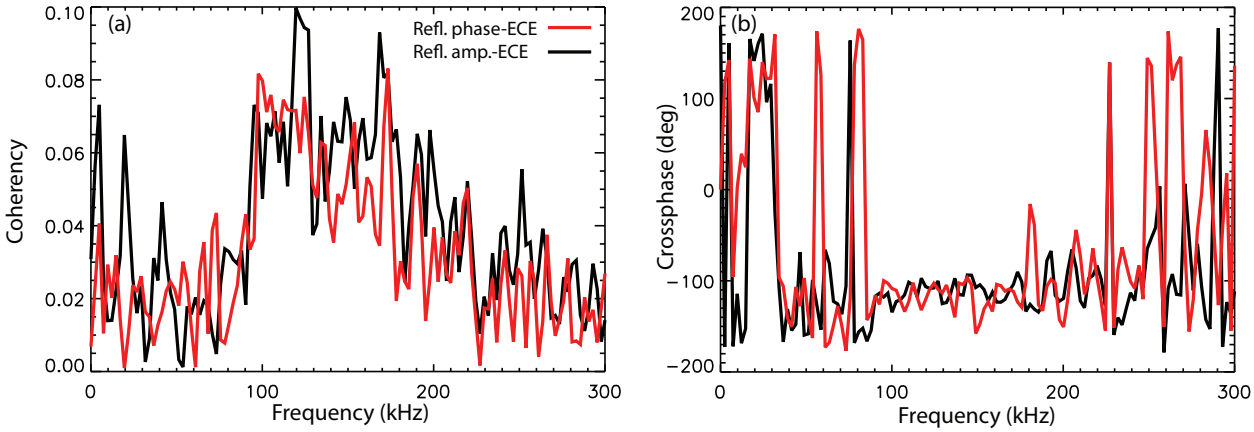

Figure F.3: (a) Coherency and (b) crossphase between a CECE channel and a reflectometer channel for both the reflectometer phase and amplitude. Shot 145181 1500-2000 ms.

and crossphase. In addition to the broadband feature, a peak in the coherency spectrum occurs at about 20 kHz, for the GAM. Consistent with expectations for the GAM, there is a rapid change in crossphase at the GAM frequency. Figure F.5 compares the correlation between a CECE channel, and the DBS amplitude, DBS phase, and DBS phase derivative for a single DBS-5 channel. The coherency for all three is similar, with the phase and phase derivative almost exactly the same, except for near zero frequency. The crossphase for the phase-ECE correlation is down-shifted by about 20° where the coherency is highest for the broadband component, which is notably different than the result for conventional reflectometry in Fig. F.3(b). The GAM component is about 90° different between the phase and amplitude, which is also different from Fig. F.3(b). The crossphase spectrum for the DBS phase derivative correlation with ECE is shifted up slightly less than 270° (or down by slightly more than 90°) from the DBS phase, which is what one would expect (*i.e.* a phase shift from $\partial/\partial t \rightarrow -i\omega$); although, the shift is not exactly 90°.

Several conclusions can be drawn from these results regarding what the DBS-CECE correlation is measuring. The toroidal correlation of the GAM with DBS shows it is temperature that is correlating with the flow. The comparison between the reflectometer-ECE correlation and the DBS-ECE correlation shows that the latter contains different information. One

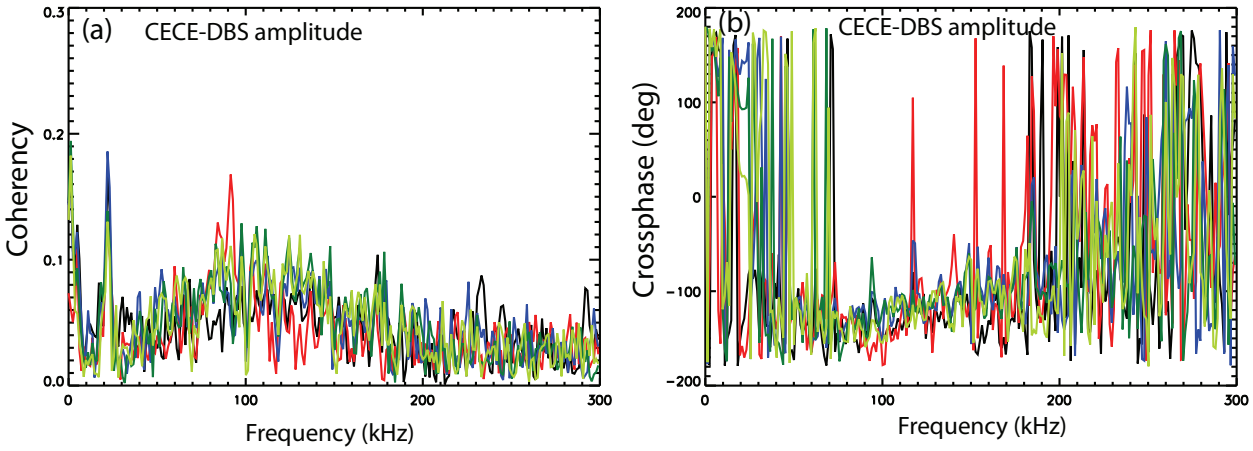

Figure F.4: (a) Coherency and (b) crossphase between a CECE channel and the DBS amplitude for the 5 DBS-5 channels. Shot 145182 1500-2000 ms.

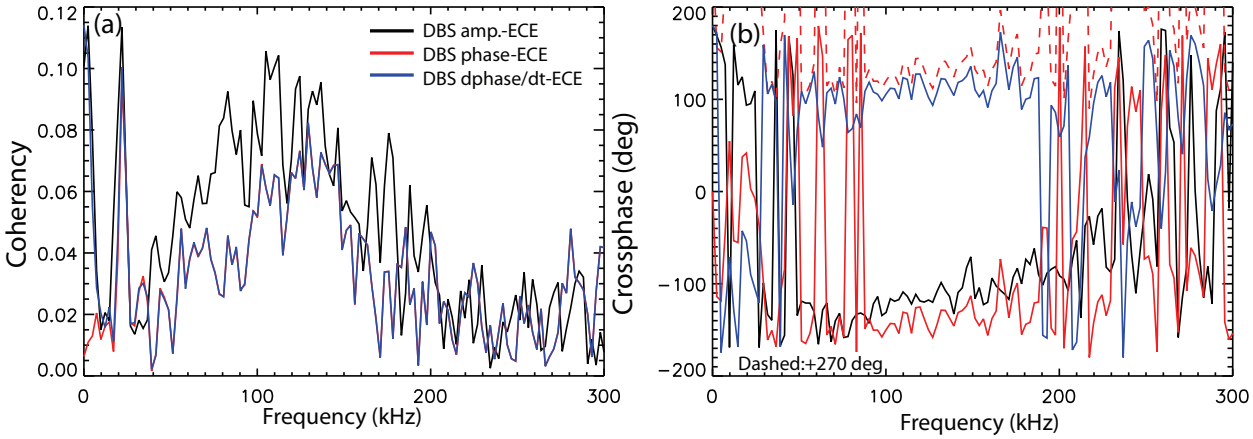

Figure F.5: (a) Coherency and (b) crossphase between a CECE channel and the DBS amplitude, DBS phase, and DBS phase deriative for a single DBS-5 channel. Dashed line in (b) is shifted by $+270°$ ($-90°$ mod 2π). Shot 145182 1500-2000 ms.

would like to be able to interpret the DBS-ECE crossphase as related to the crossphase between electron temperature and radial electric field fluctuations; however, there are some unanswered questions about the data. For instance, why does the DBS amplitude correlate with ECE? This could be due to the reflected beam being detected at the same time as the backscattered signal, so that the measured crossphase is a weighted averaged of the density-temperature and flow-temperature crossphase. A larger set of comparisons and additional plasma conditions might be able to resolve interpretation issues in future work.

F.3 Cross-correlation of DBS amplitude with DBS phase

The interpretation of ideal DBS measurements is that the amplitude, A_{DBS}, is associated with density fluctuations and the phase, φ_{DBS}, is associated with flow fluctuations. These quantities can be correlated together. In Fig. F.6, the DBS amplitude from `d8` is cross-correlated with the DBS phase from all eight channels of DBS-8. There is a large correlation between A_{DBS} and φ_{DBS} for `d8`, which is not present in the correlation with the other channels. Figure F.7, uses the same data, but for the reference uses the DBS amplitude from `d6`. There is again a higher frequency component, in the megahertz range, which has a crossphase of about $-90°$; additionally, there is a low frequency component at ~ 50 khz, with a different crossphase. That peak also shows up for correlations of φ_{DBS} or A_{DBS} between channels, but obviously the auto-correlation of those quantities for a single channel is always unity, so the megahertz component of the signal is not apparent. The amount of power in the auto-spectra at ~ 1 MHz is also much smaller than the power at low frequencies; this difference is normalized out in the coherency.

There are several conclusions that can be drawn from these plots. The correlations of the low frequency component between spatially disparate channels indicates that there is a non-local component to the DBS signal, possibly due to small angle scattering due to long wavelength density fluctuations along the beam path. The fact that the megahertz component shows up only on one channel implies that there is localization, whether spatial

or in wave number. The high frequency component is also much higher that the standard DBS peak, which occurs at a few hundred kHz.

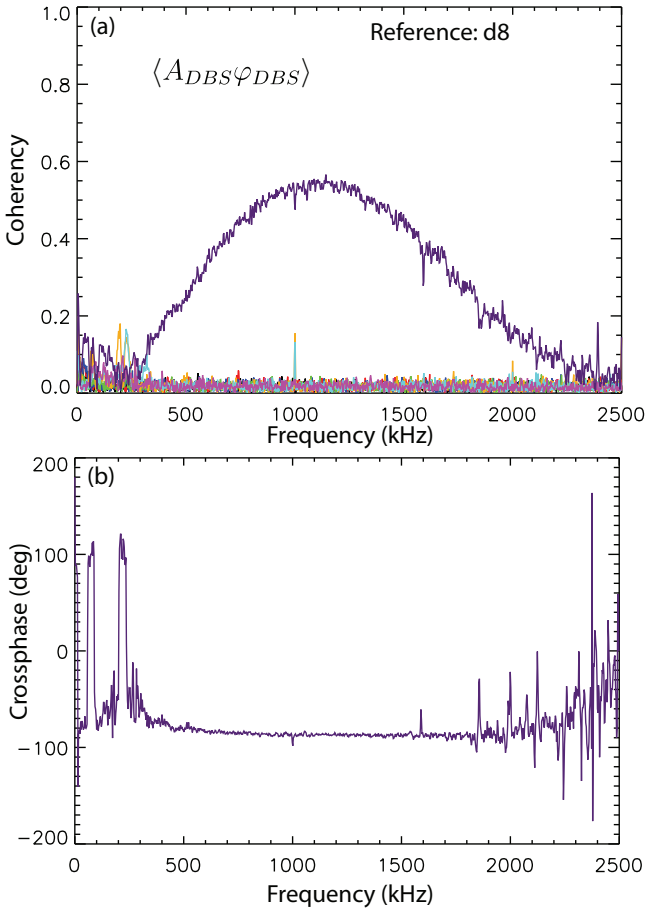

Figure F.6: (a) Coherency between A_{DBS} from d8 and φ_{DBS} from all eight DBS-8 channels. (b) Crossphase for d8 only. Shot 144579 3800-4400 ms.

The frequency range is suggestive of ETG-scale fluctuations. Figure F.8 shows the amplitude-phase correlation for three shots from the a/L_{T_e} experiment. TGLF calculations in Sec. 5.4.1.5 did show that growth rates would be expected to increase at all wave numbers, up to a few dozen $k_\theta \rho_s$. The measurement location for `d6` was about $\rho = 0.5$, so the beam travels through the region of the plasma where $L_{T_e}^{-1}$ was scanned; the coherency at ~ 1 MHz monotonically increases with the $L_{T_e}^{-1}$ scan. A consistent explanation would be that the megahertz range component of the DBS signal is occurring due to backscattering, where, somewhere along the path, the mismatch is minimized (as discussed in Sec. 3.5.3.3

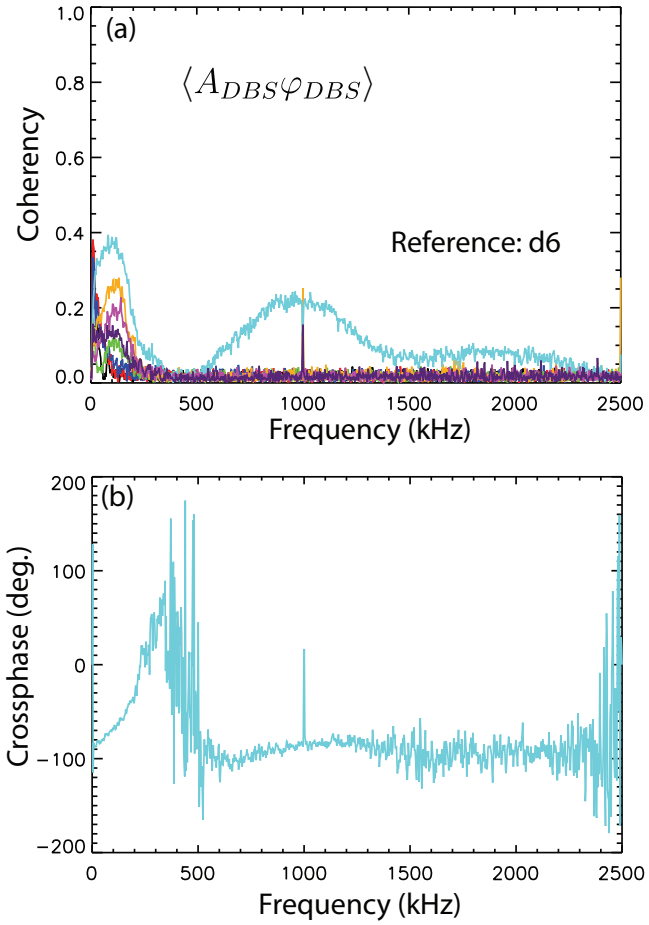

Figure F.7: (a) Coherency between A_{DBS} from d6 and φ_{DBS} from all eight DBS-8 channels. (b) Crossphase for d6 only. Shot 144579 3800-4400 ms.

and references therein). The different frequencies for the DBS-8 channels then leads to the mismatch being minimized for different wave numbers and/or in different locations, resulting in no correlation between channels.

If the origin of the megahertz range signal in the DBS data can be thoroughly understood, it could substantially increase the versatility of the diagnostic. Application of similar analysis to the better understood backscattering system at DIII-D [208], where the 2^{nd} ECE harmonic is used as a beam dump, might be able to shed light on these results, if that data is similar. Resonant Bragg backscattering for reflectometry has been investigated [272], where scattering resonant with radially coherent fluctuations was investigated. A similar process could be occurring here.

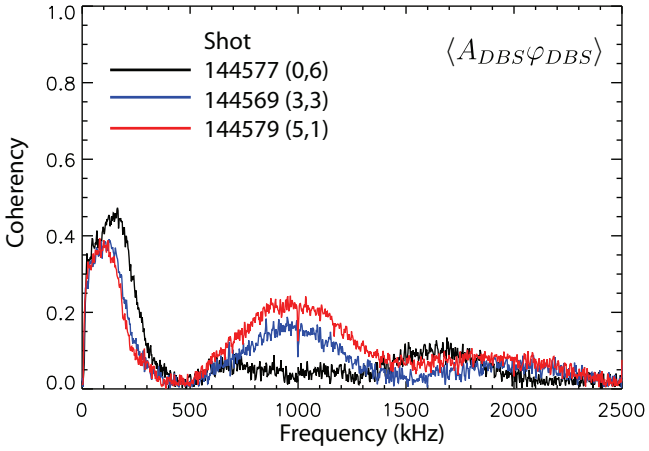

Figure F.8: Coherency between A_{DBS} and φ_{DBS} for three shots.

F.4 The DBS amplitude spectrum

The DBS amplitude spectrum was briefly discussed in Sec. 5.3.3.4. Another set of data comparing the DBS quadrature spectrum and the DBS amplitude spectrum is shown in Fig. F.9. This data is from `d6`, which has a better signal to noise level than the `d5` data in Sec. 5.3.3.4. The spatial location is $\rho \approx 0.5$. Two features of the data are evident. One is that there is clearly a direct correlation of the increase in the Doppler shifted peak in

Fig. 5.3.3.4(a) and the peak at $\sim 50-70$ kHz in Fig. 5.3.3.4(b). The second is that there is no change in the frequency of the rising peak in Fig. 5.3.3.4(b), while there is a significant change to the Doppler shifted peak in Fig. 5.3.3.4(a). This is consistent with the DBS amplitude spectra reflecting the plasma frame changes to the turbulence.

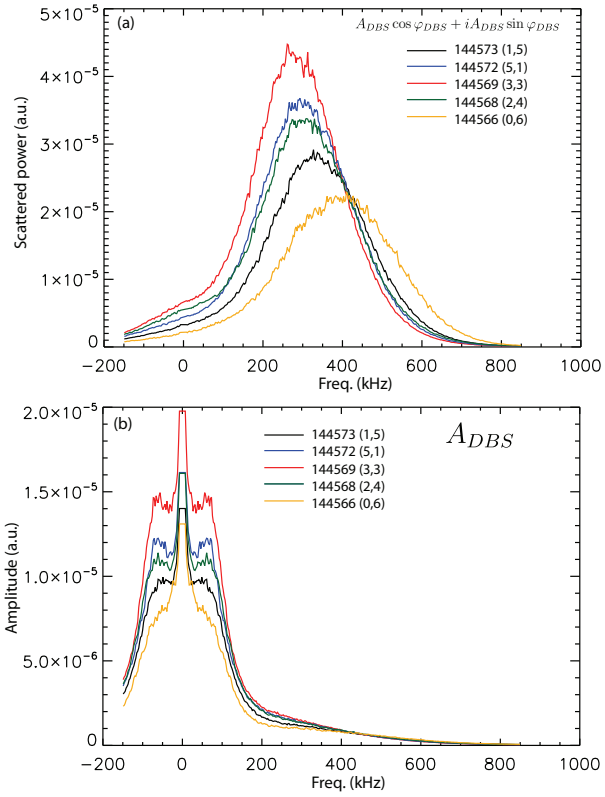

Figure F.9: (a) Quadrature spectrum and (b) DBS amplitude spectrum for ECH+Bal-NBI plasmas for DBS-8 channel d6.

F.5 The $\partial\varphi_{DBS}/\partial t$ spectrum

Figure F.10 shows the $\partial\varphi_{DBS}/\partial t$ spectrum for the same data in Fig. F.9. The φ_{DBS} spectrum itself is dominated by the contribution of the equilibrium flow. There is a clear increase in the spectra as the Doppler shift in Fig. F.9(a) increases, consistent with the equilibrium flow impacting the spectrum. The opposite trend is observed at low frequencies, compared to the DBS amplitude in Fig. F.9(b), with a large increase in the (0,6) case. Further analysis

is required to clearly separate broadband contributions to the $\partial\varphi_{DBS}/\partial t$ spectrum.

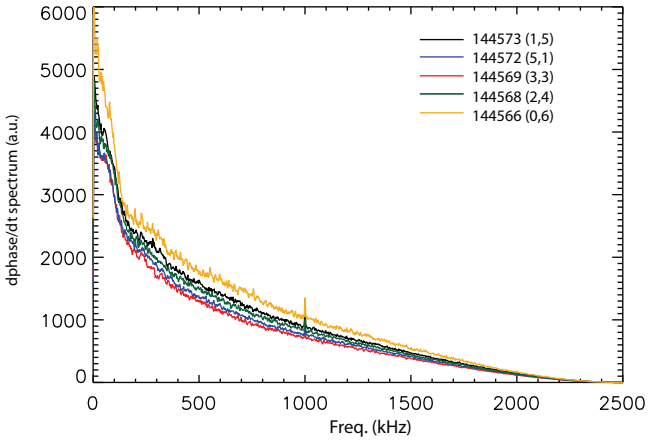

Figure F.10: DBS phase derivative spectrum for ECH+Bal-NBI plasmas for DBS-8 channel d6.

APPENDIX G

Survey of additional DBS observations

Over the years during which the work and results presented in the primary chapters of the dissertation were acquired, a number of additional experimental observations were made with the DIII-D DBS systems. An observational survey of these additional results are presented in this Appendix without the depth of analysis presented for results in the primary chapters.

G.1 Alfvén eigenmodes

Fast ion and energetic particle modes are often driven unstable by neutral beam heating during the current ramp in DIII-D [273]. Most of these modes are one of some variety of Alfvén eigenmode. Plotted in G.1 is a spectrogram of the DBS phase derivative from a shot early beam heating. A GAM is weakly visible at low frequencies, $\sim$ 15 kHz. Two types of modes are visible between $\sim$ 70 kHz and $\sim$ 150 kHz. The modes which chirp upwards in frequency are reverse shear Alfvén eigenmodes, or RSAEs. The modes in that frequency range that remain at a constant frequency in time are toroidicity-induced Alfvèn eigenmodes (TAEs), which are essentially standing waves created by counter-propagating shear Alfvén waves with $\Delta m = \pm 1$. The modes which occur at about twice the frequency of the RSAEs and TAEs are prospectively identified as ellipticity-induced Alfvèn eigenmodes (EAEs). Similar to TAEs, those would be standing wave created by counter-propagating shear Alfvén waves with $\Delta m = \pm 2$.

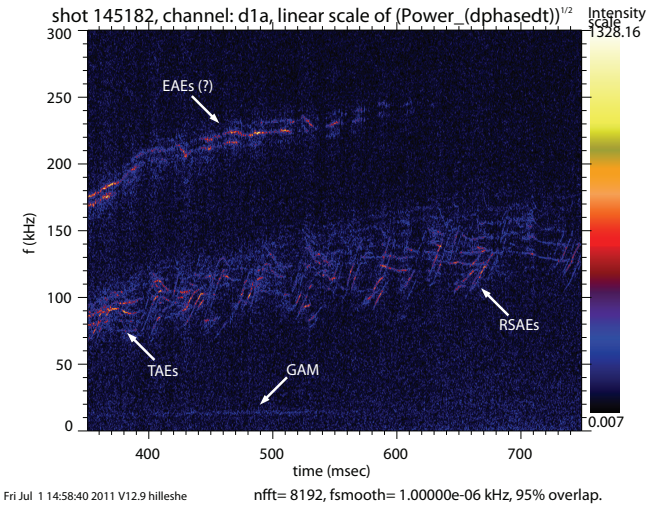

Figure G.1: Spectrogram of DBS phase derivative showing sea of Alfvén eigenmodes and a GAM.

G.2 Coherent modes in the H-mode pedestal

Coherent modes have been observed in the H-mode pedestal in DIII-D with Beam Emission Spectroscopy [274], which are thought to be kinetic ballooning modes (KBMs). These modes are also observed with Doppler Backscattering. Figure G.2 shows DBS phase derivative measurements during the dynamics of an ELMing H-mode pedestal. Edge localized modes (ELMs) are a violent instability that periodically relaxes the pedestal in standard H-modes. Figure G.2(a) shows a spectrogram of the DBS phase derivative through several ELM cycles. Figure G.2(b) shows the spectral amplitude integrated over the coherent modes visible around $\sim 50 - 80$ kHz. Figure G.2(c) shows a trace of D_α light; the spikes indicate ELMs. The high frequency mode, ~ 85 kHz appeared to be related to a neoclassical tearing mode. Each inter-ELM period appears to start with a stable period, then a period of time occurs where the prospective KBMs rapidly grow, and then saturate. After a period of saturation or slower growth, the ELM is triggered and the prospective KBMs disappear. These observations are generally consistent with the EPED pedestal model [106], which describes two constraints governing pedestal stability: KBMs limiting the pedestal gradient between ELMs and a total pedestal energy constraint for the ELMs.

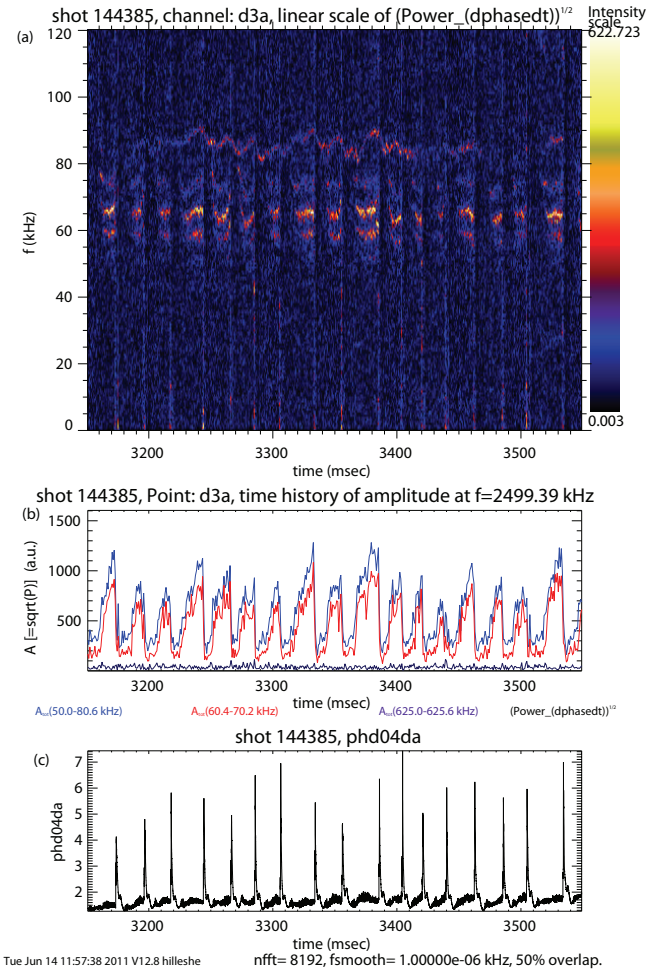

Figure G.2: (a) Spectrogram of DBS phase derivative showing coherent instabilities in the pedestal of an H-mode plasma. (b) Integrated spectral amplitude. (c) D_α light.

Different dynamics than those depicted in Fig. G.2 can occur. Figure G.3 shows two more examples of measurements in H-mode pedestal conditions. Figure G.3(a) shows DBS data during an ELM-free phase following an H-mode transition. There appears to be a broad spectrum $\sim 150 - 300$ kHz, with remnant coherent peaks. Figure G.3(b) shows another example of an ELMing H-mode; the ELMs are indicated by the broadband bursts. During the inter-ELM periods there are both a low frequency mode, ~ 20 kHz, and a sequence of higher frequency modes, $\sim 100 - 250$ kHz.

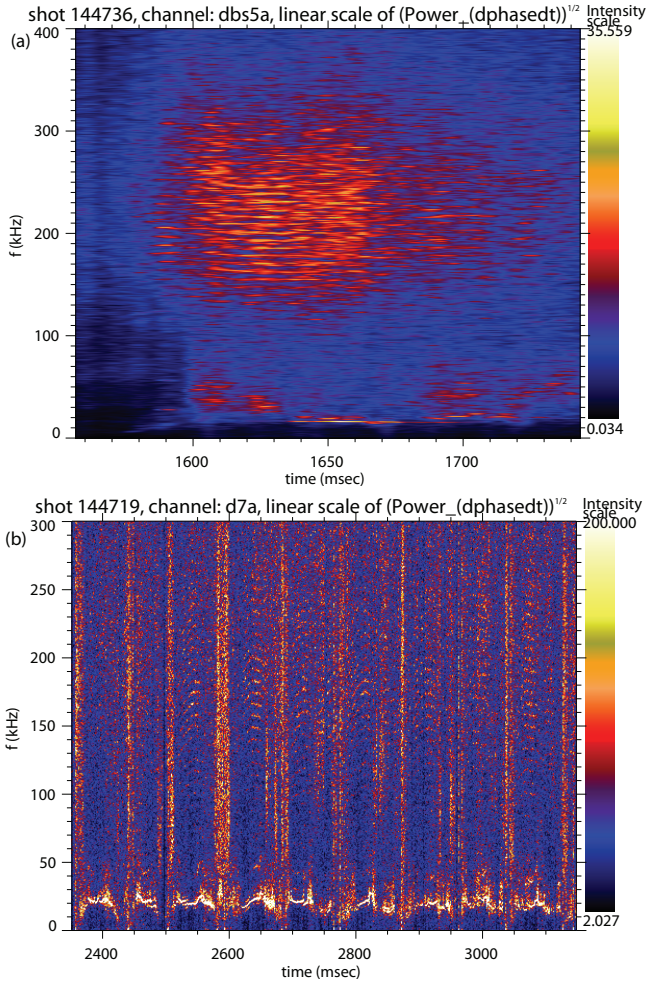

Figure G.3: (a-b) Spectrogram of DBS phase derivative showing coherent instabilities in the pedestal of a H-mode plasmas.

G.3 Low frequency flows in L-mode plasmas with an internal transport barrier

Figure G.4 shows the temperature profiles, averaged over 400 ms centered at 1745 ms and 2745 ms from shot 145174. The dashed line is from the earlier time, the data and solid line are from the later time. The earlier time was an L-mode plasma with ECH and NBI heating. At about 2000 ms, the ECH is removed and more NBI was added for a total of about 7 MW of NBI. Later shots in the run day changed the inner gap and went into H-mode with the same amount of beam heating as the later time. Particularly for the ion temperature, it appears that an internal transport barrier (ITB) forms.

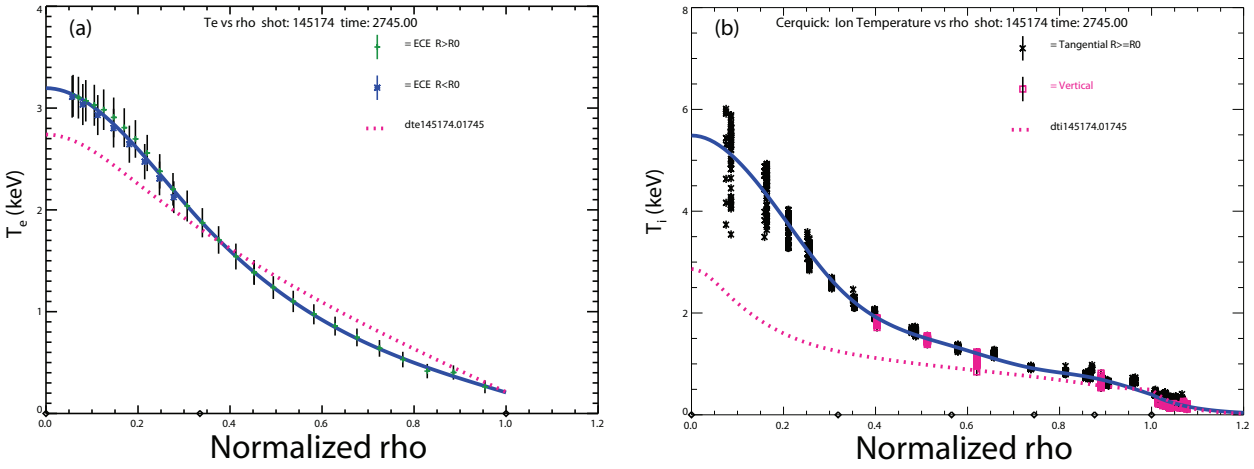

Figure G.4: (a) Electron and (b) ion temperature profiles before and after development of an internal transport barrier.

Figure G.5 shows contours plots of the low frequency flows during the earlier time, a more standard L-mode plasma, and the later time, with the ITB. There is a stark difference, with much stronger low frequency flows during the ITB time. Note that the ITB forms in the core of the plasma, at smaller radii than the DBS measurements are from. The point is not necessarily that the flows have to do with the ITB formation. Instead, Fig. G.5(b) is notable since both the GAM and the ~ 1 kHz flows are observed to co-exist at the same radii. For most cases, it is only one or the other (see Sec. 4.6). Locally, the increased amplitude of the

flows must correlate with higher heat flux, due to the added NBI heat input to the core. One *caveat* for the plots is that Zipfit density profiles were used–more careful analysis might yield somewhat different positions for the DBS channels, but this would not affect the qualitative observation of the co-exist of both the GAM and LFZF.

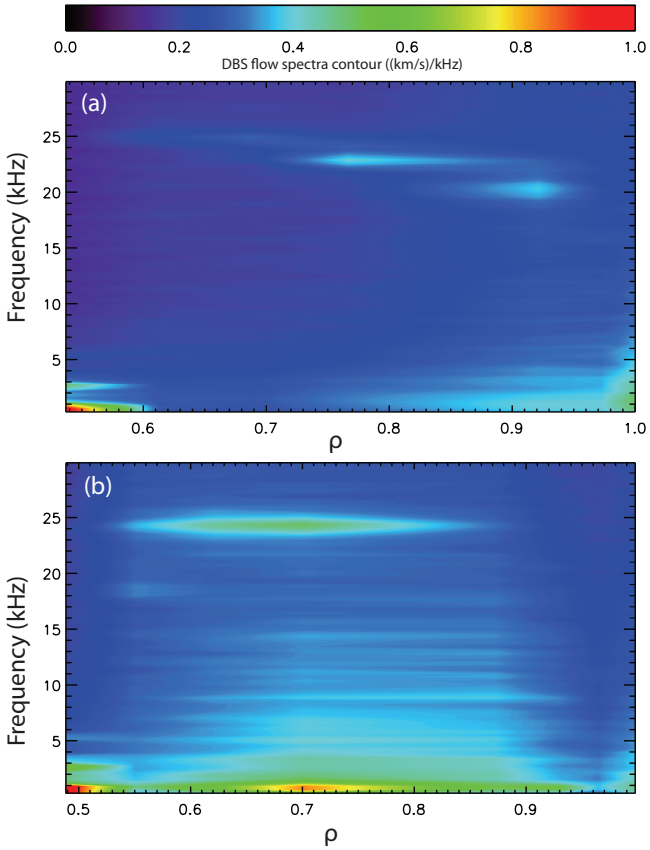

Figure G.5: Low frequency flows from DBS-8 from shot 145174 averaged over (a) 1500-2000 ms and (b) 2500-3000 ms.

G.4 On the transition from L-mode to limit cycle oscillations

A study of slow L-H transitions, where an intermediate limit cycle phase occurred, was reported on in Ref. [21]. During the limit cycle oscillation (LCO) phase, the GAM disappears and there is only the low frequency flow. One point not immediately apparent in Ref. [21] is that the limit cycle oscillation can extend quite deep into the core of the plasma. Figure G.6

shows flow contour plots from an L-mode phase and from a limit cycle oscillation phase of shot 147724. The mode at $\sim$ 2 kHz is the same oscillation studied in-depth in Ref. [21], which focused on the region within a few cm of the last closed flux surface. The contours in Fig. G.6 above 1.0 (km/s)/kHz are truncated to keep the same scale.

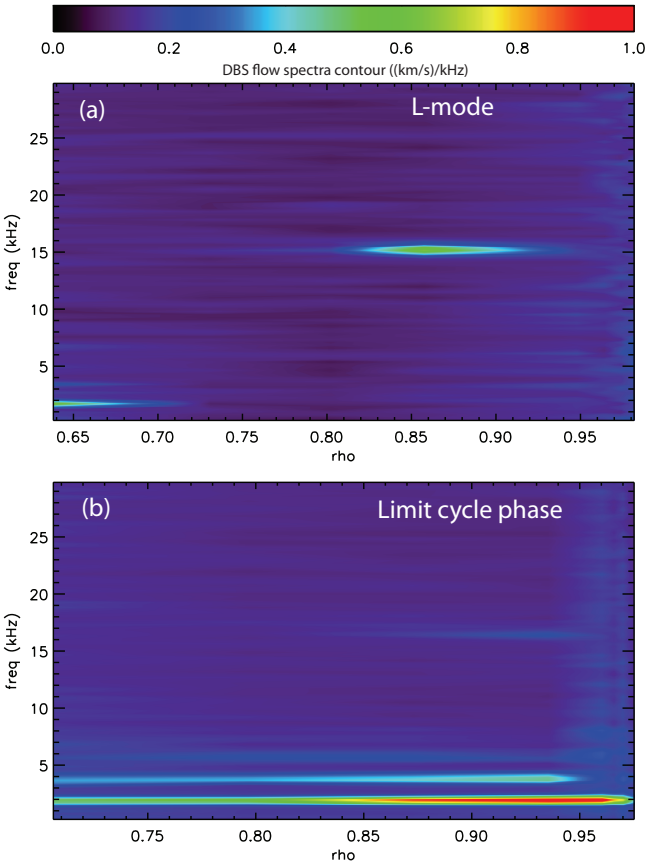

Figure G.6: Low frequency flows from DBS-8 from shot 147724 averaged over (a) 1300-1500 ms and (b) 1550-1750 ms.

Figure G.7 shows the coherency between `d1` and the seven other DBS-8 channels, for the same data in Fig. G.6. The LCO itself, at $\sim$ 2 kHz, correlates with coherency greater than 0.75 between `d1` and `d8`. The broadband contribution decreases as the channel separation increases. Figure G.7 demonstrates that the LCO is not a phenomena localized to near the last closed flux surface, but is instead a coherency plasma oscillation over more than 1/4 the minor radius of the plasma.

A similar *caveat* exists for this data as for the previous section; the density profiles for the ray tracing used Zipfits and can be improved with more careful analysis. Figure G.6(b) also provides an interesting counterpoint to Fig. G.5(b), where both the GAM and a LFZF co-exist. It is important to note that the plasma in Fig. G.5(b) does not exhibit the D_α signature that characterizes the LCO. The LCO oscillation also appears to be much more coherent spectrally, with no broadband component, as seen in Fig. G.5(b).

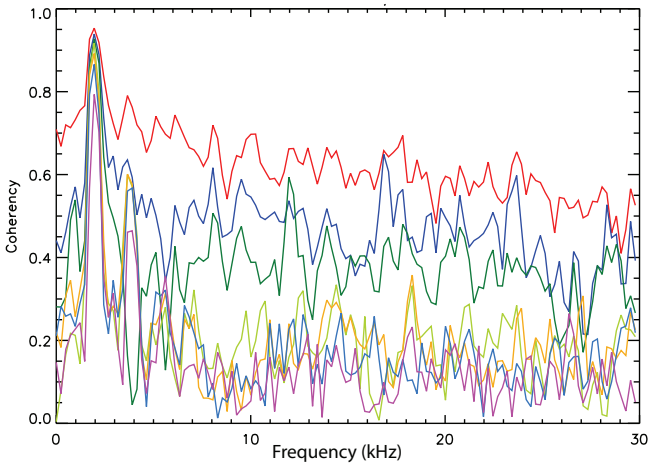

Figure G.7: Coherency of DBS phase derivative between d1 and the seven other DBS-8 channels during the limit cycle oscillation phase.

Bibliography

[1] J. Wesson, *Tokamaks*, 3rd ed. (Oxford University Press, USA, 2004).

[2] L. Schmitz, G. Wang, J. C. Hillesheim, T. L. Rhodes, W. A. Peebles, A. E. White, L. Zeng, T. A. Carter, and W. Solomon, Review of Scientific Instruments **79**, 10F113 (2008).

[3] A. E. White, L. Schmitz, W. A. Peebles, T. A. Carter, T. L. Rhodes, E. J. Doyle, P. A. Gourdain, J. C. Hillesheim, G. Wang, C. Holland, G. R. Tynan, M. E. Austin, G. R. McKee, M. W. Shafer, K. H. Burrell, J. Candy, J. C. DeBoo, R. Prater, G. M. Staebler, R. E. Waltz, and M. A. Makowski, Review of Scientific Instruments **79**, 103505 (2008).

[4] L. Schmitz, A. White, G. Wang, J. DeBoo, J. deGrassie, G. McKee, J. Hillesheim, W. Peebles, T. Rhodes, T. Carter, E. Doyle, L. Zeng, K. Burrell, C. Petty, J. Kinsey, W. Solomon, G. Staebler, and the DIII-D Team, Nuclear Fusion **49**, 095004 (2009).

[5] L. Schmitz, C. Holland, T. Rhodes, G. Wang, L. Zeng, A. White, J. Hillesheim, W. Peebles, S. Smith, R. Prater, G. McKee, Z. Yan, W. Solomon, K. Burrell, C. Holcomb, E. Doyle, J. DeBoo, M. Austin, J. deGrassie, and C. Petty, Nuclear Fusion **52**, 023003 (2012).

[6] J. C. Hillesheim, W. A. Peebles, T. L. Rhodes, L. Schmitz, T. A. Carter, P.-A. Gourdain, and G. Wang, Review of Scientific Instruments **80**, 083507 (2009).

[7] W. A. Peebles, T. L. Rhodes, J. C. Hillesheim, L. Zeng, and C. Wannberg, Review of Scientific Instruments **81**, 10D902 (2010).

[8] T. L. Rhodes, W. A. Peebles, X. Nguyen, J. C. Hillesheim, L. Schmitz, A. E. White, and G. Wang, Review of Scientific Instruments **81**, 10D912 (2010).

[9] J. C. DeBoo, C. Holland, T. L. Rhodes, L. Schmitz, G. Wang, A. E. White, M. E. Austin, E. J. Doyle, J. Hillesheim, W. A. Peebles, C. C. Petty, Z. Yan, and L. Zeng, Physics of Plasmas **17**, 056105 (2010).

[10] C. Holland, J. DeBoo, T. Rhodes, L. Schmitz, J. Hillesheim, G. Wang, A. White, M. Austin, E. Doyle, W. Peebles, C. Petty, L. Zeng, and J. Candy, Nuclear Fusion **52**, 063028 (2012).

[11] J. C. Hillesheim, C. Holland, L. Schmitz, S. Kubota, T. L. Rhodes, and T. A. Carter, Review of Scientific Instruments **83**, 10E331 (2012).

[12] J. C. DeBoo, C. C. Petty, A. E. White, K. H. Burrell, E. J. Doyle, J. C. Hillesheim, C. Holland, G. R. McKee, T. L. Rhodes, L. Schmitz, S. P. Smith, G. Wang, and L. Zeng, "Electron profile stiffness and critical gradient studies," (2012), submitted to Phys. Plasmas.

[13] J. C. Hillesheim, J. C. DeBoo, W. A. Peebles, T. A. Carter, G. Wang, T. L. Rhodes, L. Schmitz, K. H. Burrell, E. J. Doyle, C. Holland, G. R. McKee, Z. Yan, G. M. Staebler, C. C. Petty, S. P. Smith, A. E. White, and L. Zeng, "Observation of a critical gradient threshold for electron temperature flucutations in the DIII-D tokamak," (2012), submitted to Phys. Rev. Lett.

[14] J. C. Hillesheim, J. C. DeBoo, W. A. Peebles, T. A. Carter, G. Wang, T. L. Rhodes, L. Schmitz, K. H. Burrell, E. J. Doyle, C. Holland, G. R. McKee, Z. Yan, G. M. Staebler, C. C. Petty, S. P. Smith, A. E. White, and L. Zeng, in *Proceedings of 39th European Physics Society Conference on Plasma Physics/16th International Congress on Plasma Physics*, P5.045 (2012).

[15] J. C. Hillesheim, W. A. Peebles, T. L. Rhodes, L. Schmitz, A. E. White, and T. A. Carter, Review of Scientific Instruments **81**, 10D907 (2010).

[16] A. E. White, W. A. Peebles, T. L. Rhodes, C. H. Holland, G. Wang, L. Schmitz, T. A. Carter, J. C. Hillesheim, E. J. Doyle, L. Zeng, G. R. McKee, G. M. Staebler, R. E.

Waltz, J. C. DeBoo, C. C. Petty, and K. H. Burrell, Physics of Plasmas **17**, 056103 (2010).

[17] G. Wang, W. A. Peebles, T. L. Rhodes, J. C. DeBoo, G. M. Staebler, J. C. Hillesheim, Z. Yan, G. R. McKee, C. C. Petty, W. M. Solomon, K. H. Burrell, E. J. Doyle, A. W. Leonard, L. Schmitz, M. A. VanZeeland, A. E. White, and L. Zeng, Physics of Plasmas **18**, 082504 (2011).

[18] C. Holland, L. Schmitz, T. L. Rhodes, W. A. Peebles, J. C. Hillesheim, G. Wang, L. Zeng, E. J. Doyle, S. P. Smith, R. Prater, K. H. Burrell, J. Candy, R. E. Waltz, J. E. Kinsey, G. M. Staebler, J. C. DeBoo, C. C. Petty, G. R. McKee, Z. Yan, and A. E. White, Physics of Plasmas **18**, 056113 (2011).

[19] T. Rhodes, C. Holland, S. Smith, A. White, K. Burrell, J. Candy, J. DeBoo, E. Doyle, J. Hillesheim, J. Kinsey, G. McKee, D. Mikkelsen, W. Peebles, C. Petty, R. Prater, S. Parker, Y. Chen, L. Schmitz, G. Staebler, R. Waltz, G. Wang, Z. Yan, and L. Zeng, Nuclear Fusion **51**, 063022 (2011).

[20] J. C. Hillesheim, W. A. Peebles, T. A. Carter, L. Schmitz, and T. L. Rhodes, Physics of Plasmas **19**, 022301 (2012).

[21] L. Schmitz, L. Zeng, T. L. Rhodes, J. C. Hillesheim, E. J. Doyle, R. J. Groebner, W. A. Peebles, K. H. Burrell, and G. Wang, Physical Review Letters **108**, 155002 (2012).

[22] S. Hirshman and D. Sigmar, Nuclear Fusion **21**, 1079 (1981).

[23] P. C. Liewer, Nuclear Fusion **25**, 543 (1985).

[24] A. J. Wootton, B. A. Carreras, H. Matsumoto, K. McGuire, W. A. Peebles, C. P. Ritz, P. W. Terry, and S. J. Zweben, Physics of Fluids B: Plasma Physics **2**, 2879 (1990).

[25] W. Horton, Reviews of Modern Physics **71**, 735 (1999).

[26] E. J. Doyle, W. A. Houlberg, Y. Kamada, V. Mukhovatov, T. H. Osbourne, A. Polevoi, G. Batemen, J. W. Connor, J. G. Cordey, T. Fujita, X. Garbet, T. S. Hahm, L. D. Horton, A. E. Hubbard, F. Imbeaux, F. Jenko, J. E. Kinsey, Y. Kishimoto, J. Li, T. C. Luce, Y. Martin, M. Ossipenko, V. Parail, A. Peeters, T. L. Rhodes, J. E. Rice, C. M. Roach, V. Rozhansky, F. Ryter, G. Saibene, R. Sartori, A. C. C. Sips, J. A. Snipes, M. Sugihara, E. J. Synakowski, H. Takenaga, T. Takizuka, K. Thomsen, M. R. Wade, H. R. Wilson, ITPA Transport Physics Topical Group, ITPA Confinement Database and Modelling Topical Group, and ITPA Pedestal and Edge Topical Group, Nuclear Fusion **47**, S18 (2007).

[27] G. R. Tynan, A. Fujisawa, and G. McKee, Plasma Physics and Controlled Fusion **51**, 113001 (2009).

[28] E. Mazzucato, Physical Review Letters **36**, 792 (1976).

[29] C. M. Surko and R. E. Slusher, Physical Review Letters **37**, 1747 (1976).

[30] E. Mazzucato, Physics of Fluids **21**, 1063 (1978).

[31] C. M. Surko and R. E. Slusher, Physics of Fluids **23**, 2425 (1980).

[32] E. Mazzucato, Physical Review Letters **48**, 1828 (1982).

[33] D. L. Brower, W. A. Peebles, N. C. Luhmann, and R. L. Savage, Physical Review Letters **54**, 689 (1985).

[34] D. Brower, W. Peebles, and N. Luhmann, Nuclear Fusion **27**, 2055 (1987).

[35] T. Crowley and E. Mazzucato, Nuclear Fusion **25**, 507 (1985).

[36] C. Yu, D. Brower, S. Zhao, R. Bravenec, J. Chen, H. Lin, J. N. Luhmann, W. Peebles, C. Ritz, P. Schoch, and X. Yang, Nuclear Fusion **32**, 1545 (1992).

[37] R. J. Fonck, G. Cosby, R. D. Durst, S. F. Paul, N. Bretz, S. Scott, E. Synakowski, and G. Taylor, Physical Review Letters **70**, 3736 (1993).

[38] S. F. Paul, N. Bretz, R. D. Durst, R. J. Fonck, Y. J. Kim, E. Mazzucato, and R. Nazikian, Physics of Fluids B: Plasma Physics **4**, 2922 (1992).

[39] E. Mazzucato and R. Nazikian, Physical Review Letters **71**, 1840 (1993).

[40] G. A. Hallock, J. Mathew, W. C. Jennings, R. L. Hickok, A. J. Wootton, and R. C. Isler, Physical Review Letters **56**, 1248 (1986).

[41] G. A. Hallock, A. J. Wootton, and R. L. Hickok, Physical Review Letters **59**, 1301 (1987).

[42] S. Sattler and H. J. Hartfuss, Physical Review Letters **72**, 653 (1994).

[43] H. Evensen, R. Fonck, S. Paul, G. Rewoldt, S. Scott, W. Tang, and M. Zarnstorff, Nuclear Fusion **38**, 237 (1998).

[44] F. Wagner, G. Becker, K. Behringer, D. Campbell, A. Eberhagen, W. Engelhardt, G. Fussmann, O. Gehre, J. Gernhardt, G. v. Gierke, G. Haas, M. Huang, F. Karger, M. Keilhacker, O. Klüber, M. Kornherr, K. Lackner, G. Lisitano, G. G. Lister, H. M. Mayer, D. Meisel, E. R. Müller, H. Murmann, H. Niedermeyer, W. Poschenrieder, H. Rapp, H. Röhr, F. Schneider, G. Siller, E. Speth, A. Stbler, K. H. Steuer, G. Venus, O. Vollmer, and Z. Yü, Physical Review Letters **49**, 1408 (1982).

[45] F. Wagner, G. Fussmann, T. Grave, M. Keilhacker, M. Kornherr, K. Lackner, K. McCormick, E. R. Müller, A. Stbler, G. Becker, K. Bernhardi, U. Ditte, A. Eberhagen, O. Gehre, J. Gernhardt, G. v. Gierke, E. Glock, O. Gruber, G. Haas, M. Hesse, G. Janeschitz, F. Karger, S. Kissel, O. Klüber, G. Lisitano, H. M. Mayer, D. Meisel, V. Mertens, H. Murmann, W. Poschenrieder, H. Rapp, H. Röhr, F. Ryter, F. Schneider, G. Siller, P. Smeulders, F. Söldner, E. Speth, K. H. Steuer, Z. Szymanski, and O. Vollmer, Physical Review Letters **53**, 1453 (1984).

[46] R. J. Taylor, M. L. Brown, B. D. Fried, H. Grote, J. R. Liberati, G. J. Morales, P. Pribyl, D. Darrow, and M. Ono, Physical Review Letters **63**, 2365 (1989).

[47] E. J. Doyle, R. J. Groebner, K. H. Burrell, P. Gohil, T. Lehecka, N. C. Luhmann, H. Matsumoto, T. H. Osborne, W. A. Peebles, and R. Philipona, Physics of Fluids B: Plasma Physics **3**, 2300 (1991).

[48] T. M. Antonsen and B. Lane, Physics of Fluids **23**, 1205 (1980).

[49] E. A. Frieman and L. Chen, Physics of Fluids **25**, 502 (1982).

[50] G. G. Howes, S. C. Cowley, W. Dorland, G. W. Hammett, E. Quataert, and A. A. Schekochihin, The Astrophysical Journal **651**, 590 (2006).

[51] A. J. Brizard and T. S. Hahm, Reviews of Modern Physics **79**, 421 (2007).

[52] M. A. Barnes, *Trinity: A Unified Treatment of Turbulence, Transport, and Heating in Magnetized Plasmas*, Ph.D. thesis, University of Maryland, College Park (2009).

[53] J. Candy and R. Waltz, Journal of Computational Physics **186**, 545 (2003).

[54] M. Kotschenreuther, G. Rewoldt, and W. Tang, Computer Physics Communications **88**, 128 (1995).

[55] W. Dorland, F. Jenko, M. Kotschenreuther, and B. N. Rogers, Physical Review Letters **85**, 5579 (2000).

[56] G. W. Hammett and F. W. Perkins, Physical Review Letters **64**, 3019 (1990).

[57] G. M. Staebler, J. E. Kinsey, and R. E. Waltz, Physics of Plasmas **12**, 102508 (2005).

[58] G. M. Staebler, J. E. Kinsey, and R. E. Waltz, Physics of Plasmas **14**, 055909 (2007).

[59] G. M. Staebler and J. E. Kinsey, Physics of Plasmas **17**, 122309 (2010).

[60] H. Biglari, P. H. Diamond, and P. W. Terry, Physics of Fluids B: Plasma Physics **2**, 1 (1990).

[61] D. R. Hatch, P. W. Terry, W. M. Nevins, and W. Dorland, Physics of Plasmas **16**, 022311 (2009).

[62] P. W. Terry, A. F. Almagri, G. Fiksel, C. B. Forest, D. R. Hatch, F. Jenko, M. D. Nornberg, S. C. Prager, K. Rahbarnia, Y. Ren, and J. S. Sarff, Physics of Plasmas **19**, 055906 (2012).

[63] P. H. Diamond, S.-I. Itoh, K. Itoh, and T. S. Hahm, Plasma Physics and Controlled Fusion **47**, R35 (2005).

[64] T. L. Rhodes, J.-N. Leboeuf, R. D. Sydora, R. J. Groebner, E. J. Doyle, G. R. McKee, W. A. Peebles, C. L. Rettig, L. Zeng, and G. Wang, Physics of Plasmas **9**, 2141 (2002).

[65] M. N. Rosenbluth and F. L. Hinton, Physical Review Letters **80**, 724 (1998).

[66] A. Fujisawa, K. Itoh, H. Iguchi, K. Matsuoka, S. Okamura, A. Shimizu, T. Minami, Y. Yoshimura, K. Nagaoka, C. Takahashi, M. Kojima, H. Nakano, S. Ohsima, S. Nishimura, M. Isobe, C. Suzuki, T. Akiyama, K. Ida, K. Toi, S.-I. Itoh, and P. H. Diamond, Physical Review Letters **93**, 165002 (2004).

[67] K. H. Burrell, Physics of Plasmas **4**, 1499 (1997).

[68] P. W. Terry, D. E. Newman, and A. S. Ware, Physical Review Letters **87**, 185001 (2001).

[69] P. J. Catto, M. N. Rosenbluth, and C. S. Liu, Physics of Fluids **16**, 1719 (1973).

[70] S. L. Newton, S. C. Cowley, and N. F. Loureiro, Plasma Physics and Controlled Fusion **52**, 125001 (2010).

[71] E. G. Highcock, M. Barnes, A. A. Schekochihin, F. I. Parra, C. M. Roach, and S. C. Cowley, Physical Review Letters **105**, 215003 (2010).

[72] E. G. Highcock, M. Barnes, F. I. Parra, A. A. Schekochihin, C. M. Roach, and S. C. Cowley, Physics of Plasmas **18**, 102304 (2011).

[73] M. Barnes, F. I. Parra, E. G. Highcock, A. A. Schekochihin, S. C. Cowley, and C. M. Roach, Physical Review Letters **106**, 175004 (2011).

[74] A. A. Schekochihin, E. G. Highcock, and S. C. Cowley, Plasma Physics and Controlled Fusion **54**, 055011 (2012).

[75] *The Plasma Dispersion Function* (Academic Press).

[76] R. Numata, G. G. Howes, T. Tatsuno, M. Barnes, and W. Dorland, 1004.0279 (2010).

[77] B. Coppi and N. Sharky, Nuclear Fusion **21**, 1363 (1981).

[78] X. Garbet, P. Mantica, F. Ryter, G. Cordey, F. Imbeaux, C. Sozzi, A. Manini, E. Asp, V. Parail, R. Wolf, and t. J. E. Contributors, Plasma Physics and Controlled Fusion **46**, 1351 (2004).

[79] B. Coppi, M. N. Rosenbluth, and R. Z. Sagdeev, Physics of Fluids **10**, 582 (1967).

[80] R. Linsker, Physics of Fluids **24**, 1485 (1981).

[81] H. Nordman and J. Weiland, Nuclear Fusion **29**, 251 (1989).

[82] F. Romanelli, Physics of Fluids B: Plasma Physics **1**, 1018 (1989).

[83] S. C. Cowley, R. M. Kulsrud, and R. Sudan, Physics of Fluids B: Plasma Physics **3**, 2767 (1991).

[84] A. M. Dimits, G. Bateman, M. A. Beer, B. I. Cohen, W. Dorland, G. W. Hammett, C. Kim, J. E. Kinsey, M. Kotschenreuther, A. H. Kritz, L. L. Lao, J. Mandrekas, W. M. Nevins, S. E. Parker, A. J. Redd, D. E. Shumaker, R. Sydora, and J. Weiland, Physics of Plasmas **7**, 969 (2000).

[85] R. J. Goldston, Plasma Physics and Controlled Fusion **26**, 87 (1984).

[86] C. L. Rettig, T. L. Rhodes, J. N. Leboeuf, W. A. Peebles, E. J. Doyle, G. M. Staebler, K. H. Burrell, and R. A. Moyer, Physics of Plasmas **8**, 2232 (2001).

[87] J. Rice, B. Duval, M. Reinke, Y. Podpaly, A. Bortolon, R. Churchill, I. Cziegler, P. Diamond, A. Dominguez, P. Ennever, C. Fiore, R. Granetz, M. Greenwald, A. Hubbard,

J. Hughes, J. Irby, Y. Ma, E. Marmar, R. McDermott, M. Porkolab, N. Tsujii, and S. Wolfe, Nuclear Fusion **51**, 083005 (2011).

[88] L. Schmitz, A. E. White, T. A. Carter, W. A. Peebles, T. L. Rhodes, K. H. Burrell, W. Solomon, and G. M. Staebler, Physical Review Letters **100**, 035002 (2008).

[89] A. E. White, L. Schmitz, W. A. Peebles, T. L. Rhodes, T. A. Carter, G. R. McKee, M. W. Shafer, G. M. Staebler, K. H. Burrell, J. C. DeBoo, and R. Prater, Physics of Plasmas **17**, 020701 (2010).

[90] B. Kadomtsev and O. Pogutse, Nuclear Fusion **11**, 67 (1971).

[91] D. R. Ernst, P. T. Bonoli, P. J. Catto, W. Dorland, C. L. Fiore, R. S. Granetz, M. Greenwald, A. E. Hubbard, M. Porkolab, M. H. Redi, J. E. Rice, K. Zhurovich, and Alcator C-Mod Group, Physics of Plasmas **11**, 2637 (2004).

[92] D. R. Ernst, J. Lang, W. M. Nevins, M. Hoffman, Y. Chen, W. Dorland, and S. Parker, Physics of Plasmas **16**, 055906 (2009).

[93] T. Dannert and F. Jenko, Physics of Plasmas **12**, 072309 (2005).

[94] F. Ryter, C. Angioni, A. G. Peeters, F. Leuterer, H. Fahrbach, and W. Suttrop, Physical Review Letters **95**, 085001 (2005).

[95] F. Jenko, W. Dorland, and G. W. Hammett, Physics of Plasmas **8**, 4096 (2001).

[96] E. Mazzucato, D. R. Smith, R. E. Bell, S. M. Kaye, J. C. Hosea, B. P. LeBlanc, J. R. Wilson, P. M. Ryan, C. W. Domier, N. C. Luhmann, H. Yuh, W. Lee, and H. Park, Physical Review Letters **101**, 075001 (2008).

[97] D. R. Smith, S. M. Kaye, W. Lee, E. Mazzucato, H. K. Park, R. E. Bell, C. W. Domier, B. P. LeBlanc, F. M. Levinton, N. C. Luhmann, J. E. Menard, and H. Yuh, Physical Review Letters **102**, 225005 (2009).

[98] H. Y. Yuh, S. M. Kaye, F. M. Levinton, E. Mazzucato, D. R. Mikkelsen, D. R. Smith, R. E. Bell, J. C. Hosea, B. P. LeBlanc, J. L. Peterson, H. K. Park, and W. Lee, Physical Review Letters **106**, 055003 (2011).

[99] Y. Ren, S. M. Kaye, E. Mazzucato, W. Guttenfelder, R. E. Bell, C. W. Domier, B. P. LeBlanc, K. C. Lee, N. C. Luhmann, D. R. Smith, and H. Yuh, Physical Review Letters **106**, 165005 (2011).

[100] Y. Ren, W. Guttenfelder, S. M. Kaye, E. Mazzucato, R. E. Bell, A. Diallo, C. W. Domier, B. P. LeBlanc, K. C. Lee, D. R. Smith, and H. Yuh, Physics of Plasmas **19**, 056125 (2012).

[101] J. F. Drake, N. T. Gladd, C. S. Liu, and C. L. Chang, Physical Review Letters **44**, 994 (1980).

[102] J. W. Connor, S. C. Cowley, and R. J. Hastie, Plasma Physics and Controlled Fusion **32**, 799 (1990).

[103] H. Doerk, F. Jenko, M. J. Pueschel, and D. R. Hatch, Physical Review Letters **106**, 155003 (2011).

[104] W. Guttenfelder, J. Candy, S. M. Kaye, W. M. Nevins, E. Wang, R. E. Bell, G. W. Hammett, B. P. LeBlanc, D. R. Mikkelsen, and H. Yuh, Physical Review Letters **106**, 155004 (2011).

[105] D. R. Hatch, M. J. Pueschel, F. Jenko, W. M. Nevins, P. W. Terry, and H. Doerk, Physical Review Letters **108**, 235002 (2012).

[106] P. B. Snyder, N. Aiba, M. Beurskens, R. J. Groebner, L. D. Horton, A. E. Hubbard, J. W. Hughes, G. T. A. Huysmans, Y. Kamada, A. Kirk, C. Konz, . W. Leonard, J. Lönnroth, C. F. Maggi, R. Maingi, T. H. Osborne, N. Oyama, A. Pankin, S. Saarelma, G. Saibene, J. L. Terry, H. Urano, and H. R. Wilson, Nuclear Fusion **49**, 085035 (2009).

[107] B. Coppi, H. P. Furth, M. N. Rosenbluth, and R. Z. Sagdeev, Physical Review Letters **17**, 377 (1966).

[108] T. Görler and F. Jenko, Physics of Plasmas **15**, 102508 (2008).

[109] P. Hennequin, Comptes Rendus Physique **7**, 670 (2006).

[110] A. E. White, L. Schmitz, G. R. McKee, C. Holland, W. A. Peebles, T. A. Carter, M. W. Shafer, M. E. Austin, K. H. Burrell, J. Candy, J. C. DeBoo, E. J. Doyle, M. A. Makowski, R. Prater, T. L. Rhodes, G. M. Staebler, G. R. Tynan, R. E. Waltz, and G. Wang, Physics of Plasmas **15**, 056116 (2008).

[111] R. V. Bravenec, J. Candy, M. Barnes, and C. Holland, Physics of Plasmas **18**, 122505 (2011).

[112] N. Winsor, J. L. Johnson, and J. M. Dawson, Physics of Fluids **11**, 2448 (1968).

[113] R. Hager and K. Hallatschek, Physics of Plasmas **16**, 072503 (2009).

[114] R. Hager and K. Hallatschek, Physics of Plasmas **17**, 032112 (2010).

[115] G. R. McKee, R. J. Fonck, M. Jakubowski, K. H. Burrell, K. Hallatschek, R. A. Moyer, D. L. Rudakov, W. Nevins, G. D. Porter, P. Schoch, and X. Xu, Physics of Plasmas **10**, 1712 (2003).

[116] G. R. McKee, R. J. Fonck, M. Jakubowski, K. H. Burrell, K. Hallatschek, R. A. Moyer, W. Nevins, D. L. Rudakov, and X. Xu, Plasma Physics and Controlled Fusion **45**, A477 (2003).

[117] T. Lan, A. D. Liu, C. X. Yu, L. W. Yan, W. Y. Hong, K. J. Zhao, J. Q. Dong, J. Qian, J. Cheng, D. L. Yu, and Q. W. Yang, Physics of Plasmas **15**, 056105 (2008).

[118] A. D. Liu, T. Lan, C. X. Yu, H. L. Zhao, L. W. Yan, W. Y. Hong, J. Q. Dong, K. J. Zhao, J. Qian, J. Cheng, X. R. Duan, and Y. Liu, Physical Review Letters **103**, 095002 (2009).

[119] Z. Gao, K. Itoh, H. Sanuki, and J. Q. Dong, Physics of Plasmas **15**, 072511 (2008).

[120] Z. Gao, P. Wang, and H. Sanuki, Physics of Plasmas **15**, 4502 (2008).

[121] G. D. Conway, C. Angioni, F. Ryter, P. Sauter, J. Vicente, and A. U. Team, Physical Review Letters **106**, 065001 (2011).

[122] A. Krämer-Flecken, S. Soldatov, H. R. Koslowski, O. Zimmermann, and TEXTOR Team, Physical Review Letters **97**, 045006 (2006).

[123] G. D. Conway, B. Scott, J. Schirmer, M. Reich, A. Kendl, and t. A. Team, Plasma Physics and Controlled Fusion **47**, 1165 (2005).

[124] G. R. McKee, D. K. Gupta, R. J. Fonck, D. J. Schlossberg, M. W. Shafer, and P. Gohil, Plasma Physics and Controlled Fusion **48**, S123 (2006).

[125] G. D. Conway, C. Tröster, B. Scott, K. Hallatschek, and the ASDEX Upgrade Team, Plasma Physics and Controlled Fusion **50**, 055009 (2008).

[126] G. D. Conway and the ASDEX Upgrade Team, Plasma Physics and Controlled Fusion **50**, 085005 (2008).

[127] X. Q. Xu, Z. Xiong, Z. Gao, W. M. Nevins, and G. R. McKee, Physical Review Letters **100**, 215001 (2008).

[128] A. V. Melnikov, V. A. Vershkov, L. G. Eliseev, S. A. Grashin, A. V. Gudozhnik, L. I. Krupnik, S. E. Lysenko, V. A. Mavrin, S. V. Perfilov, D. A. Shelukhin, S. V. Soldatov, M. V. Ufimtsev, A. O. Urazbaev, G. V. Oost, and L. G. Zimeleva, Plasma Physics and Controlled Fusion **48**, S87 (2006).

[129] Y. Nagashima, K. Hoshino, A. Ejiri, K. Shinohara, Y. Takase, K. Tsuzuki, K. Uehara, H. Kawashima, H. Ogawa, T. Ido, Y. Kusama, and Y. Miura, Physical Review Letters **95**, 095002 (2005).

[130] Y. Nagashima, K. Itoh, S.-I. Itoh, K. Hoshino, A. Fujisawa, A. Ejiri, Y. Takase, M. Yagi, K. Shinohara, K. Uehara, Y. Kusama, and JFT-2M Group, Plasma Physics and Controlled Fusion **48**, A377 (2006).

[131] L. Yan, J. Cheng, W. Hong, K. Zhao, T. Lan, J. Dong, A. Liu, C. Yu, D. Yu, J. Qian, Y. Huang, Q. Yang, X. Ding, Y. Liu, and C. Pan, Nuclear Fusion **47**, 1673 (2007).

[132] J. Cheng, L. Yan, K. Zhao, J. Dong, W. Hong, J. Qian, Q. Yang, X. Ding, X. Duan, and Y. Liu, Nuclear Fusion **49**, 085030 (2009).

[133] C. Silva, P. Duarte, H. Fernandes, H. Figueiredo, I. Nedzelskij, C. Hidalgo, and M. A. Pedrosa, Plasma Physics and Controlled Fusion **51**, 085009 (2009).

[134] K. J. Zhao, J. Q. Dong, L. W. Yan, W. Y. Hong, A. Fujisawa, C. X. Yu, Q. Li, J. Qian, J. Cheng, T. Lan, A. D. Liu, H. L. Zhao, D. F. Kong, Y. Huang, Y. Liu, X. M. Song, Q. W. Yang, X. T. Ding, X. R. Duan, and Y. Liu, Plasma Physics and Controlled Fusion **52**, 124008 (2010).

[135] A. D. Liu, T. Lan, C. X. Yu, W. Zhang, H. L. Zhao, D. F. Kong, J. F. Chang, and B. N. Wan, Plasma Physics and Controlled Fusion **52**, 085004 (2010).

[136] T. Ido, Y. Miura, K. Kamiya, Y. Hamada, K. Hoshino, A. Fujisawa, K. Itoh, S.-I. Itoh, A. Nishizawa, H. Ogawa, Y. Kusama, and JFT-2M Group, Plasma Physics and Controlled Fusion **48**, S41 (2006).

[137] T. Ido, Y. Miura, K. Hoshino, K. Kamiya, Y. Hamada, A. Nishizawa, Y. Kawasumi, H. Ogawa, Y. Nagashima, K. Shinohara, Y. Kusama, and JFT-2M Group, Nuclear Fusion **46**, 512 (2006).

[138] K. Itoh, S.-I. Itoh, P. H. Diamond, A. Fujisawa, M. Yagi, T. Watari, Y. Nagashima, and A. Fukuyama, Plasma and Fusion Research **1**, 037 (2006).

[139] Z. Gao, K. Itoh, H. Sanuki, and J. Q. Dong, Physics of Plasmas **13**, 100702 (2006).

[140] F. Zonca and L. Chen, EPL (Europhysics Letters) **83**, 35001 (2008).

[141] A. I. Smolyakov, C. Nguyen, and X. Garbet, Plasma Physics and Controlled Fusion **50**, 115008 (2008).

[142] C. Nguyen, X. Garbet, and A. I. Smolyakov, Physics of Plasmas **15**, 112502 (2008).

[143] A. Kendl, Physics of Plasmas **18**, 072303 (2011).

[144] R. E. Waltz and C. Holland, Physics of Plasmas **15**, 122503 (2008).

[145] C. Holland, G. R. Tynan, R. J. Fonck, G. R. McKee, J. Candy, and R. E. Waltz, Physics of Plasmas **14**, 056112 (2007).

[146] F. Liu, Z. Lin, J. Q. Dong, and K. J. Zhao, Physics of Plasmas **17**, 112318 (2010).

[147] M. Abramowitz and I. A. Stegun, *Handbook of Mathematical Functions: with Formulas, Graphs, and Mathematical Tables* (Dover Publications, 1965).

[148] P. W. Terry, M. Greenwald, J.-N. Leboeuf, G. R. McKee, D. R. Mikkelsen, W. M. Nevins, D. E. Newman, D. P. Stotler, Task Group on Verification and Validation, U. B. P. Organization, and U. T. T. Force, Physics of Plasmas **15**, 062503 (2008).

[149] M. Greenwald, Physics of Plasmas **17**, 058101 (2010).

[150] W. M. Nevins, G. W. Hammett, A. M. Dimits, W. Dorland, and D. E. Shumaker, Physics of Plasmas **12**, 122305 (2005).

[151] A. Casati, T. Gerbaud, P. Hennequin, C. Bourdelle, J. Candy, F. Clairet, X. Garbet, V. Grandgirard, . D. Grcan, S. Heuraux, G. T. Hoang, C. Honor, F. Imbeaux, R. Sabot, Y. Sarazin, L. Vermare, and R. E. Waltz, Physical Review Letters **102**, 165005 (2009).

[152] C. Bourdelle, T. Gerbaud, L. Vermare, A. Casati, T. Aniel, J. Artaud, V. Basiuk, J. Bucalossi, F. Clairet, Y. Corre, P. Devynck, G. Falchetto, C. Fenzi, X. Garbet, R. Guirlet, . Grcan, S. Heuraux, P. Hennequin, G. Hoang, F. Imbeaux, L. Manenc,

P. Monier-Garbet, P. Moreau, R. Sabot, J.-L. Sgui, A. Sirinelli, D. Villegas, and the Tore Supra Team, Nuclear Fusion **51**, 063037 (2011).

[153] L. Lin, M. Porkolab, E. M. Edlund, J. C. Rost, C. L. Fiore, M. Greenwald, Y. Lin, D. R. Mikkelsen, N. Tsujii, and S. J. Wukitch, Physics of Plasmas **16**, 012502 (2009).

[154] L. Lin, M. Porkolab, E. M. Edlund, J. C. Rost, M. Greenwald, N. Tsujii, J. Candy, R. E. Waltz, and D. R. Mikkelsen, Plasma Physics and Controlled Fusion **51**, 065006 (2009).

[155] M. W. Shafer, R. J. Fonck, G. R. McKee, C. Holland, A. E. White, and D. J. Schlossberg, Physics of Plasmas **19**, 032504 (2012).

[156] C. Holland, A. E. White, G. R. McKee, M. W. Shafer, J. Candy, R. E. Waltz, L. Schmitz, and G. R. Tynan, Physics of Plasmas **16**, 052301 (2009).

[157] J. Luxon, Nuclear Fusion **42**, 614 (2002).

[158] E. Holzhauer, M. Hirsch, T. Grossmann, B. Brañas, and F. Serra, Plasma Physics and Controlled Fusion **40**, 1869 (1998).

[159] M. Hirsch, E. Holzhauer, J. Baldzuhn, B. Kurzan, and B. Scott, Plasma Physics and Controlled Fusion **43**, 1641 (2001).

[160] E. Z. Gusakov and A. V. Surkov, Plasma Physics and Controlled Fusion **46**, 1143 (2004).

[161] C. Lechte, IEEE Transactions on Plasma Science **37**, 1099 (2009).

[162] M. Hirsch and E. Holzhauer, Plasma Physics and Controlled Fusion **46**, 593 (2004).

[163] T. Happel, E. Blanco, and T. Estrada, Review of Scientific Instruments **81**, 10D901 (2010).

[164] G. D. Conway, J. Schirmer, S. Klenge, W. Suttrop, E. Holzhauer, and the ASDEX Upgrade Team, Plasma Physics and Controlled Fusion **46**, 951 (2004).

[165] J. Schirmer, G. D. Conway, H. Zohm, W. Suttrop, and the ASDEX Upgrade Team, Nuclear Fusion **46**, S780 (2006).

[166] E. Trier, L.-G. Eriksson, P. Hennequin, C. Fenzi, C. Bourdelle, G. Falchetto, X. Garbet, T. Aniel, F. Clairet, and R. Sabot, Nuclear Fusion **48**, 092001 (2008).

[167] T. Estrada, T. Happel, L. Eliseev, D. Lpez-Bruna, E. Ascasbar, E. Blanco, L. Cupido, J. M. Fontdecaba, C. Hidalgo, R. Jimnez-Gmez, L. Krupnik, M. Liniers, M. E. Manso, K. J. McCarthy, F. Medina, A. Melnikov, B. van Milligen, M. A. Ochando, I. Pastor, M. A. Pedrosa, F. L. Tabars, D. Tafalla, and TJ-II Team, Plasma Physics and Controlled Fusion **51**, 124015 (2009).

[168] J. Schirmer, G. D. Conway, E. Holzhauer, W. Suttrop, H. Zohm, and the ASDEX Upgrade Team, Plasma Physics and Controlled Fusion **49**, 1019 (2007).

[169] R. Nazikian, G. J. Kramer, and E. Valeo, Physics of Plasmas **8**, 1840 (2001).

[170] R. Nazikian and E. Mazzucato, Review of Scientific Instruments **66**, 392 (1995).

[171] V. A. Vershkov, V. V. Dreval, and S. V. Soldatov, Review of Scientific Instruments **70**, 1700 (1999).

[172] E. de la Luna, J. Sanchez, V. Zhuravlev, I. Garcia-Cortes, G. R. Hanson, J. B. Wilgen, J. H. Harris, J. Dunlap, R. Kaita, B. Leblanc, the PBX-M Team, G. R. Tynan, L. Schmitz, and L. Blush, Review of Scientific Instruments **66**, 403 (1995).

[173] M. Hirsch, H.-J. Hartfuss, T. Geist, and E. de la Luna, Review of Scientific Instruments **67**, 1807 (1996).

[174] G. R. Hanson, J. B. Wilgen, T. S. Bigelow, I. Collazo, and C. E. Thomas, Review of Scientific Instruments **63**, 4658 (1992).

[175] A. E. White, *Experimental Study of Electron Temperature Fluctuations in the DIII-D Tokamak*, Ph.D. thesis, University of California, Los Angeles (2008).

[176] L. Lao, H. St. John, R. Stambaugh, A. Kellman, and W. Pfeiffer, Nuclear Fusion **25**, 1611 (1985).

[177] A. P. Smirnov and R. W. Harvey, Bull. Am. Phys. Soc. **40**, 1837 (1995).

[178] G. Conway, C. Angioni, R. Dux, F. Ryter, A. Peeters, J. Schirmer, C. Troester, C. R. Group, and t. A. U. team, Nuclear Fusion **46**, S799 (2006).

[179] P. Hennequin, C. Honore, A. Truc, A. Quemeneur, N. Lemoine, J.-M. Chareau, and R. Sabot, Review of Scientific Instruments **75**, 3881 (2004).

[180] T. Happel, T. Estrada, E. Blanco, V. Tribaldos, A. Cappa, and A. Bustos, Review of Scientific Instruments **80**, 073502 (2009).

[181] V. V. Bulanin, L. G. Askinazi, S. V. Lebedev, M. V. Gorohov, V. A. Kornev, A. V. Petrov, A. S. Tukachinsky, and M. I. Vildjunas, Plasma Physics and Controlled Fusion **48**, A101 (2006).

[182] L. Vermare, P. Hennequin, O. D. Gürcan, and the Tore Supra Team, Nuclear Fusion **52**, 10.1088/0029-5515/52/6/063008.

[183] T. Estrada, T. Happel, and E. Blanco, Nuclear Fusion **52**, 082002 (2012).

[184] C. Honor, P. Hennequin, A. Truc, and A. Qumneur, Nuclear Fusion **46**, S809 (2006).

[185] L. D. Landau and E. Lifshitz, *The Classical Theory of Fields, Fourth Edition: Volume 2*, 4th ed. (Butterworth-Heinemann, 1980).

[186] R. Prater, D. Farina, Y. Gribov, R. Harvey, A. Ram, Y.-R. Lin-Liu, E. Poli, A. Smirnov, F. Volpe, E. Westerhof, A. Zvonkov, and the ITPA Steady State Operation Topical Group, Nuclear Fusion **48**, 035006 (2008).

[187] K. H. Burrell, Plasma Physics and Controlled Fusion **48**, A347 (2006).

[188] H. Hojo, Y. Kurosawa, and A. Mase, Review of Scientific Instruments **70**, 983 (1999).

[189] B. C. Rose, S. Kubota, and W. A. Peebles, 18^{th} Topical High Temperature Plasmas Diagnostics Conference, Wildwood, NJ (2010).

[190] A. E. White, L. Schmitz, G. R. McKee, C. Holland, W. A. Peebles, T. A. Carter, M. W. Shafer, M. E. Austin, K. H. Burrell, J. Candy, J. C. DeBoo, E. J. Doyle, M. A. Makowski, R. Prater, T. L. Rhodes, G. M. Staebler, G. R. Tynan, R. E. Waltz, and G. Wang, Physics of Plasmas **15**, 056116 (2008).

[191] J. C. Rost, L. Lin, and M. Porkolab, Physics of Plasmas **17**, 062506 (2010).

[192] S. Leerink, V. V. Bulanin, E. Z. Gusakov, J. A. Heikkinen, S. J. Janhunen, T. P. Kiviniemi, T. Korpilo, M. Nora, and F. Ogando, Contributions to Plasma Physics **50**, 242 (2010).

[193] F. da Silva, S. Heuraux, N. Lemoine, C. Honorè, P. Hennequin, M. Manso, and R. Sabot, Review of Scientific Instruments **75**, 3816 (2004).

[194] E. Blanco, T. Estrada, and J. Sãnchez, Plasma Physics and Controlled Fusion **48**, 699 (2006).

[195] E. Blanco and T. Estrada, Plasma Physics and Controlled Fusion **50**, 095011 (2008).

[196] Y. Ishii, H. Hojo, A. Mase, M. Yoshikawa, M. Ichimura, Y. Haraguchi, and T. Imai, Plasma and Fusion Research **5**, S2094 (2010).

[197] G. D. Conway, B. Kurzan, B. Scott, E. Holzhauer, and M. Kaufmann, Plasma Physics and Controlled Fusion **44**, 451 (2002).

[198] Y. Lin, R. Nazikian, J. H. Irby, and E. S. Marmar, Plasma Physics and Controlled Fusion **43**, L1 (2001).

[199] E. Z. Gusakov, G. Leclert, I. Boucher, S. Heuraux, S. Hacquin, M. Colin, V. V. Bulanin, A. V. Petrov, B. O. Yakovlev, F. Clairet, and X. L. Zou, Plasma Physics and Controlled Fusion **44**, 1565 (2002).

[200] E. Z. Gusakov, A. V. Surkov, and A. Y. Popov, Plasma Physics and Controlled Fusion **47**, 959 (2005).

[201] G. Bekefi, *Radiation processes in plasmas*, 1st ed. (Wiley, 1966).

[202] E. Holzhauer and J. H. Massig, Plasma Physics **20**, 867 (1978).

[203] R. E. Slusher and C. M. Surko, Physics of Fluids **23**, 472 (1980).

[204] P.-A. Gourdain and W. A. Peebles, Plasma Physics and Controlled Fusion **50**, 025004 (2008).

[205] P.-A. Gourdain and W. A. Peebles, Review of Scientific Instruments **79**, 10F102 (2008).

[206] A. Truc, A. Quéméneur, P. Hennequin, D. Grésillon, F. Gervais, C. Laviron, J. Olivain, S. K. Saha, and P. Devynck, Review of Scientific Instruments **63**, 3716 (1992).

[207] P. Devynck, X. Garbet, C. Laviron, J. Payan, S. K. Saha, F. Gervais, P. Hennequin, A. Quemeneur, and A. Truc, Plasma Physics and Controlled Fusion **35**, 63 (1993).

[208] T. L. Rhodes, W. A. Peebles, X. Nguyen, M. A. VanZeeland, J. S. deGrassie, E. J. Doyle, G. Wang, and L. Zeng, Review of Scientific Instruments **77**, 10E922 (2006).

[209] M. Bornatici, R. Cano, O. De Barbieri, and F. Engelmann, Nuclear Fusion **23**, 1153 (1983).

[210] G. Cima, R. V. Bravenec, A. J. Wootton, T. D. Rempel, R. F. Gandy, C. Watts, and M. Kwon, Physics of Plasmas **2**, 720 (1995).

[211] I. H. Hutchinson, *Principles of Plasma Diagnostics*, 2nd ed. (Cambridge University Press, 2005).

[212] C. Watts, H. J. Hartfuss, and M. Hase, Review of Scientific Instruments **75**, 3177 (2004).

[213] A. D. Piliya and A. Y. Popov, Plasma Physics and Controlled Fusion **44**, 2051 (2002).

[214] C. Watts, R. F. Gandy, and G. Cima, Physical Review Letters **76**, 2274 (1996).

[215] M. E. Austin and J. Lohr, Review of Scientific Instruments **74**, 1457 (2003).

[216] A. I. Anisimov and et al., Soviet Phys. Technical Phys **5**, 9 (1961).

[217] R. J. Colchin, ORMAK Technical Memo no. 93/105 (1973).

[218] E. Mazzucato, Bull. Am. Phys. Soc. **20**, 1241 (1975).

[219] A. E. Costley, P. Cripwell, R. Prentice, and A. C. C. Sips, Review of Scientific Instruments **61**, 2823 (1990).

[220] T. L. Rhodes, W. A. Peebles, and E. J. Doyle, Review of Scientific Instruments **63**, 4661 (1992).

[221] J. Sanchez, B. Braas, E. de la Luna, and T. Estrada, Review of Scientific Instruments **64**, 487 (1993).

[222] M. Gilmore, W. A. Peebles, and X. V. Nguyen, Review of Scientific Instruments **70**, 1085 (1999).

[223] M. Gilmore, W. A. Peebles, and X. V. Nguyen, Review of Scientific Instruments **72**, 293 (2001).

[224] L. Zeng, W. A. Peebles, E. J. Doyle, T. L. Rhodes, and G. Wang, Plasma Physics and Controlled Fusion **49**, 1277 (2007).

[225] N. A. Crocker, W. A. Peebles, S. Kubota, J. Zhang, R. E. Bell, E. D. Fredrickson, N. N. Gorelenkov, B. P. LeBlanc, J. E. Menard, M. Podest, S. A. Sabbagh, K. Tritz, and H. Yuh, Plasma Physics and Controlled Fusion **53**, 105001 (2011).

[226] E. Mazzucato, Plasma Physics and Controlled Fusion **46**, 1271 (2004).

[227] T. L. Rhodes, R. J. Taylor, and W. A. Peebles, Review of Scientific Instruments **66**, 824 (1995).

[228] T. L. Rhodes, W. A. Peebles, E. J. Doyle, P. Pribyl, M. Gilmore, R. A. Moyer, and R. D. Lehmer, Plasma Physics and Controlled Fusion **40**, 493 (1998).

[229] M. Gilmore, W. A. Peebles, and X. V. Nguyen, Plasma Physics and Controlled Fusion **42**, L1 (2000).

[230] T. Munsat, E. Mazzucato, H. Park, C. W. Domier, N. C. Luhmann, A. J. H. Donn, and M. v. d. Pol, Plasma Physics and Controlled Fusion **45**, 469 (2003).

[231] M. Hase, M. Hirsch, and H. J. Hartfuss, Review of Scientific Instruments **70**, 1014 (1999).

[232] E. Blanco, T. Estrada, and T. Happel, in *Proc. 9th Intl. Reflectometry Workshop - IRW9* (2009).

[233] H. Sugama and T.-H. Watanabe, Physics of Plasmas **13**, 012501 (2006).

[234] A. Krmer-Flecken, S. Soldatov, D. Reiser, M. Kantor, and H. R. Koslowski, Plasma Physics and Controlled Fusion **51**, 015001 (2009).

[235] N. Kasuya, M. Yagi, M. Azumi, K. Itoh, and S.-I. Itoh, Journal of the Physical Society of Japan **76**, 044501 (2007).

[236] P. Popovich, M. V. Umansky, T. A. Carter, and B. Friedman, Physics of Plasmas **17**, 122312 (2010).

[237] M. V. Umansky, P. Popovich, T. A. Carter, B. Friedman, and W. M. Nevins, Physics of Plasmas **18**, 055709 (2011).

[238] J. D. Huba, *NRL Plasma Formulary* (Naval Research Laboratory, Washington, DC, 2009).

[239] R. K. Janev, W. D. Langer, and K. Evans, *Elementary processes in Hydrogen-Helium plasmas - Cross sections and reaction rate coefficients*, Springer Series on Atoms and Plasmas (Springer, Berlin, 1987).

[240] D. K. Gupta, R. J. Fonck, G. R. McKee, D. J. Schlossberg, and M. W. Shafer, Physical Review Letters **97**, 125002 (2006).

[241] T. S. Hahm, M. A. Beer, Z. Lin, G. W. Hammett, W. W. Lee, and W. M. Tang, Physics of Plasmas **6**, 922 (1999).

[242] K. Hallatschek and R. Hager, Proceedings of the 23rd IAEA Fusion Energy Conference, Daejeon , THC/P8 (2010).

[243] T. Estrada, C. Hidalgo, T. Happel, and P. H. Diamond, Physical Review Letters **107**, 245004 (2011).

[244] Y. Sechrest, T. Munsat, D. A. DIppolito, R. J. Maqueda, J. R. Myra, D. Russell, and S. J. Zweben, Physics of Plasmas **18**, 012502 (2011).

[245] G. S. Xu, B. N. Wan, H. Q. Wang, H. Y. Guo, H. L. Zhao, A. D. Liu, V. Naulin, P. H. Diamond, G. R. Tynan, M. Xu, R. Chen, M. Jiang, P. Liu, N. Yan, W. Zhang, L. Wang, S. C. Liu, and S. Y. Ding, Physical Review Letters **107**, 125001 (2011).

[246] H. team, M. Xu, G. R. Tynan, P. H. Diamond, P. Manz, C. Holland, N. Fedorczak, S. C. Thakur, J. H. Yu, K. J. Zhao, J. Q. Dong, J. Cheng, W. Y. Hong, L. W. Yan, Q. W. Yang, X. M. Song, Y. Huang, L. Z. Cai, W. L. Zhong, Z. B. Shi, X. T. Ding, X. R. Duan, and Y. Liu, Physical Review Letters **108**, 245001 (2012).

[247] P. Mantica, D. Strintzi, T. Tala, C. Giroud, T. Johnson, H. Leggate, E. Lerche, T. Loarer, A. G. Peeters, A. Salmi, S. Sharapov, D. Van Eester, P. C. de Vries, L. Zabeo, and K.-D. Zastrow, Physical Review Letters **102**, 175002 (2009).

[248] P. Mantica, C. Angioni, C. Challis, G. Colyer, L. Frassinetti, N. Hawkes, T. Johnson, M. Tsalas, P. C. deVries, J. Weiland, B. Baiocchi, M. N. A. Beurskens, A. C. A. Figueiredo, C. Giroud, J. Hobirk, E. Joffrin, E. Lerche, V. Naulin, A. G. Peeters, A. Salmi, C. Sozzi, D. Strintzi, G. Staebler, T. Tala, D. Van Eester, and T. Versloot, Physical Review Letters **107**, 135004 (2011).

[249] G. T. Hoang, C. Bourdelle, X. Garbet, G. Giruzzi, T. Aniel, M. Ottaviani, W. Horton, P. Zhu, and R. V. Budny, Physical Review Letters **87**, 125001 (2001).

[250] D. R. Baker, C. M. Greenfield, K. H. Burrell, J. C. DeBoo, E. J. Doyle, R. J. Groebner, T. C. Luce, C. C. Petty, B. W. Stallard, D. M. Thomas, M. R. Wade, and D. Team, Physics of Plasmas **8**, 4128 (2001).

[251] Y. Camenen, A. Pochelon, A. Bottino, S. Coda, F. Ryter, O. Sauter, R. Behn, T. P. Goodman, M. A. Henderson, A. Karpushov, L. Porte, and G. Zhuang, Plasma Physics and Controlled Fusion **47**, 1971 (2005).

[252] P. Deschamps, R. Gravier, C. Renaud, and A. Samain, Physical Review Letters **31**, 1457 (1973).

[253] A. K. Sen, J. Chen, and M. Mauel, Physical Review Letters **66**, 429 (1991).

[254] X. Wei, V. Sokolov, and A. K. Sen, Physics of Plasmas **17**, 042108 (2010).

[255] D. R. Smith, E. Mazzucato, W. Lee, H. K. Park, C. W. Domier, and N. C. Luhmann, Review of Scientific Instruments **79**, 123501 (2008).

[256] T. L. Rhodes, W. A. Peebles, M. A. Van Zeeland, J. S. deGrassie, R. V. Bravenec, K. H. Burrell, J. C. DeBoo, J. Lohr, C. C. Petty, X. V. Nguyen, E. J. Doyle, C. M. Greenfield, L. Zeng, and G. Wang, Physics of Plasmas **14**, 056117 (2007).

[257] J. Kinsey, G. Staebler, J. Candy, R. Waltz, and R. Budny, Nuclear Fusion **51**, 083001 (2011).

[258] H. E. S. John, T. S. Taylor, Y. R. Lin-Liu, and A. D. Turnball, Plasma Phys. Control. Nucl. Fusion Research **3**, 603 (1994).

[259] W. W. Heidbrink, J. M. Park, M. Murakami, C. C. Petty, C. Holcomb, and M. A. Van Zeeland, Physical Review Letters **103**, 175001 (2009).

[260] G. McKee, R. Ashley, R. Durst, R. Fonck, M. Jakubowski, K. Tritz, K. Burrell, C. Greenfield, and J. Robinson, Review of Scientific Instruments **70**, 913 (1999).

[261] F. Imbeaux and X. Garbet, Plasma Physics and Controlled Fusion **44**, 1425 (2002).

[262] A. Casati, C. Bourdelle, X. Garbet, and F. Imbeaux, Physics of Plasmas **15**, 042310 (2008).

[263] A. G. Peeters, C. Angioni, M. Apostoliceanu, F. Jenko, F. Ryter, and the ASDEX Upgrade team, Physics of Plasmas **12**, 022505 (2005).

[264] B. D. Scott, New Journal of Physics **4**, 52 (2002).

[265] K. D. Makwana, P. W. Terry, J.-H. Kim, and D. R. Hatch, Physics of Plasmas **18**, 012302 (2011).

[266] W. M. Nevins, E. Wang, and J. Candy, Physical Review Letters **106**, 065003 (2011).

[267] E. Wang, W. M. Nevins, J. Candy, D. Hatch, P. Terry, and W. Guttenfelder, Physics of Plasmas **18**, 056111 (2011).

[268] J. Rice, A. Ince-Cushman, J. deGrassie, L.-G. Eriksson, Y. Sakamoto, A. Scarabosio, A. Bortolon, K. Burrell, B. Duval, C. Fenzi-Bonizec, M. Greenwald, R. Groebner, G. Hoang, Y. Koide, E. Marmar, A. Pochelon, and Y. Podpaly, Nuclear Fusion **47**, 1618 (2007).

[269] Y. C. Kim and E. J. Powers, IEEE Transactions on Plasma Science **7**, 120 (1979).

[270] J. S. Bendat and A. G. Piersol, *Random Data: Analysis & Measurement Procedures*, 3rd ed. (Wiley-Interscience, 2000).

[271] K. Itoh, Y. Nagashima, S.-I. Itoh, P. H. Diamond, A. Fujisawa, M. Yagi, and A. Fukuyama, Physics of Plasmas **12**, 102301 (2005).

[272] E. Z. Gusakov, S. Heuraux, and A. Y. Popov, Plasma Physics and Controlled Fusion **51**, 065018 (2009).

[273] W. W. Heidbrink, Physics of Plasmas **15**, 055501 (2008).

[274] Z. Yan, G. R. McKee, R. J. Groebner, P. B. Snyder, T. H. Osborne, and K. H. Burrell, Physical Review Letters **107**, 055004 (2011).